MEASUREMENT AND CALCULATION OF LIBERATION IN CONTINUOUS MILLING CIRCUITS

by

Claudio Luiz Schneider

A dissertation submitted to the Faculty of
The University of Utah
in partial fulfillment of the requirements for the degree of

Doctor of Philosophy

Department of Metallurgical Engineering

The University of Utah

August 1995

ABSTRACT

The liberation phenomenon is of paramount importance in mineral processing science; however, it is generally not well understood, primarily because the liberation spectrum in a particle population is very difficult to measure by any means. In this work, a complete procedure based on Image Analysis and Stereology is proposed for the measurement of the binary liberation spectra in two-phase particles that are in narrow size ranges. The procedure includes a technique for the measurement of the transformation function that relates one- and three-dimensional spectra based on dense liquid fractionation, a model for the transformation function based on the incomplete beta function and a solution to the Fredholm Integral equation of the first kind associated with the stereological correction problem. The transformation function was successfully measured and calibrated for a Dolomite-Sphalerite ore. The measurement procedure is shown to be consistent throughout the work. A symmetrical transformation function for ores with nearly symmetrical texture is derived from the test texture of the test ore.

With a successful procedure for measuring the liberation spectra, at least in the test ore, it was possible to carry out the first experimental measurement of the quadrivariate breakage, including its internal structure. The measurement was successful, and a complete model, also based on the incomplete beta function, for the quadrivariate breakage function is proposed and calibrated for the test ore. The model was implemented in MODSIM, a simulation package, with King's solution to the population

balance model equation that includes the liberation phenomenon.

An emulated closed continuous grinding experiment, under controlled lab conditions, was carried out to verify the liberation model and King's calculation procedure. The unitary operations, namely the ball mill and the elutriator, were characterized and modeled in detail, so that the results from the liberation calculation were not masked by any other phenomena in the experimental. The liberation calculation was successful; however it required a value for the geometrical texture parameter different than predicted, indicating that the parameter is probably dependent on particle size.

Finally, an industrial grinding circuit that process Taconite ore was characterized with respect to liberation. The Taconite texture is nearly symmetrical, and stereological correction using the symmetric transformation function proved to be consistent. The liberation model had to be adjusted according to the Taconite texture, showing that reparameterization alone was not sufficient. Circuit simulation with the adjusted model was successful, showing excellent agreement between measured and calculated liberation spectra.

In memory of Andre Barreta Graff

TABLE OF CONTENTS

LIST OF TABLES

LIST OF FIGURES

LIST OF SYMBOLS

$absorbance^{j}$	Average absorbance of liquid phase in time interval j
A	Index that designates the continuous, usually gangue, phase
$b(D;D')$	Bivariate breakage function. Fraction, by weight, of particles that report to size D from breakage of particles that have size D'
$b(D;g',D')$	Fraction, by weight, of particles that report to size D from breakage of particles that have grade g' and size D'
$b(g,D;g',D')$	Quadrivariate breakage function. Fraction, by weight, of particles that report to grade g and size D, from breakage of particles that have grade g' and size D'
$b(g,D/D';g')$	Normalized quadrivariate breakage function. Fraction, by weight, of particles that report to grade g and fractional size D/D', from breakage of particles that have grade g'
$b(g \mid D;g',D')$	Conditional quadrivariate breakage function. Fraction, by weight, of particles that report to grade g that have size D, from breakage of particles that have grade g' and size D'
$b(g_v \mid D;g_v',D')$	Conditional quadrivariate breakage function. Fraction, by weight, of particles that report to volumetric grade g_v that have size D, from breakage of particles that have volumetric grade g_v' and size D'
b_{ij}	The discrete bivariate breakage function. Fraction, by weight, of particles that report to size class i, from breakage of particles that are in size class j
b_{ℓ}^{klij}	Fraction, by length, of particles that report to linear grade range

$\left(g_\ell^{\,k}, g_\ell^{\,k-1}\right)$ that are in size range $\left(D^{\,l}, D^{\,l-1}\right)$ from breakage of particles in volumetric grade range $\left(g_v'^{\,j}, g_v'^{\,j-1}\right)$ and size range $\left(D'^{\,i}, D'^{\,i-1}\right)$

$b_\ell\left(g_\ell \mid D; g_v', D'\right)$ Fraction, by length, of particles that report linear grade g_ℓ that have size *D*, from breakage of particles that have volumetric grade g_v' and size D'

b_v^{klij} The discrete, conditional on progeny size, quadrivariate breakage function. Fraction, by volume, of particles that report to volumetric grade range $\left(g_v^{\,k}, g_v^{\,k-1}\right)$ that are in size range $\left(D^{\,l}, D^{\,l-1}\right)$ from breakage of particles in volumetric grade range $\left(g_v'^{\,j}, g_v'^{\,j-1}\right)$ and size range $\left(D'^{\,i}, D'^{\,i-1}\right)$

$b_v\left(g_v \mid D; g_v', D'\right)$ Conditional quadrivariate breakage function. Fraction, by volume, of particles that report to volumetric grade g_v that have size *D*, from breakage of particles that have volumetric grade g_v' and size D'

$b_v^{kl}\left(g_v', D'\right)$ Fraction, by volume, of particles that report to volumetric grade range $\left(g_v^{\,k}, g_v^{\,k-1}\right)$ that are in size range $\left(D^{\,l}, D^{\,l-1}\right)$ from breakage of particles that have volumetric grade g_v' and size D'

B Index that designates the dispersed, usually ore mineral, phase

$B\left(\alpha, \beta\right)$ Beta function

B_{ij} The discrete, cumulative bivariate breakage function. Cumulative fraction, by weight, of particles that report to size class *i* and smaller, from breakage of particles that are in size class *j*

$B_v\left(g_v \mid D; g_v', D'\right)$ Cumulative fraction, by volume, of particles that report to volumetric grade g_v that have size *D*, from breakage of particles that have volumetric grade g_v' and size D'

$B_v\left(g_v^{\,k} \mid D; g_v', D'\right)$ Cumulative fraction, by volume, of particles that report to volumetric grade range $\left(g_v^{\,k}, g_v^{\,k-1}\right)$ that have size *D*, from breakage of particles

	that have volumetric grade g_v' and size D'
$B_{vu}(g_v \mid D; g_v', D')$	Cumulative fraction, by volume, of unliberated particles that report to volumetric grade g_v that have size D, from breakage of particles that have volumetric grade g_v' and size D'
$c(d_p, g_v)$	Actual classification function in terms of representative size and volumetric grade used in hydrocyclone model
$c(g_v, d_p)$	Actual classification function in terms of volumetric grade and representative size used in wet magnetic drum separation model
$c(t)$	Tracer concentration distribution density
$c(v_t)$	Actual classification function in terms of terminal settling velocity used in elutriator model
c^j	Average tracer concentration in time interval j
C_i	Classification factor in postclassification model for particles that are in size class i used in the discrete *PBM* model
CPU	Central Processing Unit
d_{50}	Parameter in postclassification function model representing the size of a particle that have equal probability of reporting to the underflow and overflow of the classifier (microns), used in the discrete *PBM* model; parameter in hydrocyclone model, equation 5.11
$d_{\max}$	Maximum ball size in a mill charge
d_p	Representative size of particles in a narrow size range
$d_p^{50}(g_v)$	Size of a particle that have equal probability of reporting to the underflow and overflow of the hydrocyclone classifier, as a function

	of particle volumetric grade
d_{pi}	Representative size of particles in a narrow size class i
D	Particle size; progeny particle size; mesh size
D'	Parent particle size; mesh size
D'^{n}	Size of parent particles at a node in the finite difference scheme
D'^{*}	Size range of parent particles
D^{*}	A finite range of particle sizes
$D_{\max}$	Maximum size in a narrow size range
$D_{\min}$	Minimum size in a narrow size range
D_{mill}	Mill internal diameter
D_A	Liberation size associated to the boundary of the accessible region that is associated to phase A
D_A^V	Limiting liberation size associated to phase A from phase volume constraints
$D_A\left(g_v;g_v',D'\right)$	Size on the boundary of the accessible region associated to phase A corresponding to volumetric grade g_v, originating at volumetric grade g_v' and size D'
$D_A^V\left(g_v;g_v',D'\right)$	Size on the limiting boundary of the accessible region associated to phase A corresponding to volumetric grade g_v, originating at volumetric grade g_v' and size D'
D_B	Liberation size associated to the boundary of the accessible region that

	is associated to phase B
D_B^V	Limiting liberation size associated to phase B from phase volume constraints
$D_B(g_v;g_v',D')$	Size on the boundary of the accessible region associated to phase B corresponding to volumetric grade g_v, originating at volumetric grade g_v' and size D'
$D_B^V(g_v;g_v',D')$	Size on the limiting boundary of the accessible region associated to phase B corresponding to volumetric grade g_v, originating at volumetric grade g_v' and size D'
$e(d_p,g_v)$	Corrected classification function in terms of representative size and volumetric grade used in hydrocyclone model
$e(g_v)$	Corrected classification function in terms of volumetric grade used in wet magnetic drum separator model
$e(v_t)$	Corrected classification function in terms of terminal velocity used in elutriator model
$f(\phi)$	Ratio between liberation and limiting liberation sizes, as a function of the geometrical texture parameter
$f(g,D)$	The distribution density, by weight, of particles that have grade g and size D in the feed to a perfectly mixed mill region in the continuous *PBM* equation
f_c	Fraction of mill volume filled by powder
f_i	Fraction, by weight, of particles in size class i, in the feed to a mill
$f_\ell^j(g_\ell \mid D^*)$	Linear grade distribution density, weighted by length, that is generated by particles in a finite size range and in volumetric grade range j

f_v	The discrete volumetric grade distribution density, by volume
f_v^j	Fraction, by volume, of particles in volumetric grade range j
f_v^l	Fraction, by volume, of particles in progeny size range $\langle D^l, D^{l-1} \rangle$
f_v^{lij}	Fraction, by volume, of particles in progeny size range $\langle D^l, D^{l-1} \rangle$ from breakage of particles in volumetric grade range $\left(g_v'^j, g_v'^{j-1} \right)$ and in size range $\langle D'^i, D'^{i-1} \rangle$
$f_v\langle D \rangle$	Volume-weighted particle size distribution density
$f_v\langle D; g_v', D' \rangle$	Volume-weighted particle size distribution density in the progeny from breakage of particles that have volumetric grade g_v' and size D'
$f_v\langle g_v \mid D \rangle$	Volume-weighted, conditional on size, volumetric grade distribution density
$f_v\left(g_v \mid D^* \right)$	Volume-weighted volumetric grade distribution density of particles in a finite size range
$f_v\langle g_v', D' \rangle$	Volume-weighted volumetric grade g_v' and size D' distribution density in the parent particles
f_{vu}^j	Fraction, by volume, of unliberated particles in volumetric grade range j
$f_{vu}\left(g_v \mid D^* \right)$	Volume-weighted unliberated volumetric grade distribution density of particles in a finite size range
f_w^j	Fraction, by weight, of particles in volumetric grade range j
f_w^{lij}	Fraction, by weight, of particles in progeny size range $\langle D^l, D^{l-1} \rangle$ from breakage of particles in volumetric grade range $\left(g_v'^j, g_v'^{j-1} \right)$ and in size range $\langle D'^i, D'^{i-1} \rangle$

$f_w(g_v \mid D)$ Mass-weighted, conditional on size, volumetric grade distribution density

$f_w(D; g_v', D')$ Particle size distribution density, by weight, in the progeny from breakage of particles that have volumetric grade g_v' and size D'

F_i Cumulative fraction, by weight, of particles in and below size class *i*, in the feed to a mill

F_ℓ The discrete, cumulative linear grade distribution density, by length

F_ℓ^i A cumulative fraction in the discrete cumulative linear grade distribution, by length. Here, *i* is used as an index to a linear grade class

$\overline{F_\ell^i}$ A measured cumulative fraction in the discrete cumulative linear grade distribution, by length. Here, *i* is used as an index to a linear grade class

$\hat{F}_\ell^i$ A calculated cumulative fraction in the discrete cumulative linear grade distribution, by length. Here, *i* is used as an index to a linear grade class

$F_\ell(g_\ell \mid D^*)$ Cumulative linear grade distribution, weighted by length, that is generated by particles in a finite size range

$F_\ell^j(g_\ell \mid D^*)$ Cumulative linear grade distribution, weighted by length, that is generated by particles in a finite size range and in volumetric grade class *j*

$F_\ell(g_\ell \mid g_v)$ Cumulative, conditional on volumetric grade, linear grade distribution weighted by length

$F_{\ell u}(g_\ell \mid g_v)$ Cumulative, conditional on volumetric grade, unliberated linear grade distribution weighted by length

$F_{\ell u}^{j}\left(g_{\ell} \mid D^{*}\right)$	Cumulative unliberated linear grade distribution, weighted by length, that is generated by particles in a finite size range and in volumetric grade class *j*
F_{v}^{lij}	Cumulative fraction, by volume, of particles in progeny size range $\left\langle D^{l}, D^{l-1}\right\rangle$ from breakage of particles in volumetric grade range $\left(g_{v}'^{j}, g_{v}'^{j-1}\right)$ and in size range $\left\langle D'^{i}, D'^{i-1}\right\rangle$
$F_{v}\left(D; g_{v}', D'\right)$	Cumulative volume-weighted particle size distribution in the progeny from breakage of particles that have volumetric grade g_{v}' and size D'
$F_{vu}\left(g_{v} \mid D^{*}\right)$	Cumulative unliberated volumetric grade distribution, weighted by volume, that is generated by particles in a finite size range
g	Fraction, by weight, of phase *B* in progeny particle; progeny grade
g'	Fraction, by weight, of phase *B* in parent particle; parent grade
g'^{m}	Volumetric grade of parent particles at a node in the finite difference scheme
g'^{*}	Grade range of parent particles
g_{ℓ}	Fraction, by length, of phase *B*; linear grade
g_{p}	Fraction, by point, of phase *B*; point grade
g_{v}	Fraction, by volume, of phase *B*; volumetric grade
g_{v}^{25}	Volumetric grade of particles that have 25% chance of reporting to the tails stream in the wet magnetic drum separator model
g_{v}^{50}	Volumetric grade of separation in wet magnetic drum separator model
g_{v}^{75}	Volumetric grade of particles that have 75% chance of reporting to the

tails stream in the wet magnetic drum separator model

$\overline{g_v^{ij}}$ Average volumetric grade of particles in volumetric grade range $\left(g_v'^{j}, g_v'^{j-1}\right)$ and in size range $\left(D'^{i}, D'^{i-1}\right)$

g_v^{j} Volumetric grade of separation corresponding to volumetric grade class *j*

$\overline{g_v^{j}}$ Average volumetric grade of particles in volumetric grade range $\left(g_v'^{j}, g_v'^{j-1}\right)$

$\overline{g_v^{l}}$ Average volumetric grade of particles in progeny size range $\left(D^{l}, D^{l-1}\right)$

$\overline{g_v^{lij}}$ Average volumetric grade of particles in progeny size range $\left(D^{l}, D^{l-1}\right)$ that is generated from breakage of particles in volumetric grade range $\left(g_v'^{j}, g_v'^{j-1}\right)$ and in size range $\left(D'^{i}, D'^{i-1}\right)$

$g_v^{\min}$ Auxiliary variable associated to the minimum progeny average volumetric grade in model for the first moment of the conditional quadrivariate breakage function

g_v^{A} Volumetric grade on the boundary of the accessible region associated to phase *A*, corresponding to $g_v^{\xi} = 0$

g_v^{B} Volumetric grade on the boundary of the accessible region associated to phase *B*, corresponding to $g_v^{\xi} = 1$

$g_v^{B,Taconite}$ Volumetric grade on the boundary of the accessible region associated to phase *B*, corresponding to $g_v^{\xi} = 1$, for the Taconite ore texture

g_v^{ξ} Fraction, by volume, of phase *B*, in the transformed ξ domain

$g_v^{\xi 0}$ Fraction, by volume, of phase *B*, in the transformed ξ domain, corresponding to $g_v = 0$

$g_v^{\xi 1}$	Fraction, by volume, of phase *B*, in the transformed ξ domain, corresponding to $g_v = 1$
$\overline{g_v}(D/D';g_v')$	Normalized first moment of the conditional quadrivariate breakage function. Average volumetric grade of particles that have fractional size D/D', generated from breakage of particles that have volumetric grade g_v' and size D'
$\overline{g_v}(D;g_v',D')$	First moment of the conditional quadrivariate breakage function. Average volumetric grade of particles that have size *D*, generated from breakage of particles that have volumetric grade g_v' and size D'
$\overline{g_v^l}(g_v',D')$	Average volumetric grade of particles in progeny size range (D^l,D^{l-1}), generated from breakage of particles that have volumetric grade g_v' and size D'
h_i	Fraction, by weight, of particles in size class *i*, in the holdup of a mill
H_i	Cumulative fraction, by weight, of particles in and below size class *i*, in the holdup of a mill
i	Index to a narrow size range; index to the size range of parent particles
I	Identity matrix
$I_x(\alpha,\beta)$	The incomplete beta function in a variable x
j	Index to a narrow volumetric grade range; index to the volumetric grade range of parent particles
J	Fractional ball filling
k	Index to a narrow volumetric grade range in the progeny; index to a narrow linear grade range

K	The discrete transformation kernel
K_{ij}	A coefficient in the discrete transformation kernel. Here *i* is used as an index to linear grade class
l	Index to a narrow size range in the progeny
m	Index to parent volumetric grade in finite difference scheme
M	Number of parent volumetric grades in finite difference scheme
M_f	Fluid magnetization, (emu/cc)
MODSIM	Modular Ore Dressing Simulator
n	Index to parent size in finite difference scheme
n_1^B	The first moment, with respect to phase *B*, of the conditional quadrivariate breakage function
n_1^{Bj}	The first moment of the unliberated linear grade distribution, by volume, that is generated by particles in a narrow grade range, with respect to phase *B*
$n_1^B\langle g_v\rangle$	The first moment of the volume-weighted conditional, on volumetric grade, unliberated linear grade distribution, with respect to phase *B*
n_{1u}^B	The first moment, with respect to phase *B*, of the unliberated conditional quadrivariate breakage function
$n_{1\xi}^B$	The first moment, with respect to phase *B*, of the unliberated conditional quadrivariate breakage function in the transformed ξ domain
n_2^{Bj}	The second moment of the unliberated linear grade distribution, by

	volume, that is generated by particles in a narrow grade range, with respect to phase *B*
$n_2^B(g_v)$	The second moment of the volume-weighted conditional, on volumetric grade, unliberated linear grade distribution, with respect to phase *B*
$n_{2\xi}^B$	The second moment, with respect to phase *B*, of the unliberated conditional quadrivariate breakage function in the transformed ξ domain
N	Number of volumetric grade classes produced by fractionation; number of parent sizes in finite difference scheme in quadrivariate breakage function parameterization; rotational speed (revolutions per minute); number of fully mixed reactors in series in *RTD* model
NSR	Normalized Sum of Residuals
p_i	Fraction, by weight, of particles in size class *i*, in the product from a mill
$p_i^{(n)}$	Fraction, by weight, of particles in size class *i*, in the product from perfectly mixed region *n* of a mill
p_i^*	Fraction, by weight, of particles in size class *i*, in the product from a perfectly mixed region with postclassification in a mill
$p(D)$	Number-weighted particle size distribution density
$p(g,D)$	The distribution density, by weight, of particles that have grade *g* and size *D* in a perfectly mixed mill region in the continuous *PBM* equation
$p(g_\ell \mid g_v, D)$	Number-weighted, conditional on volumetric grade and particle size, linear grade distribution density

$p(g_v \mid D)$	Number-weighted, conditional on size, volumetric grade distribution density
$p(V \mid D)$	Number-weighted, conditional on size, particle volume distribution density
p_b	Formal bed porosity, in a mill
p_A	Auxiliary variable in model of the boundary of the accessible region associated to phase *A*
p_B	Auxiliary variable in model of the boundary of the accessible region associated to phase *B*
$P(g_\ell \mid D)$	Cumulative, conditional on size, linear grade distribution, weighted by number
$P(g_\ell \mid D^*)$	Cumulative linear grade distribution that is generated by particles in a finite size range, weighted by number
$P(g_\ell \mid g_v)$	Cumulative, conditional on volumetric grade, linear grade distribution, weighted by number
$P(g_\ell \mid g_v, D)$	Cumulative, conditional on size and volumetric grade, linear grade distribution, weighted by number
$P(\ell \mid D^*)$	Cumulative chord length distribution that is generated by particles in a narrow size range, weighted by number
P_i	Cumulative fraction, by weight, of particles in and below size class *i*, in the product of a mill
PBM	Population Balance Modeling
PSIG	Pounds per Square Inch Gage; gage pressure is absolute pressure

	minus prevailing barometric pressure
$r(t)$	The response for a number of unequal fully mixed reactors in series to an impulse test
$\Re$	Real numbers
R'	Region in the parent particle size and grade domain from within which a particle can produce progeny of grade g and size D by breakage
RPM	Revolutions Per Minute
RTD	Residence Time Distribution
S	Surface area of the convex hull of a particle
S_1	Parameter in selection function model (min^{-1})
$\overline{S_D}$	Number-weighted average surface area S in a particle population each of which is exactly of mesh size D
S_i	Rate of breakage of particles in size class i; discrete selection function
SEM	Scanning Electron Microscope
SI	Separation Index
$S(g,D)$	rate of breakage (selection function) of particles that have grade g and size D
S_V	Surface area per unit volume
S_V^A	Phase A surface area per unit volume

S_V^{Aij}	Phase *A* surface area per unit volume of particles in volumetric grade range $\left(g_v'^{j}, g_v'^{j-1}\right)$ and in size range $\left(D'^{i}, D'^{i-1}\right)$
S_V^{AB}	Interphase area per unit volume of phase *A*
S_V^{ABij}	Average interphase area per unit volume of phase *A* of particles in volumetric grade range $\left(g_v'^{j}, g_v'^{j-1}\right)$ and in size range $\left(D'^{i}, D'^{i-1}\right)$
S_V^{B}	Phase *B* surface area per unit volume
S_V^{Bij}	Phase *B* surface area per unit volume of particles in volumetric grade range $\left(g_v'^{j}, g_v'^{j-1}\right)$ and in size range $\left(D'^{i}, D'^{i-1}\right)$
S_V^{BA}	Interphase area per unit volume of phase *B*
S_V^{BAij}	Average interphase area per unit volume of phase *B* of particles in volumetric grade range $\left(g_v'^{j}, g_v'^{j-1}\right)$ and in size range $\left(D'^{i}, D'^{i-1}\right)$
S_V^{P}	Particle surface area per unit volume
S_V^{Pij}	Surface area per unit volume of particles in volumetric grade range $\left(g_v'^{j}, g_v'^{j-1}\right)$ and in size range $\left(D'^{i}, D'^{i-1}\right)$
t	time
t_d	time lag or time delay in *RTD* experiment
t_j^{end}	Time at end of collection of the j^{th} sample in *RTD* experiments
t_j^{start}	Time at beginning of collection of the j^{th} sample in *RTD* experiments
u	Progeny size domain transformation in model for the first moment of the quadrivariate breakage function
$u^{\min}$	Auxiliary variable in model for the first moment of the conditional

	quadrivariate breakage function
U	Powder/ball loading ratio
v_t	Terminal settling velocity of an irregular particle
v_{25}	Terminal velocity of a particle that has 25% chance of being recovered in the overflow of the elutriator
v_{50}	Separation velocity in the elutriator
v_{75}	Terminal velocity of a particle that has 75% chance of being recovered in the overflow of the elutriator
V	Particle volume
V'	Parent particle volume
V_A	Volume of phase *A*
V_B	Volume of phase *B*
$\overline{V_D}$	Number-weighted average volume *V* in a particle population each of which is exactly of mesh size *D*
$\alpha(d_p)$	By-pass function in wet magnetic drum separator model
α	Parameter of the incomplete beta function; exponential parameter in selection function model, equation 4.22; by-pass fraction in equation 4.27 and in equation 5.8
$\alpha(g_v)$	Parameter associated to $n_1^B(g_v)$ and $n_2^B(g_v)$, of the incomplete beta function
α_1, α_2	Auxiliary variables in model for the first moment of the conditional

	quadrivariate breakage function
α_r	Regularization parameter
β	Progeny particle volume shape factor; parameter of the incomplete beta function; power parameter in bivariate breakage function model, equation 4.23; particle surface area per unit volume shape factor in equation 4.25
β'	Parent particle volume shape factor
$\beta(g_v)$	Parameter associated to $n_1^B(g_v)$ and $n_2^B(g_v)$, of the incomplete beta function
δ	Exponential factor used in hydrocyclone model, equation 5.11
Δ^0	Progeny size, in the transformed domain *u*, at which progeny average volumetric grade equals parent volumetric grade
Δ^{min}	Progeny size, in the transformed domain *u*, at which progeny average volumetric grade is at a minimum
γ	Auxiliary parameter of the incomplete beta function; power parameter in bivariate breakage function model, equation 4.23
$\gamma(g_v)$	Auxiliary parameter associated to $n_1^B(g_v)$ and $n_2^B(g_v)$, of the incomplete beta function
Γ^{min}	Parameter associated to the minimum progeny average volumetric grade
κ	By-pass factor in wet magnetic drum separator model
K	Proportionality constant

$\mathfrak{L}_A$	Fraction of particles that are pure, liberated, phase *A*
$\mathfrak{L}_{Aj}^{(1)}$	Apparent linear liberation of phase *A* generated by particles in volumetric grade class *j*
$\mathfrak{L}_A^{(1)}\left(1-g_v\right)$	Fraction of all particle intercepts that reports as liberated phase *A* that is generated by particles of volumetric grade g_v; apparent linear liberation of phase *A*
$\mathfrak{L}_B$	Fraction of particles that are pure, liberated, phase *B*
$\mathfrak{L}_{Bj}^{(1)}$	Apparent linear liberation of phase *B* generated by particles in volumetric grade class *j*
$\mathfrak{L}_B^{(1)}\left(g_v\right)$	Fraction of all particle intercepts that reports as liberated phase *B* that is generated by particles of volumetric grade g_v; apparent linear liberation of phase *B*
λ	Exponential parameter in logistic separation function, equation 4.28, and in Rosin-Rammler separation function, equation 5.6
Λ	Exponential factor in selection function model for abnormal breakage region
μ	Number-weighted average chord length; parameter in selection function model for abnormal breakage region (microns), equation 4.22
μ^A	Number-weighted average chord length measured on phase *A*
μ^{Aij}	Number-weighted average chord length measured on phase *A* of particles in volumetric grade range $\left(g_v'^j, g_v'^{j-1}\right)$ and in size range $\left(D'^i, D'^{i-1}\right)$
μ^B	Number-weighted average chord length measured on phase *B*

μ^{Bij}	Number-weighted average chord length measured on phase *B* of particles in volumetric grade range $\left(g_v'^{j}, g_v'^{j-1}\right)$ and in size range $\left(D'^{i}, D'^{i-1}\right)$
μ^{P}	Number-weighted average chord length measured on particles
μ^{Pij}	Number-weighted average chord length measured on particles in volumetric grade range $\left(g_v'^{j}, g_v'^{j-1}\right)$ and in size range $\left(D'^{i}, D'^{i-1}\right)$
$\omega_1, \omega_2, \omega_3, \omega_4$	Arbitrary parameters in functional forms for the variance of the transformation kernel models for Dolomite-Sphalerite and symmetric textures
$\%SiO_2^j$	Average percentage of silica in solid phase during time interval *j*
$\%SiO_2^{Limestone}$	Percentage of silica contained in the limestone used in the *RTD* tests
ϕ	Geometrical texture parameter
$\phi\langle D\rangle$	Geometrical texture parameter produced by particles of size *D*
ϕ_c	Fraction of critical speed
ϕ_A	Geometrical texture parameter associated to phase *A*
ϕ_A^C	Critical texture parameter associated to phase *A*
ϕ_B	Geometrical texture parameter associated to phase *B*
ϕ_B^C	Critical texture parameter associated to phase *B*
Φ	Parameter in bivariate breakage function model, equation 4.23
Ψ	Particle sphericity

ρ	Density; composite particle density; power parameter in postclassification function model, equation 4.24
$\overline{\rho}$	Average density of a particle population
$\overline{\rho^{ij}}$	Average density of particles in volumetric grade range $\left(g_v'^{j}, g_v'^{j-1}\right)$ and in size range $\left(D'^{i}, D'^{i-1}\right)$
ρ^{j}	Density of separation corresponding to volumetric grade range j
$\overline{\rho^{j}}$	Average density of particles in volumetric grade range j; average density of parent particles in volumetric grade range $\left(g_v'^{j}, g_v'^{j-1}\right)$
$\overline{\rho^{lij}}$	Average density of particles in progeny size range $\left(D^{l}, D^{l-1}\right)$ that is generated from breakage of particles in volumetric grade range $\left(g_v'^{j}, g_v'^{j-1}\right)$ and in size range $\left(D'^{i}, D'^{i-1}\right)$
ρ_f	Fluid density
ρ_s	Separation density
ρ_A	Density of pure, liberated phase A
ρ_B	Density of pure, liberated phase B
Λ	Exponential factor in selection function model for abnormal breakage region
$\overline{\rho}(D)$	Average density of particles that have size D
$\rho(g_v)$	Density of particles that have volumetric grade g_v
σ^{2j}	The variance of the unliberated linear grade distribution, by volume, that is generated by particles in a narrow grade range, with respect to phase B

$\sigma^2(g_v)$	The variance of the volume-weighted conditional, on volumetric grade, unliberated linear grade distribution, with respect to phase *B*
σ_ξ^2	Variance of the unliberated conditional quadrivariate breakage function in the transformed ξ domain
ς	Exponential factor to control by-pass in the model for wet magnetic drum separator
τ	Mean residence time in a perfectly mixed mill region
τ'	Mean residence time in a perfectly mixed mill region with postclassification
τ_i	Mean residence time in the i^{th} perfectly mixed mill region in series
T	Average residence time in a mill
$\theta_1, \theta_2, \theta$	Arbitrary parameters in functional forms for the first moment of the transformation kernel models for Dolomite-Sphalerite and symmetric textures
ξ	Designates the transformed incomplete beta function domain
ξ_1, ξ_2	Arbitrary parameters in the functional form for the apparent linear liberation corresponding to the transformation kernel model for symmetric texture
ξ_1^A, ξ_2^A	Arbitrary parameters in the functional form for the apparent linear liberation of phase *A* corresponding to the transformation kernel model for Dolomite-Sphalerite texture
ξ_1^B, ξ_2^B	Arbitrary parameters in the functional form for the apparent linear liberation of phase *B* corresponding to the transformation kernel model for Dolomite-Sphalerite texture

ζ	Arbitrary parameter in the model for the variance of the unliberated, conditional quadrivariate breakage function

ACKNOWLEDGMENTS

I wish to express my deepest gratitude to the extraordinary competence and effectiveness with which Professor R.P. King advised and directed this research during the many years this endeavor lasted.

I am also grateful for the support and cooperation of Professor J.D. Miller and Dr. C.L. Lin, who in fact seeded this research and co-advised during the first two years of the study, Dr. Raj K. Rajamani for unlimited computer time, and Mike Loveless for his extensive and painstaking labor in the experimental in Chapters 3 and 4.

It is very difficult to properly acknowledge the support and the incentive from my family and many friends in the U.S. and in Brazil. I would like to specially thank Karen Haynes for her delightful personality and for being a friend since my first day in the U.S. Thanks to my special friends Mike Nettessheim, Eduardo Momberger, Luis Alberto Jacobus and Bayard M. Feltes for the incentive, motivation and all the great moments. I would like to thank Jose C.M. Feltes for the incentive in the very beginning of my undergraduate years, and Jorge Rubio, for introducing me to the academic career. The support and incentive from my family, specially my parents Gunther and Ellen, were paramount. I am much indulged.

During the past winter, a wonderful person, a friend I was very fortunate to have known, was tragically killed in Brazil, and his absence is deeply regretted.

This research has been supported by the Department of the Interior's Mineral

Institute Program administered by the U.S. Bureau of Mines through the Generic Mineral Technology Center for Comminution under grant numbers G1105149, G1115149, G1125249, G1135249 and G1145249.

The sponsoring of the Conselho Nacional de Pesquisa, CNPq, during the initial research stage, and of Minnesota Power, for the case study, are also acknowledged.

CHAPTER 1

INTRODUCTION

In mineral processing jargon, the term "liberation" is used as synonymous to the study of mineral particle composition. In the same way, "liberation spectrum" is used in a broad manner to refer to the distribution of grades in a particle population. This distribution can be multidimensional since there is no upper limit for the number of phases present in a mineral particle population. The simplest system, and probably the most common, is the binary ore, where one phase is regarded as gangue and the other as valuable. The liberation spectrum of a binary ore can be represented as the distribution by volume of volumetric grades, $f_v(g_v)$, with g_v being the volumetric abundance of the valuable phase of the particle. This distribution has a very well-defined domain, since as g_v can only have fractional values contained in $\Re[0,1]$. However, $f_v(g_v)$ has two important discontinuities in its domain, one at $g_v = 0$, pure gangue particles, and the other at $g_v = 1$, pure valuable particles. Usually these particles are referred to as liberated, whereas all other particles contained in $\Re(0,1)$ are referred to as unliberated particles. More or less "liberation" means more or less liberated particles of both phases. The process by which liberation is achieved is usually that of size reduction, and the liberation spectrum is intimately associated with the size spectrum, or the particle size distribution, $f(D)$. It is intuitive that, for a given ore, the finer the size distribution, the more liberated particles will be present. This is true if no other process besides that of

size reduction takes place, and the liberation spectrum produced is then referred to as the natural liberation spectrum of the ore. If, on the other hand, a concentration process takes place simultaneously with size reduction, liberation can be accelerated or decelerated, depending upon which particles are selected to undergo size reduction, and the liberation spectrum produced is no longer a natural liberation spectrum. This concept is important in practical mineral processing. A major portion of the scientific work on liberation has focused on the prediction of the natural liberation spectrum; considerably less attention has been given to the problem of predicting the liberation spectrum produced when concentration processes occur simultaneously to that of size reduction. Such concentration processes are very common in mineral processing operations, the definitive example being milling in closed circuit with a hydrocyclone. This is not surprising, since liberation is a very complex process and the prediction of the natural liberation spectrum is a formidable task, requiring complex mathematical formulation. Concentration effects further complicate the problem. Also contributing to the difficulties on studying liberation is the measurement problem. There is no single procedure that can measure the liberation spectrum of any ore accurately. Most procedures will work to a certain extent for a given ore, for example, dense liquid fractionation for coal. For ores and even coals that contain particles with densities higher than about 2.8 g/cc, dense liquid fractionation is no longer practical, and other procedures must be used. As a result of this, much research on liberation to date lacks reliable supporting experimental data.

The first attempt to develop a procedure for predicting the natural liberation spectrum was made by Gaudin [1] in 1939. He was, perhaps, the first to recognize that

a knowledge of liberation is of absolute importance in mineral processing. Liberation is indeed essential to any further improvement in modelling almost all known mineral processing unit operations, with very few exceptions. This is because in mineral processing operations, the particles are submitted to magnetic, chemical and gravitational forces in order to modify their state, size and/or concentration. Each of the phases in a single particle has its own particular properties, i.e., density, chemical affinity, brittleness, magnetic susceptibility and so on, and the relative amount of these phases will dictate the properties of the particle as a unit. Thus, in order to calculate the behavior of a particle population when submitted to a process, this process being characterized by a set of forces and a chemical environment, it is essential to know the phase distribution in the particle population.

Gaudin's approach was essentially geometrical, based on the superposition of very simple regular fracture and texture patterns. However simplistic the cubic patterns proposed by Gaudin, the idea of superimposing fracture and texture patterns seeded the work that followed to date. Wiegel and Li [2] randomized Gaudin's model, recognizing that the textural structure of real mineralogical materials is better described by probabilistic models. The latest expansion of Gaudin's model is due to Meloy et al. [3], who proposed solutions to the superimposition of a randomized fracture pattern that produces spherical particles in shape and four distinct, regular texture patterns. It is essential however that both fracture and texture patterns be much more realistic if a successful solution to the prediction of the natural liberation spectrum is to be obtained. This demand was recognized as early as 1972, and two distinct, more promising

approaches have emerged. The first, known as the integral geometry approach, is due to Barbery [4], and the second, known as the stereological approach, is due to King [5].

The integral geometry approach is the ultimate application of superimposition of complex, more realistic, texture patterns with fracture patterns, both controlled by random polyhedral processes, in three dimensions. However, it is rather complicated to model the liberation process directly in three-dimensional space, which makes King's approach considerably more attractive. This consists of modelling texture and fracture in one-dimensional space with great advantage in simplicity. The resulting one-dimensional distributions are then used for the calculation of the corresponding volumetric distributions by means of stereology, with an appropriate transformation function. King's work on the calculation of the natural liberation spectra is relevant in the sense that it brought stereology to the context of liberation studies, and the stereological relationship between linear and volumetric grade distribution was established. This has become a powerful tool for the measurement of the liberation spectra in a particle population by means of image analysis. However, no realistic transformation function was available until 1985, when Lin et al. [6] first measured it from computer generated PARGEN particles. Following that work, Lin [7] generated the first solutions to the stereological transformation equation, and the first attempts to measure the liberation spectra of real mineralogical particles were made. Finally, Schneider et al. [8] presented a procedure for inverting the stereological equation which generated a mildly constrained volumetric grade distribution, which was used for the first time in conjunction with King's Random Fracture Model to predict the natural liberation spectra produced by the breakage of a

copper and an iron ore.

The events described above leave us with a procedure to effectively measure particle volumetric grade distribution by image analysis. However, the level of accuracy required for this work demands a yet more realistic transformation function than the one obtained with PARGEN particles. The second chapter of this dissertation is therefore dedicated to the measurement of the stereological transformation function from real mineralogical particles, which are themselves, the ultimate texture model. A complete procedure to achieve such measurement is described in detail and the use of the stereological transformation equation is discussed thoroughly.

Having established a sufficiently accurate procedure for measurement of the volumetric grade distribution in a particle population by image analysis, it is now possible to study, in detail, the liberation process.

The only known method for predicting the liberation spectra produced by the breakage of mineralogical particles is the one based on population balance modelling. This is because the texture of the original unbroken ore is not retained during processes that involve concentration of any of the phases present in the ore. Once concentration takes place, the grade distributions produced in the progeny by comminution are no longer the natural grade distributions produced by the breakage of the original texture of the ore. On the other hand, the population balance approach works because it can be coupled with a model description of the concentration process in question, and the calculation can then be carried out simultaneously. A typical, very common example in mineral processing is the classic ball mill in closed circuit with a hydrocyclone. In the hydrocyclone,

separation is achieved on the basis of particle weight; both size and density contributing to the net force acting upon the particle. Consequently, a higher concentration of not only larger but also denser particles is encountered in the underflow stream. This underflow is then added to the fresh feed to the circuit, and the mixture constitutes the ball mill feed. Clearly, any method that is based on the texture of the unbroken ore will fail to assess the liberation spectra in both feed and product of the ball mill. The population balance approach is, however, based on the texture of broken particles, allowing for classification, concentration and breakage processes to be handled simultaneously.

Central to the problem of solving the population balance equation in the mill is the characterization of the transfer coefficients between size and grade classes, known as the quadrivariate breakage function. In other words, how do the progenies from breakage of a particle of known size and grade distribute with respect to size and grade? The conventional solution requires massive parameter estimation and the breakage process is regarded as a black box. An alternative to this first appeared in 1990, when King [9] proposed a solution based on theoretical considerations about the breakage process. In that work, two major contributions were made. The first, and perhaps most important, is a solution to the population balance equation based on a knowledge of the quadrivariate breakage function. The second is a detailed description of the properties of the quadrivariate breakage function, its constraints and how it can be related to particle texture. Also in that work, a model for the quadrivariate breakage function based on PARGEN simulations is proposed, and incorporated into MODSIM [10], the Modular Ore Dressing Simulator. This model has not been verified to date, because there simply is no

experimental data on liberation available from either laboratory experiments or industrial mineral processing plants. Through the stereological correction procedure for measurement of the liberation spectra by image analysis presented in this work, such verification is now possible. Furthermore, measurement of the transfer coefficients among the size and grade classes can be achieved for real mineralogical particles. In Chapter 3 of this dissertation, a procedure for measuring the quadrivariate breakage function from real mineralogical particles, for one parent size, is carried out. A model, based on this measurement, is proposed and implemented.

Chapters 4 and 5 are dedicated to the experimental verification of the proposed models. Chapter 4 describes a laboratory grinding experiment under very well controlled conditions for which the ball mill has been thoroughly characterized with respect to transport. The concentration effect is achieved by elutriation, and all the streams involved are characterized with respect to size and grade distributions. The measured liberation spectra are compared to those predicted by the models for every stream, and mill holdups. Chapter 5 is a case study. The models and procedures are put to work for the characterization of an industrial grinding circuit. The Fairlane plant, located in the Minnesota iron range, produces iron pellets for steel making. The taconite ore presents problematic liberation characteristics and is considerably hard, which makes this particular ore an excellent choice for this study. The grinding circuit of the Fairlane plant is particularly interesting because the desired concentration effects are boosted by the presence of low intensity magnetic drum separators that concentrate the product of a ball mill before feeding the hydrocyclone. All streams immediately involved were sampled

and analyzed for size and liberation. The simulation results are compared to the experimental data.

This dissertation is rather extensive, mainly because of the tremendous amount of experimental data that is made available. Whenever possible, the data have been treated with particular care, especially to correct for the discretization of the density distributions, which is commonly overlooked in mineral processing practice. Also, the work is complete in itself, from theory to application, which facilitates the understanding of almost all aspects of the liberation problem for binary mineralogical systems.

CHAPTER 2

STEREOLOGICAL CORRECTION OF LINEAR GRADE DISTRIBUTIONS FOR MINERAL LIBERATION

Background

Stereological correction of the distribution of linear grades is a very important problem when dealing with both the measurement and prediction of mineral liberation. It is comparatively easy to measure the distribution of linear grades in a sample of mineralogical material in particulate form. In fact, it was measurements made by Jones [11] that provided much of the impetus for research in mineral liberation that has been undertaken during the past 20 years.

By contrast, measurement of the distribution of volumetric particle composition directly by particle fractionation is usually difficult and often impossible. However, the measurement of liberation is not the only application for making the stereological correction. In 1979 King [5] showed that it is possible to predict the linear grade distribution that will be obtained when a binary ore is comminuted, and the application of the stereological correction extends the prediction to the full distribution of particle volume grade.

The stereological correction is required because a linear probe through multiphase particulate material will report a significantly larger fraction of liberated intercepts than there are liberated particles. The entire linear distribution is considerably more dispersed

than the volumetric distribution of grades that generates the linear distribution.

The stereological correction procedure has been known, at least in principle, since 1982 [12] for particle populations of a single size. The correction procedure is based on the generation of solutions $p(g_v \mid D)$ to the integral equation 2.1.

$$P(g_l \mid D) = \int_0^1 P(g_l \mid g_v, D)\; p(g_v \mid D)\; dg_v \qquad (2.1)$$

when the distribution of linear grades $P(g_l \mid D)$ is known from a probe measurement or a linear model prediction [13]. In equation 2.1, $P(g_l \mid g_v, D)$ is the cumulative distribution of linear grades from particles of size D that have a volume fraction of mineral equal to g_v. Equation 2.1 shows the relationship between the volumetric grade distribution $p(g_v \mid D)$ (also called the liberation spectrum) and the distribution of linear grades in a binary mineral system. The volumetric grade g_v, by convention, refers to the volume fraction of the valuable mineral phase, which is denominated phase B in this work, while the gangue minerals are denominated phase A, and their volumetric grade is indicated by the complement $1 - g_v$.

Although equation 2.1 appears to be simple, it poses some difficulties in the way of its routine use in practical applications. Firstly, it has no closed-form solutions for practically useful cases and its numerical solution is notoriously difficult because of instability problems. Equation 2.1 is technically known as a linear Fredholm integral equation of the first kind. These equations have some rather unpleasant characteristics and Wing [14] gives a convenient summary of their properties.

Secondly, the kernel function $P(g_l \mid g_v, D)$ must be known and at present there are

no known theoretical models available from which it may be determined for real mineralogical particles. In fact, when equation 2.1 was first proposed as a potentially practical solution in 1982, the only kernels that were known had been determined by computer simulation of linear probe responses through two-phase spheres and cubes having very simply oriented interfaces between the phases [15]. These kernel functions could not represent any real mineral particles. Although these simulated results were not directly useful for practical work they did provide valuable insights into the nature of the kernel function and how it might vary with texture. It was not until 1984 that a useful kernel was developed by simulation of irregular two-phase particles by Lin et al. [6] and equation 2.1 began to be used for practical correction of linear intercept data.

In the original presentation of the stereological correction method using equation 2.1, King [12] pointed out that the kernel function can be determined directly by experiment, using real mineral particles. However the experimental procedure would be very difficult because representative samples of material having particles all of the same size, D, and same composition, g_v, must be collected and examined by image analysis. The best that can be hoped for is samples that have been fractionated into narrow ranges of size and composition. Even this is difficult to achieve with respect to composition although size fractionation can be done relatively easily. The work presented here reports a study designed to determine the transformation kernel as accurately as possible from linear grade distributions measured on carefully fractionated mineral particles.

Theory

Equation 2.1 is, in fact, only an approximation when particles are not all of the same shape which is the normal case in practical applications. In addition due allowance must be made for the concavity of the particles since it is unwise to restrict analysis to convex particles only. However, some restriction is made on the shape of particles considered here. Specifically we will consider only particles that are sufficiently regular in shape to ensure that the particle itself will be intersected by a line probe whenever the probe intersects the convex hull of the particle. This restriction excludes particles with holes such as doughnut-shaped particles and also saddle-shaped particles. Those shapes are almost never encountered in mineral processing work and can be safely neglected. The concavities encountered on the surfaces of typical mineral particles are sufficiently shallow to ensure that whenever a linear probe intersects the convex hull of the particle it will also intersect the particle.

Let S represent the surface area of the convex hull of a particle. In any population of particles all having mesh size exactly D, there will be a distribution of values of S. Let $\overline{S_D}$ represent the mean value of this distribution. Equation 2.1 should be modified as shown in equation 2.2 for the finite range of particles in any real sample.

$$P\left(g_\ell \mid D^*\right) = \frac{\int_{Dmin}^{Dmax} \int_{0}^{1} \overline{S_D}\, P\left(g_\ell \mid g_v, D\right)\, p\left(g_v \mid D\right)\, p\left(D\right)\, dg_v\, dD}{\int_{Dmin}^{Dmax} \overline{S_D}\, p\left(D\right)\, dD} \qquad (2.2)$$

In equation 2.2 $P\left(g_\ell \mid D^*\right)$ is the cumulative number distribution of linear grades

corresponding to particles in the finite size range $D^* = [Dmax, Dmin]$. It is more useful to write equation 2.2 in terms of the volume-weighted size distribution density $f_v(D)$ which is normally measured in practice by screening, and the, conditional on size, volume-weighted volumetric grade distribution $f_v(g_v|D)$. Let $\overline{V_D}$ represent the number-weighted average particle volume in a sample of particles each of which is exactly of mesh size D,

$$\overline{V_D} = \int_0^\infty V\, p(V|D)\, dV \tag{2.3}$$

then the relationship between $p(D)$ and $f_v(D)$ is

$$f_v(D) = \frac{\overline{V_D}\, p(D)}{\int_0^\infty \overline{V_D}\, p(D)\, dD} \tag{2.4}$$

and since particle volume is not a function of particle composition, it also follows that:

$$f_v(g_v|D) = p(g_v|D) \tag{2.5}$$

Equation 2.2 becomes:

$$P(g_\ell|D^*) = \frac{\int_{Dmin}^{Dmax}\int_0^1 \frac{\overline{S_D}}{\overline{V_D}}\, P(g_\ell|g_v,D)\, f_v(g_v|D)\, f_v(D)\, dg_v dD}{\int_{Dmin}^{Dmax} \frac{\overline{S_D}}{\overline{V_D}}\, f_v(D)\, dD} \tag{2.6}$$

Equation 2.6 is not useful in the above form because there is no known method to determine the average surface area of the convex hulls of the particles. However a good

practical working approximation is that the ratio $\overline{S_D} / \overline{V_D}$ is proportional to $1 / D$ over the entire size range. In addition it is assumed that $p(g_\ell \mid g_v, D)$ is not a function of D:

$$P(g_\ell \mid g_v, D) = P(g_\ell \mid g_v) \tag{2.7}$$

These assumptions reflect the fractal nature of the particle surface and the interphase boundary but much more experimental work will be required to asses their validity. With these assumptions equation 2.6 becomes:

$$P(g_\ell \mid D^*) = \frac{\int_0^1 P(g_\ell \mid g_v) \int_{Dmin}^{Dmax} f_v(g_v \mid D) \frac{f_v(D)}{D} \, dD \, dg_v}{\int_{Dmin}^{Dmax} \frac{f_v(D)}{D} \, dD} \tag{2.8}$$

Equation 2.8 requires a simultaneous solution for both $f_v(g_v \mid D)$ and $f_v(D)$. This could be achieved by measuring $P(g_\ell \mid D^*)$ and $P(\ell \mid D^*)$ simultaneously, the last term being the cumulative distribution of intercept lengths generated by particles in the narrow size range $[Dmax, Dmin]$, which is related to $f_v(D)$ by means of an integral equation, provided the particle shape does not change significantly in the size domain. The relationships governing the transformation of linear intercept data into volumetric size distribution for irregularly shaped particles are described in King [12]. Much more work will be required to implement such simultaneous solution. At this stage, equation 2.8 is solved for the volumetric grade distribution of the particles in the finite size range $[Dmax, Dmin]$, which is defined as follows:

$$f_v\left(g_v \mid D^*\right) = \frac{\int_{Dmin}^{Dmax} f_v\left(g_v \mid D\right) \frac{f_v(D)}{D}\, dD\, dg_v}{\int_{Dmin}^{Dmax} \frac{f_v(D)}{D}\, dD} \tag{2.9}$$

With this, equation 2.8 becomes:

$$P\left(g_\ell \mid D^*\right) = \int_0^1 P\left(g_\ell \mid g_v\right) f_v\left(g_v \mid D^*\right) dg_v \tag{2.10}$$

It is interesting to note that the kernel $P\left(g_\ell \mid g_v\right)$ is exact for both equations 2.8 and 2.10, keeping in mind that the objective here is its measurement from real mineralogical particles of a given texture.

For convenience, equation 2.10 can be rewritten in terms of the corresponding length weighted linear grade distributions, as shown in equation 2.11. In this form, the transformation kernel $F_\ell\left(g_\ell \mid g_v\right)$ is more amenable for modelling, and also, we have found that the transformation equation becomes more stable for inversion.

$$F_\ell\left(g_\ell \mid D^*\right) = \int_0^1 F_\ell\left(g_\ell \mid g_v\right) f_v\left(g_v \mid D^*\right) dg_v \tag{2.11}$$

An Experimental Approach

The approach used in this work was to fractionate a narrowly sized population of two phase mineral particles into composition. The resulting samples, which approximated to mono-size, mono-grade fractions were mounted, sectioned, and polished, and the

distribution of linear grades was determined for each fraction by image analysis. A complete description of the image processing steps involved in such measurement is available in King and Schneider [16]. Particular care was taken to produce the cleanest possible grade fractions using a MAGSTREAM™ magnetic fluid fractionation device.

The measured linear grade distributions by length were taken as approximations to the kernel function $F_\ell(g_\ell \mid g_v)$ at the average grade $\overline{g_v}$ for each fraction. These crude estimates were used to formulate an empirical model for the kernel which was then refined using equation 2.11 to account for the finite width of the grade fractions. After fractionation of narrow sized particles, a set of N narrow grade samples was obtained each in a grade range g_v^{j-1}, g_v^j for j = 0 to 7, with $g_v^0 = 0$ and $g_v^7 = 1$. For a sample in a narrow size, narrow grade interval, equation 2.11 can be written as:

$$F_\ell^j\left(g_\ell \mid D^*\right) = \frac{\int_{g_v^{j-1}}^{g_v^j} F_\ell(g_\ell \mid g_v)\, f_v\left(g_v \mid D^*\right)\, dg_v}{\int_{g_v^{j-1}}^{g_v^j} f_v\left(g_v \mid D^*\right)\, dg_v} \qquad (2.12)$$

Equation 2.12 is the working equation used to effectively model the kernel function $F_\ell(g_\ell \mid g_v)$. The distributions $F_\ell^j\left(g_\ell \mid D^*\right)$ can be measured directly by image analysis for each of the 7 narrow grade samples. If the fractionation is carried out over the whole grade spectrum and enough samples are obtained, the resulting volumetric grade distribution $f_v\left(g_v \mid D^*\right)$ can be calculated from the weight fraction of each sample and the average density of particles in each sample.

The first element required for a model of the kernel function is the magnitude of

the steps at each end of its domain. These represent the apparent linear liberation of each phase. The apparent linear liberation $\mathfrak{L}_A^{(1)}(1-g_v)$ of phase *A* is the fraction of all particle intercepts that reports as liberated mineral *A* measured in a particle sample of volumetric grade g_v, that is $\mathfrak{L}_A^{(1)}(1-g_v) = F_\ell(g_\ell = 0 \mid g_v)$. Similarly defined is the apparent linear liberation $\mathfrak{L}_B^{(1)}(g_v) = 1 - F_\ell(g_\ell = 1 \mid g_v)$ of phase *B*.

The second component is the distribution of linear grades of all linear intercepts that are reported as unliberated. The unliberated linear grade distribution is calculated from the linear grade distribution using the following definition, Barbery [17]:

$$F_{\ell u}(g_\ell \mid g_v) = \frac{F_\ell(g_\ell \mid g_v) - \mathfrak{L}_A^{(1)}(1-g_v)}{1 - \mathfrak{L}_A^{(1)}(1-g_v) - \mathfrak{L}_B^{(1)}(g_v)} \tag{2.13}$$

$F_{\ell u}(g_\ell \mid g_v)$ is strictly continuous in the domain [0,1] and does not have step discontinuities at $g_\ell = 0$ and $g_\ell = 1$ as $F_\ell(g_\ell \mid g_v)$ does. It is convenient and sensible to model the two discontinuities $\mathfrak{L}_A^{(1)}(1-g_v)$ and $\mathfrak{L}_B^{(1)}(g_v)$ and the internal distributions $F_{\ell u}(g_\ell \mid g_v)$ separately and to generate the actual kernel function $F_\ell(g_\ell \mid g_v)$ from equation 2.13. It is shown below that $\mathfrak{L}_A^{(1)}(1-g_v)$, $\mathfrak{L}_B^{(1)}(g_v)$ and $F_{\ell u}(g_\ell \mid g_v)$ can be modeled by a set of simple continuous functions.

The remaining terms in equation 2.12 can also be written in terms of their liberated and unliberated components, as follows:

$$F_{\ell u}^j(g_\ell \mid D^*) = \frac{F_\ell^j(g_\ell \mid D^*) - \mathfrak{L}_{Aj}^{(1)}}{1 - \mathfrak{L}_{Aj}^{(1)} - \mathfrak{L}_{Bj}^{(1)}} \tag{2.14}$$

and,

$$\frac{\partial F_{vu}\left(g_v \mid D^*\right)}{\partial g_v} = f_{vu}\left(g_v \mid D^*\right) = \frac{f_v\left(g_v \mid D^*\right)}{F_v\left(g_v = 1 \mid D^*\right) - F_v\left(g_v = 0 \mid D^*\right)} \tag{2.15}$$

Equation 2.16 is obtained by substituting the definitions of apparent linear liberation and unliberated linear grade distributions shown in equations 2.13 and 2.14 into equation 2.12. In this form, equation 2.10 is entirely written in terms of its liberated and unliberated components. Each integrated term in the left hand side of equation 2.14 has an integral sibling in the right hand side which can be immediately recognized.

$$\begin{aligned} F_{\ell u}^{j}\left(g_\ell \mid D^*\right) - F_{\ell u}^{j}\left(g_\ell \mid D^*\right)\left(\mathfrak{L}_{Aj}^{(1)} + \mathfrak{L}_{Bj}^{(1)}\right) + \mathfrak{L}_{Aj}^{(1)} = {} & \frac{\int_{g_v^{j-1}}^{g_v^{j}} F_{\ell u}\left(g_\ell \mid g_v\right) f_v\left(g_v \mid D^*\right) dg_v}{\int_{g_v^{j-1}}^{g_v^{j}} f_v\left(g_v \mid D^*\right) dg_v} - \\ & \frac{\int_{g_v^{j-1}}^{g_v^{j}} F_{\ell u}\left(g_\ell \mid g_v\right)\left(\mathfrak{L}_A^{(1)}\left(1-g_v\right) + \mathfrak{L}_B^{(1)}\left(g_v\right)\right) f_v\left(g_v \mid D^*\right) dg_v}{\int_{g_v^{j-1}}^{g_v^{j}} f_v\left(g_v \mid D^*\right) dg_v} + \\ & \frac{\int_{g_v^{j-1}}^{g_v^{j}} \mathfrak{L}_A^{(1)}\left(1-g_v\right) f_v\left(g_v \mid D^*\right) dg_v}{\int_{g_v^{j-1}}^{g_v^{j}} f_v\left(g_v \mid D^*\right) dg_v} \end{aligned} \tag{2.16}$$

Here, we are only interested in two components of equation 2.16, as follows:

$$F_{\ell u}^{j}\left(g_{\ell} \mid D^{*}\right) = \frac{\int_{g_v^{j-1}}^{g_v^{j}} F_{\ell u}\left(g_{\ell} \mid g_v\right)\, f_v\left(g_v \mid D^{*}\right)\, dg_v}{\int_{g_v^{j-1}}^{g_v^{j}} f_v\left(g_v \mid D^{*}\right)\, dg_v} \tag{2.17}$$

and

$$\mathfrak{L}_{Aj}^{(1)} = \frac{\int_{g_v^{j-1}}^{g_v^{j}} \mathfrak{L}_{A}^{(1)}\left(1-g_v\right)\, f_v\left(g_v \mid D^{*}\right)\, dg_v}{\int_{g_v^{j-1}}^{g_v^{j}} f_v\left(g_v \mid D^{*}\right)\, dg_v} \tag{2.18}$$

Now, if the phase of interest is switched to phase A in equations 2.12 and 2.13, using the same argument as above, the final expression needed for the evaluation of the transformation kernel, shown in equation 2.19, is obtained.

$$\mathfrak{L}_{Bj}^{(1)} = \frac{\int_{g_v^{j-1}}^{g_v^{j}} \mathfrak{L}_{B}^{(1)}\left(g_v\right)\, f_v\left(g_v \mid D^{*}\right)\, dg_v}{\int_{g_v^{j-1}}^{g_v^{j}} f_v\left(g_v \mid D^{*}\right)\, dg_v} \tag{2.19}$$

The terms on the left hand side of equations 2.17, 2.18 and 2.19 are the unliberated and liberated components of the linear grade distributions generated by two-phase particles in a narrow size, narrow grade interval. Each of these functions can be measured directly by image analysis, provided that appropriate samples of particles can be generated by fractionation. Equations 2.17, 2.18 and 2.19 are important because they

allow modeling of the unliberated and liberated components of the transformation kernel to be carried out independently. Successful modelling can be achieved by means of suitable functional forms, which are continuous in the grade domain, for the distributions $F_{\ell u}(g_\ell \mid g_v)$, $\mathfrak{L}_A^{(1)}(1-g_v)$ and $\mathfrak{L}_B^{(1)}(g_v)$.

It is easy to separate particles in narrow size intervals, and this can be accomplished with a standard sieving procedure. However, separation in different grade classes can be messy, depending on either separation method or test ore properties. The choice of a test ore which is essentially composed of two phases with distinct densities facilitates the separation, and sink-and-float fractionation can be used to produce clean samples. Conventional sink-and-float fractionation requires the use of high density organic liquids. When relatively high separation densities are required, it is necessary to use organic liquids that are also highly toxic, carcinogenic, expensive, and can only be diluted in comparatively expensive organic liquids. Alternatively, fractionation can be accomplished with the use of ferromagnetic colloidal suspensions. These suspensions produce a useful density gradient when submitted to a magnetic field. The MAGSTREAM™ [18] is a device that uses an iron oxide colloidal suspension which is subject to a magnetic field of constant magnitude. The particles are immersed in this fluid, which circulates downwards inside of a cylindrical fixture, which in turn rotates around its axes. The rotation subjects the particles to centrifugal forces, consequently accelerating them towards the increasing density gradient near the outer wall of the cylinder. Particles of higher density will penetrate the density gradient deeper, thus producing stratification along the radial direction. This is illustrated in Figure 2.1. As

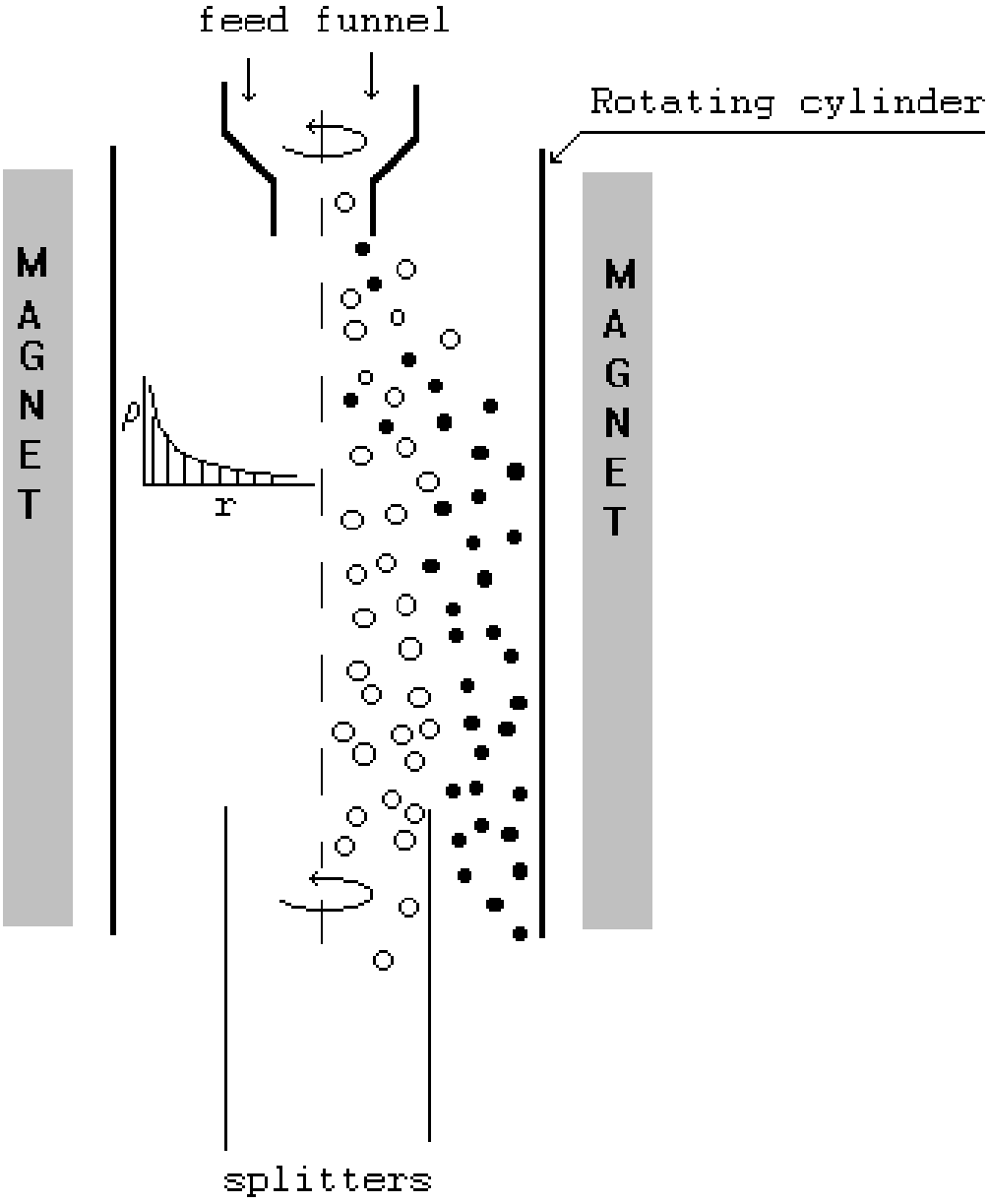

Figure 2.1 The MAGSTREAM™ separation concept. Stratification is achived by balancing centrifugal and bouyancy forces

particles approach the bottom end of the cylinder, they are split and follow either the lights or heavies stream. The separation density is set by adjusting the speed at which the cylinder rotates. It is also a function of the colloid concentration, which can be easily measured with a hydrometer. One of the main advantages of the MAGSTREAM™ is that it allows separation densities as high as 20 g/cc. It is also environmentally safe. If operated carefully, the MAGSTREAM™ produces a very sharp separation curve, minimizing the amount of misplaced material. However, depending on the relative amounts of Near Gravity Material (*NGM*) at the separation density, contamination can still be very high. This problem can be satisfactorily overcome by repeated separations in an organized fashion, as described later in this paper.

An image analysis system based on a Scanning Electron Microscope (*SEM*) has been implemented at the University of Utah. The system is described in King and Schneider [16], and provides a number of image processing routines that allow precise measurement of linear grade intercepts through cross sections of composite particles, provided the SEM can produce images with good phase discrimination. This system has been used successfully in this work for accurately measuring the linear grade distributions generated by narrow size, narrow grade particle samples. The complete procedure to achieve such a measurement is described in detail in the following sections of this chapter.

Experimental

The test ore was Dolomite-Sphalerite from the ASARCO Young Mill, Tennessee. A sample weighing approximately 260 kg was collected from the heavy media cone

concentrate stream. The particles in this particular stream are mostly locked Dolomite-Sphalerite measuring between 38.1 and 9.5 mm with a suitable grade for liberation studies. A representative sample weighing 20 kg was initially separated from the bulk by riffling, and then crushed in a small jaw crusher with closed size set at 10 mm. Further crushing was carried out in a roll crusher. One pass was made with the gap between rolls set at 9.5 mm. Repeated passes were then carried out with the gap set at 3.2 mm until all particles passed a 6.35 mm screen, to avoid exaggerated fines generation. Finally, repeated passes were carried out with touching rolls, until all particles passed the 1 mm screen. The crushed particles were then screened at 710 microns. The particles in the range of 1000 to 710 microns, weighing approximately 3.0 kg, were then separated for dense liquid fractionation.

MAGFLUID™ was diluted with water to a fluid density of ρ_f = 1.064 g/cc, which corresponded to a fluid magnetization of M_f = 2.05 emu/cc. Separation densities of 2.9, 3.1, 3.3, 3.5, 3.7 and 4.0 g/cc were chosen to provide enough particles in each of the seven density ranges. The rotating speeds corresponding to these separation densities are found by means of equation 2.20, for nonmagnetic materials. A good description of the force balance on mineral particles immersed in rotating magnetic fluids is given in Walker and Devernoe [18].

$$N = 347 \sqrt{\frac{M_f}{\rho_s - \rho_f}} \tag{2.20}$$

Here ρ_s is the separation density and N is in revolutions per minute. The separation sequence is shown diagrammatically in Figure 2.2. Because of the relatively higher

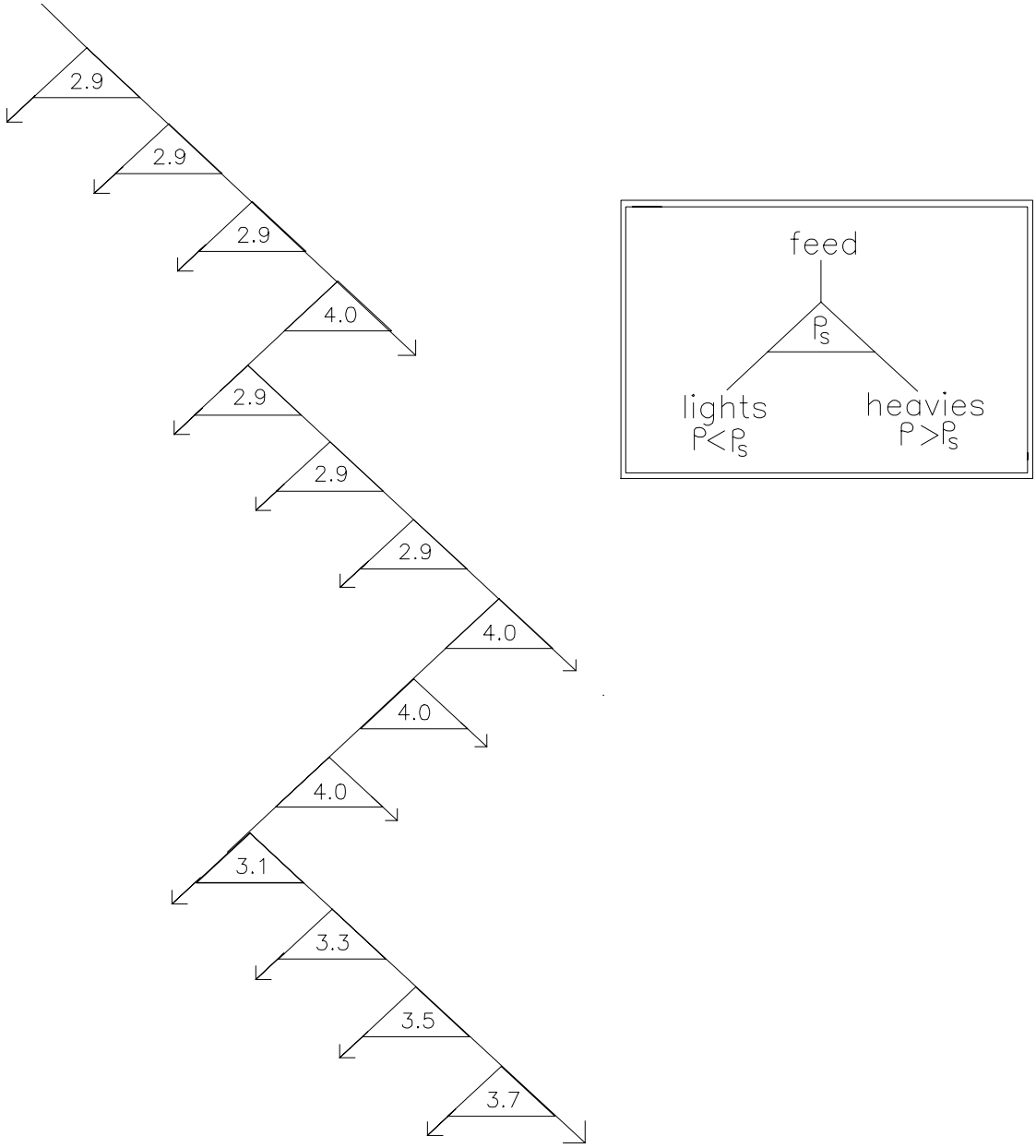

Figure 2.2 The separation sequence for the preparation of narrow grade Dolomite-Sphalerite particles in the MAGSTREAM™

amount of particles near the end densities, approaching that of liberated Dolomite and liberated Sphalerite, it is necessary to perform repeated separations to minimize the amounts of misplaced particles. Once these are separated, the intermediate cuts can be carried out with a single pass. The density of the resulting seven narrow size/grade samples was then checked with a helium pycnometer, to ensure that their average density was in the correspondent separation density range, and for later correlation with the average grades measured by image analysis. The MAGSTREAM™ separation results are shown in Table 2.1. The weight fractions shown in that table are defined as the distribution of particle densities, by weight, integrated over the density range that is defined by the separation densities used in the narrow size sample fractionation. Because there is direct correspondence between g_v and ρ, the index *j* is also used for density, i.e.,

$$f_w^j = \int_{\rho^{j-1}}^{\rho^j} f_w\left(\rho \mid D^*\right)\, d\rho \qquad (2.21)$$

for j = 1 to 7, $\rho^0 = \rho_A$ and $\rho^7 = \rho_B$.

A representative sample of about 6 g from each of the seven narrow size/grade particles was separated with a PULVERIT™ automatic sampler and then mounted in epoxide resin. It is very important that the particles are randomly oriented in each mount. The particles were placed under weak vacuum in a lab desiccator. A BUEHLER 32 mm reusable rubber mounting cup will ideally hold approximately 6 g of particulate material, so 18 g of epoxide resin/epoxide hardener mixture was carefully stirred in a small paper cup to avoid the formation of air bubbles, until the mixture was completely homogenized. One third of this mixture was initially poured into the mounting cup. The particles were

Table 2.1 MAGSTREAM™ separation results, density check with a Helium Pycnometer and measured volumetric grades by image analysis

Density range, g/cc	Density/ grade range *j*	Fraction in range by weight, f_w^j	Average density g/cc, from Helium Pycnometer, $\overline{\rho^j}$	Average volumetric grade % by image analysis, $\overline{g_v^j}$
-2.9	1	0.7879	2.851	0.73
-3.1 +2.9	2	0.0327	2.959	9.47
-3.3 +3.1	3	0.0125	3.133	27.27
-3.5 +3.3	4	0.0120	3.316	40.49
-3.7 +3.5	5	0.0086	3.522	58.00
-4.0 +3.7	6	0.0167	3.746	79.38
+4.0	7	0.1296	4.005	94.64

then removed from the vacuum and carefully poured into the resin in the mounting cup where they slowly sank in the resin, ensuring that all surfaces are wet. After the particles completely settled, the resin/particle mixture was gently stirred, literally pushing the particles against each other. In this way, each individual particle experiences forces from a number of directions, resulting in mostly random orientation. Following this procedure, a label was inserted and the mounting cup was filled with the remaining resin/hardener mixture.

The sample mounts were ground with 60 grit silicon carbide abrasive paper to remove the first few layers of particles. The grinding stage was completed by lapping with 120, 320 and 600 grit silicon carbide abrasive paper.

Dolomite and Sphalerite are easily polished and lapping with 1 micron alumina followed by 0.3 micron alumina is sufficient. The polished surface must be cleaned in an ultrasonic bath before and after each polishing stage to avoid alumina contamination. After polishing, the surface was carbon coated for image acquisition in the *SEM*.

A set of 20 images per specimen was collected in the *SEM*, using a back-scattered electron detector. The set covered the entire surface of the specimen, with no image overlapping. The magnification was kept at 20x for all images. Scanning speed was kept at 0.79 frames/second and an 8 frame averaged image was collected in order to reduce random noise. The images collected in this way were compressed and stored on tapes, from which they may be selectively retrieved for image processing. The images were stored as raw binary files in a 512x436x8 format. The images were converted to 512x512x8 format for processing using interpolation of grade level to stretch the 436

pixel rows to 512 pixel rows.

Figures 2.3, 2.4 and 2.5 are 512x512 grey level images from the particles in the density ranges 3.1 to 3.3 g/cc, 3.3 to 3.5 g/cc and 3.5 to 3.7 g/cc, respectively, after background correction, prior to delineation filtering. Background correction is necessary due to background intensity variations inherent to the *SEM*. All images were corrected to the same level of background prior to further processing. This also ensured that the average gray level of the background (epoxy), was at the same grey level intensity, in this case 30, for all images, prior to delineation and segmentation.

Delineation filtering followed background correction. It is required to eliminate the halo that surrounds the phases with higher grey values, by converting the steep grey level ramps that define the phase boundaries in a grey level image into sharp steps so that the transition from one phase to the next is accomplished in a single pixel.

In Figures 2.3, 2.4 and 2.5 the phases can be easily identified. The darker points are the back-scattered electron intensities detected from the epoxy mounting media. The brighter areas are back-scattered electron intensities detected from the Sphalerite. The intermediate grey levels represent Dolomite. From the images is readily observed the low degree of two-dimensional liberation, which is expected from particles in intermediate grade levels. There is also good correlation with sample grade, and the relative areal fraction of Sphalerite increases as particle density increases. The images also show excellent phase discrimination. The grey level histogram corresponding to the image in Figure 2.4 is shown in Figure 2.6. Again, good phase discrimination is observed in the histogram. The peak on the left side of the histogram are back-scattered intensities

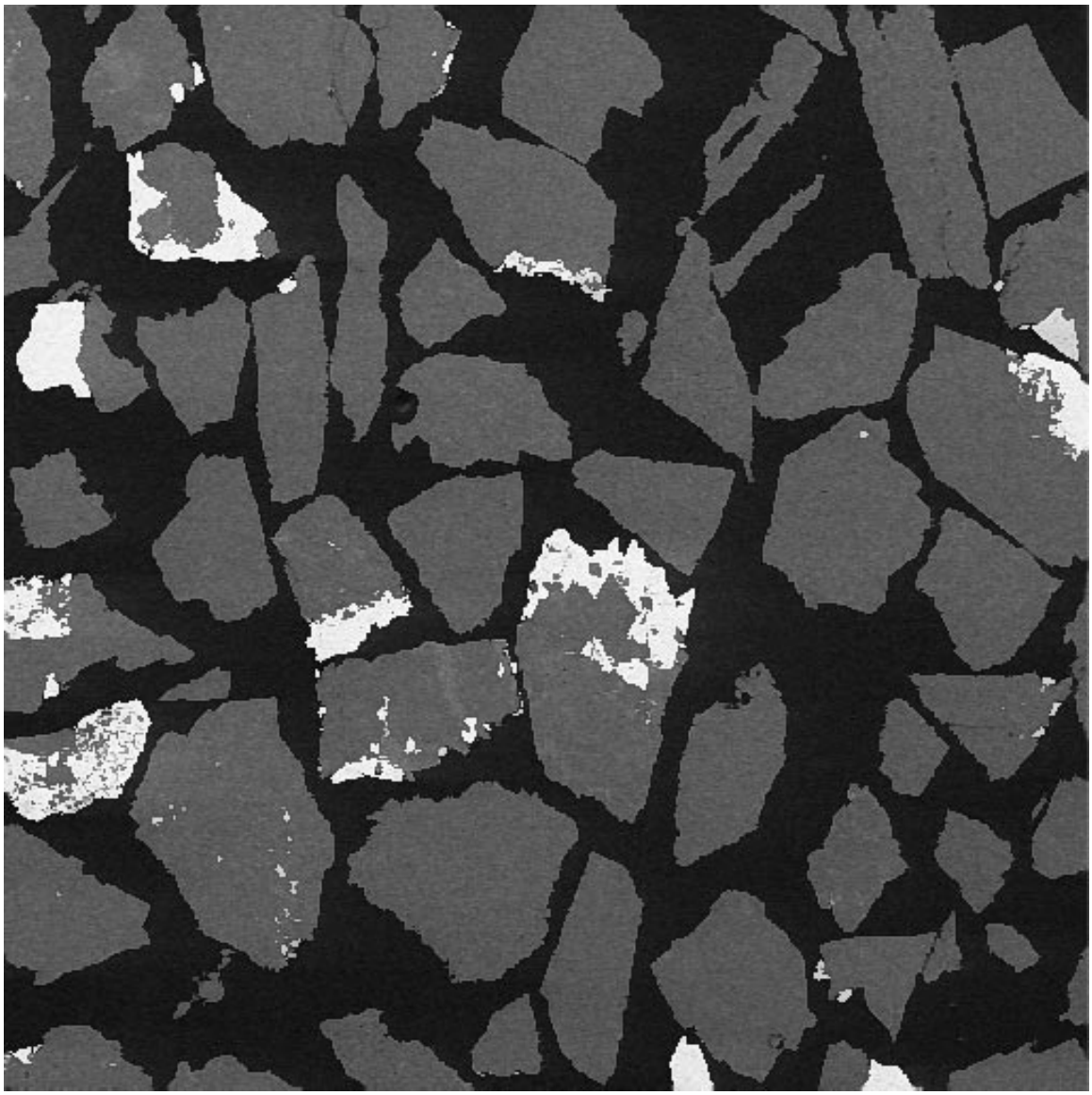

Figure 2.3 A 512x512 backscattered electron image of Dolomite-Sphalerite particles in the 3.1 to 3.3 g/cc density range

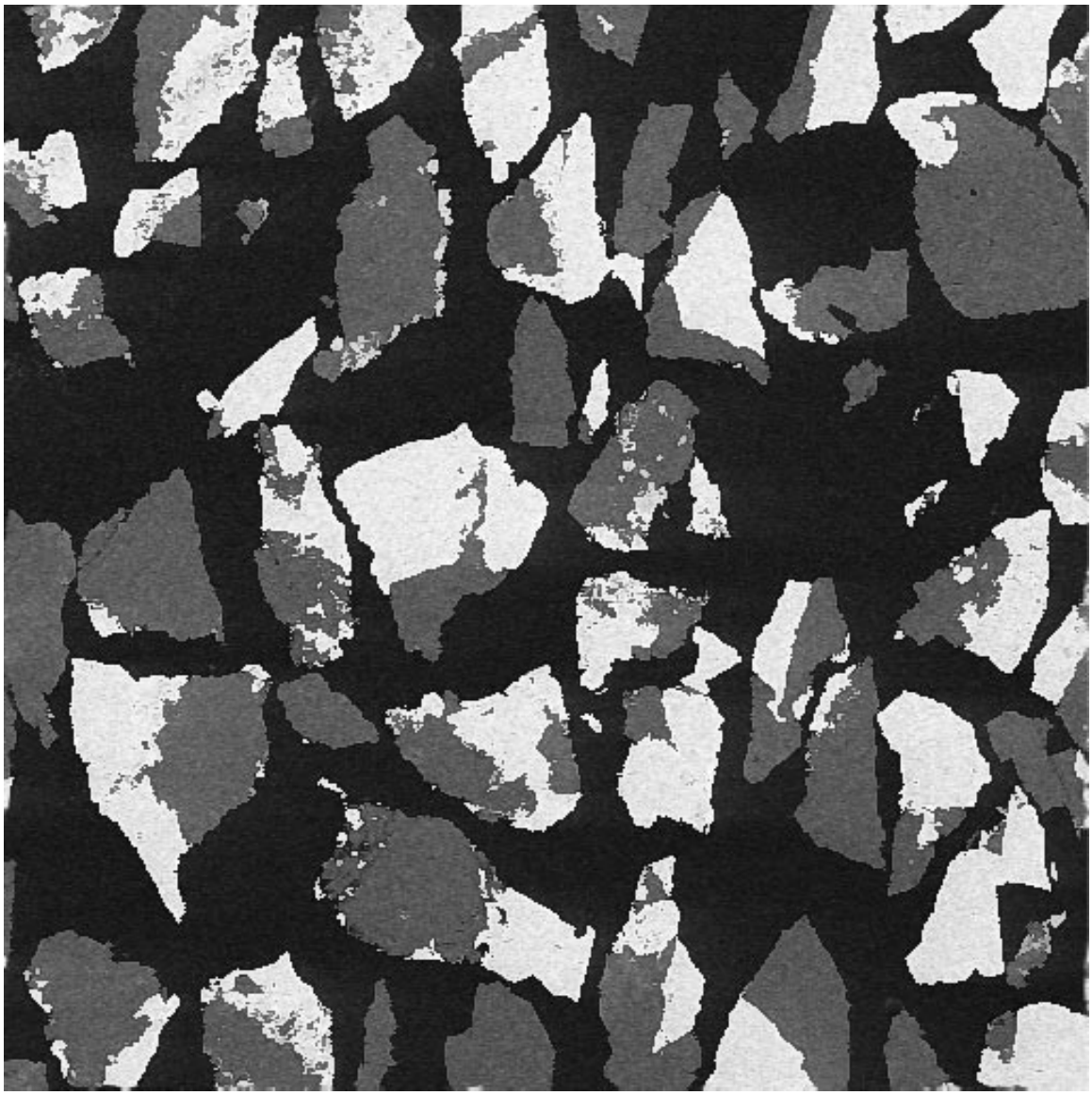

Figure 2.4 A 512x512 backscattered electron image of Dolomite-Sphalerite particles in the 3.3 to 3.5 g/cc density range

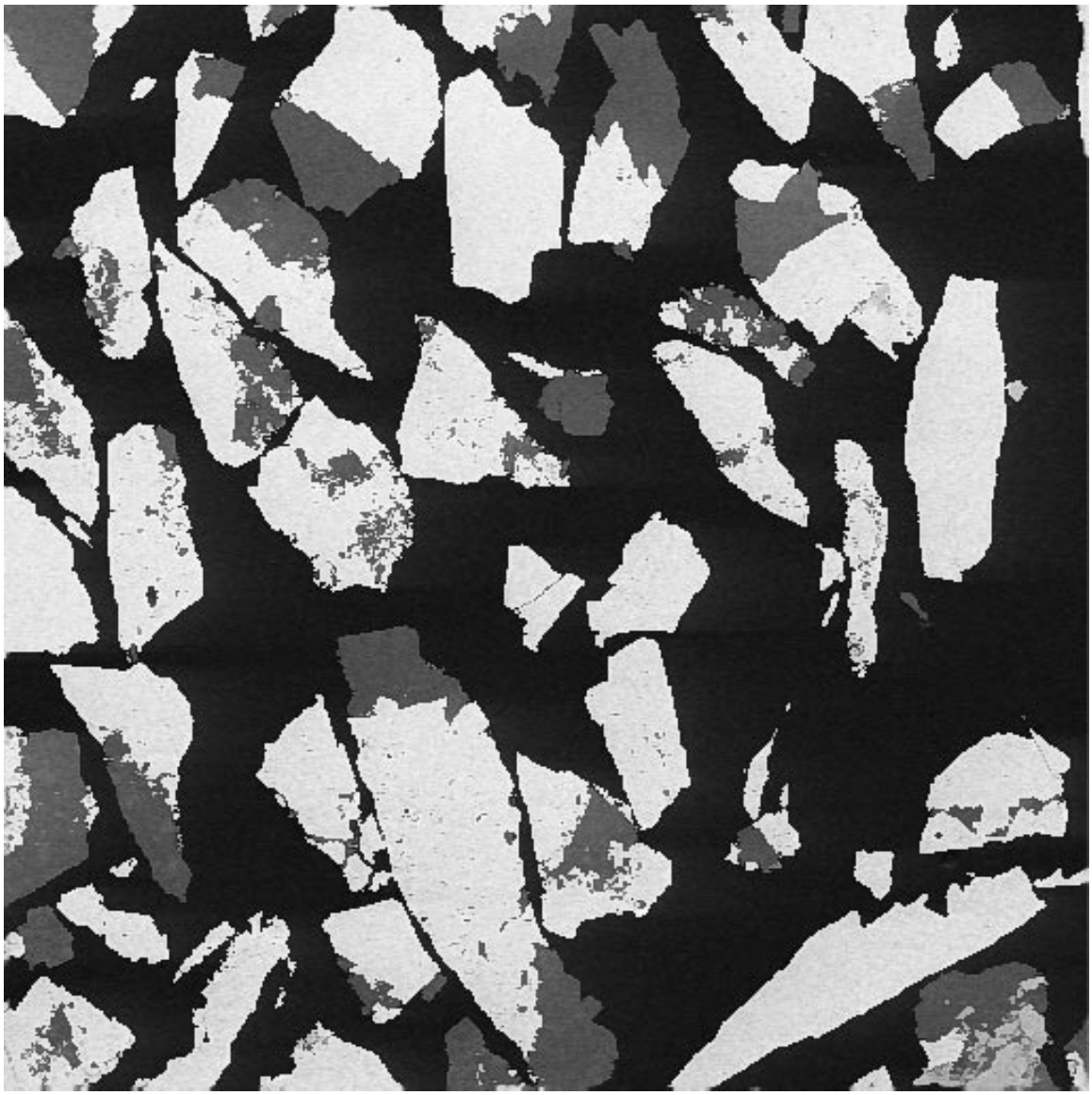

Figure 2.5 A 512x512 backscattered electron image of Dolomite-Sphalerite particles in the 3.5 to 3.7 g/cc density range

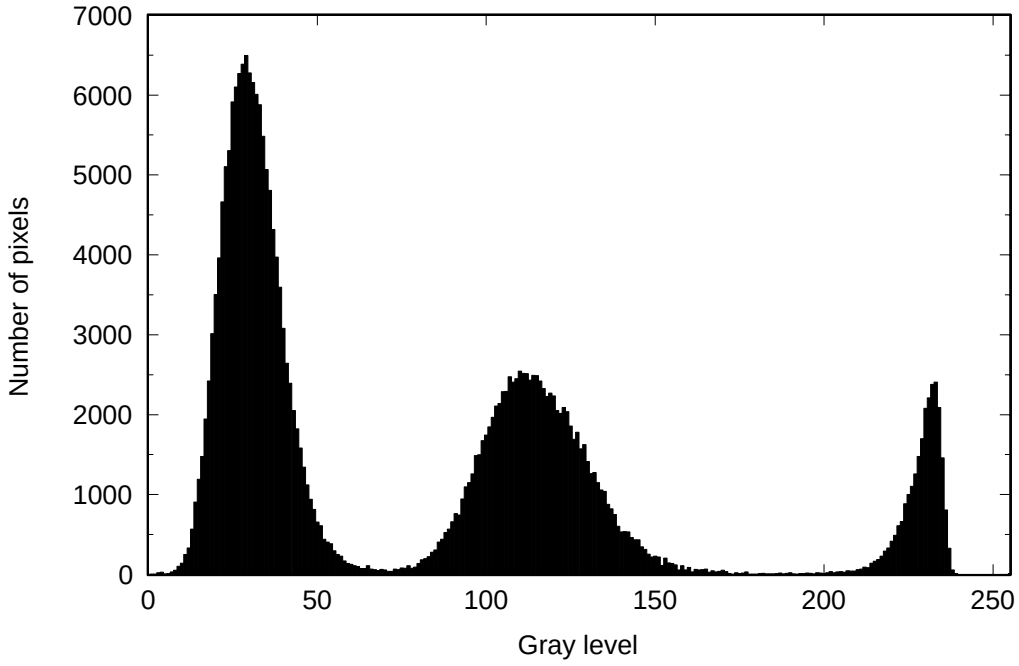

Figure 2.6 The grey level histogram corresponding to the image shown in Figure 2.4

detected from the background (epoxy). The middle peak corresponds to the Dolomite and the peak to the right, at higher gray levels, corresponds to the Sphalerite. Phase segmentation is achieved by grey level thresholding coupled with feature filling and fingerprinting. Binary segmentation of the Sphalerite is achieved by thresholding the image at the lowest frequency in the histogram corresponding to a grey level between the Sphalerite and the Dolomite peaks. The resulting binary image is then filled, to correct for polishing imperfections and holes on the Sphalerite surface, which might be confused with Dolomite inclusions. This filling procedure will generate an error in that it also wipes out any traces of Dolomite that are completely surrounded by Sphalerite. However, filling the Sphalerite areas does not affect significantly the measurement of the linear grade distributions due to the predominantly coarse texture that characterizes this Dolomite-Sphalerite system. Feature segmentation follows by thresholding the image at the lowest frequency corresponding to a grey level between the background and the Dolomite peak. The thresholding procedure incorrectly identifies small artifacts in the mounting medium as particles. These are usually rejected using a size criterium but an alternative and apparently more reliable method is used here. This technique is called fingerprint. A fingerprint of the features can be produced by thresholding the image at a level slightly higher than the Dolomite peak. This produces a highly fragmented image of the features. Any area on the original segmented feature image that does not have at least one pixel in the fingerprint image is discarded. The features are then filled, and combined with the segmented Sphalerite image to produce a ternary image, which is ready for measurement. The result is not sensitive to the segmentation level that is used

to generate the fingerprint image and the method can be incorporated safely in automatic image analysis sequences. The fingerprint image of the features corresponding to the image in Figure 2.4 is shown in Figure 2.7, to illustrate the fingerprinting procedure.

The linear grade distribution is obtained by superimposing a set of linear probes on the ternary image, and counting the number of intercepts that have linear grade in one of twelve linear grade classes, for each intercept length. This is illustrated in Figure 2.8, which is the ternary equivalent of the image shown in Figure 2.4. The inset is a histogram corresponding to the measured linear grade distribution $f_\ell^j\left(g_\ell \mid D^*\right)$ for this particular image. For this measurement, only intercepts that start within a measuring frame are recorded, and all intercepts that are not completed before striking the edge of the image frame are rejected. The width of the measuring frame for this work was 510 pixels. With this, the proper frame correction procedure [16] can be carried out when calculating the linear grade distributions from the measured linear intercept distributions.

The average volumetric grade $\overline{g_v^j}$ of each sample can be measured by calculating the relative fraction of the phases in the correspondent images. The direct measurement of three-dimensional grades from particle cross sections is based on the fundamental law of stereology [19], which states that point, linear, areal and volumetric grades are equal,

$$g_p = g_\ell = g_a = g_v \tag{2.22}$$

The average volumetric grade of the narrow size, narrow grade particles, shown in Table 2.1, can be directly correlated to their average density, as measured by helium pycnometer, as shown in Figure 2.9. The relationship is given by a mass balance between the phases,

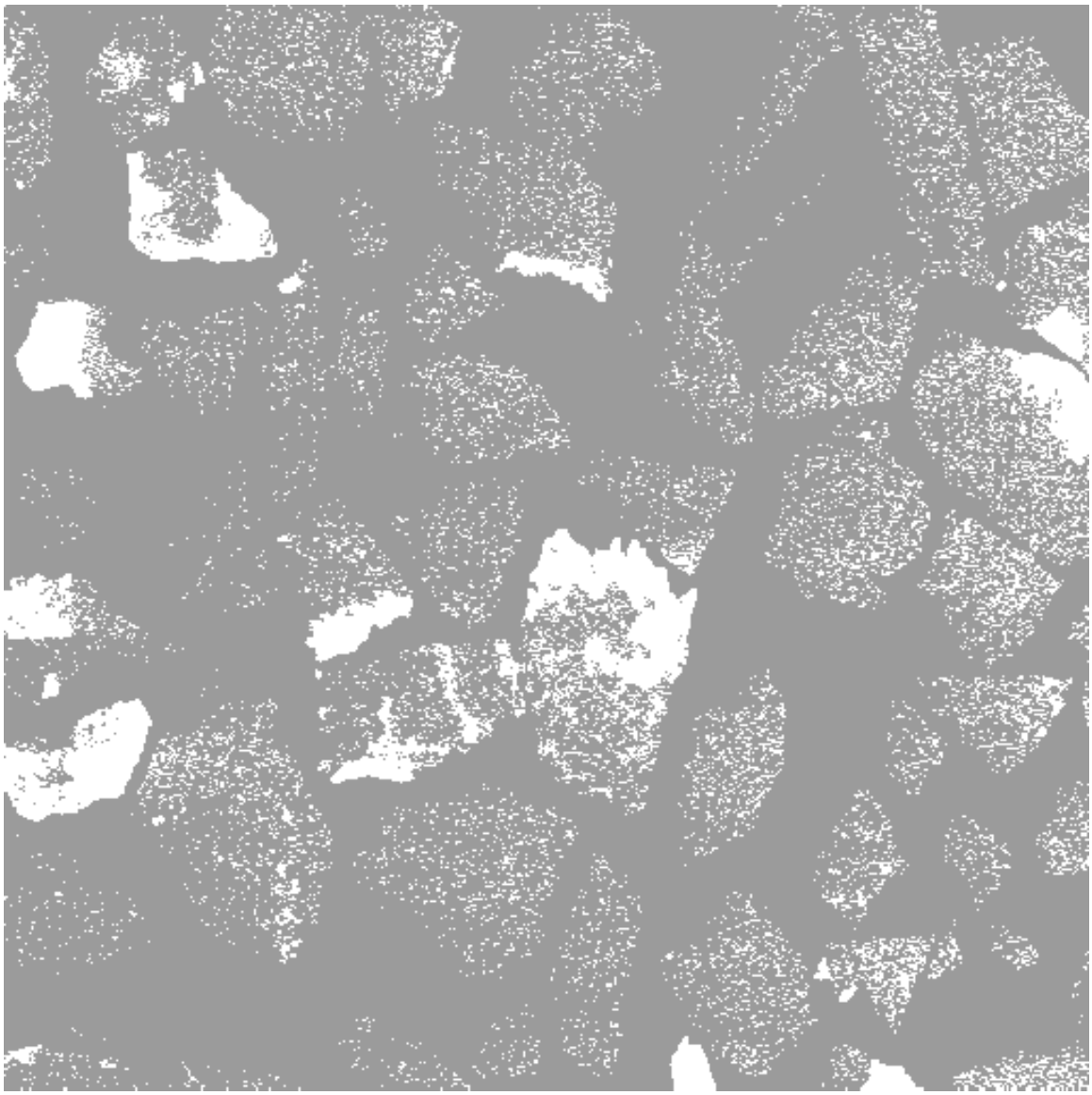

Figure 2.7 The fingerprint image corresponding to the background corrected image in Figure 2.3

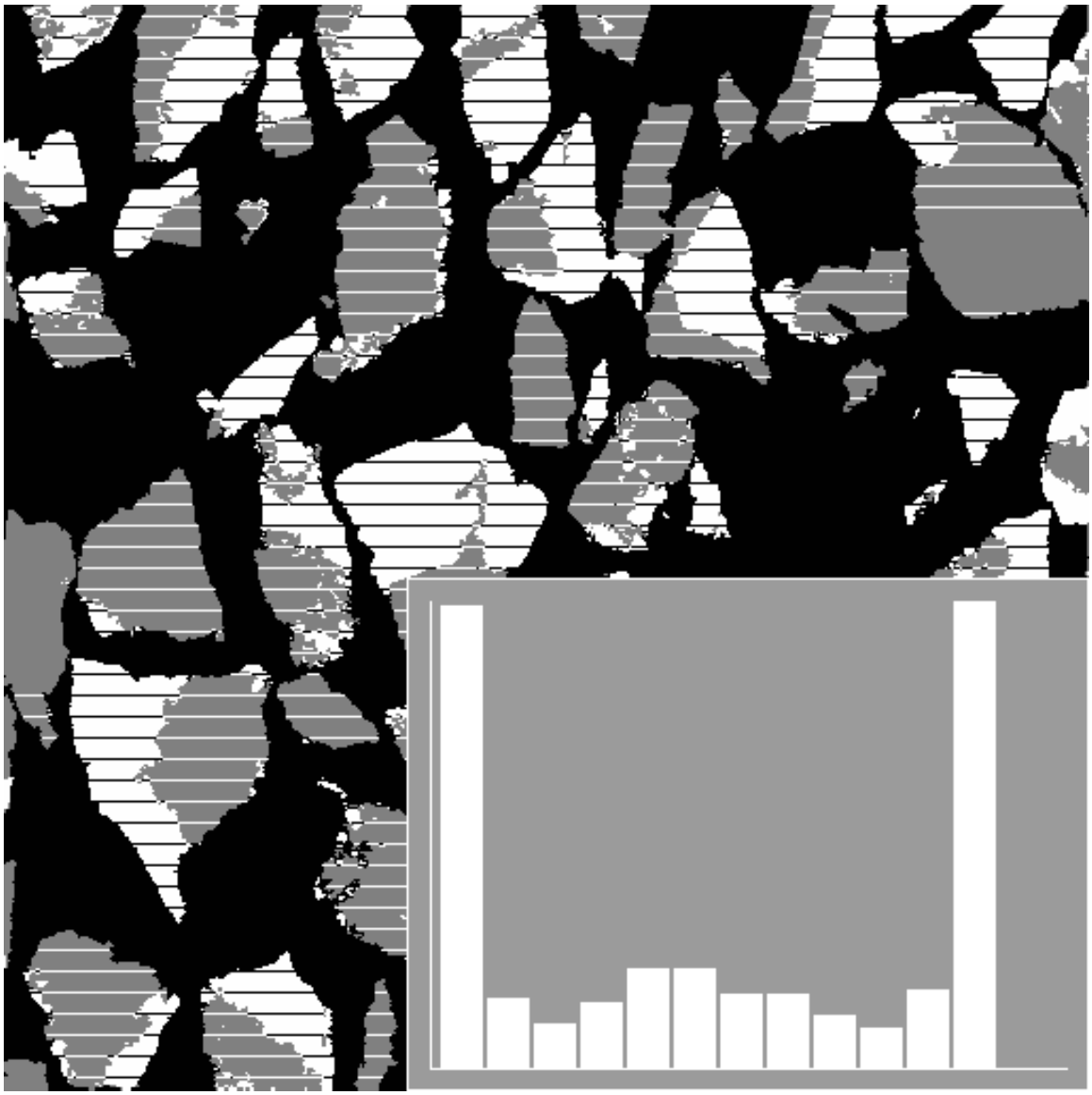

Figure 2.8 The overlaying linear probes and the linear grade distribution histogram in the processed ternary version of the image in Figure 2.4

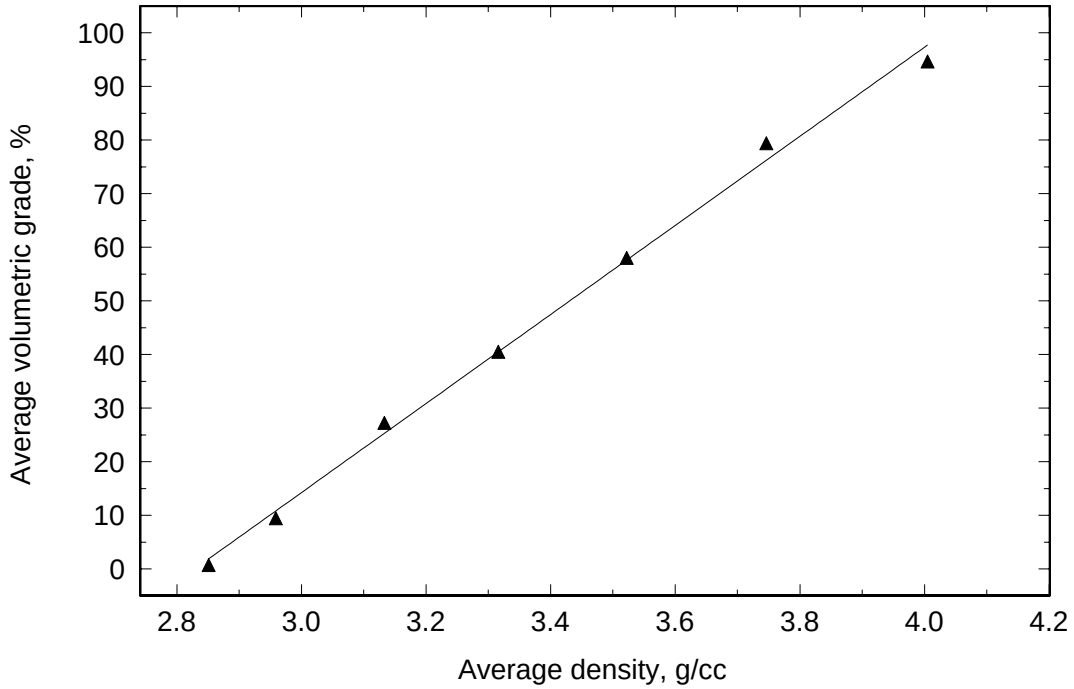

Figure 2.9 Correlation between average sample density by Helium Pycnometry and average sample volumetric grade by image analysis

$$\rho = (\rho_B - \rho_A)\, g_v + \rho_A \tag{2.23}$$

where ρ_A is the density of pure Dolomite and ρ_B is the density of pure Sphalerite. Linear regression yield ρ_A = 2.830 g/cc and ρ_B = 4.030 g/cc. These densities are in agreement with the standard density ranges listed in Dana's Manual of Mineralogy [20], which reports a density of 2.85 g/cc for commonly found Dolomite and 3.9 to 4.1 g/cc for Sphalerite. The very good correlation obtained again indicates that the fractionation was indeed successful. With the values of the densities for each phase, it is possible to assign narrow volumetric grade intervals g_v^{j-1}, g_v^j to the corresponding narrow density intervals, again using equation 2.23. The volume fraction corresponding to each grade interval is simply calculated from the weight fractions and average densities in Table 2.1, using the following definition:

$$f_v^j = \frac{\bar{\rho}\, f_w^j}{\overline{\rho^j}} \tag{2.24}$$

where $\overline{\rho^j}$ are the average densities of each fraction as measured with the helium pycnometer, and $\bar{\rho}$ is the average density of the sample.

$$\bar{\rho} = \frac{1}{\sum_{j=1}^{N} \frac{f_w^j}{\overline{\rho^j}}} \tag{2.25}$$

The resulting volumetric grade ranges and the calculated discrete volumetric grade distribution density are shown in Table 2.2. The corresponding volumetric grade distribution of the unliberated particles is calculated using the discrete version of equation

Table 2.2 Calculated volumetric grade distribution by volume f_v^j, unliberated volumetric grade distribution by volume f_{vu}^j and corresponding volumetric grade ranges

j	Volumetric grade range, % $-g_v^j \; +g_v^{j-1}$	Fraction in range by volume, f_v^j	Fraction in range by volume, f_{vu}^j
1	-5.80 +0.00	0.8268	0.1672
2	-22.47 +5.80	0.0330	0.3301
3	-39.14 +22.47	0.0120	0.1198
4	-55.81 +39.14	0.0108	0.1083
5	-72.48 +55.81	0.0073	0.0733
6	-97.48 +72.48	0.0133	0.1332
7	-100.00 +97.48	0.0968	0.0681

2.15, as shown in equation 2.26.

$$f_{vu}^{j} = \frac{f_{v}^{j}}{F_{v}\left(g_{v} = 1 \mid D^{*}\right) - F_{v}\left(g_{v} = 0 \mid D^{*}\right)} \tag{2.26}$$

The cumulative volumetric grade distribution is plotted against the upper volumetric grade of each fraction, and this is shown in Figure 2.10. Since repeated fractionation of the particles were carried out at volumetric grades very close to both ends of the spectrum, the distribution can be extrapolated without much error to get good estimates of the volume fraction of liberated Dolomite and Sphalerite in the sample. This is shown in Figure 2.10 as well, and the estimates for both extremes are $F_{v}\left(g_{v} = 0 \mid D^{*}\right) = 0.810$ and $F_{v}\left(g_{v} = 1 \mid D^{*}\right) = 0.906$. These values were used in equation 2.26 to calculate the discrete volumetric grade distribution density of the unliberated particles corresponding to $f_{vu}\left(g_{v} \mid D^{*}\right)$. The resulting fractions for the unliberated distribution are shown in Table 2.2, and the cumulative unliberated distribution is also plotted in Figure 2.10.

The fractions in 12 selected linear grade classes corresponding to the linear grade distributions $f_{\ell}^{j}\left(g_{\ell} \mid D^{*}\right)$ for each narrow grade sample, as measured by image analysis and after frame correction are shown in Table 2.3. The apparent linear liberation fractions, defined as $\mathfrak{L}_{Aj}^{(1)} = F_{\ell}^{j}\left(g_{\ell} = 0 \mid D^{*}\right)$ and $\mathfrak{L}_{Bj}^{(1)} = 1 - F_{\ell}^{j}\left(g_{\ell} = 1 \mid D^{*}\right)$, can be read directly in Table 2.3, and the unliberated linear grade distributions $F_{\ell u}^{j}\left(g_{\ell} \mid D^{*}\right)$ can be calculated directly from the data in Table 2.3, using the definition in equation 2.14. The results are shown in Table 2.4.

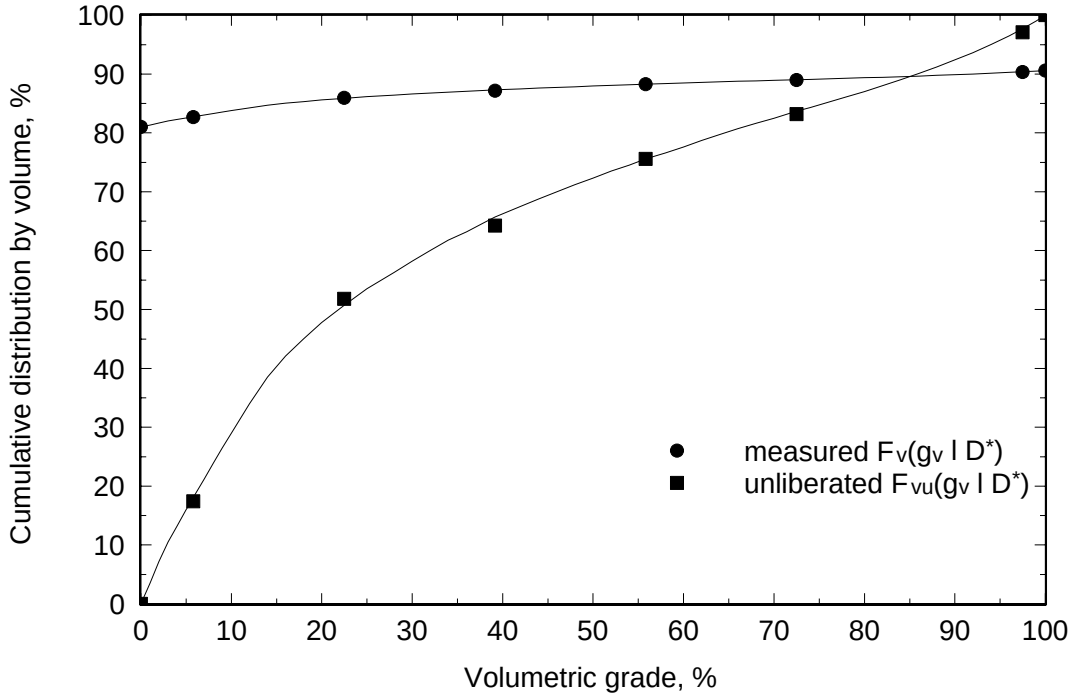

Figure 2.10 The cumulative volumetric grade distributions $F_v(g_v|D^*)$ and $F_{vu}(g_v|D^*)$ from fractionation of particles in the -1000+710 microns size range

Table 2.3 The measured, conditional on size, linear grade distributions by length, for each narrow grade sample produced by fractionation. Also shown are the % of apparent linear liberation $\mathfrak{L}_{Aj}^{(1)}$ and $\mathfrak{L}_{Bj}^{(1)}$ in rows $i = 1$ and $i = 12$

Conditional on size linear grade distributions % Volumetric grade interval %, $-g_v^j + g_v^{j-1}$								
i	Linear grade interval %, $-g_\ell^i + g_\ell^{i-1}$	j = 1, -5.80 +0.00	j = 2, -22.47 +5.80	j = 3, -39.14 +22.47	j = 4, -55.81 +39.14	j = 5, -72.48 +55.81	j = 6, -97.48 +72.48	j = 7, -100.00 +97.48
1	0	97.27	72.69	35.65	25.86	16.02	5.29	1.59
2	-10 +0	1.23	8.08	9.97	6.04	3.21	1.27	0.26
3	-20 +10	0.51	5.88	9.75	7.96	4.68	1.77	0.41
4	-30 +20	0.26	3.19	8.95	7.27	4.49	2.20	0.42
5	-40 +30	0.18	2.33	7.47	7.60	6.08	2.55	0.42
6	-50 +40	0.04	1.58	5.99	7.70	6.48	3.34	0.64
7	-60 +50	0.11	1.05	4.45	7.69	6.84	4.30	0.58
8	-70 +60	0.05	0.74	3.37	5.31	6.42	5.06	0.84
9	-80 +70	0.01	0.69	2.23	3.98	5.81	5.62	1.35
10	-90 +80	0.04	0.62	1.78	2.89	5.30	6.48	1.91
11	-100 +90	0.06	0.52	1.58	3.00	3.95	7.03	6.09
12	100	0.24	2.63	8.81	14.70	30.72	55.09	85.49

Table 2.4 The cumulative, conditional on size, unliberated linear grade distributions by length $F_{\ell u}^{j}(g_{\ell}^{i} \mid D^{*})$

Cumulative, conditional on size, unliberated linear grade distributions %, Volumetric grade interval %, $-g_v^j + g_v^{j-1}$								
i	Linear grade %, $-g_{\ell}^{i}$	j = 1, -5.80 +0.00	j = 2, -22.47 +5.80	j = 3, -39.14 +22.47	j = 4, -55.81 +39.14	j = 5, -72.48 +55.81	j = 6, -97.48 +72.48	j = 7, -100.00 +97.48
2	10	49.40	32.74	17.95	10.17	6.03	3.21	2.01
3	20	69.88	56.56	35.51	23.55	14.81	7.67	5.19
4	30	80.32	69.49	51.62	35.78	23.24	13.23	8.44
5	40	87.55	78.93	65.07	48.57	34.66	19.66	11.69
6	50	89.16	85.33	75.86	61.52	46.83	28.09	16.64
7	60	93.57	89.59	83.87	74.46	59.67	38.95	21.13
8	70	95.58	92.59	89.94	83.40	71.72	51.72	27.63
9	80	95.98	95.38	93.95	90.09	82.63	65.90	38.08
10	90	97.59	97.89	97.16	94.95	92.58	82.26	52.86
11	100	100.00	100.00	100.00	100.00	100.00	100.00	100.00

A Model for the Dolomite-Sphalerite Transformation Kernel

With the data in Tables 2.2, 2.3 and 2.4 it is possible to develop a transformation kernel $f_\ell(g_\ell \mid g_v)$ for the Dolomite-Sphalerite texture, using equations 2.17, 2.18 and 2.19. The first step in constructing the transformation kernel, is to establish a functional form for the apparent linear liberation that is generated by particles of volumetric grade equal to g_v. The apparent linear liberation fractions shown in Table 2.3 can be plotted against the average volumetric grades $\overline{g_v^j}$ measured for each sample in order to select an appropriate functional form for the functions $\mathcal{L}_A^{(1)}(1-g_v)$ and $\mathcal{L}_B^{(1)}(g_v)$. The plot of the measured apparent linear liberation fractions versus average volumetric grade is shown in Figure 2.11, for both phases. The solid line in that figure represent the functional form that was adopted for the model proposed here. Also, the proposed functional form has to satisfy both $\mathcal{L}^{(1)}(0) = 0$ and $\mathcal{L}^{(1)}(1) = 1$. The shape of the apparent linear liberation distribution is strictly a function of texture and, furthermore, $\mathcal{L}_A^{(1)}(1-g_v)$ is not equal to $\mathcal{L}_B^{(1)}(g_v)$ unless the texture is perfectly symmetric. The function $\mathcal{L}^{(1)}(g_v)$ is known analytically for a number of regular textures. The apparent linear liberation for spheres with planar interface [21] and for concentric spheres [22] is shown in Figure 2.11 for comparison. The case of concentric spheres is particularly interesting since this texture represents a limiting case for the function $\mathcal{L}^{(1)}(g_v)$. This is because for any value of g_v, the apparent linear liberation of the inner phase will be equal to zero, except at the limit when the volume of the inner phase equals the volume of the sphere. Whereas $\mathcal{L}^{(1)}(g_v)$ is minimum for the inner phase, it must be maximum for the outer phase. Therefore, it is expected that, for other, more realistic textures, the value of apparent linear liberation

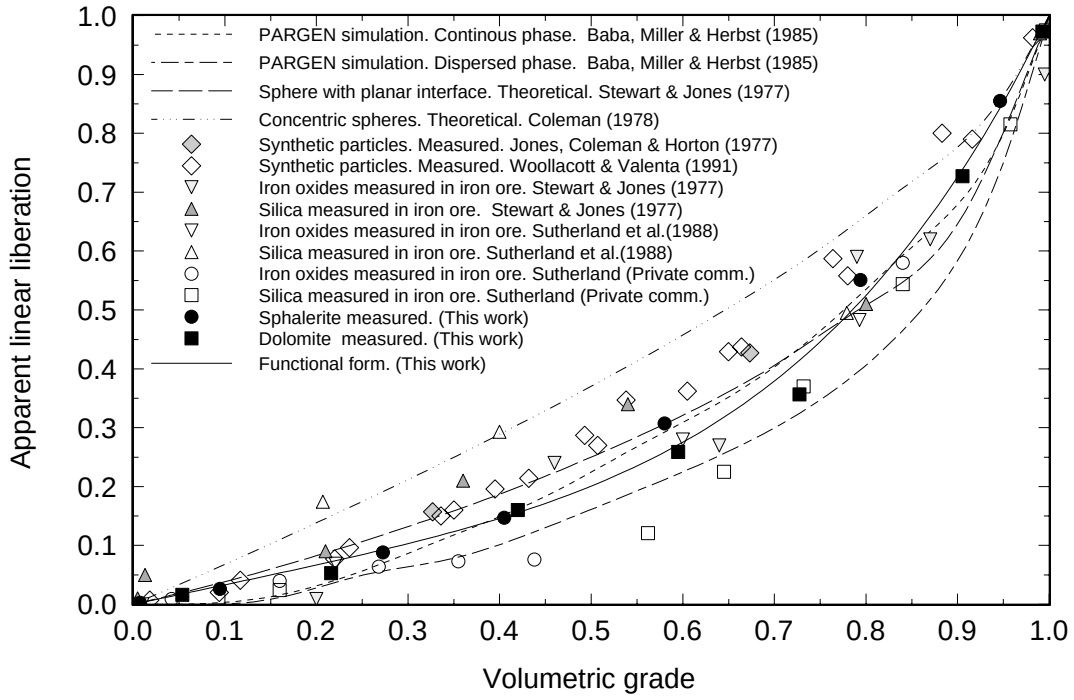

Figure 2.11 The apparent linear liberation distribution for theoretical, simulated, synthetic and real particles from the literature as compared to the Dolomite-Sphalerite system in this work

should be less than the one for concentric spheres for all grades, except at $g_v = 0$ and at $g_v = 1$. Figure 2.11 also includes data from computer generated PARGEN particles [6] and measured data from synthetic particles [15,23]. Finally, two data sets, both from a Silica-Iron Oxide system are added to Figure 2.11. The first set is due to Stewart and Jones [21], who separated narrow grade samples by dense liquid fractionation and segregation in a fluidised bed. The linear grade distributions were measured manually on particles cross sections. The second set, due to Sutherland et al. [24], was prepared similarly, but the measurement was carried out in the QEM*SEM. It is immediately observed in Figure 2.11 that the apparent linear liberation measured from the Dolomite-Sphalerite particles falls inside the range of spread of the other textures shown in the figure. This is relevant because it indicates that the texture of the Dolomite-Sphalerite ore can be representative of common mineralogical textures, which are also expected to fall in the same region. Furthermore, the distributions shown are, with the possible exception of the QEM*SEM data, well below the concentric spheres limiting case, which indicates that the data sets are reliable. The experimental points for Dolomite-Sphalerite fall close to a single line and this, at least, ensures that the same functional form can be used for both $\mathfrak{L}_A^{(1)}(1-g_v)$ and $\mathfrak{L}_B^{(1)}(g_v)$. Here, the following form is proposed,

$$\mathfrak{L}_A^{(1)}(1-g_v) = \xi_1^A (1-g_v)^{\xi_2^A} + (1-\xi_1^A)\,(1-g_v) \tag{2.27}$$

and

$$\mathfrak{L}_B^{(1)}(g_v) = \xi_1^B g_v^{\xi_2^B} + (1-\xi_1^B)\, g_v \tag{2.28}$$

where ξ_1 and ξ_2 are textural parameters for apparent linear liberation, and these have

slightly different values for the two components.

The second step in constructing the transformation kernel is to establish a functional form for the conditional, on volumetric grade, unliberated linear grade distribution. A plot of the cumulative fractions corresponding to the functions $F_{\ell u}^{j}\left(g_{\ell} \mid D^{*}\right)$ in Table 2.4, as shown in Figure 2.12, is useful to select an appropriate functional form for the distribution $F_{\ell u}\left(g_{\ell} \mid g_{v}\right)$. The Incomplete Beta function is a good choice in this context, not only because it can take the shapes of the distributions shown in Figure 2.12, but also because its domain is that of grade and its parameters are a function of its first and second moments. It is also convenient because on the symmetry relation $I_{x}\left(\alpha, \beta\right) = 1 - I_{1-x}\left(\beta, \alpha\right)$, which will be used later in this work. The transformation kernel for the unliberated particles is written in terms of the Incomplete Beta function as

$$F_{\ell u}\left(g_{\ell} \mid g_{v}\right) = I_{g_{\ell}}\left(\alpha\left(g_{v}\right), \beta\left(g_{v}\right)\right) \tag{2.29}$$

with

$$\alpha\left(g_{v}\right) = n_{1}^{B}\left(g_{v}\right)\ \gamma\left(g_{v}\right) \tag{2.30}$$

and

$$\beta\left(g_{v}\right) = \left(1 - n_{1}^{B}\left(g_{v}\right)\right)\ \gamma\left(g_{v}\right) \tag{2.31}$$

where

$$\gamma\left(g_{v}\right) = \frac{n_{1}^{B}\left(g_{v}\right) - n_{2}^{B}\left(g_{v}\right)}{n_{2}^{B}\left(g_{v}\right) - \left(n_{1}^{B}\left(g_{v}\right)\right)^{2}} \tag{2.32}$$

with $n_{1}^{B}\left(g_{v}\right)$ and $n_{2}^{B}\left(g_{v}\right)$ the first and second moments of the unliberated linear grade

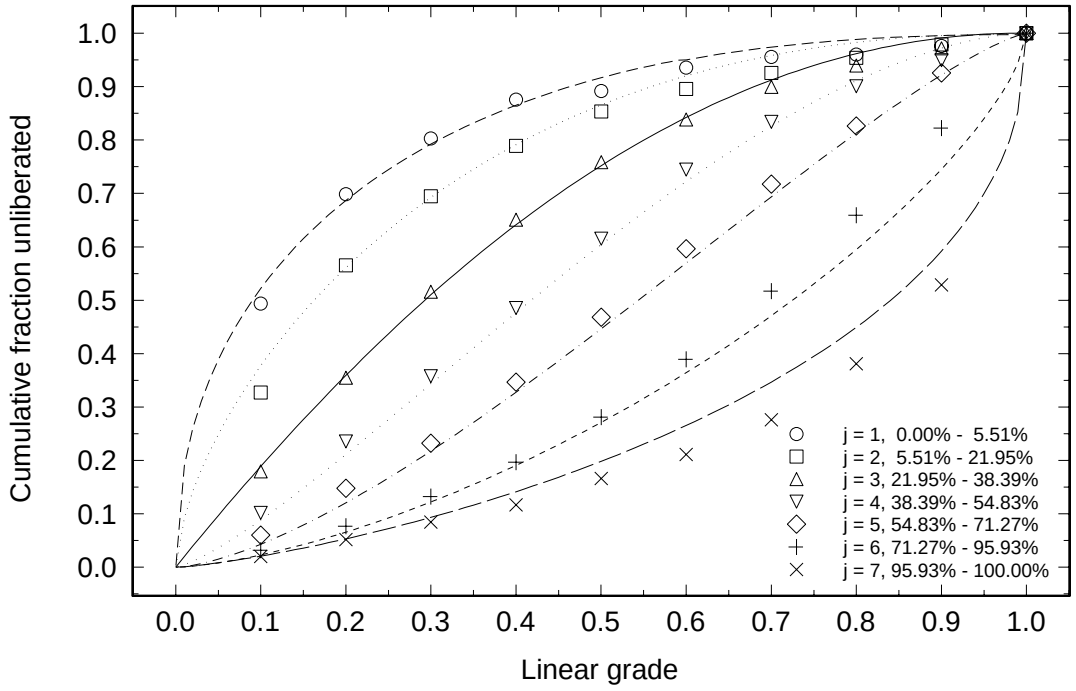

Figure 2.12 The measured cumulative unliberated linear grade distributions $F_{u\ell}^{j}(g_\ell|D^*)$ and the best fit with the model for the Dolomite-Sphalerite texture

distribution produced by particles of volumetric grade g_v. The second moment of the distribution can be written in terms of its first moment and its variance,

$$n_2^B(g_v) = \sigma^2(g_v) + (n_1^B(g_v))^2 \tag{2.33}$$

thus, the complete set of transformation kernels for any combination of linear and volumetric grades can be constructed for the unliberated distributions from a knowledge of the behavior of the first moment and the variance as functions of volumetric grade, by means of equations 2.29 through 2.33. Crude estimates for both the variance function and first moment function of $F_{lu}(g_l \mid g_v)$ can be obtained from the measured cumulative fractions corresponding to the functions $F_{lu}^j(g_l \mid D^*)$ in Table 2.4. The crude estimates of the first moment and the variance of the unliberated linear grade distributions are shown in Table 2.5, and these are plotted against the average volumetric grade of each sample, as shown in Figure 2.13, so that the appropriate functional forms can be assigned. The first moment is well described by a straight line as in equation 2.34.

$$n_1^B(g_v) = (1-\theta_1-\theta_2)g_v + \theta_1 \tag{2.34}$$

The variance requires a more versatile functional form because of the more complex shape shown in Figure 2.13, and also because that particular shape may not be retained by the variance of the transformation kernel. The following form was found to perform very well for the Dolomite-Sphalerite texture:

$$\sigma^2(g_v) = \omega_1(1-g_v)g_v^{\omega_2} + \omega_3(1-g_v) + \omega_4 g_v \tag{2.35}$$

where θ_1, θ_2, ω_1, ω_2, ω_3 and ω_4 are textural parameters that characterize the first

Table 2.5 Crude estimates, based on measured discrete fractions, of the first and second moments and the variance of the cumulative unliberated linear grade distributions $F_{\ell u}^{j}(g_{\ell} \mid D^{*})$

j	Average volumetric grade %, $\overline{g_v^j}$	First moment, $n_1^B j$	Second moment, $n_2^B j$	Variance, $\sigma^2 j$
1	0.73	0.1910	0.0819	0.0455
2	9.47	0.2515	0.1172	0.0540
3	27.27	0.3391	0.1741	0.0591
4	40.49	0.4275	0.2480	0.0653
5	58.00	0.5178	0.3360	0.0679
6	79.38	0.6393	0.4744	0.0657
7	94.64	0.7663	0.6488	0.0616

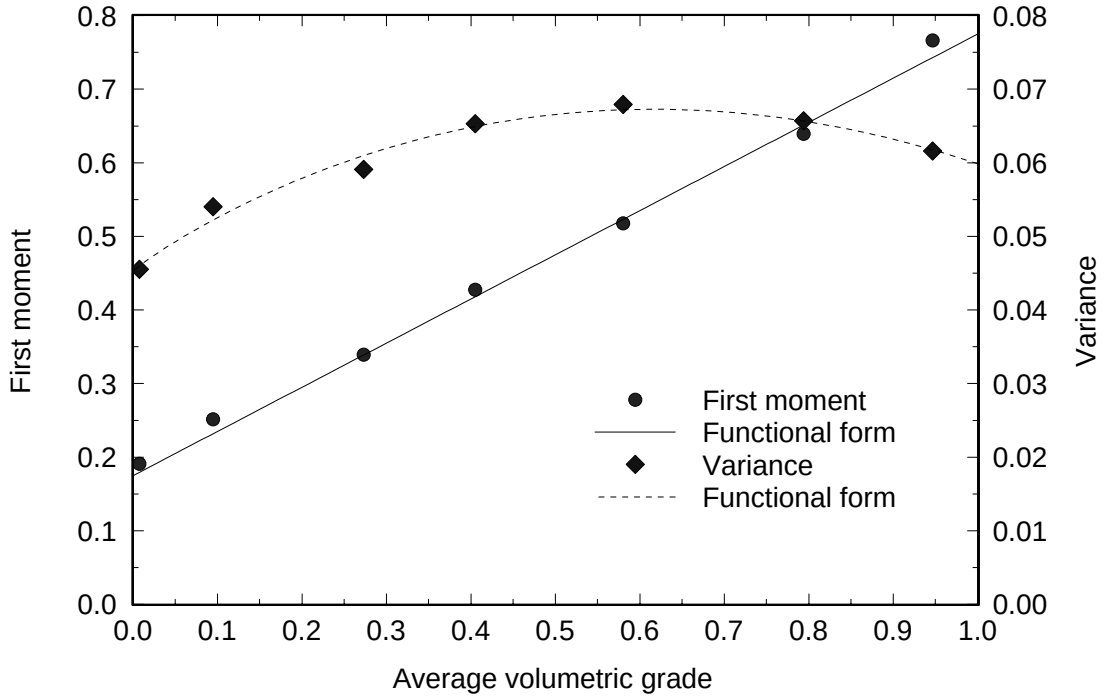

Figure 2.13 Crude estimates of the first moment and variance of the unliberated linear grade distributions plotted against average volumetric grade and the proposed functional forms in equations 2.34 and 2.35

moment and the variance of the unliberated transformation kernel for the Dolomite-Sphalerite ore.

The Dolomite-Sphalerite Transformation Kernel

Parameterization of the transformation kernel is a computer intensive calculation, because a set of parameters that will satisfy equation 2.17 for j=1 to N simultaneously is needed. Similar calculations are needed for equations 2.18 and 2.19. This involves the use of a good optimization procedure coupled with numerical integration. The Rosenbrock Hillclimb procedure was used for parameter optimization. The objective function was the sum of squares of the residuals between the measured fractions and the calculated fractions generated by Romberg integration of equations 2.17, 2.18 and 2.19, for j = 1 to 7, simultaneously. The Romberg integration was carried out with values of $f_v\left(g_v \mid D^*\right)$ obtained from the slopes of the corresponding cumulative distribution. The slopes were calculated from an interpolation to the measured values in Table 2.2. The interpolation was generated by drawing, with the help of a flexible ruler, the curve through the points in the measured cumulative distribution, as shown in Figure 2.10.

The following set of parameters was obtained for the Dolomite-Sphalerite texture. The resulting fit for the integrated, unliberated transformation kernel is shown in Figure 2.12.

Apparent linear liberation parameters for phase A (Dolomite), $\mathfrak{L}_A^{(1)}\left(1-g_v\right)$:

ξ_1^A = 0.6228 and ξ_2^A = 4.065

Apparent linear liberation parameters for phase B (Sphalerite), $\mathfrak{L}_B^{(1)}\left(g_v\right)$:

ξ_1^B = 0.6656 and ξ_2^B = 6.205

Unliberated transformation kernel, $F_{\ell u}(g_\ell \mid g_v)$, first moment parameters:

θ_1 = 0.1515 and θ_2 = 0.2461

Unliberated transformation kernel, $F_{\ell u}(g_\ell \mid g_v)$, variance parameters:

ω_1 = 0.0282 , ω_2 = 0.5737 , ω_3 = 0.0333 and ω_4 = 0.0698

The set of parameters that result when performing the integrations in equations 2.17, 2.18 and 2.19 corresponding to each narrow grade range of each sample is considerably different than the set of parameters that would be obtained if the model functions were interpolated through the average volumetric grade of each sample.

The set of parameters given above fully describe the texture of the Dolomite-Sphalerite ore, and a transformation kernel for any number of grade classes in the grade domain can be built using the appropriate functional forms and equation 2.13. The Dolomite-Sphalerite transformation kernel is shown in Figure 2.14 for several values of g_v.

Usually, the transformation kernel is discretized in 12 linear and 12 volumetric grade classes for use in the discrete version of equation 2.11. The corresponding cumulative fractions of $F_\ell(g_\ell \mid g_v)$ are calculated for g_ℓ = 0.0, g_ℓ < 0.1, 0.2, ..., 0.9, 1.0 and g_ℓ = 1.0 and at the median volumetric grades g_v = 0.00, 0.05, 0.15, ..., 0.95 and 1.00. In this form, the discretized transformation kernel for the Dolomite-Sphalerite ore is shown in matrix form in equation 2.36.

The transformation matrix in equation 2.36 is used in the discrete version of equation 2.11 for calculating the volumetric grade distribution corresponding to a linear grade distribution measured in cross sections of Dolomite-Sphalerite particles. This is the

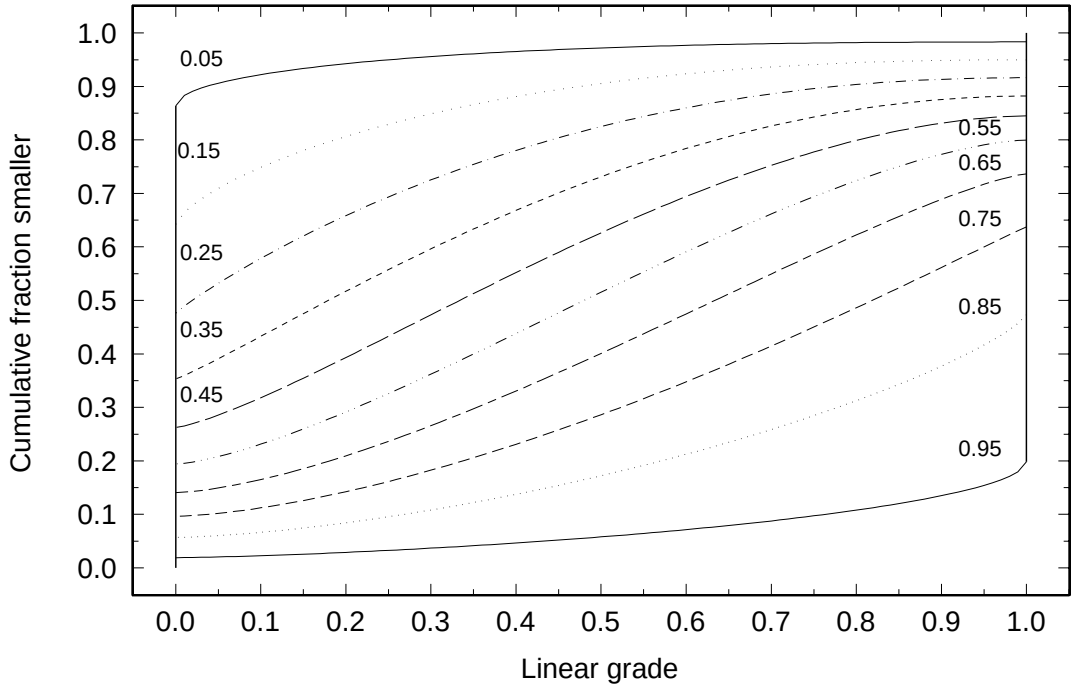

Figure 2.14 The Dolomite-Sphalerite transformation kernel

$$K = \begin{vmatrix} 1.0000 & 0.8640 & 0.6423 & 0.4763 & 0.3533 & 0.2623 & 0.1940 & 0.1407 & 0.0965 & 0.0569 & 0.0189 & 0.0000 \\ 1.0000 & 0.9221 & 0.7486 & 0.5785 & 0.4328 & 0.3180 & 0.2311 & 0.1649 & 0.1121 & 0.0662 & 0.0226 & 0.0000 \\ 1.0000 & 0.9426 & 0.8064 & 0.6586 & 0.5169 & 0.3932 & 0.2913 & 0.2094 & 0.1423 & 0.0841 & 0.0288 & 0.0000 \\ 1.0000 & 0.9559 & 0.8489 & 0.7252 & 0.5963 & 0.4730 & 0.3621 & 0.2658 & 0.1825 & 0.1080 & 0.0367 & 0.0000 \\ 1.0000 & 0.9653 & 0.8811 & 0.7803 & 0.6682 & 0.5519 & 0.4379 & 0.3306 & 0.2309 & 0.1374 & 0.0464 & 0.0000 \\ 1.0000 & 0.9721 & 0.9056 & 0.8250 & 0.7311 & 0.6265 & 0.5152 & 0.4010 & 0.2863 & 0.1721 & 0.0578 & 0.0000 \\ 1.0000 & 0.9768 & 0.9236 & 0.8600 & 0.7839 & 0.6942 & 0.5908 & 0.4747 & 0.3477 & 0.2123 & 0.0714 & 0.0000 \\ 1.0000 & 0.9800 & 0.9363 & 0.8860 & 0.8260 & 0.7525 & 0.6615 & 0.5495 & 0.4147 & 0.2586 & 0.0876 & 0.0000 \\ 1.0000 & 0.9820 & 0.9445 & 0.9036 & 0.8567 & 0.7991 & 0.7238 & 0.6223 & 0.4862 & 0.3124 & 0.1077 & 0.0000 \\ 1.0000 & 0.9830 & 0.9487 & 0.9134 & 0.8756 & 0.8313 & 0.7732 & 0.6887 & 0.5615 & 0.3770 & 0.1348 & 0.0000 \\ 1.0000 & 0.9833 & 0.9498 & 0.9163 & 0.8820 & 0.8448 & 0.7998 & 0.7367 & 0.6375 & 0.4729 & 0.1982 & 0.0000 \\ 1.0000 & 1.0000 & 1.0000 & 1.0000 & 1.0000 & 1.0000 & 1.0000 & 1.0000 & 1.0000 & 1.0000 & 1.0000 & 1.0000 \end{vmatrix} \quad (2.36)$$

first time that such a transformation kernel has been established from real mineral particles. It is also understood that this kernel will hold only, without further assumptions, for the Dolomite-Sphalerite ore used in this work, unless the exact same texture occurs in some other ore. The procedure described here can be used for evaluating the transformation kernel of practically any ore which is suitable for precise fractionation and image analysis. Depending on how accurate volumetric grade distributions must be from measurement on particle cross sections, the procedure should be carried out for establishing the correct transformation kernel for the texture in question. However, either because of time constraints, equipment availability and/or because accuracy can be relaxed, which is very common for preliminary ore characterization, it is useful to have an approximate transformation kernel at hand. Figure 2.11 shows that the Dolomite-Sphalerite ore is pretty much average for a variety of textures previously studied, which fortunately makes it the natural choice for this purpose. The same figure also shows that the apparent linear liberation fractions could almost be described by a single line, i.e., a single set of parameters for both phases. This is one of the reasons the Dolomite-Sphalerite texture has been called "almost symmetric." In Figure 2.14, the near

symmetry is once again observed, and it can be translated as $F_{\ell}(g_{\ell} \mid g_{v}) \sim 1 - F_{\ell}(1 - g_{\ell} \mid 1 - g_{v})$. This symmetry property is important because ores that have a similar symmetric texture can be readily identified by visual inspection of its particle's cross section images, by inverting the grey level of the relevant phases. The unaware observer will not be able to detect the switch, if the ore texture of the ore is symmetric or close to symmetric. Also, a large number of mineral systems of interest in the field of mineral processing have a somewhat symmetric texture. Therefore, a transformation kernel for a perfectly symmetric texture would be useful at least for mineral processing engineers. The symmetric transformation kernel is developed in the following sections of this chapter.

A Transformation Kernel for Symmetric Texture

A transformation kernel for perfectly symmetric texture cannot be established from real mineral particles because an ore with such texture probably does not exist. However, observations on several widely differing ores suggest that many ores display symmetrical characteristics. The best one can hope for is an ore with a very close to symmetric texture. Fortunately, the Dolomite-Sphalerite system is such an ore, and for the development of this transformation kernel, it is assumed that the Dolomite-Sphalerite texture is perfectly symmetric.

The first condition for symmetry is that the apparent linear liberation for both phases is described by a unique function with equal parameters ξ_1 and ξ_2,

$$\mathfrak{L}_A^{(1)}(1-g_v) = \xi_1(1-g_v)^{\xi_2} + (1-\xi_1)(1-g_v)$$
$$\mathfrak{L}_B^{(1)}(g_v) = \xi_1 g_v^{\xi_2} + (1-\xi_1)g_v \tag{2.37}$$

This ensures that the same amount of apparent linear liberation is produced for both phases at any volumetric grade of phase. The second condition is that the unliberated particles transformation kernel must be symmetric with respect to the two phases,

$$F_{\ell u}(g_\ell \mid g_v) = 1 - F_{\ell u}(1-g_\ell \mid 1-g_v) \tag{2.38}$$

Equation 2.38 can be written in terms of Incomplete Beta functions,

$$I_{g_\ell}\left(\alpha(g_v),\beta(g_v)\right) = 1 - I_{1-g_\ell}\left(\alpha(1-g_v),\beta(1-g_v)\right) \tag{2.39}$$

and the symmetry property $I_x(\alpha,\beta) = 1 - I_{1-x}(\beta,\alpha)$ applies only if

$$\alpha(g_v) = \beta(1-g_v) \tag{2.40}$$

and

$$\beta(g_v) = \alpha(1-g_v) \tag{2.41}$$

Equations 2.40 and 2.41 hold under the condition that the variance $\sigma^2(g_v)$ is symmetric about 0.5, and the first moment of the distribution has the following property:

$$1 - n_1^B(g_v) = n_1^B(1-g_v) \tag{2.42}$$

These conditions can be easily verified algebraically.

Thus, the following functional forms for the first moment and the variance will produce a symmetric transformation kernel for the unliberated particles:

$$n_1^B(g_v) = (1-2\theta)g_v + \theta \tag{2.43}$$

and

$$\sigma^2(g_v) = \omega_1 + \omega_2 \sin^{\omega_3}(\pi g_v) \tag{2.44}$$

The parameterization of the symmetric transformation kernel is carried out in the same manner as the Dolomite-Sphalerite transformation kernel, using the functional forms in equations 2.37, 2.43 and 2.44. The following is the set of parameters obtained for the symmetric texture:

Apparent linear liberation parameters, $\mathfrak{L}_A^{(1)}(1-g_v)$ and $\mathfrak{L}_B^{(1)}(g_v)$:

ξ_1 = 0.6590 and ξ_2 = 4.6147

Unliberated transformation kernel, $F_{lu}(g_l \mid g_v)$, first moment parameter:

θ = 0.1971

Unliberated transformation kernel, $F_{lu}(g_l \mid g_v)$, second moment parameters:

ω_1 = 0.0556 , ω_2 = 0.0133 and ω_3 = 4.3825

The fitted unliberated, integrated transformation kernel is shown in Figure 2.15, for the set of parameters above. Clearly, the unliberated linear grade distributions produced by the Dolomite-Sphalerite ore do not hold symmetry, especially for the intermediate volumetric grades. There is an indication, however, that for volumetric grades approaching 0 and 1, i.e., the liberated ends, this texture presents symmetric properties, as corroborated by the plot in Figure 2.15, the behavior of the apparent linear liberation shown in Figure 2.11, and the symmetric appearance shown in the images in Figures 2.3, 2.4 and 2.5. Still, the symmetric kernel parameter set shown above, is the

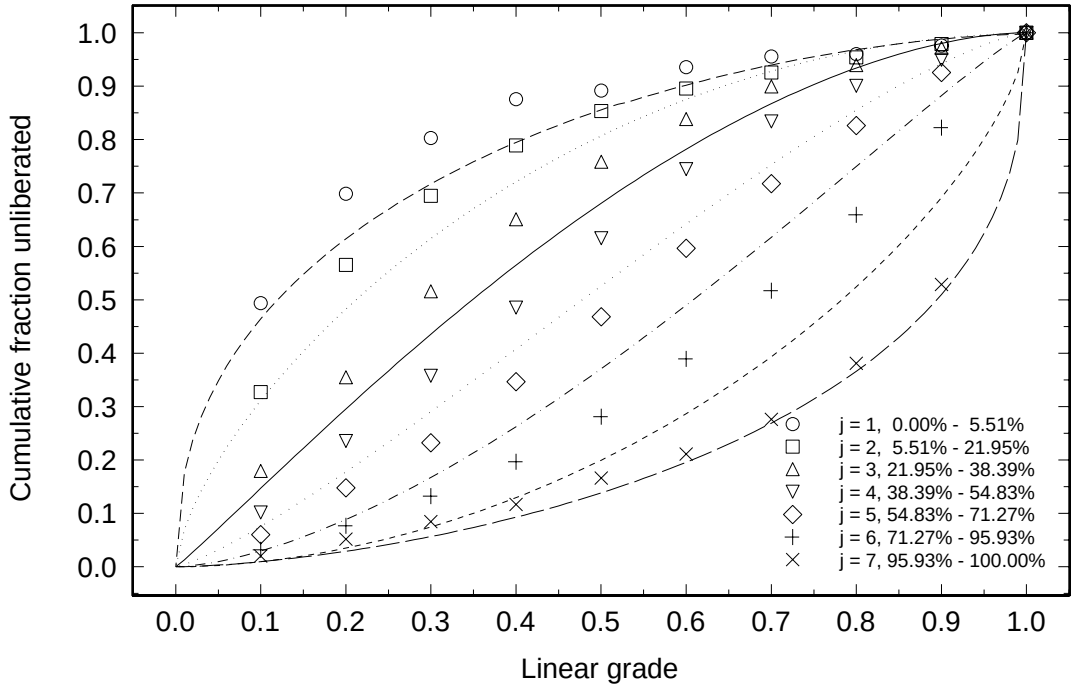

Figure 2.15 The measured cumulative unliberated linear grade distributions $F_{u\ell}^{j}(g_\ell|D^*)$ and the best fit with the model for the symmetric texture

only available textural information ever obtained, in the form of a transformation kernel, that can be used to describe ores with symmetric texture.

The discrete, symmetric transformation kernel is shown in matrix form in equation 2.45, for the customary 12 grade classes, and in Figure 2.16, where the symmetry condition becomes transparent. Figures 2.14 and 2.16 show transformation kernels that appear to be very much alike, but subtle differences between these two transformation kernels become apparent when the figures are compared by superimposing one onto the other.

$$K = \begin{vmatrix} 1.0000 & 0.8440 & 0.6011 & 0.4305 & 0.3119 & 0.2293 & 0.1700 & 0.1245 & 0.0863 & 0.0513 & 0.0170 & 0.0000 \\ 1.0000 & 0.9031 & 0.6978 & 0.5164 & 0.3795 & 0.2788 & 0.2005 & 0.1394 & 0.0928 & 0.0543 & 0.0183 & 0.0000 \\ 1.0000 & 0.9252 & 0.7590 & 0.5949 & 0.4558 & 0.3437 & 0.2496 & 0.1709 & 0.1100 & 0.0629 & 0.0210 & 0.0000 \\ 1.0000 & 0.9406 & 0.8072 & 0.6654 & 0.5317 & 0.4138 & 0.3084 & 0.2143 & 0.1370 & 0.0768 & 0.0253 & 0.0000 \\ 1.0000 & 0.9524 & 0.8465 & 0.7277 & 0.6043 & 0.4858 & 0.3735 & 0.2672 & 0.1733 & 0.0963 & 0.0310 & 0.0000 \\ 1.0000 & 0.9617 & 0.8783 & 0.7815 & 0.6718 & 0.5573 & 0.4427 & 0.3282 & 0.2185 & 0.1217 & 0.0383 & 0.0000 \\ 1.0000 & 0.9690 & 0.9037 & 0.8267 & 0.7328 & 0.6265 & 0.5142 & 0.3957 & 0.2723 & 0.1535 & 0.0476 & 0.0000 \\ 1.0000 & 0.9747 & 0.9232 & 0.8630 & 0.7857 & 0.6916 & 0.5862 & 0.4683 & 0.3346 & 0.1928 & 0.0594 & 0.0000 \\ 1.0000 & 0.9789 & 0.9371 & 0.8900 & 0.8291 & 0.7504 & 0.6563 & 0.5442 & 0.4051 & 0.2410 & 0.0748 & 0.0000 \\ 1.0000 & 0.9817 & 0.9457 & 0.9072 & 0.8606 & 0.7995 & 0.7212 & 0.6205 & 0.4836 & 0.3022 & 0.0969 & 0.0000 \\ 1.0000 & 0.9830 & 0.9487 & 0.9137 & 0.8755 & 0.8300 & 0.7707 & 0.6881 & 0.5695 & 0.3989 & 0.1560 & 0.0000 \\ 1.0000 & 1.0000 & 1.0000 & 1.0000 & 1.0000 & 1.0000 & 1.0000 & 1.0000 & 1.0000 & 1.0000 & 1.0000 & 1.0000 \end{vmatrix} \quad (2.45)$$

A great deal has been learned about the Dolomite-Sphalerite texture by exploring its symmetry properties. It is expected that the symmetric kernel may be useful for applications where the transformation kernel for the ore under study has not been established, if its texture show symmetry to some extent.

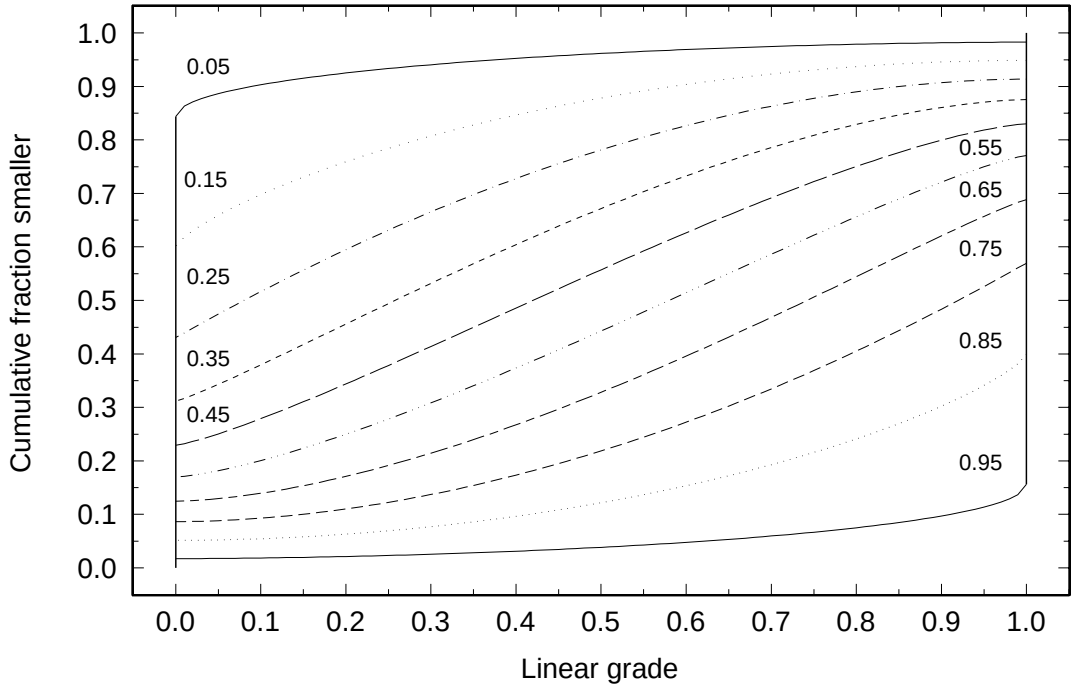

Figure 2.16 The symmetric transformation kernel

Inversion of the Transformation Equation

for Stereological Correction

Equation 2.11 is the basis for the calculation of the distribution of volumetric grades $f_v\left(g_v \mid D^*\right)$ when the distribution of linear grades $F_\ell\left(g_\ell \mid D^*\right)$ is known, and it is recognized as a linear Fredholm Integral Equation of the first kind. Although the transformation kernel in equation 2.11 for stereological correction, as developed in the previous sections of this work, can be written in terms of continuous functions in the domains of linear and volumetric grades, there are no known functional forms that can consistently describe the volumetric and linear grade distributions in this particular integral equation. Thus, in order to solve for the distribution of volumetric grades, equation 2.11 must be dealt with in its discretized form,

$$F_\ell^i = \sum_{j=1}^{12} K_{ij}\, f_v^j \qquad 1 <= i <= 12 \tag{2.46}$$

where K_{ij} are the matrix coefficients of the discrete transformation kernel as shown in equations 2.36 and 2.45, for the traditional 12 grade classes. By the same token, F_ℓ^i are the vector coefficients of the discrete, cumulative, linear grade distribution, and f_v^j are the coefficients of the discrete volumetric grade distribution. In matrix notation, equation 2.46 becomes:

$$F_\ell = K\, f_v \tag{2.47}$$

Direct inversion of equation 2.47 gives:

$$f_v = K^{-1}\, F_\ell \tag{2.48}$$

Unfortunately, stereological transformation from one-dimensional space to three-

dimensional space is a very well known ill-posed problem and the transformation from linear to volumetric grade distribution is not an exception. In practice, to evaluate whether a useful solution can be obtained by direct inversion, we examine the determinant and the condition number of the discrete transformation kernels. The condition number is estimated by calculating the ratio between the largest and the smallest singular values, in module, of the transformation matrix. The condition number for both transformation kernels in this work is of the order of 10^{9}, while the determinants are of the order of 10^{-32}. Now, assuming the transformation kernel is exact, the measured linear grade distribution in the right-hand side of equation 2.48 will undoubtedly contain a certain amount of error, which arises from a diversity of sources, such as sampling and mounting, image quality, touching particles, image processing routines, measuring frame effect, and the like. Thus,

$$\overline{F_{\ell}^{i}} = F_{\ell}^{i} + \varepsilon^{i} \tag{2.49}$$

where $\overline{F_{\ell}^{i}}$ are the coefficients of the measured cumulative linear grade distribution. Equation 2.48 can be written in terms of the exact, unperturbed linear grade distribution and the associated random, measurement error ε.

$$f_{v} = K^{-1} (F_{\ell} + \varepsilon) \tag{2.50}$$

This implies that errors as small as 0.001 in the measurement of the linear grade distribution will produce perturbations in the order of magnitude of 10^{6} in the calculated volumetric grade distribution, due to the magnitude of the transformation kernel condition number. Clearly, direct inversion of equation 2.47 will not produce a useful solution, and a specialized inversion procedure is required. Fortunately, ill-posed problems are

common enough in science and engineering, that regularization procedures are available for computing stabilized solutions. However, a solution is required that is not only stabilized, but also constrained, so that the resulting volumetric grade distributions can be used in practical mineral processing applications. The required constraints are very mild. First, the volumetric grade distribution must satisfy the consistency condition

$$\sum_{j=1}^{12} f_v^j = 1 \tag{2.51}$$

which does not impose important limitations on the form of the distribution. Second, and last, the cumulative volumetric grade distribution $F_v\left(g_v \mid D^*\right)$ must increase monotonically with the volumetric grade. Such a solution can be obtained by means of a constrained optimization procedure, and the choice should involve an efficient and effective search procedure, simple yet powerful and constrainable. The Rosenbrock Hillclimb procedure has been used successfully for this purpose since 1991 [8]. The method proposed by Rosenbrock [25] has been proven effective in solving some problems where the optimization variables are constrained. Furthermore, when the number of independent variables is kept small, the efficiency of the procedure is optimum. For the particular format adopted here, the number of grade classes in which the distributions are discretized equals 12, leaving only 11 independent variables to be calculated, due to the consistency condition in equation 2.51. Best results are achieved when minimizing the normalized sum of residuals

$$NSR = \sum_{i=0}^{n} \frac{|\overline{F_\ell^i} - \hat{F}_\ell^i|}{\overline{F_\ell^i}} \tag{2.52}$$

subject to $F_v^1 \leq F_v^2 \leq ... \leq F_v^j \leq ... \leq F_v^{11} \leq F_v^{12} = 1$ for all j. In this solution, the optimization variables are the cumulative fractions F_v^j, and the condition that $0 \leq f_v^j \leq 1$ and the consistency condition in equation 2.51 are satisfied simultaneously. *NSR* (Normalized Sum of Residuals) is the value of the objective function, and $\hat{F}_\ell^i$ are the coefficients of the cumulative linear grade distribution back-calculated using equation 2.47 with the calculated coefficients of the volumetric grade distribution vector. Fortunately, *NSR* seems to be unimodal when defined as in equation 2.50, and only one set of starting values for f_v^j is required for initialization. In fact, this was verified by computing all solutions that exist in a discrete mesh that represents the constrained solutions with arbitrary accuracy. The construction of such an algorithm is complex, and, for higher accuracy, computing time incraeses tremendously. However, the best solution to a noise free problem generated by PARGEN particles was found to be independent of the initial data set and of the mesh accuracy, clearly indicating that *NSR* is indeed unimodal. Nevertheless, it is important that the initial set of volumetric fractions be as close as possible to the optimal solution, in order to ensure consistent convergency of the optimization procedure to the minimum value of *NSR*, when solving with measured linear grade distributions that contain some error. Such initial set can be obtained by solving the unconstrained problem with any direct or iterative regularization method. Tikhonov regularization has been used successfully for this purpose. The choice of a direct

regularization procedure is important because it does not require a convergence test, and consequently, a solution will always be produced. Furthermore, Tikhonov regularization is simple to implement and fast, in a 12x12 system. The procedure is defined as, in matrix notation,

$$f_v = (K + \alpha_r \mathrm{I})^{-1} F_\ell \tag{2.53}$$

where I is the identity matrix and α_r is the regularization parameter. The value of the regularization parameter is proportional to the amount of filtering desired. This is a balance between the amount of regularization error, which increases with more filtering, and perturbation error, which increases with less filtering. The optimum value of the regularization parameter can be approximated by means of the *L-curve criterion*, (see Hansen [26] for a detailed discussion). Here, the values of ε do not change order of magnitude from one transformation problem to another. Consequently the regularization parameter is constant, and estimated by trial and error to be equal to 0.1, for linear grade distributions measured as described in the experimental section of this work. The resulting fractions from Tikhonov regularization cannot be used directly for initialization because the constrained Rosenbrock Hillclimb procedure requires an initial set that is constrained. A constrained initial set for the vector f_v can be obtained from the Tikhonov solution by making any negative fraction in Tikhonov's solution equal to a small positive fraction, followed by vector normalization so that the consistency condition in equation 2.51 is satisfied. In this work, the small fraction used for normalization was equal to 0.001. The normalized Tikhonov solution has been found to be a consistent starting set for Rosenbrock optimization.

Stereological Correction Procedure Verification

It is necessary to verify if the procedure previously described yields volumetric grade distributions that are accurate enough for practical use in mineral processing calculations. In order to achieve this, it is necessary to measure the distribution of linear grades generated by particles of known composition and texture. The obvious choice is the narrow size, narrow grade Dolomite-Sphalerite particle samples used for the measurement of the transformation kernel. The measured linear grade distributions for these samples are given in Table 2.3. The resulting Tikhnov regularization (unconstrained) volumetric grade distributions, using the Dolomite-Sphalerite transformation kernel and α_r = 0.1, were used for initializing optimization with Rosenbrock Hillclimb. The resulting, constrained, volumetric grade distributions, along with the measured and back-calculated cumulative linear grade distributions, are shown in Tables 2.6 to 2.12. The back-calculated linear grade distributions must match the measured distributions, giving the smallest normalized sum of residuals *NSR*, as shown in the tables. Excellent agreement is observed, indicating that the calculated liberation spectra must be a good approximation of that of the particle population, provided the transformation kernel is correct. The liberation spectra corresponding to these narrow grade samples is expected to take the form of a set of step functions in each narrow grade range, under ideal conditions, i.e. no noise due to the inversion of the ill-posed problem, no perturbation error introduced during measurement (image analysis), and also no experimental error, such as imperfections during the MAGSTREAM™ fractionation procedure, sampling and/or mounting. The calculated volumetric grade distributions are

Table 2.6 The calculated, conditional on size, volumetric grade distribution by volume f_v^j, for the -2.9 g/cc Dolomite-Sphalerite sample produced by fractionation. Here, j is used as an index to a volumetric grade class rather than the volumetric grade range of the particles that generated the distributions. Also shown, the measured and back-calculated cumulative linear grade distributions and the final value of the objective function after constrained optimization with Rosenbrock Hillclimb

Stereological Correction Results -2.9 g/cc particles				
i, j	Linear/volumetric grade interval %, $-g_\ell^i + g_\ell^{i-1}$, $-g_v^j + g_v^{j-1}$	$\overline{F_\ell^i}$, %	$\hat{F}_\ell^i$, %	f_v^j, %
1	0	97.27	98.14	89.18
2	-10 +0	98.77	98.77	10.08
3	-20 +10	99.01	99.01	0.25
4	-30 +20	99.18	99.18	0.07
5	-40 +30	99.31	99.31	0.02
6	-50 +40	99.40	99.40	0.07
7	-60 +50	99.48	99.48	0.04
8	-70 +60	99.54	99.54	0.04
9	-80 +70	99.58	99.58	0.09
10	-90 +80	99.62	99.62	0.06
11	-100 +90	99.64	99.64	0.09
12	100	100.00	100.00	0.00
NSR		0.020044		

Table 2.7 The calculated, conditional on size, volumetric grade distribution by volume f_v^j, for the -3.1+2.9 g/cc Dolomite-Sphalerite sample produced by fractionation. Here, j is used as an index to a volumetric grade class rather than the volumetric grade range of the particles that generated the distributions. Also shown, the measured and back-calculated cumulative linear grade distributions and the final value of the objective function after constrained optimization with Rosenbrock Hillclimb

Stereological Correction Results -3.1 +2.9 g/cc particles				
i, j	Linear/volumetric grade interval %, $-g_\ell^i + g_\ell^{i-1}$, $-g_v^j + g_v^{j-1}$	$\overline{F_\ell^i}$, %	$\hat{F}_\ell^i$, %	f_v^j, %
1	0	72.69	74.55	1.04
2	-10 +0	80.77	82.80	46.54
3	-20 +10	86.65	86.80	50.92
4	-30 +20	89.84	89.69	1.01
5	-40 +30	92.17	91.86	0.00
6	-50 +40	93.75	93.49	0.40
7	-60 +50	94.80	94.70	0.01
8	-70 +60	95.54	95.55	0.00
9	-80 +70	96.23	96.10	0.02
10	-90 +80	96.85	96.38	0.00
11	-100 +90	97.37	96.47	0.05
12	100	100.00	100.00	0.00
NSR		0.076890		

Table 2.8 The calculated, conditional on size, volumetric grade distribution by volume f_v^j, for the -3.3+3.1 g/cc Dolomite-Sphalerite sample produced by fractionation. Here, j is used as an index to a volumetric grade class rather than the volumetric grade range that generated the distributions. Also shown, the measured and back-calculated cumulative linear grade distributions and the final value of the objective function after constrained optimization with Rosenbrock Hillclimb

Stereological Correction Results -3.3 +3.1 g/cc particles				
i, j	Linear/volumetric grade interval %, $-g_\ell^i + g_\ell^{i-1}$, $-g_v^j + g_v^{j-1}$	$\overline{F_\ell^i}$, %	$\hat{F}_\ell^i$, %	f_v^j, %
1	0	33.65	39.98	0.00
2	-10 +0	45.62	48.68	0.11
3	-20 +10	55.37	56.82	1.65
4	-30 +20	64.32	64.18	38.36
5	-40 +30	71.79	70.67	54.55
6	-50 +40	77.78	76.25	4.02
7	-60 +50	82.23	80.88	0.93
8	-70 +60	85.60	84.52	0.22
9	-80 +70	87.83	87.15	0.05
10	-90 +80	89.61	88.76	0.10
11	-100 +90	91.19	89.33	0.00
12	100	100.00	100.00	0.00
NSR		0.318869		

Table 2.9 The calculated, conditional on size, volumetric grade distribution by volume f_v^j, for the -3.5+3.3 g/cc Dolomite-Sphalerite sample produced by fractionation. Here, j is used as an index to a volumetric grade class rather than the volumetric grade range that generated the distributions. Also shown, the measured and back-calculated cumulative linear grade distributions and the final value of the objective function after constrained optimization with Rosenbrock Hillclimb

Stereological Correction Results -3.5 +3.3 g/cc particles				
i, j	Linear/volumetric grade interval %, $-g_\ell^i + g_\ell^{i-1}$, $-g_v^j + g_v^{j-1}$	$\overline{F_\ell^i}$, %	$\hat{F}_\ell^i$, %	f_v^j , %
1	0	25.86	27.51	0.00
2	-10 +0	31.90	33.16	0.12
3	-20 +10	39.86	40.00	0.28
4	-30 +20	47.13	47.18	20.85
5	-40 +30	54.73	54.35	2.18
6	-50 +40	62.43	61.24	27.26
7	-60 +50	70.12	67.64	46.26
8	-70 +60	75.43	73.36	2.79
9	-80 +70	79.41	78.16	0.03
10	-90 +80	82.30	81.77	0.12
11	-100 +90	85.30	83.59	0.11
12	100	100.00	100.00	0.00
NSR		0.239132		

Table 2.10 The calculated, conditional on size, volumetric grade distribution by volume f_v^j, for the -3.7+3.5 g/cc Dolomite-Sphalerite sample produced by fractionation. Here, j is used as an index to a volumetric grade class rather than the volumetric grade range that generated the distributions. Also shown, the measured and back-calculated cumulative linear grade distributions and the final value of the objective function after constrained optimization with Rosenbrock Hillclimb

Stereological Correction Results -3.7 +3.5 g/cc particles				
i, j	Linear/volumetric grade interval %, $-g_\ell^i + g_\ell^{i-1}$, $-g_v^j + g_v^{j-1}$	$\overline{F_\ell^i}$, %	$\hat{F}_\ell^i$, %	f_v^j, %
1	0	16.02	16.28	0.00
2	-10 +0	19.23	19.30	0.17
3	-20 +10	23.91	23.76	2.38
4	-30 +20	28.40	29.01	0.10
5	-40 +30	34.48	34.74	8.52
6	-50 +40	40.96	40.78	2.77
7	-60 +50	47.80	46.96	21.31
8	-70 +60	54.22	53.14	27.50
9	-80 +70	60.03	59.17	19.38
10	-90 +80	65.33	64.85	15.95
11	-100 +90	69.28	69.95	1.91
12	100	100.00	100.00	0.01
NSR		0.128170		

Table 2.11 The calculated, conditional on size, volumetric grade distribution by volume f_v^j, for the -4.0+3.7 g/cc Dolomite-Sphalerite sample produced by fractionation. Here, j is used as an index to a volumetric grade class rather than the volumetric grade range that generated the distributions. Also shown, the measured and back-calculated cumulative linear grade distributions and the final value of the objective function after constrained optimization with Rosenbrock Hillclimb

Stereological Correction Results -4.0 +3.7 g/cc particles				
i, j	Linear/volumetric grade interval %, $-g_\ell^i + g_\ell^{i-1}$, $-g_v^j + g_v^{j-1}$	$\overline{F_\ell^i}$, %	$\hat{F}_\ell^i$, %	f_v^j, %
1	0	5.29	5.64	0.00
2	-10 +0	6.56	6.59	0.06
3	-20 +10	8.33	8.32	0.10
4	-30 +20	10.53	10.60	0.10
5	-40 +30	13.08	13.34	0.10
6	-50 +40	16.42	16.50	0.16
7	-60 +50	20.72	20.07	0.10
8	-70 +60	25.78	24.05	5.17
9	-80 +70	31.40	28.50	20.59
10	-90 +80	37.88	33.57	38.21
11	-100 +90	44.91	40.71	25.99
12	100	100.00	100.00	9.42
NSR		0.501310		

Table 2.12 The calculated, conditional on size, volumetric grade distribution by volume f_v^j, for the +4.0 g/cc Dolomite-Sphalerite sample produced by fractionation. Here, j is used as an index to a volumetric grade class rather than the volumetric grade range that generated the distributions. Also shown, the measured and back-calculated cumulative linear grade distributions and the final value of the objective function after constrained optimization with Rosenbrock Hillclimb

Stereological Correction Results +4.0 g/cc particles				
i, j	Linear/volumetric grade interval %, $-g_\ell^i + g_\ell^{i-1}$, $-g_v^j + g_v^{j-1}$	$\overline{F_\ell^i}$, %	$\hat{F}_\ell^i$, %	f_v^j, %
1	0	1.59	1.51	0.28
2	-10 +0	1.85	1.74	0.00
3	-20 +10	2.26	2.11	0.10
4	-30 +20	2.68	2.58	0.10
5	-40 +30	3.10	3.14	0.10
6	-50 +40	3.74	3.80	0.10
7	-60 +50	4.32	4.57	0.05
8	-70 +60	5.16	5.46	0.02
9	-80 +70	6.51	6.54	0.10
10	-90 +80	8.42	7.92	6.66
11	-100 +90	14.51	10.76	34.52
12	100	100.00	100.00	57.96
NSR		0.683610		

shown graphically in Figure 2.17, where the fractions in each volumetric grade class of the calculated distributions are plotted against their original separation densities. Excellent correlation between density and volumetric grade is immediately observed. Furthermore, the residual noise from stereological correction is not significant. Also, it is apparent that fractionation was successful to a great extent, considering the difficulties associated with fractionation at high separation densities and the amounts of Near Gravity Material (*NGM*) at separation densities nearing that of liberated Dolomite and Sphalerite. Also in Figure 2.17, the measured linear grade distributions, before setereological correction, are shown for comparison purposes. Clearly, the linear, one-dimensional distributions are substantially different than the stereologically corrected distributions, showing that stereological correction is indeed necessary for practical mineral processing applications.

The experimental verification of the setereological correction procedure can be achieved by comparing the measured liberation spectrum of a particle sample that is in a narrow size range and that contain particles of all grades, including the liberated ends. This is called here a narrow size, composite particle sample. A sample of the Dolomite-Sphalerite particles was crushed, as described in the experimental section of this chapter, and a fraction of -1000+710 microns particles sampled for image analysis. The linear grade distribution of this composite sample was measured (see Table A.1 in Appendix A) and the calculated cumulative volumetric grade distribution, by weight, using this stereological correction procedure with the measured Dolomite-Sphalerite transformation kernel is shown in Figure 2.18. This is compared with the fractionation results from

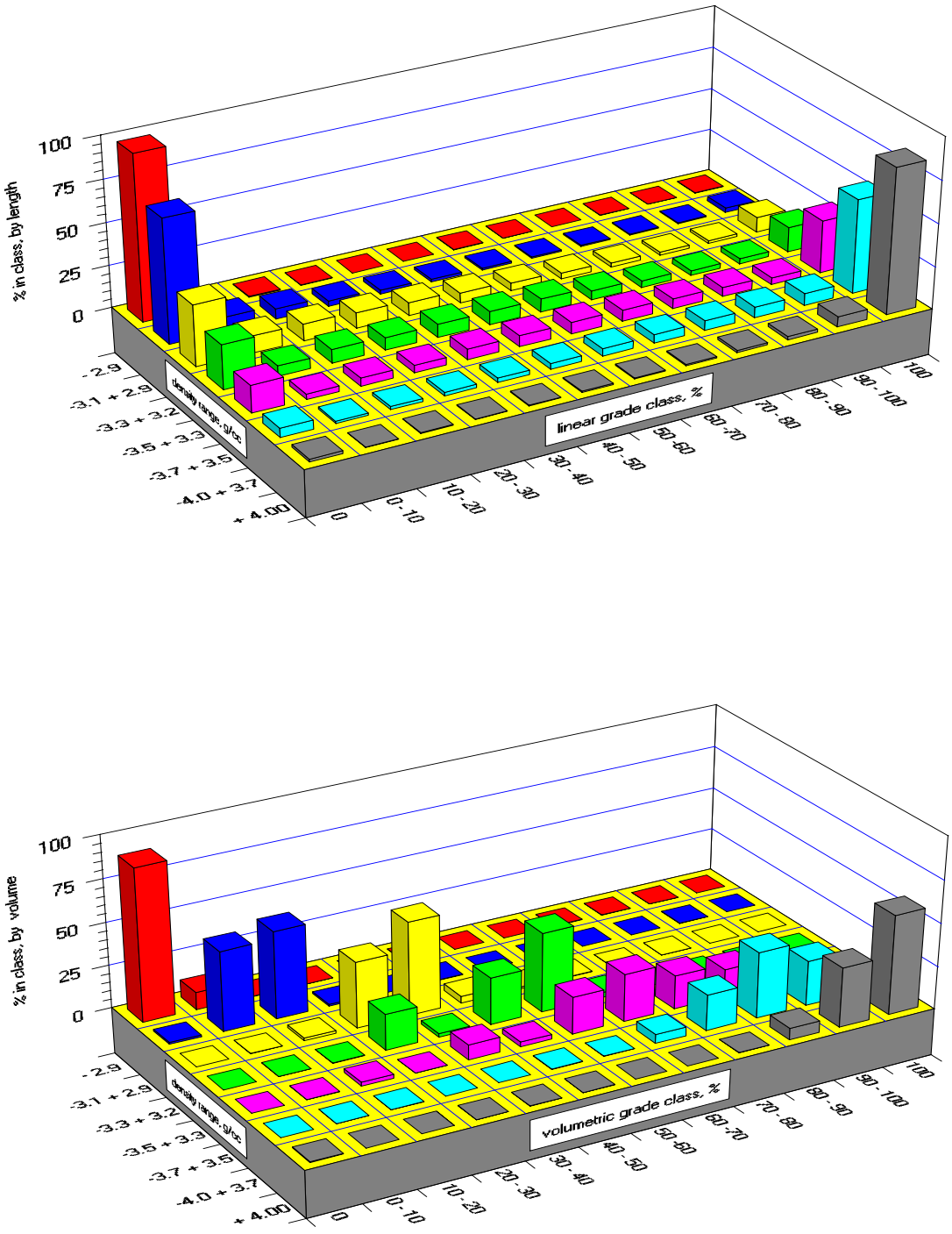

Figure 2.17 The measured linear grade distributions (top) and the calculated, using the stereological correction procedure, volumetric grade distributions (bottom) in the fractionated particles

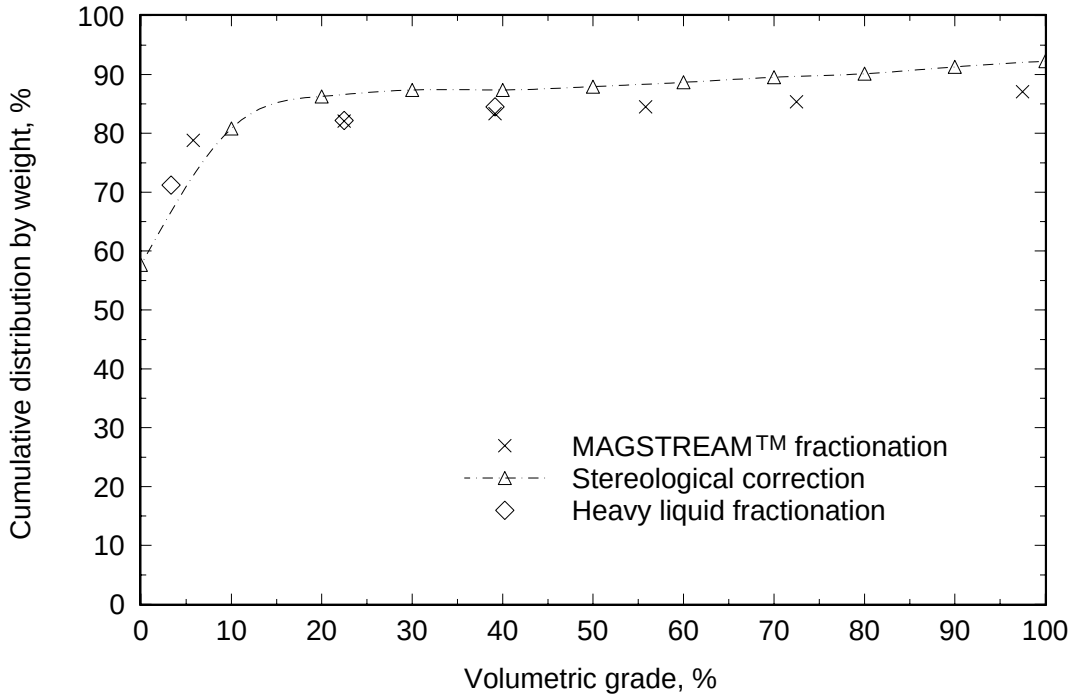

Figure 2.18 The liberation spectrum of -1000+710 microns Dolomite-Sphalerite particles measured by stereological correction, MAGSTREAM™ fractionation and heavy liquid fractionation

MAGSTREAM™ separation described in the experimental section of this chapter, also shown in Figure 2.18. The two distributions show good correlation, and the small differences in the spectra are due to noise, inherent to the inversion procedure and to some imprecision in the magnetic fluid fraction of the particles. A further check was carried out, and this consisted of fractionating the crushed particles using heavy liquids, at 2.87 g/cc, using tetrabromoethane, 3.1 g/cc using diluted diodomethane ant at 3.3 g/cc using diodomethane. Heavy liquid fractionation produces very sharp separation, and the amounts of misplaced material should be considerably less than the amounts produced in the MAGSTREAM™ at these separation densities. The heavy liquid fractionation produced three points in the lower grades of the narrow size, composite Dolomite-Sphalerite particles liberation spectrum, and these are also shown in Figure 2.18. Again, good agreement is observed, and the heavy liquid fractionation results confirm that the MAGSTREAM™ separation was efficient, at least for the lower separation densities, and that the stereological correction procedure is accurate.

These results are of additional importance, because they also indicate that the measured transformation kernel for the Dolomite-Sphalerite system is indeed correct. This is the first time that such transformation kernel has been evaluated experimentally from real mineral particles. Also, the difficulties associated with the inversion of the transformation function have been overcome, and the stereological correction procedure here described is feasible.

Discussion and Conclusions

There are a number of issues of crucial importance which have been addressed in this work that are very well worth discussing due to their impact in the field of mineral processing. First, a complete procedure for the measurement and parameterization of the transformation kernel for stereological correction for real mineral particles has been established. The procedure requires samples of narrow grade, narrow size particles, that are clean enough, that contamination by misplaced material does not interfere strongly with the parameterization. In this work, magnetic fluid fractionation with a MAGSTREAM™, coupled with a carefully designed separation sequence, was used successfully to obtain clean, narrow grade particle samples over the entire grade spectrum of a Dolomite-Sphalerite ore. There are several other fractionation procedures that can be used to the same end, and the choice should be based on the physical properties of the ore under study. Also, image analysis systems are becoming more affordable, and more capable of providing very precise measurements of particle cross-sections. More importantly, the transformation kernel can be evaluated from such measurements, completely compensating for the fact that the particles are not monograde, but are rather distributed in a narrow grade range, with use of a simple set of integrations that must be carried out simultaneously for the correct texture parameterization. Furthermore, an excellent set of functional forms is made available for modelling the form of the transformation kernels, when decoupled into the unliberated and apparent linear liberation components.

Also included in this work are the conditions that have to be satisfied by the

functional forms in order to produce a symmetric kernel have been established. A symmetric kernel has been developed from the Dolomite-Sphalerite data. Now, the development of a quantitative parameter for textural symmetry or degree of symmetry of a given ore is required for assessing the usefulness of the symmetric transformation kernel for such ore. However, for ores other than the Dolomite-Sphalerite, which have a symmetrical texture, this transformation kernel can and should be used at a stage of preliminary investigation, and if the actual transformation kernel cannot be measured. The symmetric kernel is with no doubt the most realistic transformation kernel for ores other than the Dolomite-Sphalerite, that posses a certain degree of symmetry. The mere existence of this symmetric kernel opens the door for the first mineral processing plant evaluations which will include phase characterization for modelling of unit operations and both plant mass and metallurgical balances. It is expected, however, that other transformation kernels will be determined for other ores, as demanded by detailed plant characterization, by means of the procedure here described.

A stable, constrained, inversion procedure for the calculation of the volumetric grade distribution that does not depend on the transformation kernel has been implemented. The procedure described in this work is accurate enough for practical application in mineral processing calculations. In fact, the optimization approach for the transformation problem has been used effectively since 1991 [8], when it was originally developed for stereological correction using the PARGEN transformation kernel, with a somewhat different initialization procedure. The introduction of Tikhonov regularization for initialization was made later, when the procedure was used by Lin and Miller [27] to

calculate the size distribution of particles on a fast-moving conveyor belt, from linear intercept measurements of the particles projected images. That actually became the first practical application of stereological correction for particle size distribution measurement by image analysis, and this was due to the fact that Lin et al. were able to determine the appropriate transformation kernel for that problem. The calculation of particle size distribution clearly requires a more robust initialization procedure because the domain of size is not closed, as is the case of grade. The procedure, with the introduction of Tikhonov regularization was then implemented, with advantage, for initializing the unregularized, optimization based, constrained solution to the stereological correction problem proposed in this work.

It is remarkable though that a number of rather sophisticated solutions to ill-posed problems are still being developed by mathematicians [26], in view of the importance and frequency of ill-posed problems in science and engineering. Several regularized solutions have become available in recent years, including constrained solutions. In this view, the difficulties that are associated to the solution of the stereological correction problem for mineral liberation should no longer be perceived as problematic.

The most important consequence of the results reported here is that we can now measure the liberation spectra of Dolomite-Sphalerite particles by image analysis, so that the requirements to further research in the area of liberation have now been fulfilled. It is now possible to study, in detail, the transfer coefficients amongst the several size/grade classes that control the liberation process. The transfer coefficients can actually be measured, directly, by measuring the conditional, on size, volumetric grade distributions

of the progenies from the breakage of narrow size/narrow grade particles. Such an experiment is fundamental for establishing the relationship between the original texture of the ore and the quadrivariate breakage function. This, in turn, leads to implementation of a procedure for predicting the liberation spectra produced by breakage of a number of ores that are common in mineral processing applications, including closed, continuous grinding circuits, where concentration occurs simultaneously with size reduction. This is discussed in detail in Chapter 3 of this dissertation.

CHAPTER 3

CHARACTERIZATION OF THE INTERNAL STRUCTURE OF THE QUADRIVARIATE BREAKAGE FUNCTION

Background

The essence of any useful liberation model is to relate the ores texture to its breakage characteristics, i.e., given a set of well-defined textural parameters that can be measured directly from the ore, it should be possible to calculate the grade distribution in the progeny produced by comminution. It is relatively easier to predict the grade distribution produced by the comminution of an ore in a batch or continuous, open circuit, grinding operation, once the resulting conditional on size grade distributions from these operations are a function of the unbroken ore texture alone. These are more properly called the natural liberation spectra of the ore. A variety of methods, based on the superimposition of texture and fracture patterns, have been developed since as early as 1939 [1], for the prediction of the natural liberation spectra. Certainly, the two most realistic approaches are the integral geometry of Barbery [4] and the random fracture model of King [12]. However, when comminution is in closed circuit with a concentration device, these methods cannot be used, since the original texture of the ore is transformed during the concentration stage and the material being comminuted becomes a combination of processed and fresh ore. The vast majority of grinding circuits of at least two phase ores will fall into this category, because common classification devices,

such as the hydrocyclone, have a strong concentration effect due to differences in phase density and the resulting force differential applied to particles which differ even slightly in composition. This is also always the case in regrind circuits. The only known approach capable of incorporating the concentration effects into the natural breakage characteristics of the ore is the population balance equation. This is shown in equation 3.1, as in Austin and Luckie review of the state of the art of liberation modelling [28], for two-phase mineral systems:

$$p(g,D) + p(g,D)\,S(g,D)\,\tau - \tau \int_{R'} b(g,D;g',D')\,S(g',D')\,p(g',D')\,dg'\,dD' = f(g,D) \tag{3.1}$$

where $p(g,D)$ is the liberation spectrum, i.e., the distribution of particles that have grade g and size D, at any time in a perfectly mixed mill region, $f(g,D)$ is the liberation spectrum of the feed, τ is the mean residence time, $S(g,D)$ is the rate of breakage and $b(g,D;g',D')$ is the quadrivariate breakage distribution function. R' is the region in the grade and size domains over which the integral operates, and represents every possible combination of grades g' and sizes D' from which a progeny of grade g and size D can be originated.

The central problem on solving equation 3.1 is to establish the quadrivariate breakage function that is associated with the ore being ground, given the mineralogical texture of the ore. The direct measurement of the quadrivariate breakage function is almost impossible because it requires the separation of several narrow size, narrow grade samples, that upon breakage will generate hundreds of combinations of progeny sizes and grades.

The conventional solutions to equation 3.1 such as those proposed by Herbst et al. [29], Choi et al. [30] and Mehta et al. [31], require the estimation of hundreds of arbitrary parameters in order to describe the quadrivariate breakage function, which render this approach almost completely useless. The need for a more appropriate description of the quadrivariate breakage function was first understood by Andrews and Mika [32] in 1975. They realized that the set of possible sizes and grades of the progeny particles is constrained by the volumetric fraction of the phases in the parent particle. This was illustrated by a diagram, which is now known as the Andrews-Mika diagram, shown in Figure 3.1. This two-dimensional diagram shows the bounds of the quadrivariate breakage function, and the phase volume constraints for the accessible region are represented by the dotted lines. Particles characterized by a single point $\langle g', D' \rangle$ in the diagram can only produce progeny, by breakage, inside the "Andrews-Mika" conservation of phase-volume bounds, i.e., inside the accessible region. Furthermore, liberated particles of phase *A* ($g = 0$) can only appear at progeny sizes bellow D_A^V and liberated particles of phase *B* ($g = 1$) bellow size D_B^V. The understanding of the limiting bounds of the quadrivariate breakage function is indeed important, but the diagram provides no information whatsoever about its internal structure, i.e., the fraction of particles originated at point $\langle g', D' \rangle$ that report to point $\langle g, D \rangle$ in the diagram.

The Andrews-Mika bounds are tightened if the mineralogical texture of the ore is considered. This was shown in a study by Lin et al. [33], in which the values of the sizes D_A and D_B, i.e., the critical sizes for phases *A* and *B* of the diagram were estimated by means of the simulation of random fracture of two phase PARGEN particles. This work

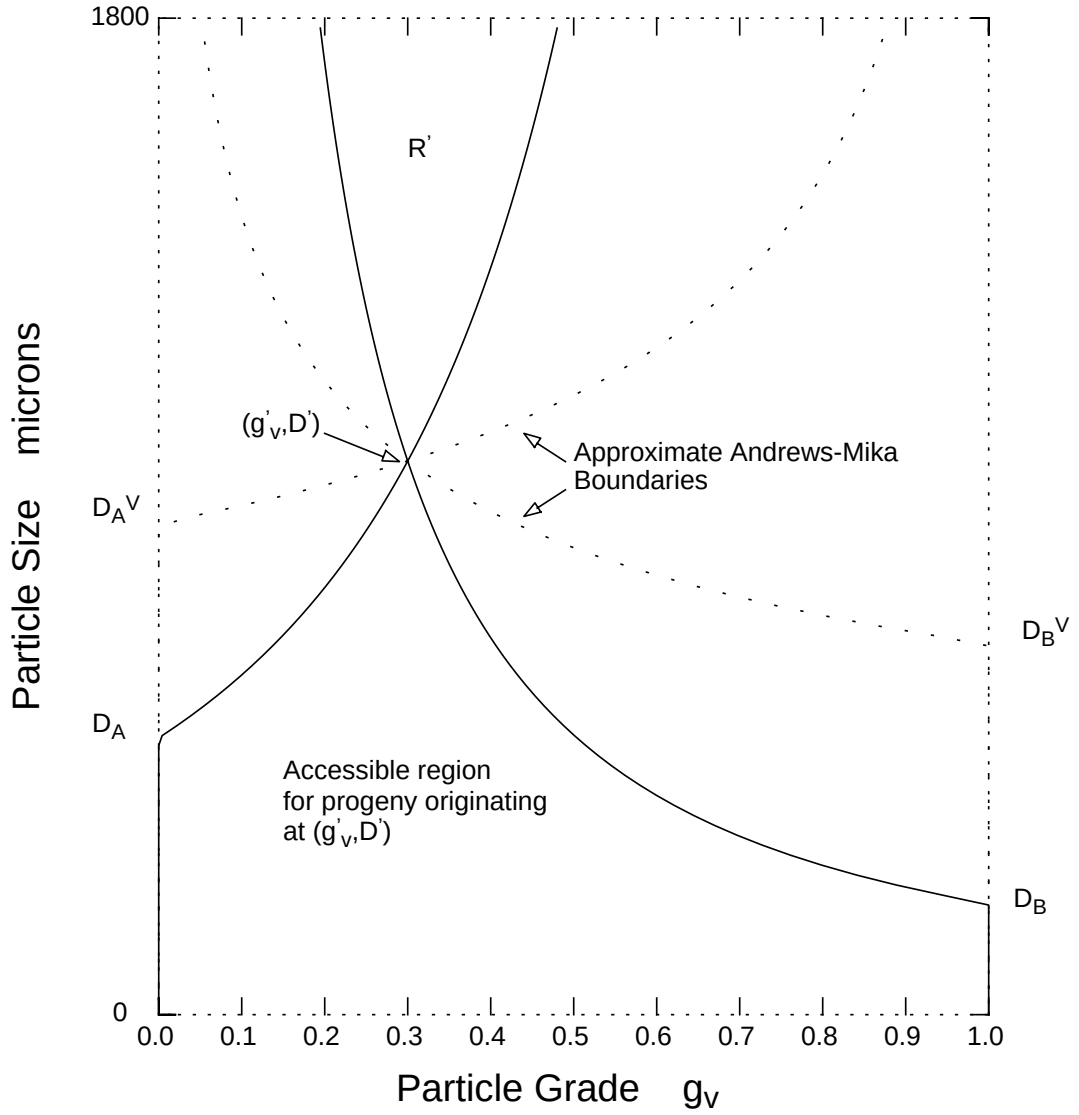

Figure 3.1 The Andrews-Mika diagram for monosize, monograde particles. The dotted lines show the bounds determined by phase-volume constraints

also provided the basis for relating texture to the conditional, on progeny size, quadrivariate breakage function, and its internal structure. In 1990, following Lin's work, King [9] proposed a solution to the population balance equation 3.1 that embeds the ore texture and allows the calculation of the liberation spectrum that is produced in the progeny from the comminution of two-phase particles. The proposed solution is particularly attractive because it requires only one arbitrary parameter. However consistent predictions are provided by the model, as shown in a sensitivity analysis by Schneider and King [34], it lacks more detailed information on the internal structure of the quadrivariate breakage function, i.e., the actual transfer coefficients among the grade/size classes in the accessible region, because the PARGEN simulation is limited to the amount of memory available to store a large enough two-phase PARGEN particle that upon breakage generates progeny in all size and grade classes in the accessible region. The present simulations produce only enough progeny to give an approximate picture of the internal structure of the accessible region. Also, the amount of data produced was just enough to investigate the relationship between the critical liberation sizes and the texture of the PARGEN particles. The texture of the PARGEN particles is exclusively granular, with well defined grain and particle shapes. A geometrical texture parameter based on the particles size and their interphase area per unit of volume of phase was found to correlate well with the fraction of phase liberated in the progeny. This geometrical texture parameter can be measured by image analysis in fractionated particles. King [9] has proposed a relationship for the calculation of the critical sizes D_A and D_B based on this parameter and on the results of the PARGEN simulations.

The development of proper image analysis techniques coupled with magnetic fluid fractionation procedures (MAGSTREAM™), as described in the previous chapter, considerably eased the task of measuring the liberation spectra produced by the breakage of narrow size, narrow grade two-phase particles from a real ore. Once the proper transformation kernel for the Dolomite-Sphalerite ore has been established, and an accurate enough solution to the transformation equation has been made available, the internal structure of the conditional, on progeny size, quadrivariate breakage function can be measured experimentally, at least for the Dolomite-Sphalerite ore, using the image analysis approach.

The measured coefficients of the breakage function provide enough information for the modeling of its internal structure and its bounds. The only known attempt to model the discrete quadrivariate breakage function is the one by King [9], based on data generated from PARGEN simulations. In this work, a model that describes the continuous quadrivariate breakage function is presented, based on experimental data from real mineralogical particles.

Approach

Our primary concern is the measurement of $b\langle g, D; g', D' \rangle$, which describes the distribution in the progeny that results from the breakage of particles of grade exactly equal to g' and size exactly equal to D'. Due to the nature of multiphase particulate systems, it is impossible to produce monosize, monograde samples of real particles. At best, very clean samples in narrow size, narrow grade classes can be produced. If a large enough number of particles is produced by any means into a narrow size/grade class, then

the distribution $b(g,D;g'^{*},D'^{*})$ can be characterized for the progeny originated from particles in the grade range g'^{*}, and size range D'^{*} by breaking these particles into several progeny sizes and measuring for each progeny size the correspondent liberation spectrum. The grade and size ranges described by g'^{*} and D'^{*} define a rectangular region in the Andrews-Mika diagram, rather then a single point. The complete characterization would then require a large number of narrow size, narrow grade particles, each sample representing a distinct rectangular region of the diagram, organized such that an entire area of the diagram is covered, including all sizes in the range of interest and the whole of the grade domain. Each sample is then broken into its progeny, followed by the measurement of the correspondent liberation spectra. Such a formidable task is nothing but discouraging. The alternative is to assume that the quadrivariate breakage function is unambiguously normalizable with respect to parent size for the given test ore, that is

$$b(g,D;g',D') = b(g,D/D';g') \tag{3.2}$$

for all D'. If the assumption in equation 3.2 holds, then the complete characterization of the breakage function can be achieved from samples in a single size range D'^{*}, along with a set of narrow grade samples that cover the width of the diagram. This greatly reduces the amount of experimental work that is necessary. The evaluation of the assumption in equation 3.2 requires that the characterization be performed for at least two sets of narrow size samples, but such evaluation escapes the main scope of this work. For now, it will be assumed that the breakage function is unambiguously normalizable with respect to D'. The characterization can be further simplified by assuming that the

liberation and fracture processes can be decoupled [9]. This is achieved by decomposing the breakage function into its liberation and fracture components,

$$b(g,D;g',D') = b(g \mid D;g',D')\; b(D;D') \tag{3.3}$$

for which the assumption

$$b(D;g',D') = b(D;D') \tag{3.4}$$

has been made.

In equation 3.3, $b(g \mid D;g',D')$ is the conditional, on progeny size, quadrivariate breakage function and $b(D;D')$ is the traditional, fairly well described and modelled [28], bivariate breakage function. The assumption in equation 3.4 is that the distribution of progeny sizes is independent of parent composition. It is possible to test this assumption by means of single fracture tests performed on narrow grade particles of the test ore. However, such test also escapes the scope of this work, and it is assumed that equation 3.4 holds for the test ore used here.

The conversion from grade, weighted by mass, to volumetric grade is trivial, and the following expression is obtained from the definition of grade and the mass balance in equation 2.23:

$$g = \frac{\rho_B\, g_v}{(\rho_B - \rho_A)\, g_v + \rho_A} \tag{3.5}$$

Conversion from mass-weighted distribution to volume-weighted is also trivial, and the volume-weighted quadrivariate breakage distribution will retain its shape, independently of the relative density of the phases in the mineralogical system. The

volume-weighted distribution is therefore the best choice when characterizing the relationship that exists between texture and the liberation process. The conversion is essentially the same as the one defined in equation 2.24 for discrete size distributions of two-phase particles. For the continuous, conditional on size, quadrivariate breakage distribution, the conversion can be written as

$$b_v(g_v \mid D; g_v', D') = \overline{\rho}(D) \frac{b(g_v \mid D; g_v', D')}{\rho(g_v)} \tag{3.6}$$

where $\rho(g_v)$ is the density of particles of volumetric grade g_v, as defined in equation 2.23, and $\overline{\rho}(D)$ is the average density of particles of size equal to *D*, which in terms of the conditional quadrivariate breakage function is defined as:

$$\frac{1}{\overline{\rho}(D)} = \int_0^1 \frac{b(g_v \mid D; g'_v, D')}{\rho(g_v)} \, dg_v \tag{3.7}$$

The conditional breakage function $b_v(g \mid D; g', D')$ is considerably more amenable to characterization, specially because it can be more easily visualized as a surface, with domain of size and grade and range from 0 to 1, that can be modelled in terms of continuous functions. For its measurement however, it must be dealt with in its discrete form. The discretization is a set of integrations over the size and grade ranges for which discrete fractions are desired. The integration process may be described in four steps. First, the cumulative, conditional on size, quadrivariate breakage function is defined as:

$$B_v(g_v \mid D; g'_v, D') = \int_0^{g_v} b_v(g_v \mid D; g'_v, D') \, dg_v \tag{3.8}$$

Then, the discrete breakage distribution that is produced by comminution of monosize,

monograde particles is written in terms of the continuous distribution as

$$b_v^{kl}\left(g_v',D'\right) = \frac{\int_{D^{l-1}}^{D^l} \left(B_v\left(g_v^k \mid D;g_v',D'\right) - B_v\left(g_v^{k-1} \mid D;g_v',D'\right)\right) f_v\left(D;g_v',D'\right)\, dD}{\int_{D^{l-1}}^{D^l} f_v\left(D;g_v',D'\right)\, dD} \qquad (3.9)$$

where $f_v\left(D;g_v',D'\right)$ is the size distribution in the progeny originated at point $\left(g_v',D'\right)$. Now, for progeny distributions originating from particles in a narrow size, narrow grade range, and using the result in equation 3.9, it follows:

$$b_v^{klij} = \int_{D'^{i-1}}^{D'^{i}} \int_{g_v'^{j-1}}^{g_v'^{j}} b_v^{kl}\left(g_v',D'\right) f_v\left(g_v',D'\right)\, dg_v'\, dD' \qquad (3.10)$$

where b_v^{klij} is the volume fraction of material in size range $\left(D^l,D^{l-1}\right)$ that report to grade range $\left(g_v^k,g_v^{k-1}\right)$ and which originate from grade range $\left(g_v'^j,g_v'^{j-1}\right)$ and size range $\left(D'^i,D'^{i-1}\right)$. The discrete quadrivariate breakage function b_v^{klij} can be measured directly, by image analysis, using the stereological correction procedure described in Chapter 2, in progeny sorted in narrow size ranges by standard screening, and that is originated from the breakage of narrow size, narrow grade particles produced by fractionation. Furthermore, and very important, the set of parameters that describe the continuous quadrivariate breakage function $b_v\left(g_v \mid D;g'_v,D'\right)$ can be estimated from the measured discrete distribution, by means of equations 3.9 and 3.10, provided that a functional form, with a limited number of parameters for $b_v\left(g_v \mid D;g'_v,D'\right)$ is known. The measured fractions also provide, together with the Andrews-Mika diagram, the basis for the modelling of the continuous quadrivariate breakage function.

Texture characterization is complete with the measurement of the geometrical texture parameters associated with the particles interphase area per unit volume of phase. Simulation of breakage of PARGEN particles suggests that the values of the groups $D\,S_v^{AB}$ and $D\,S_v^{BA}$ are invariant with size, and also that they increase linearly as particle grade increases:

$$D\,S_V^{AB} = \phi_A\; g_v \tag{3.11}$$

and

$$D\,S_V^{BA} = \phi_B\; (1 - g_v) \tag{3.12}$$

where S_V^{AB} is the interphase area per unit volume of phase *A* and S_V^{BA} is the interphase area per unit volume of phase *B*, and ϕ_A and ϕ_B are the geometrical texture parameters. These parameters can be measured directly from the fractionated particles, by discretizing equations 3.11 and 3.12 as follows:

$$d_p\,S_V^{ABij} = \int_{D'^{i-1}}^{D'^{i}} \int_{g'^{j-1}_v}^{g'^{j}_v} \phi_A\; g'_v\; f_v\left(g'_v, D'\right)\; dg'_v\; dD' \tag{3.13}$$

and

$$d_p\,S_V^{BAij} = \int_{D'^{i-1}}^{D'^{i}} \int_{g'^{j-1}_v}^{g'^{j}_v} \phi_B\; (1 - g'_v)\; f_v\left(g'_v, D'\right)\; dg'_v\; dD' \tag{3.14}$$

In equations 3.13 and 3.14, it was assumed that the size distribution in the parent particles narrow size range is uniform, and d_p is the representative size of the range. Since ϕ_A and ϕ_B are constant, they can be taken out of the integral in equations 3.13 and 3.14, leaving each of them with the definition of average grade in the parent particles. Thus,

$$d_p\,S_V^{ABij} = \phi_A\; \overline{g_v^{ij}} \tag{3.15}$$

and

$$d_p S_V^{BAij} = \phi_B \left(1 - \overline{g_v^{ij}}\right) \tag{3.16}$$

Measurement of the Discrete Quadrivariate Breakage Function

In Chapter 2, seven narrow size, narrow grade samples of the Dolomite-Sphalerite test ore were produced by magnetic fluid fractionation for the measurement of the Dolomite-Sphalerite transformation kernel for stereological correction. Only a fraction of those particles was used for that measurement. The remaining particles constitute the test material for the characterization of the quadrivariate breakage function. The seven samples are contained in a single size range of -1000+710 microns, defining one size class in the parent $\left(D'^i, D'^{i-1}\right)$, with i = 1. The samples also define the set of parent grades $\left(g_v'^j, g_v'^{j-1}\right)$ for j = 1 to 7.

The seven parent particle samples were crushed in an ultrasonic mill. This device produces a progeny size distribution that is more uniform. This is preferable because on the limited amount of material in each narrow size, narrow grade sample. During crushing, enough material must be produced in each progeny size range, and the ultrasonic mill is the best choice. The interested reader may refer to Lo et al. [35] for a description of the ultrasonic mill. The particles were crushed with the gap between the grinding surface and the roll set to 100 microns. Repeated passes were carried out until all particles cleared the 710 micron screen. These progenies were then carefully sieved in 500, 355, 250, 180 and 106 microns screens. The set of screens define the progeny

size ranges $\left(D^{l},D^{l-1}\right)$, for l = 1 to 6. The progeny size distribution resulting from each narrow size, narrow grade parent sample, corresponding to f_w^{lij}, which is the discrete version of $f_w\left(D;g',D'\right)$, is shown in Table 3.1.

The 42 progeny particle samples were then mounted, ground and polished using the exact same sample preparation procedure described in Chapter 2. A set of approximately 60 images, whenever possible, was acquired from each specimen cross-section, totaling 2422 images. Special care was taken during the image acquisition so that the peaks characterizing each phase were located at predetermined gray level ranges, with optimum phase discrimination. This allows the processing of the images to be carried out automatically, with no interference from the operator, in a matter of hours. This not only facilitates the processing of large number of images, but also eliminates human error. The image acquisition and processing followed exactly the same recipe described in Chapter 2. All images were compressed and stored in tapes for future reference.

The average volumetric grade of each sample as measured by areal fraction of phase in each image set corresponding to a progeny narrow size range, and originating from a narrow size, narrow grade sample $\overline{g_v^{lij}}$ is shown in Table 3.2. In general, a tendency to concentrate Sphalerite in the smaller sizes can be observed for the lower grade particles. However, this does not appear to be a very strong tendency. This behavior is relevant because it indicates that particle fracture was not completely random for this grinding experiment. A more concise indicator of fracture randomness is the distribution of volumetric grades in the progeny $\overline{g_v^{l}}$, which is produced by the breakage of unfractionated particles that are contained in a narrow size range. The calculation of

Table 3.1 Progeny size distribution after ultrasonic grinding

size range, (D^{l}, D^{l-1}) microns	Progeny size distributions resulting from each narrow size, narrow grade sample, f_w^{lij}. Density range, g/cc						
%	-2.9	-3.1 +2.9	-3.3 +3.1	-3.5 +3.3	-3.7 +3.5	-4.0 +3.7	+4.0
-710+500	11.76	3.91	2.27	2.88	2.11	0.93	1.46
-500+355	27.86	14.66	13.64	12.98	11.97	10.25	9.12
-355+250	24.15	25.73	29.55	29.33	34.51	31.05	29.20
-250+180	9.91	15.96	18.18	18.27	19.72	21.12	21.53
-180+106	10.53	15.31	16.36	15.87	14.79	17.08	19.71
-106	15.79	24.43	20.00	20.67	16.90	19.57	18.98

Table 3.2 Sample average volumetric grade measured by image analysis

size range, (D^{l}, D^{l-1}) microns	Progeny average volumetric grade for each narrow size, narrow grade sample, $\overline{g_v^{lij}}$. Density range, g/cc						
%	-2.9	-3.1 +2.9	-3.3 +3.1	-3.5 +3.3	-3.7 +3.5	-4.0 +3.7	+4.0
-710+500	0.60	6.44	19.98	35.19	46.35	77.59	93.41
-500+355	0.68	7.57	19.77	35.35	56.39	75.36	94.35
-355+250	0.99	7.93	23.30	39.37	57.41	77.48	93.76
-250+180	1.07	8.58	25.50	41.38	60.00	76.98	94.99
-180+106	1.44	10.57	24.07	43.73	62.21	74.26	94.61
-106	2.29	12.25	33.32	47.75	62.78	76.83	92.81

$\overline{g_v^l}$, from the fractionated particles data, requires the values of the volume-weighted progeny size distribution resulting from each narrow size, narrow grade parent sample f_v^{lij}, which is the discrete version of $f_v(D;g',D')$. The distribution $f_v(D;g',D')$ is important not only for the calculation of $\overline{g_v^l}$, but also for the discretization of the quadrivariate breakage function in equation 3.9. The first step in calculating the fractions f_v^{lij} is to get the average densities $\overline{\rho^{lij}}$ that correspond to the measured volumetric grades in the progeny $\overline{g_v^{lij}}$. The conversion is carried out using equation 2.23 and the data in Table 3.2. The resulting average densities are shown in Table 3.3. The calculated average densities in each progeny sample vary linearly with volumetric grade in two-phase ores. In this sense, no new information is generated by calculating these values, since the behavior of phase distribution is already shown in Table 3.2 in terms of volumetric grades. Nevertheless, in this form, it is observed that the progeny densities for the particles generated from parent particles of density higher then 4.0 g/cc all measured smaller then 4.0 g/cc. Consequently, the parent particles must also have had density smaller then 4.0 g/cc, indicating that the true separation density during magnetic fluid fractionation was actually smaller then 4.0 g/cc. It is suspected that equation 2.20, which relates the settings of the MAGSTREAM™ to separation density, is less accurate for higher separation densities. Unfortunately, there is no method at hand to calculate the correct separation density for that experiment, and the intended separation density of 4.0 g/cc will be retained here. With the average densities $\overline{\rho^{lij}}$ in Table 3.3, it is possible to calculate $\overline{\rho^{ij}}$, which is the average density in the progeny produced by comminution of the narrow size, narrow grade samples. The calculation is carried out using the same principle as in

Table 3.3 Calculated progeny average density

size range, (D^{l}, D^{l-1}) microns	Progeny average density for each narrow size, narrow grade sample, $\overline{\rho^{lij}}$. Density range, g/cc						
%	-2.9	-3.1 +2.9	-3.3 +3.1	-3.5 +3.3	-3.7 +3.5	-4.0 +3.7	+4.0
-710+500	2.8376	2.9077	3.0701	3.2526	3.3865	3.7613	3.9511
-500+355	2.8386	2.9212	3.0776	3.2545	3.5070	3.7346	3.9624
-355+250	2.8423	2.9255	3.1100	3.3028	3.5192	3.7600	3.9553
-250+180	2.8432	2.9333	3.1363	3.3269	3.5503	3.7540	3.9701
-180+106	2.8477	2.9572	3.1192	3.3551	3.5768	3.7214	3.9655
-106	2.8579	2.9774	3.2302	3.4033	3.5836	3.7522	3.9439

equations 2.25 and 3.7, which are basically the first moment of the distribution in question with respect to density. Here, in discrete form, this is

$$\overline{\rho^{ij}} = \frac{1}{\sum_{l=1}^{6} \frac{f_w^{lij}}{\overline{\rho^{lij}}}} \tag{3.17}$$

The calculated average densities $\overline{\rho^{ij}}$ are expected to be in the separation density range, with the exception of the one calculated for the +4.0 g/cc particles, as discussed above. The values of $\overline{\rho^{ij}}$ can be used to calculate the average volumetric grades $\overline{g_v^{ij}}$ using, once again, equation 2.23. The calculated average densities $\overline{\rho^{ij}}$ can be directly compared with the average densities in the fractionated particles measured with the helium picnometer, in Table 2.1. Also, the calculated average volumetric grades $\overline{g_v^{ij}}$ are compared with those of the fractionated particles measured by image analysis, in Table 2.1. This is shown in Table 3.4, and both the calculated grades and densities from the progeny show very good consistency with the values measured by picnometry and image analysis in the parent, indicating that the progeny is consistent with the parent particles. The possible exception is the Helium Pycnometer density measured for the +4.0 g/cc particles, which read too high. This may have been caused by poor sampling or incorrect calibration of the pycnometer. Nevertheless, the measured values by picnometry are only used for comparison purposes, and as an indication of average density during fractionation.

With the values of $\overline{\rho^{lij}}$ in Table 3.3, $\overline{\rho^{ij}}$ in Table 3.4 and f_w^{lij} in Table 3.1 it is possible to calculate the volume-weighted progeny size distribution f_v^{lij} using equation 2.24, which can be redefined here as:

Table 3.4 Comparison between the measured average densities and volumetric grades in the fractionated parent particles and the averages calculated from the progeny

Density range, g/cc	Average density g/cc, from Helium Pycnometer, $\overline{\rho^{j}}$	Calculated density g/cc, from progeny, $\overline{\rho^{ij}}$	Average volumetric grade %, from image analysis, $\overline{g_v^{j}}$	Calculated volumetric grade %, from progeny, $\overline{g_v^{ij}}$
-2.9	2.851	2.8438	0.73	1.12
-3.1 +2.9	2.959	2.9428	9.47	9.37
-3.3 +3.1	3.133	3.1328	27.27	25.20
-3.5 +3.3	3.316	3.3278	40.49	41.46
-3.7 +3.5	3.522	3.5401	58.00	59.15
-4.0 +3.7	3.746	3.7480	79.38	76.48
+4.0	4.005	3.9589	94.64	94.06

$$f_v^{lij} = \frac{\overline{\rho^{ij}}\, f_w^{lij}}{\overline{\rho^{lij}}} \tag{3.18}$$

The resulting volume-weighted progeny size distributions are shown in Table 3.5. Curiously enough, but not surprising, they are not much different then the mass-weighted distributions, and the assumption that $f_w^{lij} = f_v^{lij}$ would not be in much error for the Dolomite-Sphalerite ore. The volume-weighted size distribution in the progeny f_v^l is calculated with f_v^{lij} in Table 3.5 and f_v^{ij} in Table 2.2, and using equation 3.19, as follows:

$$f_v^l = \sum_j f_v^{lij}\, f_v^{ij} \tag{3.19}$$

Finally, the volumetric grades in the progeny $\overline{g_v^l}$ are calculated as follows:

$$\overline{g_v^l} = \frac{\sum_j f_v^{lij}\, f_v^{ij}\, g_v^{lij}}{\sum_j f_v^{lij}\, f_v^{ij}} \tag{3.20}$$

The resulting volume-weighted size distribution in the progeny is shown in Table 3.6, along with corresponding average volumetric grades at each progeny size range. The results clearly indicate that the Sphalerite concentrates in the smaller size ranges. This behavior must be due to differential friability in the Dolomite-Sphalerite mineralogical system, and indicates that the Sphalerite is considerably more friable than the Dolomite. This differential friability must be taken in account when modelling the quadrivariate breakage function, and it is anticipated that most ores will exhibit differential friability, at least to a certain extent. The variation of average grade with size in the progeny is defined as $\overline{g_v}\langle D; g_v', D' \rangle$, which is continuous in the progeny size domain. This

Table 3.5 Volume-weighted progeny size distribution after ultrasonic grinding

size range, (D^l, D^{l-1}) microns	Progeny size distributions resulting from each narrow size, narrow grade sample, f_v^{lij}. Density range, g/cc						
%	-2.9	-3.1 +2.9	-3.3 +3.1	-3.5 +3.3	-3.7 +3.5	-4.0 +3.7	+4.0
-710+500	11.79	3.96	2.32	2.95	2.11	0.93	1.46
-500+355	27.91	14.77	13.93	13.27	12.08	10.29	9.11
-355+250	24.16	25.88	29.77	29.55	34.71	30.95	29.23
-250+180	9.91	16.01	18.16	18.28	19.66	21.09	21.47
-180+106	10.52	15.24	16.43	15.74	14.64	17.20	19.68
-106	15.71	24.15	19.40	20.21	16.69	19.55	19.05

Table 3.6 The volume-weighted size distribution and the average volumetric grades in the progeny

size range, (D^l, D^{l-1}) microns	Volume-weighted size distribution f_v^l, %	Average volumetric grade $\overline{g_v^l}$, %
-710 +500	10.10	2.31
-500 +355	24.98	5.07
-355 +250	25.00	14.40
-250 +180	11.64	21.93
-180 +106	11.81	19.86
-106	16.47	15.61

distribution is important because it represents the variation of the first moment of the conditional quadrivariate breakage function with progeny size, i.e.,

$$\overline{g_v}\left(D;g_v',D'\right) = \int_0^1 g_v \; b_v\left(g_v \mid D;g_v',D'\right) \, dg_v \tag{3.21}$$

Again, the distribution $\overline{g_v}\left(D;g_v',D'\right)$ can be measured only from narrow size progeny samples that are originated by breakage of particles in a narrow size, narrow grade range. The average grades $\overline{g_v^{lij}}$ shown in Table 3.2 are in fact, the result of such measurement. These are related to the continuous distribution by:

$$\overline{g_v^{l}}\left(g_v',D'\right) = \frac{\int_{D^{l-1}}^{D^{l}} \overline{g_v}\left(D;g_v',D'\right) \, f_v\left(D;g_v',D'\right) \, dD}{\int_{D^{l-1}}^{D^{l}} f_v\left(D;g_v',D'\right) \, dD} \tag{3.22}$$

and

$$\overline{g_v^{lij}} = \int_{g_v'^{j-1}}^{g_v'^{j}} \int_{D'^{i-1}}^{D'^{i}} \overline{g_v^{l}}\left(g_v',D'\right) \, f_v\left(g_v',D'\right) \, dD' \, dg_v' \tag{3.23}$$

The double integration in equation 3.23 is analogous to the integrations in equation 3.10, only here the integrand is average grade, thus the same approach is used to discretize both the quadrivariate breakage function and the average grade distribution in the progeny. Again, a functional form is required for $\overline{g_v}\left(D;g_v',D'\right)$, and the parameterization can be carried out with the values of $\overline{g_v^{lij}}$ in Table 3.2 and equations 3.22 and 3.23.

The measurement of the distribution of both the particles and the phases in the progeny size classes is complete, with the data shown in Tables 3.2 through 3.6. The results provide with fundamental information about the breakage characteristics of the test ore. They also show consistency between the parent and the progeny, which indicates that the experimental procedure was carried out successfully, i.e., no sample segregation, no contamination, proper sample mounting, good image sampling and good image thresholding. The next step is the measurement of the linear grade distributions for each of the 42 narrow size progeny samples. The measurement is carried out in exactly the same manner as in Chapter 2, and the intercepts are corrected for the probability they intercept the measuring frame. The measured linear grade distributions are, in the context of this experiment, and in the stereological sense, the one-dimensional internal structure of the conditional quadrivariate breakage function. The measured linear grades were sorted in the traditional 12 linear grade classes, defining the progeny linear grade ranges $\left(g_\ell^k, g_\ell^{k-1}\right)$, for k = 1 to 12. The resulting length-weighted, one-dimensional, conditional on size linear grade distributions b_ℓ^{klij}, which are the discrete version of $b_\ell\left(g_\ell \mid D; g_v', D'\right)$, are shown in Tables 3.7 through 3.13. The corresponding volumetric grade distributions are calculated using the stereological correction procedure described in Chapter 2, with the measured Dolomite-Sphalerite transformation kernel. Upon stereological correction the progeny linear grade ranges are transformed into the corresponding progeny volumetric grade ranges $\left(g_v^k, g_v^{k-1}\right)$, with k = 1 to 12, and the coefficients of the three-dimensional, volume-weighted, conditional quadrivariate breakage function b_v^{klij}, which is the discrete version of $b_v\left(g_v \mid D, g_v', D'\right)$, are obtained. The stereological correction

Table 3.7 Conditional on size linear grade distributions measured by image analysis for the -1000+710 microns parent particles with volumetric grade between 0 and 5.80 % and their progeny after grinding in the ultrasonic mill

Linear grade %	Conditional on size linear grade distributions. Size range, microns						
%	-106 µ	-180 +106 µ	-250 +180 µ	-355 +250 µ	-500 +355 µ	-710 +500 µ	-1000 +710 µ
0	97.59	98.10	98.04	97.99	98.12	98.10	97.27
0 - 10	0.19	0.25	0.47	0.75	0.79	0.81	1.23
10 - 20	0.08	0.14	0.26	0.29	0.32	0.44	0.51
20 - 30	0.05	0.05	0.23	0.15	0.15	0.20	0.26
30 - 40	0.01	0.08	0.13	0.17	0.13	0.07	0.18
40 - 50	0.02	0.07	0.03	0.06	0.12	0.05	0.04
50 - 60	0.04	0.06	0.05	0.09	0.05	0.03	0.11
60 - 70	0.01	0.06	0.02	0.02	0.01	0.03	0.05
70 - 80	0.04	0.04	0.05	0.04	0.01	0.04	0.01
80 - 90	0.03	0.02	0.05	0.02	0.03	0.03	0.04
90 - 100	0.19	0.06	0.09	0.02	0.04	0.07	0.06
100	1.75	1.07	0.58	0.40	0.23	0.13	0.24

Table 3.8 Conditional on size linear grade distributions measured by image analysis for the -1000+710 microns parent particles with volumetric grade between 5.80 and 22.47 % and their progeny after grinding in the ultrasonic mill

Linear grade %	Conditional on size linear grade distributions. Size range, microns						
%	-106 µ	-180 +106 µ	-250 +180 µ	-355 +250 µ	-500 +355 µ	-710 +500 µ	-1000 +710 µ
0	86.86	84.29	84.38	82.13	80.07	79.82	72.69
0 - 10	0.68	2.36	3.61	4.65	6.04	6.48	8.08
10 - 20	0.27	1.41	1.99	2.90	3.26	4.50	5.88
20 - 30	0.30	0.96	1.21	1.87	2.03	2.38	3.19
30 - 40	0.23	0.76	0.82	1.36	1.66	1.57	2.33
40 - 50	0.22	0.67	0.59	1.07	1.03	1.10	1.58
50 - 60	0.11	0.71	0.77	0.90	0.91	0.60	1.05
60 - 70	0.09	0.61	0.67	0.67	0.73	0.66	0.74
70 - 80	0.12	0.51	0.49	0.63	0.51	0.44	0.69
80 - 90	0.23	0.43	0.51	0.68	0.42	0.37	0.62
90 - 100	0.47	0.55	0.46	0.42	0.37	0.25	0.52
100	10.42	6.74	4.50	2.72	2.97	1.83	2.63

Table 3.9 Conditional on size linear grade distributions measured by image analysis for the -1000+710 microns parent particles with volumetric grade between 22.47 and 39.14 % and their progeny after grinding in the ultrasonic mill

Linear grade %	Conditional on size linear grade distributions. Size range, microns						
%	-106 µ	-180 +106 µ	-250 +180 µ	-355 +250 µ	-500 +355 µ	-710 +500 µ	-1000 +710 µ
0	62.94	66.97	61.78	58.14	54.52	48.58	35.65
0 - 10	1.59	3.85	4.83	6.35	9.88	10.79	9.97
10 - 20	0.86	2.18	3.01	4.83	7.26	8.62	9.75
20 - 30	1.00	1.73	2.64	3.77	5.41	7.00	8.95
30 - 40	0.43	1.34	2.34	3.28	3.94	6.16	7.47
40 - 50	0.62	0.97	2.02	2.53	2.93	4.28	5.99
50 - 60	0.65	1.15	1.57	2.21	2.57	3.03	4.45
60 - 70	0.54	1.08	1.34	1.91	2.00	2.08	3.37
70 - 80	0.63	0.84	1.45	1.71	1.71	2.05	2.23
80 - 90	0.64	1.00	1.20	1.42	1.48	1.35	1.78
90 - 100	1.73	1.16	1.28	1.29	1.15	0.93	1.58
100	28.37	17.73	16.54	12.56	7.15	5.13	8.81

Table 3.10 Conditional on size linear grade distributions measured by image analysis for the -1000+710 microns parent particles with volumetric grade between 39.14 and 55.81 % and their progeny after grinding in the ultrasonic mill

Linear grade %	Conditional on size linear grade distributions. Size range, microns						
%	-106 µ	-180 +106 µ	-250 +180 µ	-355 +250 µ	-500 +355 µ	-710 +500 µ	-1000 +710 µ
0	47.64	44.83	43.91	41.18	37.74	32.88	25.86
0 - 10	1.57	3.94	4.86	5.75	7.74	8.23	6.04
10 - 20	1.19	2.15	3.60	4.40	6.47	8.08	7.96
20 - 30	0.47	2.10	2.84	3.98	5.49	7.74	7.27
30 - 40	0.49	1.51	2.55	4.03	5.44	5.86	7.60
40 - 50	0.47	1.40	1.98	3.15	4.44	5.65	7.70
50 - 60	0.75	1.53	2.46	3.26	4.06	4.58	7.69
60 - 70	0.82	1.54	1.74	2.40	3.22	4.49	5.31
70 - 80	0.65	1.62	1.82	2.19	2.98	3.93	3.98
80 - 90	0.98	1.71	2.07	2.26	2.62	2.93	2.89
90 - 100	2.05	1.59	2.14	2.34	2.42	2.44	3.00
100	42.92	36.08	30.03	25.06	17.38	13.19	14.70

Table 3.11 Conditional on size linear grade distributions measured by image analysis for the -1000+710 microns parent particles with volumetric grade between 55.81 and 72.48 % and their progeny after grinding in the ultrasonic mill

Linear grade %	Conditional on size linear grade distributions. Size range, microns						
%	-106 µ	-180 +106 µ	-250 +180 µ	-355 +250 µ	-500 +355 µ	-710 +500 µ	-1000 +710 µ
0	31.85	29.07	27.26	25.79	21.41	23.20	16.02
0 - 10	1.44	2.21	3.09	4.37	4.63	6.08	3.21
10 - 20	1.35	1.64	2.65	3.37	4.99	7.69	4.68
20 - 30	1.10	1.58	2.24	2.87	4.21	6.35	4.49
30 - 40	0.75	1.34	2.38	3.01	3.98	6.05	6.08
40 - 50	0.49	1.49	1.99	2.86	3.59	5.75	6.48
50 - 60	0.73	1.74	2.54	2.89	4.09	5.96	6.84
60 - 70	0.68	1.66	2.18	3.22	3.98	4.89	6.42
70 - 80	0.91	1.63	2.42	3.51	4.39	5.22	5.81
80 - 90	1.38	2.14	2.97	3.16	4.13	3.98	5.30
90 - 100	3.07	3.12	3.01	3.82	4.33	4.07	3.95
100	56.25	52.38	47.27	41.13	36.27	20.76	30.72

Table 3.12 Conditional on size linear grade distributions measured by image analysis for the -1000+710 microns parent particles with volumetric grade between 72.48 and 97.48 % and their progeny after grinding in the ultrasonic mill

Linear grade %	Conditional on size linear grade distributions. Size range, microns						
%	-106 µ	-180 +106 µ	-250 +180 µ	-355 +250 µ	-500 +355 µ	-710 +500 µ	-1000 +710 µ
0	17.53	16.82	12.44	10.49	10.46	7.53	5.29
0 - 10	1.31	2.36	2.71	2.32	2.26	1.72	1.27
10 - 20	0.75	1.44	1.96	1.85	2.32	2.09	1.77
20 - 30	0.70	1.62	1.64	2.03	2.45	2.08	2.20
30 - 40	0.85	1.45	1.48	2.10	2.41	2.72	2.55
40 - 50	0.63	1.25	1.60	2.12	2.48	3.04	3.34
50 - 60	0.77	1.40	1.72	2.41	2.88	3.39	4.30
60 - 70	0.60	1.44	1.67	2.49	3.24	3.21	5.06
70 - 80	0.92	1.59	2.06	2.93	3.34	3.95	5.62
80 - 90	1.36	2.07	2.50	3.51	3.91	3.60	6.48
90 - 100	3.24	2.88	3.09	4.17	4.54	5.49	7.03
100	71.34	65.68	67.13	63.58	59.71	61.18	55.09

Table 3.13 Conditional on size linear grade distributions measured by image analysis for the -1000+710 microns parent particles with volumetric grade between 97.48 and 100.00 % and their progeny after grinding in the ultrasonic mill

Linear grade %	Conditional on size linear grade distributions. Size range, microns						
%	-106 µ	-180 +106 µ	-250 +180 µ	-355 +250 µ	-500 +355 µ	-710 +500 µ	-1000 +710 µ
0	4.05	2.92	2.27	2.70	2.25	2.70	1.59
0 - 10	0.59	0.47	0.54	0.63	0.51	0.87	0.26
10 - 20	0.36	0.23	0.34	0.37	0.31	0.33	0.41
20 - 30	0.15	0.24	0.33	0.37	0.41	0.42	0.42
30 - 40	0.19	0.28	0.28	0.48	0.47	0.28	0.42
40 - 50	0.17	0.35	0.33	0.59	0.48	0.34	0.64
50 - 60	0.15	0.41	0.36	0.50	0.67	0.59	0.58
60 - 70	0.26	0.55	0.64	0.70	0.89	1.20	0.84
70 - 80	0.42	0.66	0.75	0.68	0.85	1.20	1.35
80 - 90	0.85	0.82	0.98	1.20	1.34	1.52	1.91
90 - 100	3.60	1.96	2.35	2.70	2.78	3.07	6.09
100	89.21	91.11	90.83	89.08	89.04	87.48	85.49

results are shown on Tables 3.14 through 3.20. These data are central for the characterization of the quadrivariate breakage function. It is also the first data set measured experimentally from a real mineralogical system. This may seem surprising in view of the importance of liberation in mineral processing, but the measurement is, by all means, extremely difficult, even when attempted by computer simulation, due to memory limitations, or by breakage of synthetic particles, when the measurement is limited to the actual number of particles available for breakage. The experimental measurement performed here was only possible due to the development of an appropriate stereological correction procedure, the fractionation of fairly large amounts of particles in grade classes across the width of the Andrews-Mika diagram and to the generation of enough progeny particles in each progeny size range by grinding with an ultrasonic mill. This constitutes a massive experimental procedure. Nevertheless, the procedure itself must be retained, so that the characterization of the quadrivariate breakage function can be performed for other mineralogical systems, with different texture.

The data are shown in graphical form in Figures 3.2 through 3.8, and the coefficients representing the linear and volumetric quadrivariate breakage function are shown as three-dimensional bar charts. The graphs also include the parent particles. The comparison of the linear and volumetric distributions show, at first, the fundamental importance of stereological correction, and it is clearly seen from the graphs that the two distributions differ very significantly, specially for particles in intermediate grades. The discrete volumetric grade distributions, representing the discrete quadrivariate breakage function, are the basis for interpreting the associated continuous surface, and a model is

Table 3.14 Conditional on size volumetric grade distributions by stereological correction for the -1000+710 microns parent particles with volumetric grade between 0 and 5.80 % and their progeny after grinding in the ultrasonic mill

Volumetric grade %	Conditional on size volumetric grade distributions. Size range, microns						
%	-106 µ	-180 +106 µ	-250 +180 µ	-355 +250 µ	-500 +355 µ	-710 +500 µ	-1000 +710 µ
0	93.86	94.62	90.53	90.82	92.20	92.73	89.18
0 - 10	4.05	3.81	8.54	8.33	7.21	6.74	10.08
10 - 20	0.00	0.11	0.08	0.18	0.12	0.16	0.25
20 - 30	0.04	0.07	0.00	0.13	0.13	0.11	0.07
30 - 40	0.07	0.08	0.08	0.03	0.01	0.03	0.02
40 - 50	0.05	0.07	0.04	0.06	0.05	0.05	0.07
50 - 60	0.17	0.07	0.05	0.03	0.01	0.03	0.04
60 - 70	0.02	0.03	0.05	0.07	0.07	0.11	0.04
70 - 80	0.00	0.10	0.24	0.05	0.09	0.03	0.09
80 - 90	0.00	0.16	0.04	0.16	0.05	0.00	0.06
90 - 100	0.06	0.30	0.28	0.14	0.08	0.00	0.09
100	1.66	0.59	0.08	0.00	0.00	0.01	0.00

Table 3.15 Conditional on size volumetric grade distributions by stereological correction for the -1000+710 microns parent particles with volumetric grade between 5.80 and 22.47 % and their progeny after grinding in the ultrasonic mill

Volumetric grade %	Conditional on size volumetric grade distributions. Size range, microns						
%	-106 µ	-180 +106 µ	-250 +180 µ	-355 +250 µ	-500 +355 µ	-710 +500 µ	-1000 +710 µ
0	82.87	42.83	34.44	33.98	22.23	34.43	1.04
0 - 10	1.13	45.61	55.09	36.32	42.39	29.70	46.54
10 - 20	4.10	0.00	1.51	23.94	29.81	34.32	50.92
20 - 30	0.52	1.14	0.60	0.00	4.08	0.75	1.01
30 - 40	0.07	0.73	0.76	3.04	0.08	0.15	0.00
40 - 50	0.00	0.79	0.87	0.06	0.03	0.11	0.40
50 - 60	0.03	0.79	0.89	1.09	0.02	0.11	0.01
60 - 70	0.09	0.90	1.43	0.01	0.02	0.11	0.00
70 - 80	0.80	0.86	1.27	0.16	0.08	0.10	0.02
80 - 90	0.00	1.08	1.21	1.32	1.18	0.10	0.00
90 - 100	1.25	4.49	1.78	0.07	0.07	0.10	0.05
100	9.14	0.80	0.16	0.00	0.00	0.00	0.00

Table 3.16 Conditional on size volumetric grade distributions by stereological correction for the -1000+710 microns parent particles with volumetric grade between 22.47 and 39.14 % and their progeny after grinding in the ultrasonic mill

Volumetric grade %	Conditional on size volumetric grade distributions. Size range, microns						
%	-106 µ	-180 +106 µ	-250 +180 µ	-355 +250 µ	-500 +355 µ	-710 +500 µ	-1000 +710 µ
0	46.43	30.72	23.31	5.82	0.00	0.23	0.00
0 - 10	15.90	33.99	25.51	32.99	27.06	0.03	0.11
10 - 20	0.00	1.31	9.46	12.15	19.10	37.17	1.65
20 - 30	2.06	11.21	18.13	26.79	22.10	43.25	38.36
30 - 40	2.57	0.74	1.64	3.92	26.44	17.38	54.55
40 - 50	2.06	0.00	0.00	2.34	1.71	1.39	4.02
50 - 60	0.17	0.10	1.91	2.12	1.78	0.11	0.93
60 - 70	0.17	1.48	1.84	2.03	0.41	0.11	0.22
70 - 80	0.92	3.19	3.06	4.46	0.90	0.12	0.05
80 - 90	1.01	3.01	3.08	0.34	0.18	0.10	0.10
90 - 100	6.25	6.03	8.82	5.87	0.00	0.10	0.00
100	22.47	8.21	3.25	1.16	0.33	0.00	0.00

Table 3.17 Conditional on size volumetric grade distributions by stereological correction for the -1000+710 microns parent particles with volumetric grade between 39.14 and 55.81 % and their progeny after grinding in the ultrasonic mill

Volumetric grade %	Conditional on size volumetric grade distributions. Size range, microns						
%	-106 µ	-180 +106 µ	-250 +180 µ	-355 +250 µ	-500 +355 µ	-710 +500 µ	-1000 +710 µ
0	37.65	16.40	11.41	1.86	0.00	0.00	0.00
0 - 10	6.00	17.62	16.36	16.75	0.00	0.06	0.12
10 - 20	0.11	11.78	13.26	16.94	29.00	0.54	0.28
20 - 30	8.10	6.80	11.57	14.14	19.42	38.52	20.85
30 - 40	1.13	0.00	7.21	6.90	14.27	25.16	2.18
40 - 50	0.19	4.84	2.05	12.13	7.34	11.58	27.26
50 - 60	0.13	0.07	3.03	1.52	10.65	12.65	46.26
60 - 70	0.55	1.83	0.00	2.91	5.65	6.54	2.79
70 - 80	0.86	2.05	0.55	3.12	3.21	4.19	0.03
80 - 90	0.00	9.71	13.14	4.27	4.80	0.76	0.12
90 - 100	12.60	6.99	11.11	19.46	5.46	0.02	0.11
100	32.68	21.91	10.31	0.00	0.10	0.00	0.00

Table 3.18 Conditional on size volumetric grade distributions by stereological correction for the -1000+710 microns parent particles with volumetric grade between 55.81 and 72.48 % and their progeny after grinding in the ultrasonic mill

Volumetric grade %	Conditional on size volumetric grade distributions. Size range, microns						
%	-106 µ	-180 +106 µ	-250 +180 µ	-355 +250 µ	-500 +355 µ	-710 +500 µ	-1000 +710 µ
0	24.21	14.64	0.00	0.00	0.00	0.00	0.00
0 - 10	3.07	7.08	21.42	11.83	0.59	0.12	0.17
10 - 20	4.05	6.96	5.02	7.95	5.71	0.00	2.38
20 - 30	2.54	1.81	2.23	9.34	19.40	19.23	0.10
30 - 40	1.01	0.51	2.50	5.29	5.44	14.85	8.52
40 - 50	0.56	0.00	1.93	3.53	5.98	23.76	2.77
50 - 60	0.71	8.61	2.64	2.67	5.29	7.44	21.31
60 - 70	0.44	0.25	9.81	5.20	14.59	10.71	27.50
70 - 80	1.62	0.21	5.79	10.96	4.35	12.71	19.38
80 - 90	8.85	12.20	5.02	13.58	17.61	10.80	15.95
90 - 100	6.25	19.65	28.34	20.73	20.23	0.39	1.91
100	46.69	28.08	15.30	8.92	0.81	0.00	0.01

Table 3.19 Conditional on size volumetric grade distributions by stereological correction for the -1000+710 microns parent particles with volumetric grade between 72.48 and 97.48 % and their progeny after grinding in the ultrasonic mill

Volumetric grade %	Conditional on size volumetric grade distributions. Size range, microns						
%	-106 µ	-180 +106 µ	-250 +180 µ	-355 +250 µ	-500 +355 µ	-710 +500 µ	-1000 +710 µ
0	11.13	0.00	0.00	0.00	0.00	0.00	0.00
0 - 10	0.00	12.51	1.56	0.00	0.73	0.11	0.06
10 - 20	6.54	4.33	5.76	8.25	3.52	0.84	0.10
20 - 30	0.58	3.04	11.04	2.62	5.58	1.05	0.10
30 - 40	2.68	0.74	0.39	1.94	2.69	2.80	0.10
40 - 50	0.66	0.16	0.00	2.28	0.53	1.95	0.16
50 - 60	0.63	1.04	2.62	0.24	3.61	1.92	0.10
60 - 70	0.27	1.07	1.24	5.17	1.78	14.73	5.17
70 - 80	0.42	8.92	4.66	3.44	17.82	12.15	20.59
80 - 90	3.67	10.01	12.18	22.08	16.03	13.76	38.21
90 - 100	14.40	8.58	11.62	29.12	25.19	27.44	25.99
100	58.91	49.60	48.92	24.87	22.54	23.25	9.42

Table 3.20 Conditional on size volumetric grade distributions by stereological correction for the -1000+710 microns parent particles with volumetric grade between 97.48 and 100.00 % and their progeny after grinding in the ultrasonic mill

Volumetric grade %	Conditional on size volumetric grade distributions. Size range, microns						
%	-106 µ	-180 +106 µ	-250 +180 µ	-355 +250 µ	-500 +355 µ	-710 +500 µ	-1000 +710 µ
0	1.32	1.14	0.01	0.02	0.51	0.00	0.28
0 - 10	0.00	0.00	1.29	0.93	0.00	0.31	0.00
10 - 20	2.19	1.20	0.43	0.29	0.53	1.87	0.10
20 - 30	2.09	0.49	0.55	1.47	0.45	0.16	0.10
30 - 40	0.13	0.52	0.20	0.28	0.44	0.08	0.10
40 - 50	0.11	0.11	0.00	0.81	0.44	0.20	0.10
50 - 60	0.10	0.11	0.20	0.11	0.64	2.03	0.05
60 - 70	0.10	0.29	0.00	0.83	1.01	0.97	0.02
70 - 80	0.10	0.95	0.01	0.73	1.70	1.04	0.10
80 - 90	1.06	4.58	6.15	3.18	1.07	0.55	6.66
90 - 100	5.13	7.81	13.47	15.38	22.57	25.32	34.02
100	87.66	82.80	77.68	75.98	70.63	67.47	57.96

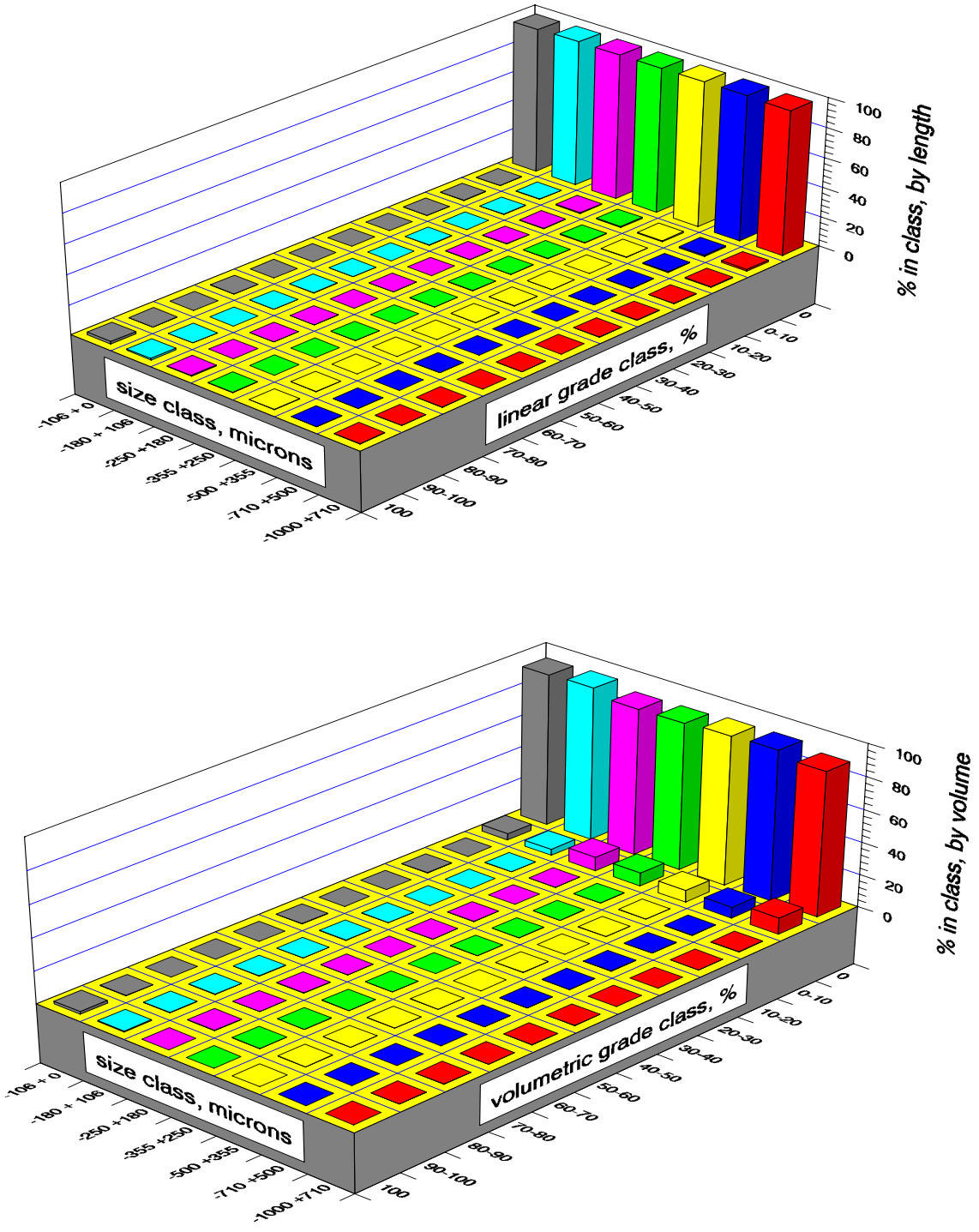

Figure 3.2 The measured, conditional on size, linear quadrivariate breakage function for the -2.9 g/cc particles (top) and the corresponding volumetric breakage function after stereological correction

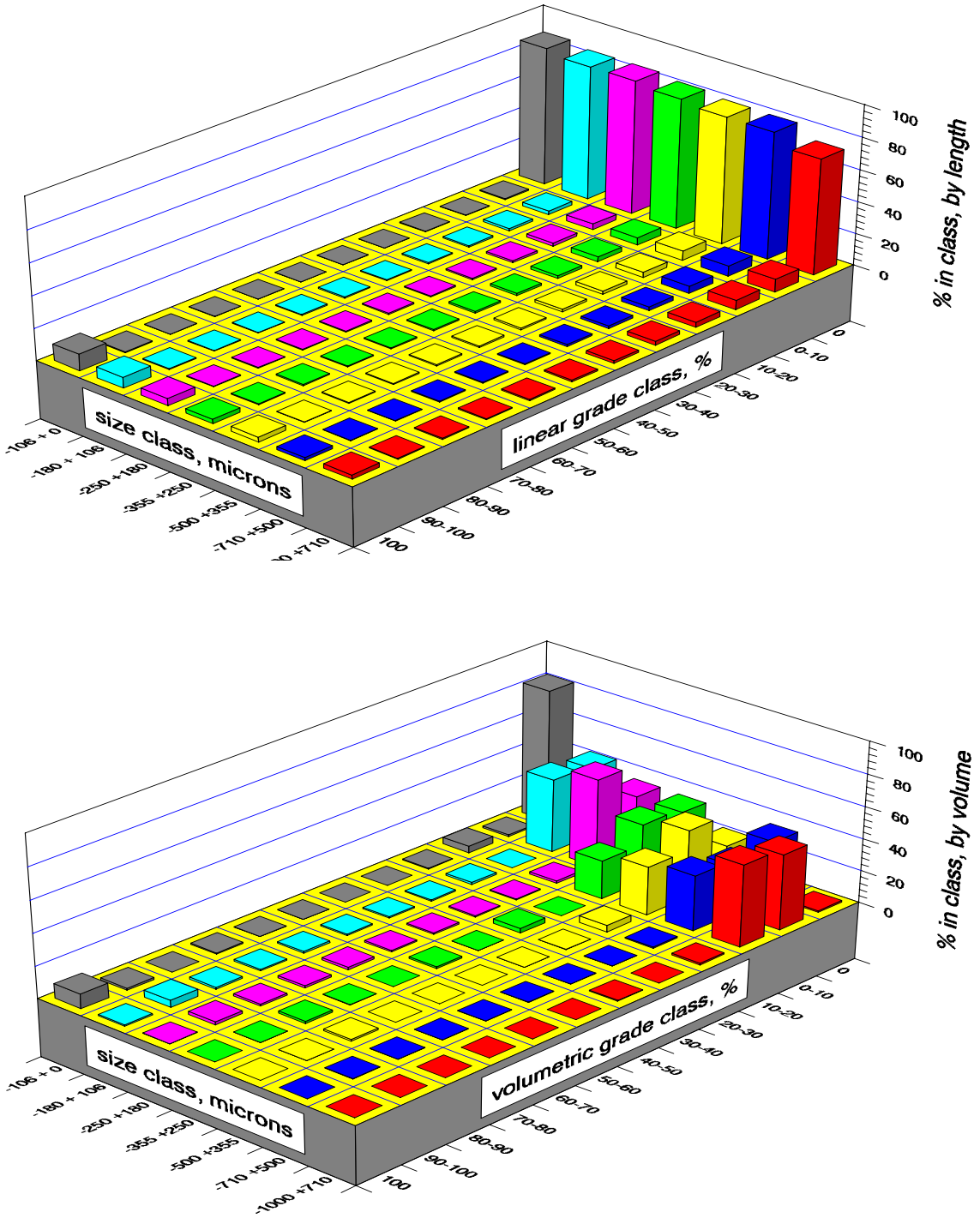

Figure 3.3 The measured, conditional on size, linear quadrivariate breakage function for the -3.1+2.9 g/cc particles (top) and the corresponding volumetric breakage function after stereological correction

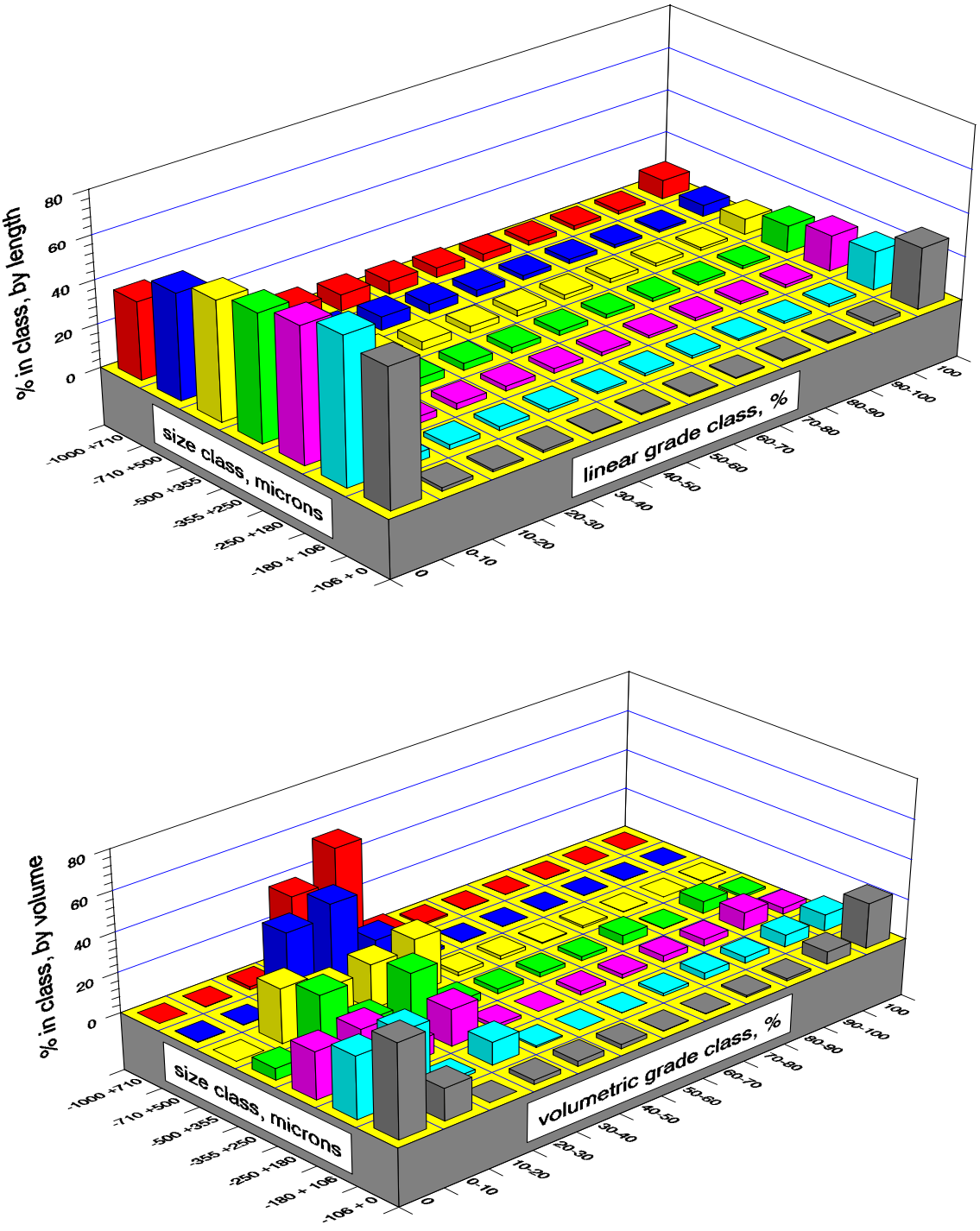

Figure 3.4 The measured, conditional on size, linear quadrivariate breakage function for the -3.3+3.1 g/cc particles (top) and the corresponding volumetric breakage function after stereological correction

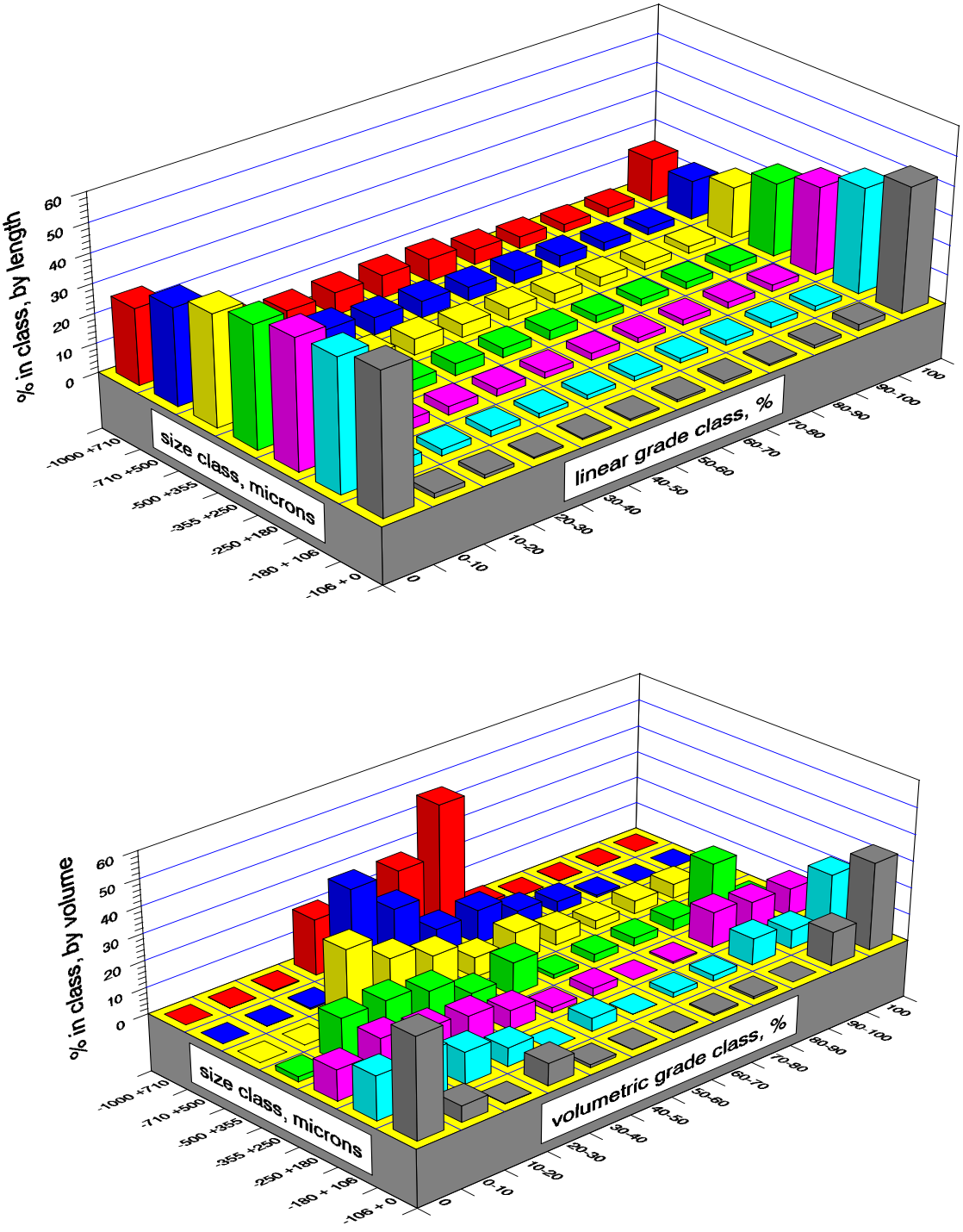

Figure 3.5 The measured, conditional on size, linear quadrivariate breakage function for the -3.5+3.3 g/cc particles (top) and the corresponding volumetric breakage function after stereological correction

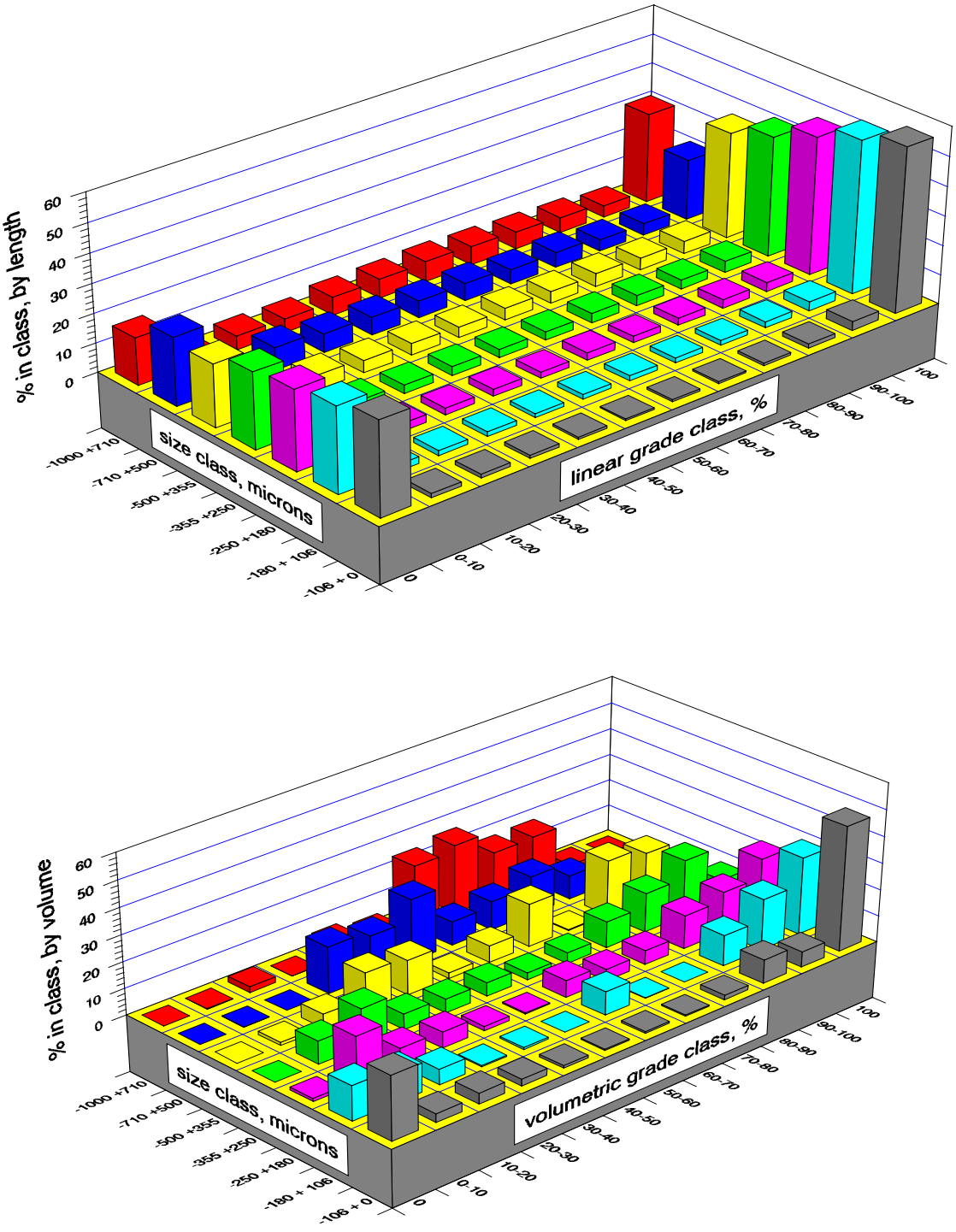

Figure 3.6 The measured, conditional on size, linear quadrivariate breakage function for the -3.7+3.5 g/cc particles (top) and the corresponding volumetric breakage function after stereological correction

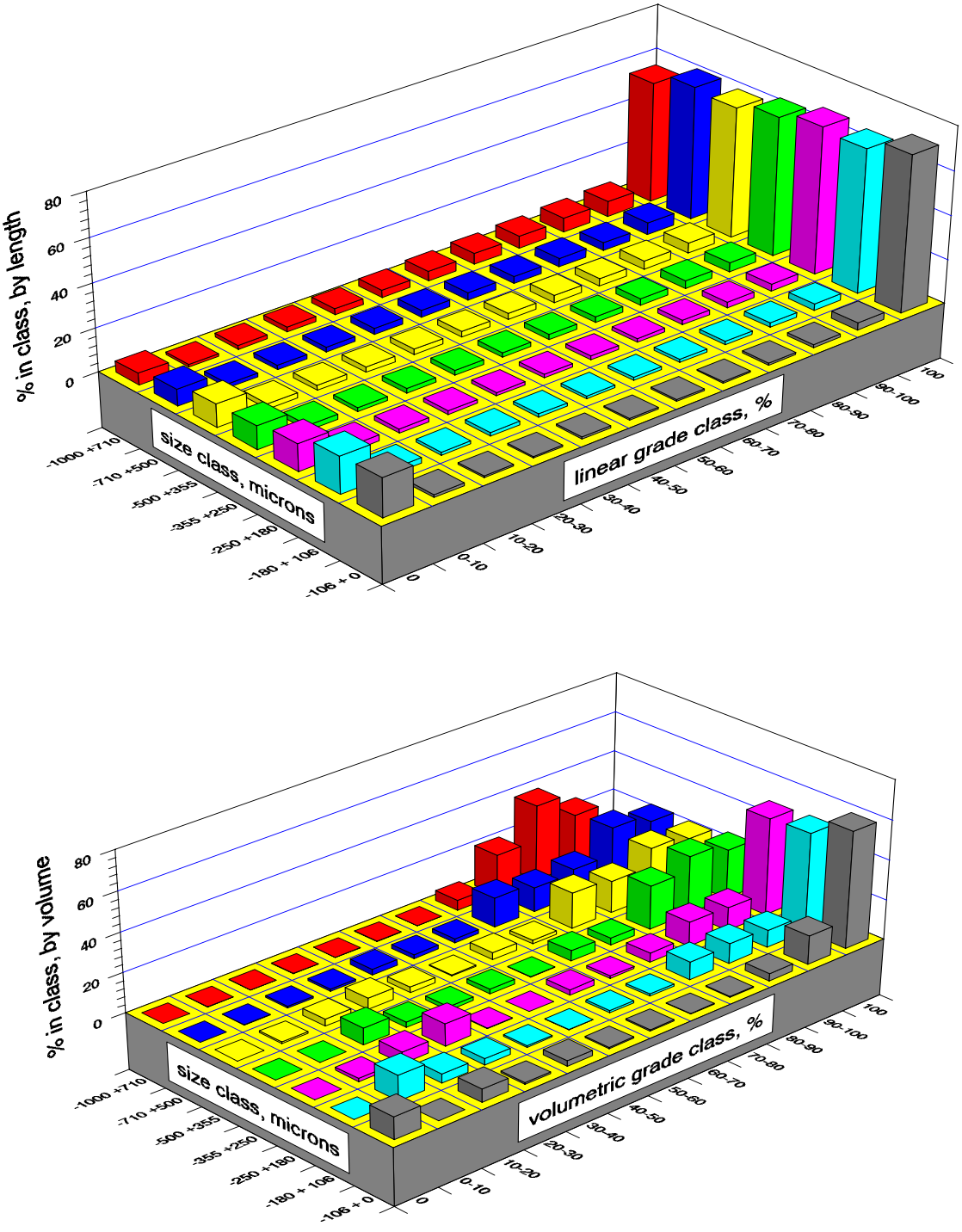

Figure 3.7 The measured, conditional on size, linear quadrivariate breakage function for the -4.0+3.7 g/cc particles (top) and the corresponding volumetric breakage function after stereological correction

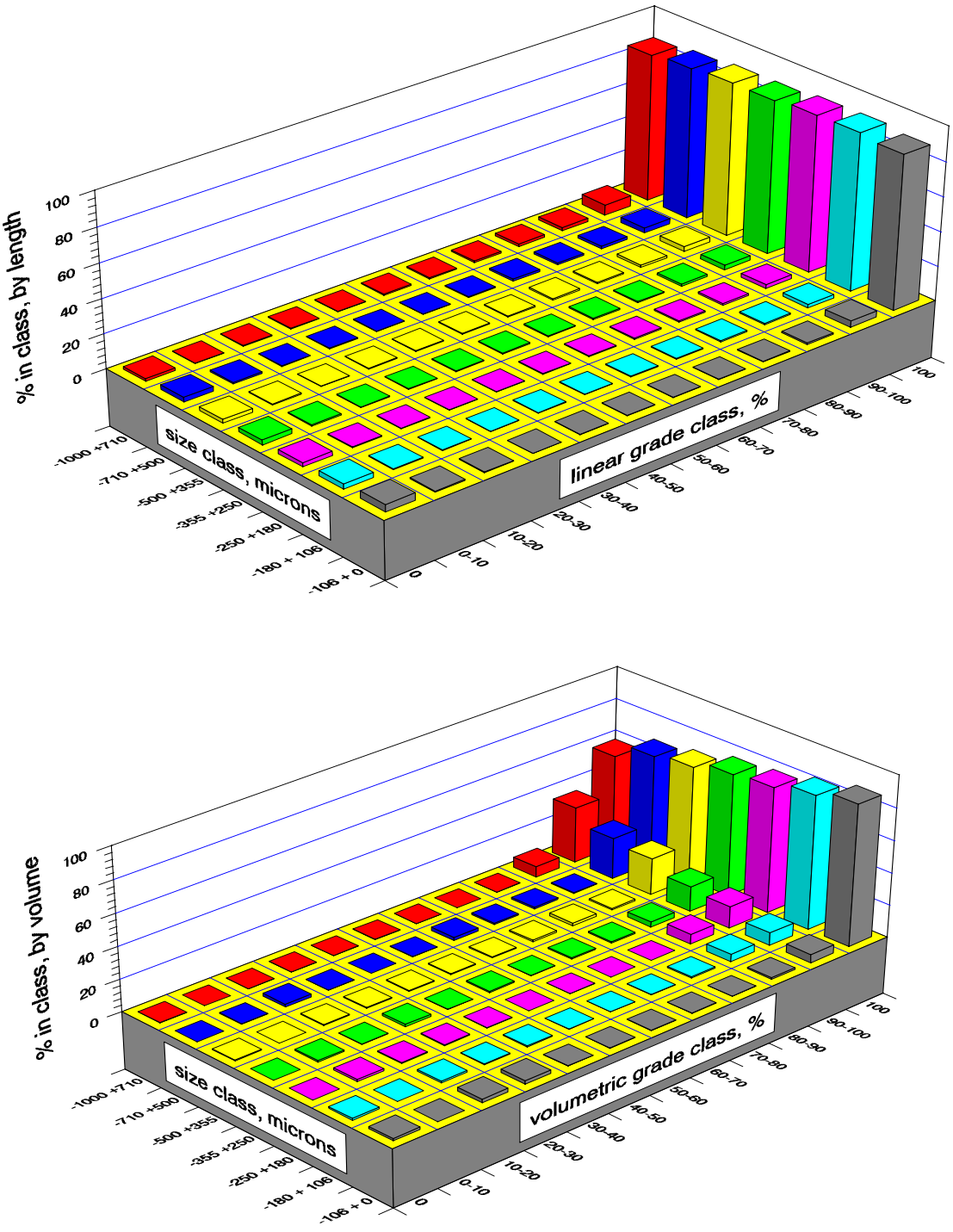

Figure 3.8 The measured, conditional on size, linear quadrivariate breakage function for the +4.0 g/cc particles (top) and the corresponding volumetric breakage function after stereological correction

proposed in the following sections in this chapter. The domain of the distributions includes the accessible region in the Andrews-Mika diagram. It is possible to identify there the fuzzy bounds, originating at the parent particles. The critical sizes, bellow which liberation starts, are also seen fairly clearly, for the distributions originating from particles in intermediate grades. More importantly, the internal structure of the accessible region is exposed, and the process by which the particles transfer from intermediate grade classes to low and high grade classes as size is reduced can be observed. A very clear correlation between the disappearance of the relative fractions of particles in the intermediate grade classes and the rate by which liberated particles appear with size reduction is also shown in the three-dimensional diagrams. Thus, every aspect of the liberation process in the accessible region is well represented, and the data are consistent enough to model the surface that represent the continuous quadrivariate breakage function originated from monosize, monograde particles.

Measurement of the Geometrical Texture Parameter

Qualitative description of mineralogical texture is probably as old as mineralogy itself. This is a very well-established science, and is very effective in identifying the nature, genesis and evolution of many mineralogical systems. Although important, the qualitative assessment of texture cannot be brought into the context of texture modelling, because real mineralogical particles are irregular and the association of the different phases in the system is complex. This requires at least one quantitative parameter that is associated with the geometrical properties of the texture. In contrast, precise quantitative assessment of the geometrical properties of texture is probably as recent as

effective image analysis. High resolution images from cross sections of particles and good phase discrimination are required because of the fractal nature of the particles hull and of the grain boundaries.

Modern image analysis permits the fairly precise estimate of surface area per unit volume from chord lengths measured on a large number of particle cross sections. The average surface area per unit volume S_V of any irregular three-dimensional feature is calculated from the average intercept length μ through the cross-sections of the feature using the following stereological formula [28]:

$$S_V = \frac{4}{\mu} \tag{3.24}$$

The measurement of the chord length distribution generated by the narrow size, narrow grade samples of the Dolomite-Sphalerite particles is illustrated in Figure 3.9. The particle outlines shown in the figure were obtained from a back-scattered electron image of particles in the range 3.3 to 3.5 g/cc, shown in Figure 2.4. The chord lengths are measured across the entire particle cross-sections, and eliminating the chords that intercept the measuring frame. After frame correction, the average intercept length associated with the particles μ^P is calculated. The calculation of the surface area per unit volume of the particles, S_V^P, is straight forward, using equation 3.24. The measurement of the average intercept length μ^A corresponding to the Dolomite phase is illustrated in Figure 3.10, for the same image. Only the chord lengths on the Dolomite phase are taken into account. Similarly, in Figure 3.11, the measurement of μ^B, for the Sphalerite, is illustrated. Again, equation 3.24 is used for calculating the surface area per unit volume S_V^A of the Dolomite

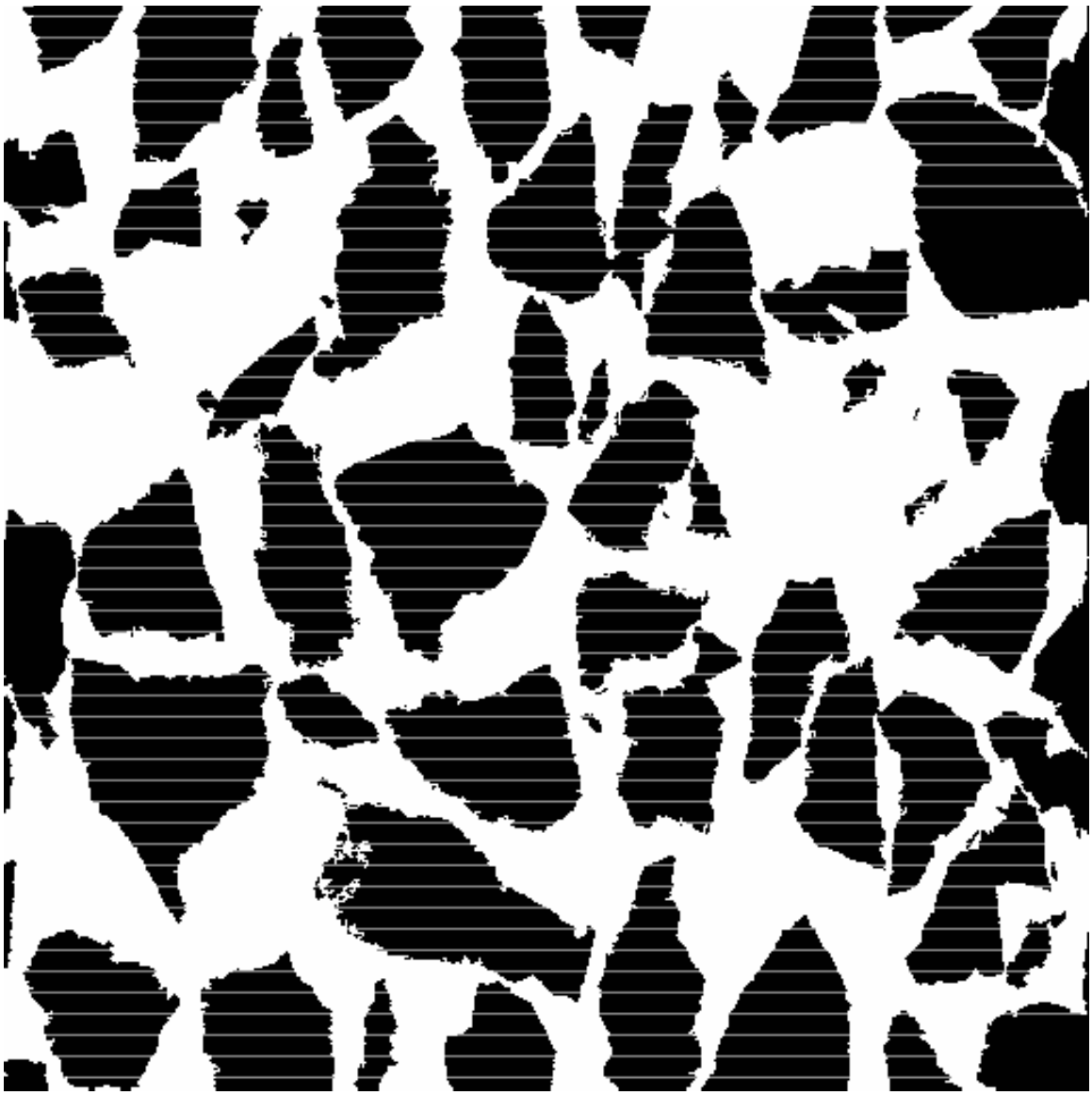

Figure 3.9 The measurement of the chord length distribution in a cross-section of Dolomite-Sphalerite particles. The original back-scattered electron image is shown in Figure 2.4

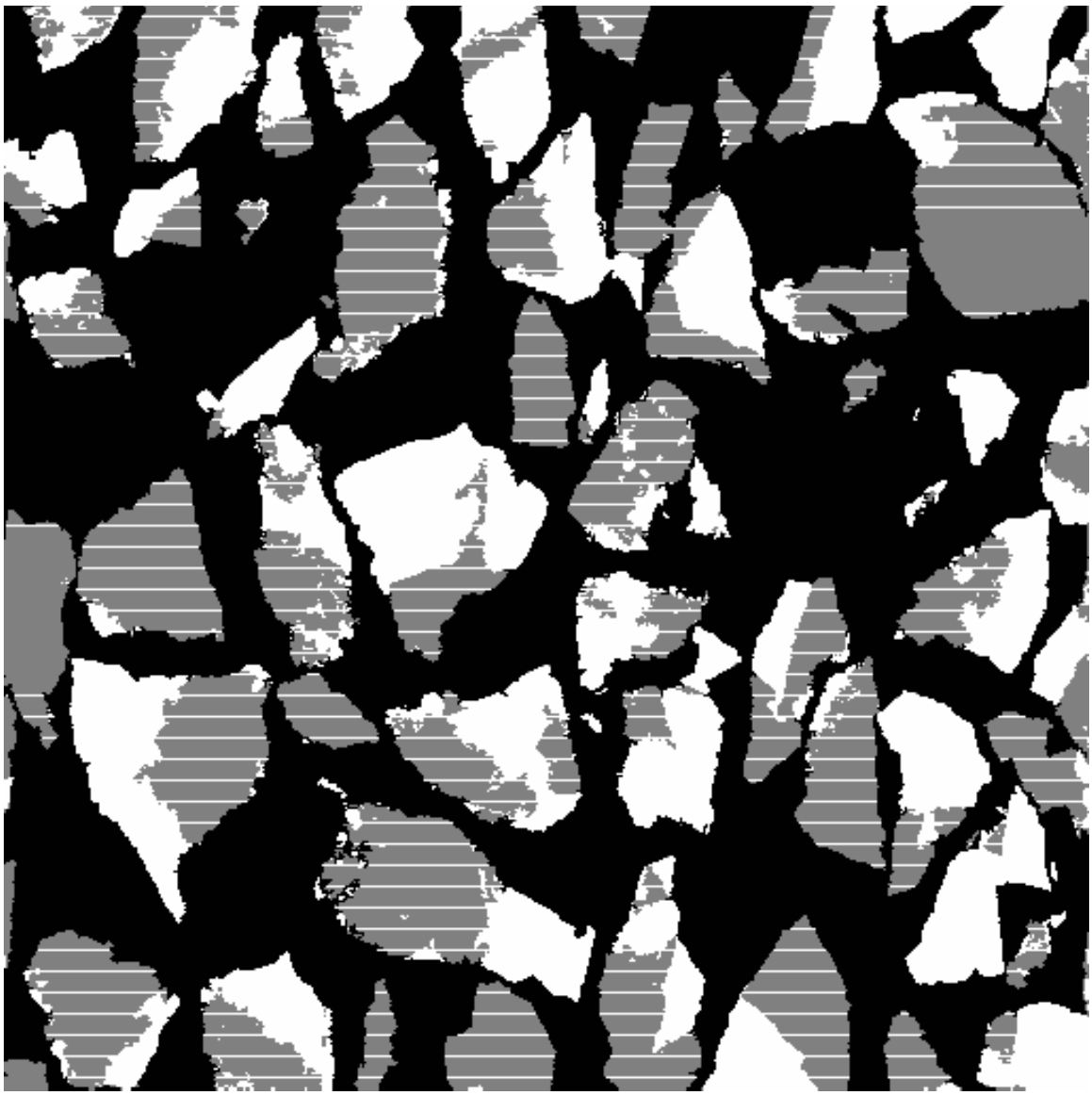

Figure 3.10 The measurement of the chord length distribution generated by the Dolomite in a cross-section of Dolomite-Sphalerite particles. The original back-scattered electron image is shown in Figure 2.4

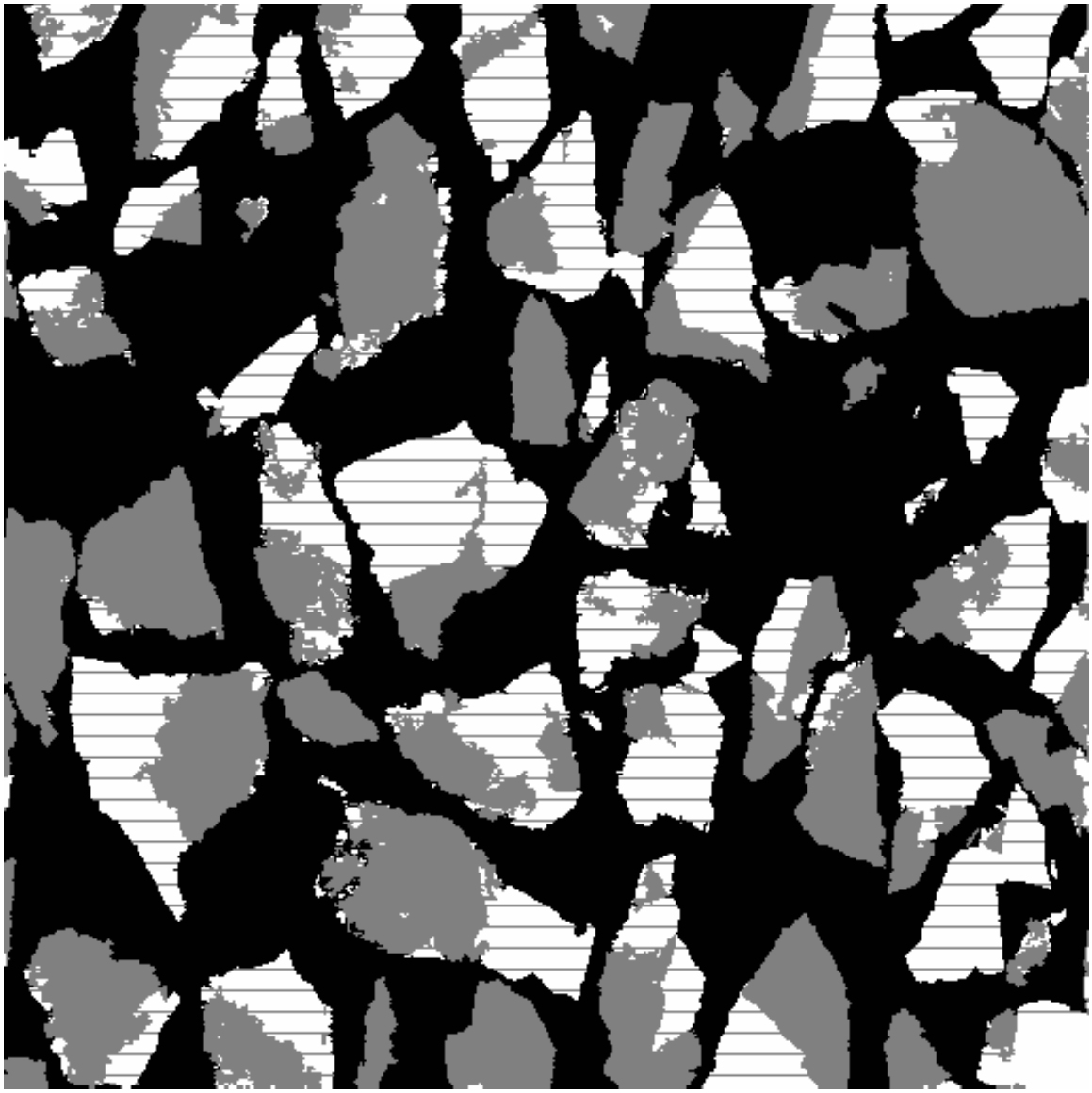

Figure 3.11 The measurement of the chord length distribution generated by the Sphalerite in a cross-section of Dolomite-Sphalerite particles. The original back-scattered electron image is shown in Figure 2.4

and S_V^B of Sphalerite.

The measurement described above was carried out for the seven sets of images acquired from the narrow size, narrow grade parent particle samples. The interphase area per unit volume of phase is calculated by balancing the surface areas of the phases and that of the particles, taking in account the volumetric abundance of each phase. This is shown in equations 3.25, for the Dolomite,

$$S_V^{AB} = \frac{(1/2)}{(1-g_v)} \left((1-g_v)\, S_V^A + g_v\, S_V^B - S_V^P\right) \tag{3.25}$$

and 3.26 for the Sphalerite,

$$S_V^{BA} = \frac{(1/2)}{g_v} \left((1-g_v)\, S_V^A + g_v\, S_V^B - S_V^P\right) \tag{3.26}$$

By substituting equations 3.25 and 3.26 into equations 3.11 and 3.12, it becomes clear that $\phi_A = \phi_B$. Thus equations 3.11 and 3.12 can be rewritten as

$$d_p\, S_V^{AB} = \phi\, g_v \tag{3.27}$$

and

$$d_p\, S_V^{BA} = \phi\, (1-g_v) \tag{3.28}$$

where ϕ is the geometrical textural parameter of the ore. For any binary system, a single geometrical texture parameter is enough to characterize the interface between the two phases in the ore. The measured surface area per unit volume for the seven parent particle samples are shown in Table 3.21, along with the calculated values of interphase area per unit volume of phase. The values of the groups $d_p\, S_V^{ABij}$ and $d_p\, S_V^{BAij}$, where

Table 3.21 Average intercept lengths and surface area per unit volume for the particles and phases *A* and *B*, and interphase area per unit volume of phase, for the seven narrow size, narrow grade parent particle samples

Property	-1000+710 microns parent particles. Density range, g/cc						
	-2.9	-3.1 +2.9	-3.3 +3.1	-3.5 +3.3	-3.7 +3.5	-4.0 +3.7	+4.0
$\overline{g_v^{ij}}$, %	0.73	9.47	27.27	40.49	58.00	79.38	94.64
μ^{Aij}, microns	379.99	310.43	229.79	194.29	168.47	127.04	97.75
μ^{Bij}, microns	86.32	93.83	117.87	141.63	189.39	253.49	358.79
μ^{Pij}, microns	385.45	370.80	367.25	344.83	352.93	355.89	392.01
S_V^{Aij}, 1/micron	1.0527 x10^{-2}	1.2885 x10^{-2}	1.7407 x10^{-2}	2.0588 x10^{-2}	2.3743 x10^{-2}	3.1485 x10^{-2}	4.0919 x10^{-2}
S_V^{Bij}, 1/micron	4.6342 x10^{-2}	4.2631 x10^{-2}	3.3936 x10^{-2}	2.8243 x10^{-2}	2.1121 x10^{-2}	1.5780 x10^{-2}	1.1148 x10^{-2}
S_V^{Pij}, 1/micron	1.0377 x10^{-2}	1.0787 x10^{-2}	1.0892 x10^{-2}	1.1600 x10^{-2}	1.1334 x10^{-2}	1.1239 x10^{-2}	1.0204 x10^{-2}
S_V^{ABij}, 1/micron	2.1114 x10^{-4}	2.7148 x10^{-3}	7.7372 x10^{-3}	1.0107 x10^{-2}	1.3000 x10^{-2}	1.8955 x10^{-2}	2.4106 x10^{-2}
S_V^{BAij}, 1/micron	2.7813 x10^{-2}	2.5946 x10^{-2}	1.9902 x10^{-2}	1.4984 x10^{-2}	9.3621 x10^{-3}	4.8722 x10^{-3}	1.3014 x10^{-3}

$d_p = (D'^1 + D'^0)/2$ = 855 microns, are plotted against the average grade of phase, and these yield a straight line as shown in Figure 3.12. Linear regression with equations 3.15 and 3.16 give ϕ = 22.05, completing the measurement of the geometrical textural parameter.

Modelling the First Moment of the Conditional

Quadrivariate Breakage Function

The experimental results obtained from the Dolomite-Sphalerite ore suggests that the average grade in the progeny varies with progeny size. It is observed that for progeny sizes approaching that of the parent, the volumetric fraction of Sphalerite is considerably smaller than that in the parent particles while for progeny at sizes comparatively smaller, the average grade is higher than that of the parent particles. This indicates that the Sphalerite concentrates in the smaller progeny sizes, probably by a higher rate of chipping and abrasion of the larger grains due to its higher friability. A phenomenological description of such process may be obtained by a detailed study of the fracture characteristics of the phases involved, and how these interact in composite particles. However, such study may also be extensive, and here a simpler, completely empirical approach is used to first touch base with the problem.

King [9], in the first attempt ever made to model the internal structure of the accessible region, has assumed that the first moment of the conditional quadrivariate breakage function is invariant with progeny size,

$$\overline{g_v}\left(D; g_v', D'\right) = g_v' \tag{3.29}$$

This is true, or at least a good approximation, when the phases have more or less the

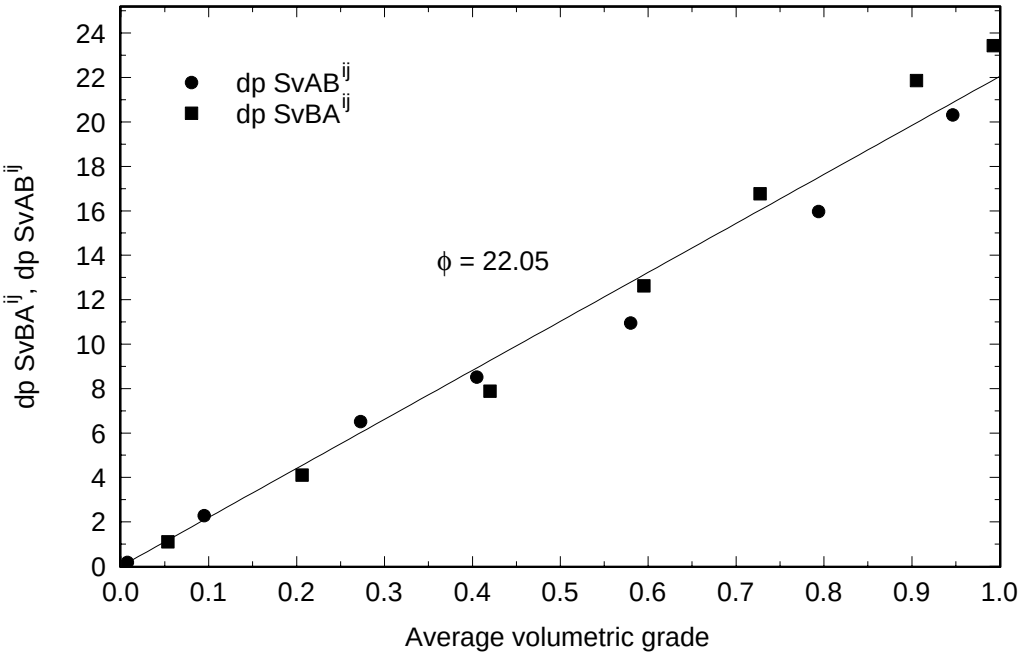

Figure 3.12 Calculation of the geometrical texture parameter for the Dolomite-Sphalerite ore from measured values of interphase area per unit volume of phase

same brittleness. Also, this would not be a very bad assumption for the Dolomite-Sphalerite ore, since the variation of average progeny grade with size is not very dramatic. However, a knowledge of the first moment is important when modelling the internal structure of the accessible region, and a more detailed description of $\overline{g_v}(D;g_V',D')$ can be obtained by establishing a functional form, continuous in the progeny size domain, with a minimum number of parameters, that can describe the variation of progeny grade with progeny size, for all combinations of parent sizes and grades. This is then introduced in equations 3.22 and 3.23 for discretization. The calculated fractions $\overline{g_v^{lij}}$ can then be compared with the corresponding measured fractions, thus allowing for parameter optimization.

The first step in calculating the discrete fractions is to carry out the integration in equation 3.22. This requires the knowledge of the size distributions in the progeny, represented by $f_v(D;g_v',D')$. Unfortunately, size distributions can rarely be described in closed form. Furthermore, the set of size distributions in equation 3.22 was generated by repeated grinding of particles in the parent size range until all particles reported to a size range in the progeny. The resulting discrete distributions are shown in Table 3.5, and these fractions are the only information available for describing $f_v(D;g_v',D')$. The relationship between the discrete fractions and the continuous fractions is best described in terms of the corresponding cumulative distributions, as shown in equation 3.30.

$$F_v^{lij} = \int_{D^{i-1}}^{D^{i}} \int_{g_v^{j-1}}^{g_v^{j}} F_v(D;g_v',D')\, dg_v'\, dD' \qquad (3.30)$$

The use of cumulative distributions eliminates the error that is made when discretizing

in the progeny size domain. Now, because no functional form is available for $F_v(D;g_v',D')$, the integration in equation 3.30 cannot be carried out. The best approximation is to assume that the cumulative size distribution is invariant inside the parent narrow size, narrow grade range, i.e.,

$$F_v^{lij} = F_v(D;g_v',D') \qquad \begin{matrix}[g_v'^{j-1} < g_v' < g_v'^{j}] \\ [D'^{i-1} < D' < D'^{i}]\end{matrix} \tag{3.31}$$

The assumption in equation 3.31 is expected to introduce a small discretization error in the integration of equation 3.22. Nevertheless, this approach is certainly preferable then assuming that $\overline{g_v^l}(g_v',D') = \overline{g_v}(d_p;g_v',D')$, which is a classic example of assumptions commonly made in mineral processing calculations. The cumulative distributions F_v^{lij} can be extrapolated without much error using a splines scheme, and this is shown in Figure 3.13, completing the modeling of $f_v(D;g_v',D')$. The second step on integrating equation 3.22 is to establish a functional form for $\overline{g_v}(D;g_v',D')$. The corresponding discrete fractions $\overline{g_v^{lij}}$, as measured by image analysis, shown in Table 3.2, can be plotted against a representative size for each narrow size range in the progeny. This is shown in Figure 3.14, together with the calculated volumetric grade in the parent $\overline{g_v^{ij}}$, represented by a horizontal dotted line across the progeny size domain. In this figure, the properties of the average progeny grade function can be identified. First, the average progeny grade must approach parent grade as progeny size approaches parent size. A minimum average progeny grade is reached at a progeny size just bellow parent size and then progeny grade increases monotonically as progeny size decreases, crossing the dotted line representing parent grade at more or less the same size for all parent grades. At least one crossing

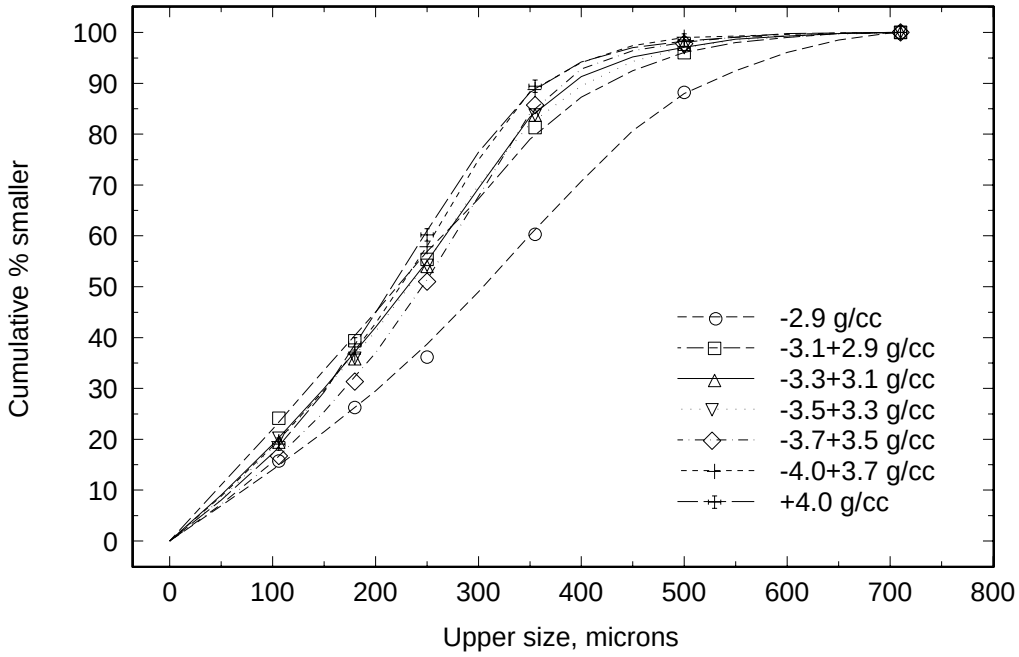

Figure 3.13 The measured volume-weighted size distributions in the progeny and the splines extrapolations representing the corresponding continuous cumulative distributions

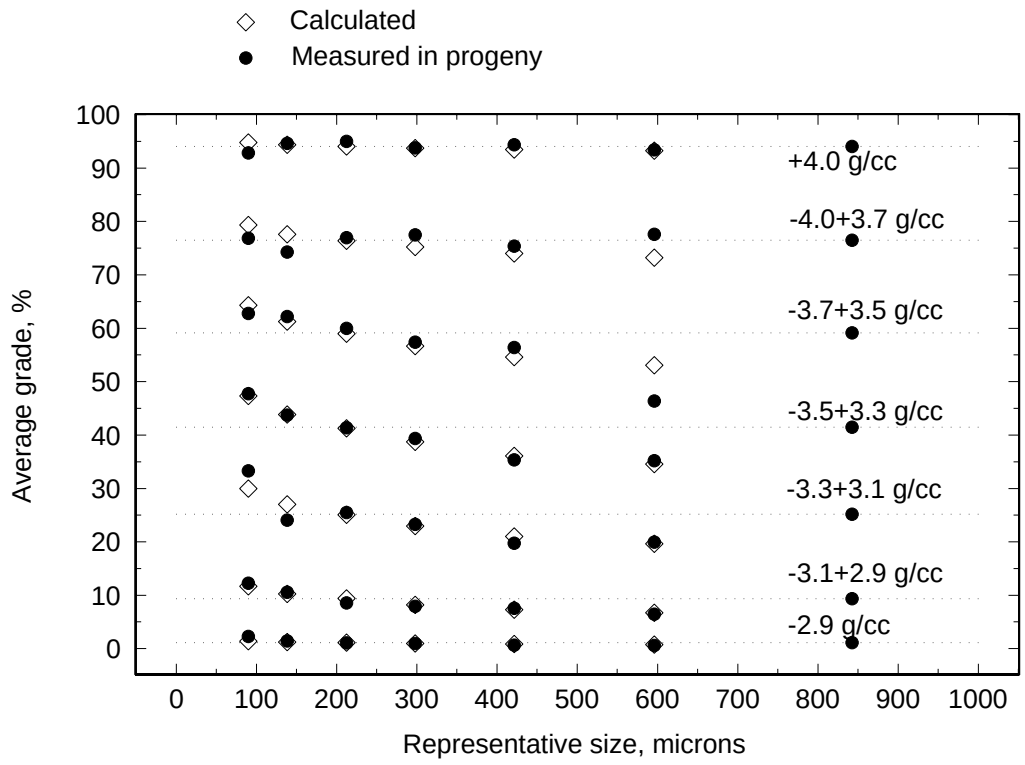

Figure 3.14 Measured average volumetric grade in the parent and progeny particles and the calculated average volumetric grade in the progeny

point in the progeny size domain must exist, so that phase volume can be conserved. This can be described by a $x \log(x)$ type of function. Three arbitrary parameters are required; the first associated with the location of the minimum grade, Δ^{min}, the second associated with the minimum average progeny grade Γ^{min}, at $D = \Delta^{min}$, and the third associated with the location of the crossing point in the progeny size domain, Δ^0. The following functional form is proposed:

$$\overline{g_v}(D; g_v', D') = g_v' + \alpha_1 \, u^{\alpha_2} \log(u) \tag{3.32}$$

where u is a domain transformation operating on the progeny size,

$$u = \frac{\left(1 - \frac{D}{D'}\right)}{(1 - \Delta^0)} \tag{3.33}$$

and the coefficients α_1 and α_2 are defined in terms of Δ^{min} and Γ^{min} as follows:

$$\alpha_1 = \frac{(g_v^{min} - g_v')}{u^{min\,\alpha_2} \log(u^{min})} \tag{3.34}$$

and

$$\alpha_2 = \frac{-1}{\log(u^{min})} \tag{3.35}$$

with the auxiliary variables g_v^{min} and u^{min} defined as:

$$g_v^{min} = g_v' \, (\, (1 - \Gamma^{min}) \, g_v' + \Gamma^{min} \,) \tag{3.36}$$

and

$$u^{\min} = \frac{(1 - \Delta^{\min})}{(1 - \Delta^{0})} \tag{3.37}$$

The functional form in equation 3.32 satisfies all the requirements to model the average grade in the progeny, including the case when the phases are equally brittle, when equation 3.32 is reduced to equation 3.29, ($\alpha_1 = 0$), and ores in which phase *A* is the more brittle phase ($\alpha_1 > 0$), thus describing a maximum grade, rather then minimum, between the parent size and the crossing point in the progeny size domain. A constraint must be imposed to the set of parameters to ensure that the average grade at all progeny sizes does not violate the limiting boundary of the accessible region for the conditional quadrivariate breakage function. A detailed discussion on the location of this limiting boundary is given in the next section, where the model of the quadrivariate breakage function is described.

The integration of equation 3.22 was carried out numerically, using an integration algorithm based on Simpson's rule [29], and required fractional accuracy of 10^{-5}. This completes the calculation of the fractions $\overline{g_v^l}(g_v', D')$.

The double integration in equation 3.23 was carried out using a more elementary approach, because some precision must be sacrificed for feasible computing time. The integration was carried out by discretizing equation 3.23 as follows:

$$\overline{g_v^{lij}} = \sum_{m=1}^{M} \sum_{n=1}^{N} \overline{g_v^l}\left(g_v'^m, D'^n\right) f_v\left(g_v'^m, D'^n\right) \tag{3.38}$$

where *M* is the number of parent grades and *N* is the number of parent sizes defining *MxN* points in the parent particle domain at which the discrete fractions in the integral

were evaluated. Naturally, better fractional accuracy is obtained when the number of points in the parent size and grade domain *MxN* is larger, and when the appropriate location of these points is chosen. The parent particle distribution $f_v(g_v', D')$ was assumed to be uniform with respect to parent size, once all parent particles are contained in one narrow size interval, and distributed in the parent grade domain according to the stereological correction results shown in Tables 2.6 through 2.12. The actual location of the *MxN* points was tailored according to each parent particle distribution in the tables. The model parameters were estimated by minimizing the sum of squares of residuals between the calculated and the measured $\overline{g_v^{lij}}$ fractions, using the Rosenbrock Hillclimb procedure [25], which does not require derivatives. The optimization procedure was carried out simultaneously for the seven sets of parent particles and the corresponding distribution of average grades in the progeny, so as to determine a unique set of parameters that is descriptive of the distribution $\overline{g_v}(D; g_v', D')$ for the Dolomite- Sphalerite ore, and satisfy the limiting boundary of the accessible region constraint. Minimum sum of squares of residuals was obtained for $\Delta^0 = 0.247331$, $\Delta^{\min} = 0.703127$ and $\Gamma^{\min} = 0.651301$. The calculated fractions $\overline{g_v^{lij}}$ from integral equations 3.22 and 3.23 and this set of parameters are compared with the corresponding measured fractions in Figure 3.14. The *fit* is close to ideal, if not remarkable, when considering the enormous complexity of both making the experimental measurement and carrying out the necessary calculations. The three arbitrary parameters in the model define a surface with domain of parent grade and the ratio between progeny and parent size, and range that can be represented as the ratio between progeny and parent grades. This is shown in Figure 3.15

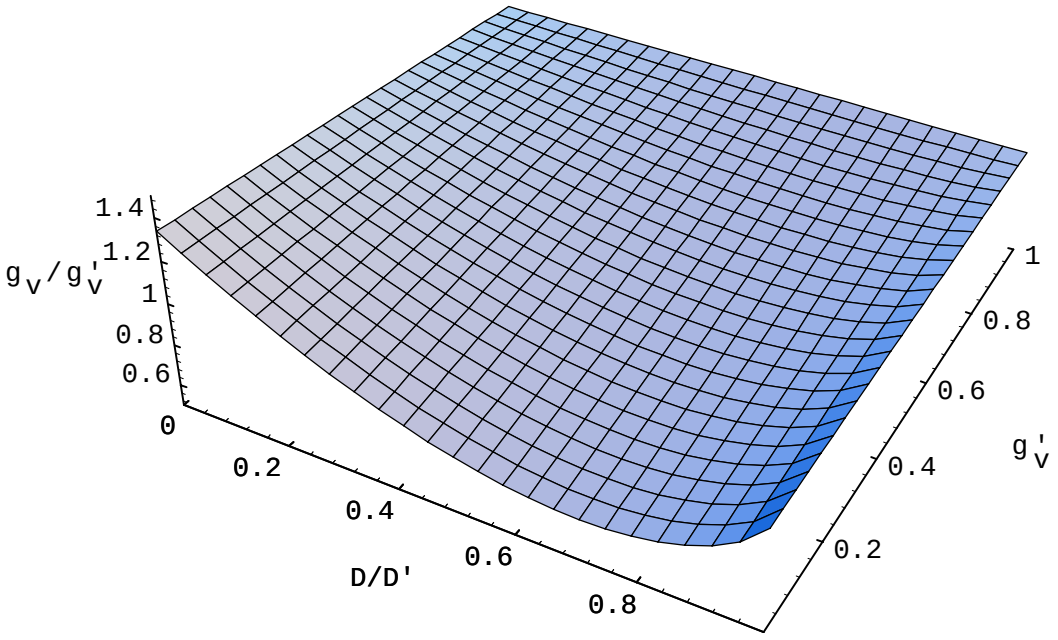

Figure 3.15 The normalized average volumetric grade surface associated with the Dolomite-Sphalerite mineralogical system

for the Dolomite-Sphalerite ore. The surface in the figure can be used to describe the variation of the first moment of the conditional quadrivariate breakage function with progeny size for any monosize, monograde parent particle, provided that the distribution is normalizable with respect to parent size, i.e.,

$$\overline{g_v}\left(D;g_v',D'\right) = \overline{g_v}\left(D/D';g_v'\right) \tag{3.39}$$

for all D'.

Modelling the Conditional Quadrivariate Breakage Function

The development of the model described here is based on the measured fractions b_v^{klij} shown in Tables 3.14 through 3.20. Because the function $b_v\left(g_v \mid D;g_v',D'\right)$ is on four independent variables, its modelling is complex. The first step is to define the boundaries of the accessible region, as shown in solid lines in Figure 3.1, that is associated with any point $\left(g_v',D'\right)$ in the parent grade/size domain. The location of the boundaries of the accessible region is a strong function of the texture of the ore. For intricate, complex textures, which are usually referred to as fine textures, the area representing the accessible region is small when compared to the limiting boundary of the accessible region which is imposed by phase volume constraints, shown in dotted lines in Figure 3.1. When the texture of the ore is plain and simple, normally called a coarse texture, the boundaries of the accessible region are located closer to the limiting boundaries. The limiting boundaries, also called Andrews-Mika boundaries, are independent of the texture of the ore, and are only based on conservation of phase-volume. Two functions are required to describe the limiting boundaries, one with respect to phase *A*, corresponding to the upper,

left hand side of the accessible region and lower, right-hand side of the region R', and the other with respect to phase *B*, corresponding to the upper, right-hand side of the accessible region and lower, left-hand side of the region R'. The approximate location of the limiting boundaries is derived by considering an arbitrary particle at point (g_v', D') in the parent grade/size domain. The volume V' of the parent particle is defined as

$$V' = \beta' D'^3 \tag{3.40}$$

where β' is the shape factor associated with the particle. The volume of phase *A*, V_A, and phase *B*, V_B, contained in this particle are given by

$$V_A = \beta' D'^3 (1 - g_v') \tag{3.41}$$

and

$$V_B = \beta' D'^3 g_v' \tag{3.42}$$

Similarly, the volume of phases *A* and *B* can be calculated for any progeny located at point (g_v, D) in the progeny size/grade domain, i.e.,

$$V_A = \beta D^3 (1 - g_v) \tag{3.43}$$

and

$$V_B = \beta D^3 g_v \tag{3.44}$$

where β is the shape factor associated with the progeny particle. Therefore, for any progeny originated at point (g_v', D') the following inequalities must hold so that the conservation of phase constraints are satisfied:

$$\beta' \, D'^{3} \, (1 - g_v') \geq \beta \, D^{3} \, (1 - g_v) \tag{3.45}$$

for phase *A* and

$$\beta' \, D'^{3} \, g_v' \geq \beta \, D^{3} \, g_v \tag{3.46}$$

for phase *B*. Now, assuming that particle shape does not change strongly with size and/or grade, i.e. $\beta' \approx \beta$, the approximate location of the limiting bounds associated with phases *A* and *B* and point (g_v', D') is obtained by resolving the inequalities in equations 3.45 and 3.46,

$$D_A^V(g_v; g_v', D') = D' \left(\frac{1 - g_v'}{1 - g_v} \right)^{\frac{1}{3}} \tag{3.47}$$

and

$$D_B^V(g_v; g_v', D') = D' \left(\frac{g_v'}{g_v} \right)^{\frac{1}{3}} \tag{3.48}$$

where $D_A^V(g_v; g_v', D')$ is the size at the limiting boundary associated with phase *A* and point (g_v', D') corresponding to grade g_v , and $D_B^V(g_v; g_v', D')$ is the size at the limiting boundary associated with phase *B* and point (g_v', D') corresponding to grade g_v. Equations 3.47 and 3.48 define the limiting boundaries of the model. It is important to note that the function in equation 3.47, representing the limiting boundary associated with phase *A*, is simultaneously asymptotic to the axes represented by the lines $g_v = 1$ and

$D = 0$, and, consequently, its domain is $(-\infty, 1)$, and its range is $(0, \infty)$. Similarly, the limiting boundary associated with phase *B*, in equation 3.48, is simultaneously asymptotic to the lines represented by $g_v = 0$ and $D = 0$, and its range and its domain are all real numbers in $(0, \infty)$. The significance of the asymptotic nature of the limiting boundaries corresponding to the region R' is clearly understood, since a liberated particle of either phase can never produce an unliberated particle at point (g_v', D') by breakage. On the other hand, the implications of the asymptotic behavior of the limiting boundaries of the accessible region are more complex, and this property will be explored later on in this chapter. The boundaries of the accessible region must be associated with the limiting boundaries, and the geometrical texture parameter ϕ. They must also have the same domain and range of the limiting boundaries. Two functional forms are required as well, each to describe the boundary of the accessible region associated with either phase *A* or *B*. The boundaries of the accessible region must also possess the same properties of the corresponding limiting boundaries. Furthermore, care must be taken to make sure that the first moment of the conditional quadrivariate breakage function $\overline{g_v}(D; g_v', D')$ is included in the accessible region. This is automatic for the case when the first moment is invariant with progeny size, and equation 3.29 holds. However, when the first moment shifts significantly with progeny size, specially for sizes immediately below parent size, the boundaries of the accessible region must be adjusted to accommodate the shift. The following functional form is proposed for the boundary of the accessible region associated with phase *A*:

$$D_A\left(g_v;g_v',D'\right) = D_A\left(g_v=0;g_v',D'\right)\left(1-\frac{g_v'}{\overline{g_v}\left(D;g_v',D'\right)}\,g_v\right)^{-p_A} \tag{3.49}$$

with

$$p_A = \frac{\log\left(\frac{D_A\left(g_v=0;g_v',D'\right)}{D'}\right)}{\log\left(1-g_v'\right)} \tag{3.50}$$

where $D_A\left(g_v;g_v',D'\right)$ is the size at the boundary of the accessible region associated with phase *A* and point $\left(g_v',D'\right)$ corresponding to grade g_v, and $D_A\left(g_v=0;g_v',D'\right)$ is the critical size at which liberated phase *A* starts appearing. The functional form in equation 3.49 has all the required properties, and the term $\frac{g_v'}{\overline{g_v}\left(D;g_v',D'\right)}$ ensures that the first moment of the conditional quadrivariate breakage function is included in the accessible region. Similarly, the boundary of the accessible region associated with phase *B* is given by

$$D_B\left(g_v;g_v',D'\right) = D_B\left(g_v=1;g_v',D'\right)\left(1-\frac{(1-g_v')}{(1-\overline{g_v}\left(D;g_v',D'\right))}\,(1-g_v)\right)^{-p_B} \tag{3.51}$$

with

$$p_B = \frac{\log\left(\frac{D_B\left(g_v=1;g_v',D'\right)}{D'}\right)}{\log\left(g_v'\right)} \tag{3.52}$$

where $D_B\left(g_v;g_v',D'\right)$ is the size at the boundary of the accessible region associated with phase *B* and point $\left(g_v',D'\right)$ corresponding to grade g_v, and $D_B\left(g_v=1;g_v',D'\right)$ is the

critical size at which liberated phase *B* starts appearing.

The modeling of the boundaries of the accessible region is completed by establishing the values of the critical sizes $D_A\left(g_v=0;g_v',D'\right)$ and $D_B\left(g_v=1;g_v',D'\right)$. These must be a fraction of the corresponding critical sizes from the limiting boundary, $D_A^V\left(g_v=0;g_v',D'\right)$ and $D_B^V\left(g_v=1;g_v',D'\right)$, and the fraction corresponding to each phase must be a function of texture, i.e.,

$$D_A\left(g_v=0;g_v',D'\right) = f\left(\phi\right) D_A^V\left(g_v=0;g_v',D'\right) \tag{3.53}$$

and

$$D_B\left(g_v=1;g_v',D'\right) = f\left(\phi\right) D_B^V\left(g_v=1;g_v',D'\right) \tag{3.54}$$

There is no information available on the shape of the function $f\left(\phi\right)$ since this would require its measurement for at least three distinct textures. Since this work is the first and only successful measurement of the discrete fractions corresponding to the continuous quadrivariate breakage function, a rather simple functional form is proposed, based on the properties of ϕ. When texture is fine, ϕ is large, and the critical sizes must be a small fraction of the corresponding Andrews-Mika critical sizes. On the other hand, when texture is coarse and consequently ϕ is small, the boundaries of the accessible region are positioned closer to the Andrews-Mika boundaries, and therefore the critical sizes are a large fraction of the Andrews-Mika critical sizes. It is conceivable that for very coarse textures, like for example spheres with planar interface, the value of ϕ is close to its minimum, and the fraction represented by $f(\phi)$ approaches unity. With this in perspective, the following forms for equations 3.53 and 3.54 is initially proposed:

$$D_A\left(g_v = 0; g_v', D'\right) = \frac{\phi_A^C}{\phi} D_A^V\left(g_v = 0; g_v', D'\right) \tag{3.55}$$

and

$$D_B\left(g_v = 1; g_v', D'\right) = \frac{\phi_B^C}{\phi} D_B^V\left(g_v = 1; g_v', D'\right) \tag{3.56}$$

where ϕ_A^C and ϕ_B^C are critical texture parameters associated with phases *A* and *B,* representing the approximate lower limit of the geometrical texture parameter ϕ.

With the above, the modeling of the boundaries of the accessible region is complete. The proposed model for the internal structure of the accessible region is based on the incomplete beta function, primarily because its range of shapes seems to allow for a proper description of the distributions at all progeny sizes. Secondly, the parameters of the incomplete beta function are calculated from the first and second moments of the distribution, as shown in equations 2.29 through 2.32, in terms of the corresponding distribution average and variance. This is particularly convenient here, since the average grades for the Dolomite-Sphalerite ore has been characterized in detail, as shown in the previous section, and also because average grade can be measured precisely, and fairly easily, by image analysis. Furthermore, for ores that have phases equally brittle, or approximately equally brittle, the assumption in equation 3.29 can be used without compromising the overall shape of the internal structure of the accessible region. On the other hand, very little is known about the variance of the distributions in the accessible region. The variance is important because it is descriptive of how fast the distributions spread toward liberation as progeny size decreases. However, because of the

characteristics of the model proposed here, the effect of variance on liberation cannot be resolved due to the strong correlation between the liberation phenomena and the location and shape of the boundaries of the accessible region. A number of functional forms with a minimal number of parameters were implemented in a trial and error basis to give the best fit for the measured fractions b_v^{klij}, and the best result for the Dolomite-Sphalerite ore is obtained when the variance of the incomplete beta functions in the accessible region is modeled as follows:

$$\sigma_\xi^2 = \zeta \left(\frac{1}{2} - \left|\frac{1}{2} - g_v'\right|\right)\left(n_{1\xi}^B - n_{1\xi}^{B\,2}\right) \tag{3.57}$$

where σ_ξ^2 is the variance in the transformed incomplete beta function domain. The required domain transformations are discussed in detail thereafter. ζ is an arbitrary parameter with range $(0,2)$ and $n_{1\xi}^B$ is the first moment of the incomplete beta function in the ξ-domain. In equation 3.57, the variance is only a function of parent grade, and does not change with progeny size. The variance is minimum at parent grades approaching completely liberated particles of either phase and maximum at g_v' = 0.5. Finally, the term $\left(n_{1\xi}^B - n_{1\xi}^{B\,2}\right)$ represents the maximum variance of the incomplete beta function in the nonimaginary space.

With the variance established, it is necessary to calculate the first moment of the incomplete beta function that represents the unliberated distribution $B_{vu}\left(g_v \mid D; g_v', D'\right)$ in the volumetric grade domain described by the boundaries of the accessible region, and the liberated fractions corresponding to both phases *A* and *B*, at any progeny size *D*. The calculation is best described when the problem is divided into four cases. Case 1 covers

all progeny sizes above the critical sizes, i.e., all progeny sizes at which no phase liberation is allowed. Case 2 corresponds to progeny sizes at which liberated particles of phase *A* are expected, but liberated particles of phase *B* are not allowed, i.e., progeny sizes below the critical size for phase *A* and above the critical size for phase *B*. Case 3 covers all progeny sizes smaller then the critical size for phase *B* but larger then the critical size for phase *A*. In principle, the calculation procedure in cases 2 and 3 is identical, since these cases treat a situation where one phase will appear as liberated and the other will not. Case 4 corresponds to all progeny sizes below the critical sizes, and both phases will appear as liberated particles.

Case 1, $D \geq D_A$ and $D \geq D_B$

This is illustrated in Figure 3.16. For progeny sizes above the critical sizes, the conditional quadrivariate breakage function is null for all volumetric grades below g_v^A and above g_v^B. This also implies that the unliberated and liberated distributions are equal, i.e. $B_v(g_v, D; g_v', D') = B_{vu}(g_v, D; g_v', D')$. The volumetric grades at the boundary that are associated with phases *A* and *B* are calculated by inverting the boundary equations 3.49 and 3.51, i.e.,

$$g_v^A = \left(1 - \left(\frac{D_A}{D}\right)^{\frac{1}{p_A}}\right) \frac{n_1^B}{g_v'} \tag{3.58}$$

and

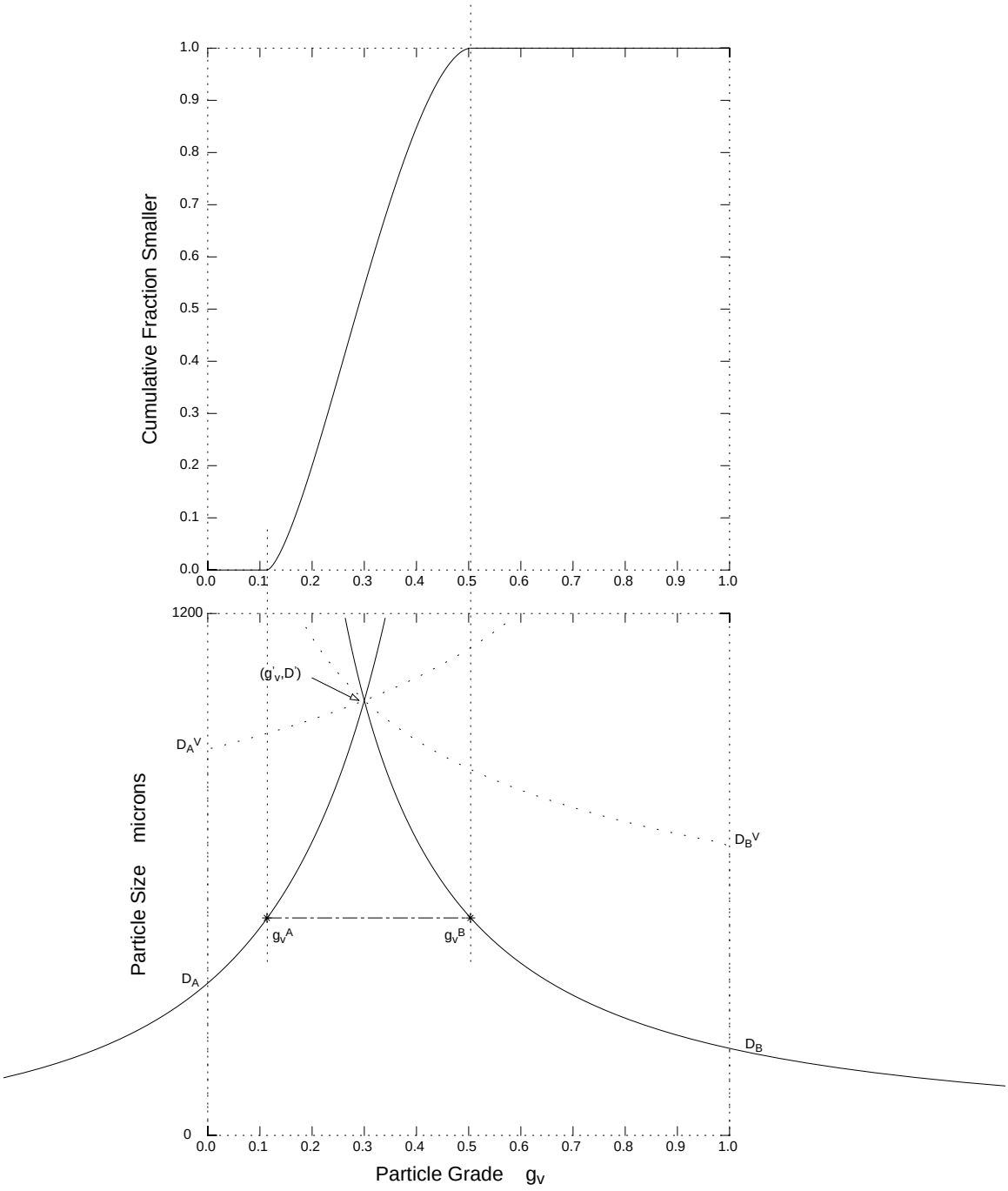

Figure 3.16 The domain of the incomplete beta function (ξ-domain) for progeny sizes above the critical sizes. No liberation is allowed

$$g_v^B = 1 - (1 - \left(\frac{D_B}{D}\right)^{\frac{1}{p_B}}) \frac{1 - n_1^B}{1 - g_v'} \tag{3.59}$$

where

$$n_1^B = \overline{g_v}(D; g_v', D') \tag{3.60}$$

Now, for progeny volumetric grades in the range (g_v^A, g_v^B), a transformation is required from the volumetric grade domain $(0,1)$ to the ξ-domain (g_v^A, g_v^B), so that the distribution can be described in terms of the incomplete beta function. Because there are no liberated particles, the first moment of the unliberated distribution is equal to the first moment of the liberated distribution, i.e.,

$$n_{1u}^B = n_1^B \tag{3.61}$$

and the calculation of the first moment in the ξ-domain is direct,

$$n_{1\xi}^B = \frac{(n_{1u}^B - g_v^A)}{(g_v^B - g_v^A)} \tag{3.62}$$

The corresponding variance in the ξ-domain can then be calculated using equation 3.57. With the values of the first moment and the variance, the second moment of the incomplete beta function in the ξ-domain is:

$$n_{2\xi}^B = \sigma_\xi^2 + n_{1\xi}^B 2 \tag{3.63}$$

The parameters α and β of the incomplete beta function are then calculated from its first

and second moments as follows:

$$\alpha = n_{1\xi}^{B}\ \gamma \tag{3.64}$$

and

$$\beta = (1 - n_{1\xi}^{B})\ \gamma \tag{3.65}$$

where

$$\gamma = \frac{n_{1\xi}^{B} - n_{2\xi}^{B}}{n_{2\xi}^{B} - n_{1\xi}^{B}{}^{2}} \tag{3.66}$$

Finally, completing the modeling of the conditional, on progeny size, quadrivariate breakage function for progeny sizes above the critical sizes,

$$B_v(g_v \mid D; g_v', D') = \begin{cases} 0 & g_v^A \geq g_v \\ I_{g_v^{\xi}}(\alpha, \beta) & g_v^A < g_v < g_v^B \\ 1 & g_v \geq g_v^B \end{cases} \tag{3.67}$$

with the incomplete beta function evaluated at the corresponding volumetric grade in the ξ-domain,

$$g_v^{\xi} = \frac{g_v - g_v^A}{g_v^B - g_v^A} \tag{3.68}$$

Case 2, $D < D_A$ and $D \geq D_B$

This case is illustrated in Figure 3.17. In this progeny size range, the conditional quadrivariate breakage function is null for all grades above g_v^B. On the other hand,

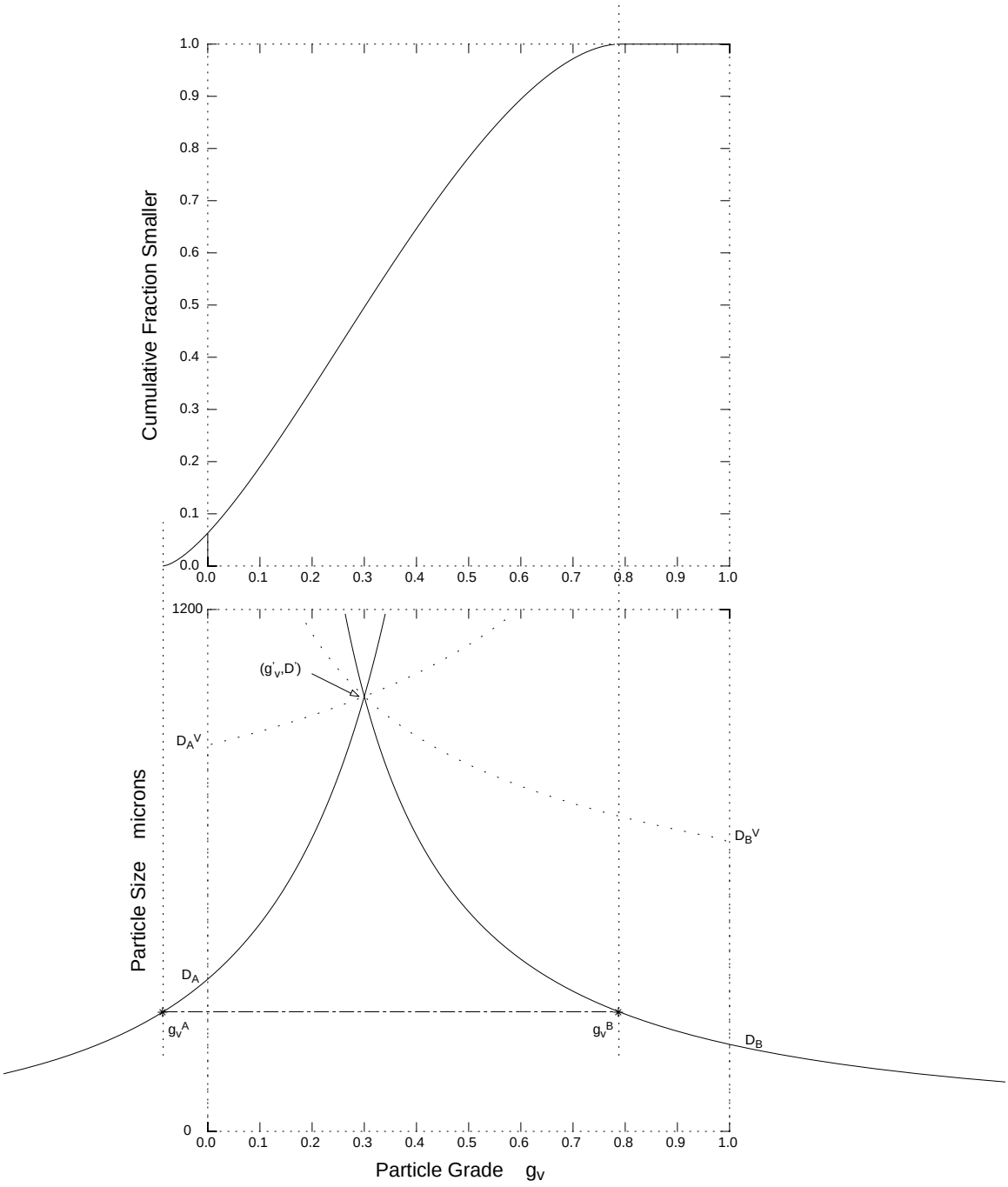

Figure 3.17 The domain of the incomplete beta function (ξ-domain) for progeny sizes bellow D_A and above D_B. Only liberated phase A is allowed

liberated particles of phase *A* are allowed. The fraction of liberated particles of phase *A*, defined as $\mathfrak{L}_A = b_v(g_v = 0 \mid D; g_v', D')$, is calculated by letting the boundary associated to phase *A* extend to negative values of g_v, as shown in the figure. Then, the volumetric grade in the transformed ξ-domain corresponding to $g_v = 0$, is defined as:

$$g_v^{\xi 0} = \frac{-g_v^A}{g_v^B - g_v^A} \tag{3.69}$$

It is postulated that the fraction of liberated particles of phase *A* is equal to the fraction of particles that have grade below $g_v^{\xi 0}$ in the ξ-domain, i.e.,

$$\mathfrak{L}_A = I_{g_v^{\xi 0}}(\alpha, \beta) \tag{3.70}$$

with the parameters α and β defined as in equations 3.64 and 3.65. This is a very appealing procedure for calculating fractional liberation because it introduces no new arbitrary parameter and because it provides a continuous and smooth transition from unliberated to liberated distribution. The drawback of this procedure is that $n_{1\xi}^B$ cannot be calculated directly, like in case 1 from equation 3.62, because the first moment of the associated unliberated distribution is now related to the average grade of the particles that have grades in the range $(g_v^{\xi 0}, 1)$ in ξ-domain:

$$(1 - \mathfrak{L}_A) n_{1u}^B = \frac{1}{B(\alpha, \beta)} \int_{g_v^{\xi 0}}^{1} g_v^{\xi (\alpha - 1)} \, (1 - g_v^{\xi})^{(\beta - 1)} \, g_v \, dg_v^{\xi} \tag{3.71}$$

where $B(\alpha, \beta)$ is the beta function. Substituting equation 3.68 into equation 3.71, we get

$$(1-\mathcal{L}_A)n_{1u}^B = \frac{(g_v^B - g_v^A)}{B(\alpha,\beta)} \int_{g_v^{\xi 0}}^{1} g_v^{\xi\,\alpha} (1-g_v^{\xi})^{(\beta-1)}\, dg_v^{\xi} + \frac{g_v^A}{B(\alpha,\beta)} \int_{g_v^{\xi 0}}^{1} g_v^{\xi(\alpha-1)} (1-g_v^{\xi})^{(\beta-1)}\, dg_v^{\xi} \quad (3.72)$$

Equation 3.72 can be written in terms of the incomplete beta function, which is defined as:

$$I_{g_v^{\xi}}(\alpha,\beta) = \frac{1}{B(\alpha,\beta)} \int_{0}^{g_v^{\xi}} g_v^{\xi(\alpha-1)} (1-g_v^{\xi})^{(\beta-1)}\, dg_v^{\xi} \quad (3.73)$$

Equation 3.72 becomes:

$$(1-\mathcal{L}_A)n_{1u}^B = (g_v^B - g_v^A)\frac{B(\alpha+1,\beta)}{B(\alpha,\beta)} (1-I_{g_v^{\xi 0}}(\alpha+1,\beta)) + g_v^A (1-I_{g_v^{\xi 0}}(\alpha,\beta)) \quad (3.74)$$

Substituting equation 3.70 into equation 3.74,

$$(1-\mathcal{L}_A)n_{1u}^B = (g_v^B - g_v^A)\frac{B(\alpha+1,\beta)}{B(\alpha,\beta)} (1-I_{g_v^{\xi 0}}(\alpha+1,\beta)) + g_v^A(1-\mathcal{L}_A) \quad (3.75)$$

Finally, the term $\frac{B(\alpha+1,\beta)}{B(\alpha,\beta)}$ is identical to the first moment of the incomplete beta function in α and β, i.e.,

$$(1-\mathcal{L}_A)n_{1u}^B = (g_v^B - g_v^A)\, n_{1\xi}^B (1-I_{g_v^{\xi 0}}(\alpha+1,\beta)) + g_v^A(1-\mathcal{L}_A) \quad (3.76)$$

The first moment of the unliberated distribution is related to that of the liberated

distribution by:

$$n_1^B = (1 - \mathfrak{L}_A - \mathfrak{L}_B)\, n_{1u}^B + \mathfrak{L}_B \tag{3.77}$$

Because liberated particles of phase B are not allowed in this range of progeny sizes, $\mathfrak{L}_B = 0$ and equation 3.76 is written in terms n_1^B as:

$$n_1^B = (g_v^B - g_v^A)\, n_{1\xi}^B\, (1 - I_{g_v^{\xi 0}}(\alpha + 1, \beta)) + g_v^A (1 - \mathfrak{L}_A) \tag{3.78}$$

Equation 3.78 is the driving equation that characterizes case 2. The solution is to find the value of $n_{1\xi}^B$ that satisfies equation 3.78 by means of an iterative procedure. In this work, a simple optimization procedure based on the bisection method coupled with a bracketing procedure has been implemented successfully. This is possible because equation 3.78 has a single root in the very well defined interval $(0,1)$. With the calculated value of the first moment of the unliberated distribution in the ξ-domain, the modelling of the conditional quadrivariate breakage function for progeny sizes below the critical size for phase *A* and above the critical size for phase *B* is completed as shown in equation 3.79 below:

$$B_v(g_v \mid D; g_v', D') = \begin{cases} I_{g_v^{\xi}}(\alpha, \beta) & g_v < g_v^B \\ 1 & g_v \geq g_v^B \end{cases} \tag{3.79}$$

with g_v^{ξ} defined as in equation 3.68.

Case 3, $D \geq D_A$ and $D < D_B$

This case, illustrated in Figure 3.18, is treated in exactly the same manner as case 2, but here only liberated particles of phase *B* are allowed, and the conditional

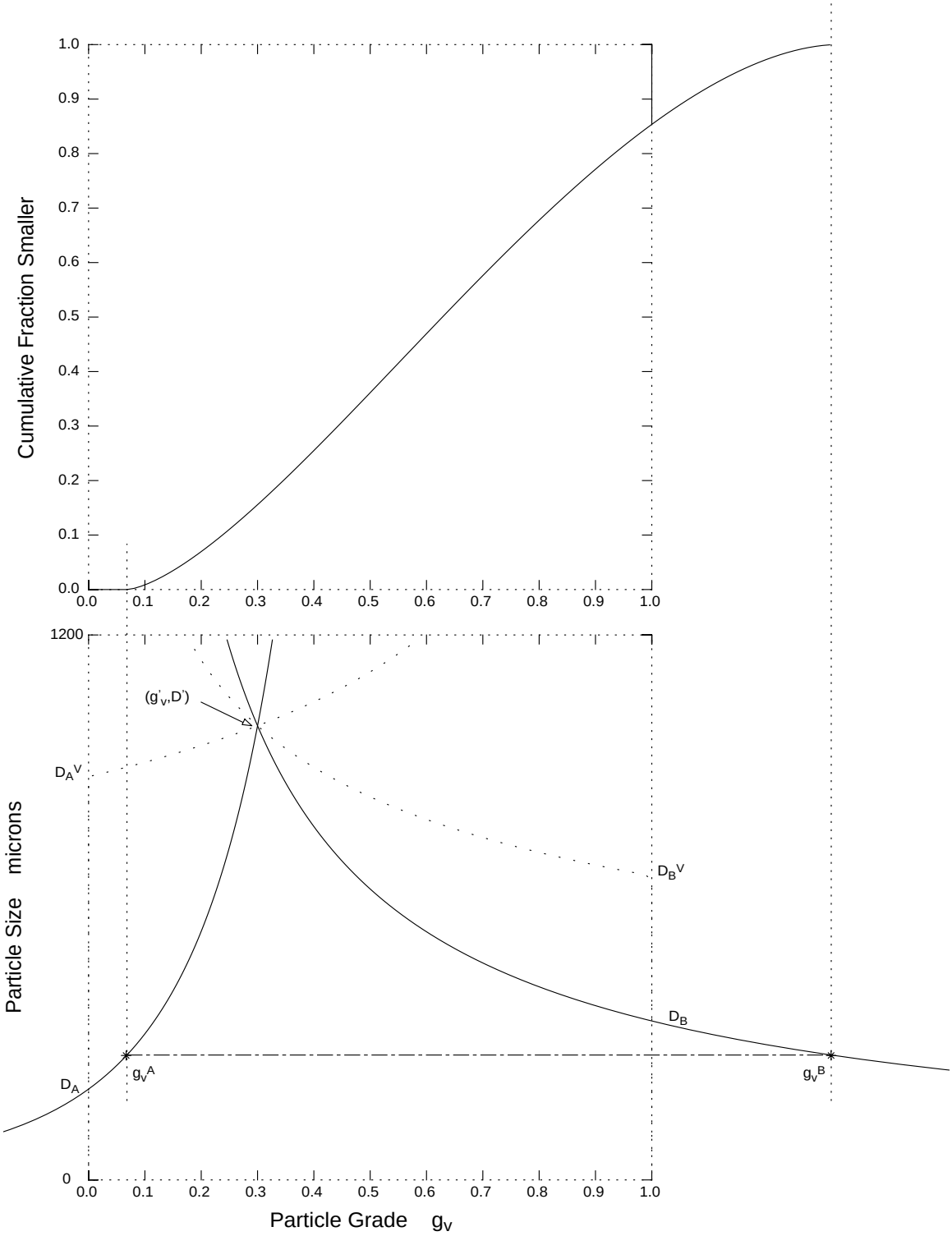

Figure 3.18 The domain of the incomplete beta function (ξ-domain) for progeny sizes bellow D_B and above D_A. Only liberated phase *B* is allowed

quadrivariate breakage function is null for all grades below g_v^A. The boundary associated to phase *B* is allowed to extend to values beyond $g_v = 1$, and it is postulated that the fraction of liberated particles of phase *B* is equal to the fraction of particles that have grade above $g_v^{\xi 1}$ in the ξ-domain,

$$\mathfrak{L}_B = 1 - I_{g_v^{\xi 1}}(\alpha, \beta) \tag{3.80}$$

where

$$g_v^{\xi 1} = \frac{1 - g_v^A}{g_v^B - g_v^A} \tag{3.81}$$

with the fraction of liberated particles of phase *B* defined as $\mathfrak{L}_B = b_v(g_v = 1 \mid D; g_v', D')$. Here, the first moment of the unliberated distribution is related to the average grade of the particles that have grades in the range $(0, g_v^{\xi 1})$ in ξ-domain:

$$(1 - \mathfrak{L}_B) n_{1u}^B = \frac{1}{B(\alpha, \beta)} \int_0^{g_v^{\xi 1}} g_v^{\xi (\alpha - 1)} \, (1 - g_v^{\xi})^{(\beta - 1)} \, g_v \, dg_v^{\xi} \tag{3.82}$$

Developing equation 3.82 in terms of the corresponding incomplete beta function and the fraction of liberated phase *B*;

$$n_1^B = (g_v^B - g_v^A) \, n_{1\xi}^B \, I_{g_v^{\xi 1}}(\alpha + 1, \beta) + g_v^A (1 - \mathfrak{L}_B) + \mathfrak{L}_B \tag{3.83}$$

which is the characteristic equation for case 3. The value of $n_{1\xi}^B$ that satisfies equation 3.83 is calculated iteratively, and the parameters α and β are calculated as shown in equations 3.64 and 3.65. The conditional quadrivariate breakage function for progeny sizes above the critical size for phase *A* and below the critical size for phase *B* is

calculated as shown in equation 3.84 below:

$$B_v(g_v \mid D; g_v', D') = \begin{cases} 0 & g_v \le g_v^A \\ I_{g_v^\xi}(\alpha, \beta) & g_v^A < g_v < 1 \\ 1 & g_v = 1 \end{cases} \tag{3.84}$$

with g_v^ξ defined as in equation 3.68.

Case 4, $D < D_A$ and $D < D_B$

Here, both phases are allowed to appear as liberated particles, and the situation is illustrated in Figure 3.19. The same approach is used to model this section of the quadrivariate breakage function, and the first moment of its associated unliberated distribution is calculated as:

$$(1 - \mathfrak{L}_A - \mathfrak{L}_B) n_{1u}^B = \frac{1}{B(\alpha, \beta)} \int_{g_v^{\xi 0}}^{g_v^{\xi 1}} g_v^{\xi(\alpha-1)} (1 - g_v^\xi)^{(\beta-1)} g_v \, dg_v^\xi \tag{3.85}$$

Again, developing equation 3.85, and with both phases appearing as liberated particles,

$$n_1^B = (g_v^B - g_v^A) \, n_{1\xi}^B \, (I_{g_v^{\xi 1}}(\alpha+1, \beta) - I_{g_v^{\xi 0}}(\alpha+1, \beta)) + g_v^A (1 - \mathfrak{L}_A - \mathfrak{L}_B) + \mathfrak{L}_B \tag{3.86}$$

Equation 3.86 is the characteristic equation for case 4, and the value of $n_{1\xi}^B$ is calculated iteratively, as described in cases 2 and 3. Finally, the cumulative distribution is written as

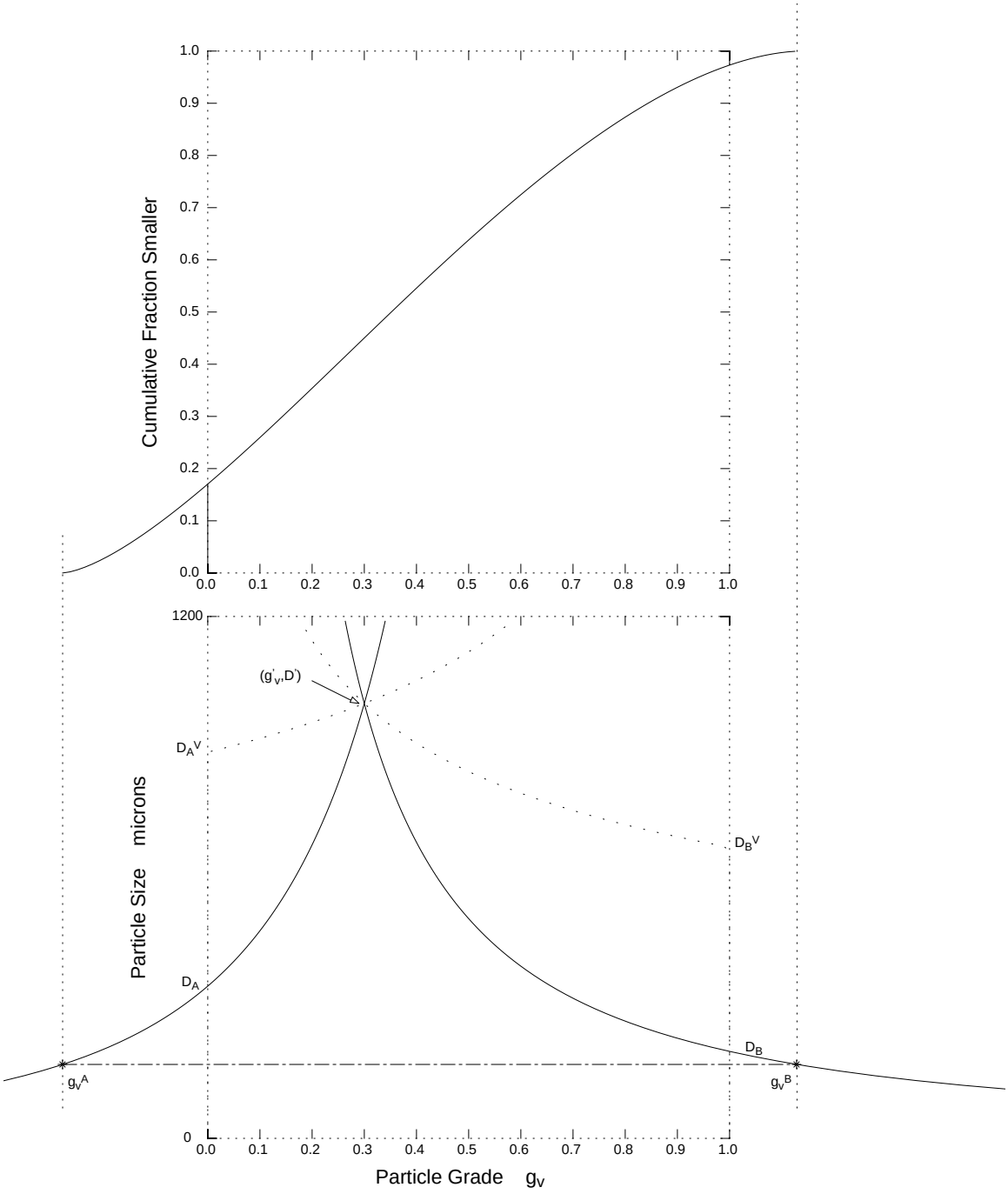

Figure 3.19 The domain of the incomplete beta function (ξ-domain) for progeny sizes bellow the critical sizes. Both liberated phases *A* and *B* are allowed

$$B_v(g_v \mid D; g_v', D') = \begin{cases} I_{g_v^{\xi}}(\alpha, \beta) & 0 \leq g_v < 1 \\ 1 & g_v = 1 \end{cases} \tag{3.87}$$

completing the modelling of the internal structure of the accessible region at all progeny sizes.

The unliberated distribution associated to the conditional quadrivariate breakage function will vanish at $D = 0$, because the model for the boundaries of the accessible region is asymptotic to the abscissas. Although the volumetric grade distribution does not exist at D = 0, the model must yield complete liberation at the limit when progeny size tend to naught.

Equation 3.86 is in fact the general characteristic equation of this model, and it is applicable at any progeny size in the progeny domain, regardless of the position of boundaries.

Model Parameterization

The model described above contains three arbitrary parameters, namely ϕ_A^C and ϕ_B^C, the critical texture parameters, and ζ, the variance parameter. This set of parameters is constrained, and the critical texture parameters must be smaller then the measured geometrical texture parameter for the mineralogical system in question, i.e., ϕ_A^C, $\phi_B^C < \phi$ so that the boundaries of the accessible region are contained in the region described by the limiting boundaries. Also, $0 \leq \zeta \leq 2$ in order to keep the variance in the range of the incomplete beta function. With these parameters, the calculation of the discrete fractions b_v^{klij} was carried out by integrating the continuous, conditional on progeny size

distribution in the corresponding progeny and parent grade and size ranges, as shown in equations 3.9 and 3.10. The integration scheme used was identical to the one used when calculating the parameters for the model of the first moment surface. The best set of parameters for the quadrivariate breakage function was calculated by minimizing the sum of squares of residuals between the calculated and measured b_v^{klij} fractions, shown in Tables 3.14 through 3.20, using once again Rosenbrock Hillclimb [25]. The optimization procedure was carried out simultaneously for the seven data sets. This was a formidable task, considering the complexity of the model, the integration procedure and the large number of function evaluations required. Nevertheless, the optimization was carried out successfully, and the set of parameters that best describe the conditional, on progeny size, quadrivariate breakage function for the Dolomite-Sphalerite ore was obtained. Minimum sum of squares of residuals was achieved for $\phi_A^C = 9.44$, $\phi_B^C = 14.95$ and $\zeta = 0.615$. A graphic comparison between the calculated b_v^{klij} fractions corresponding to the set of parameters above and the equivalent measured fractions is shown in Figures 3.20 to 3.26. The fit is remarkably good, clearly demonstrating that the model surface is descriptive of the breakage properties inherent to the Dolomite-Sphalerite mineralogical system. In fact, the overall shape of the measured distributions is so very well reproduced by the model, that the local differences between calculated and measured fractions are only apparent due to the stereological correction noise that is present in the measured fractions, with the exception of the set corresponding to the parent particles in the -3.1 +2.9 g/cc range, for which the trend of the measured distribution is not reproduced by the model with such remarkable perfection. It is actually stunning to realize that such calculation could be

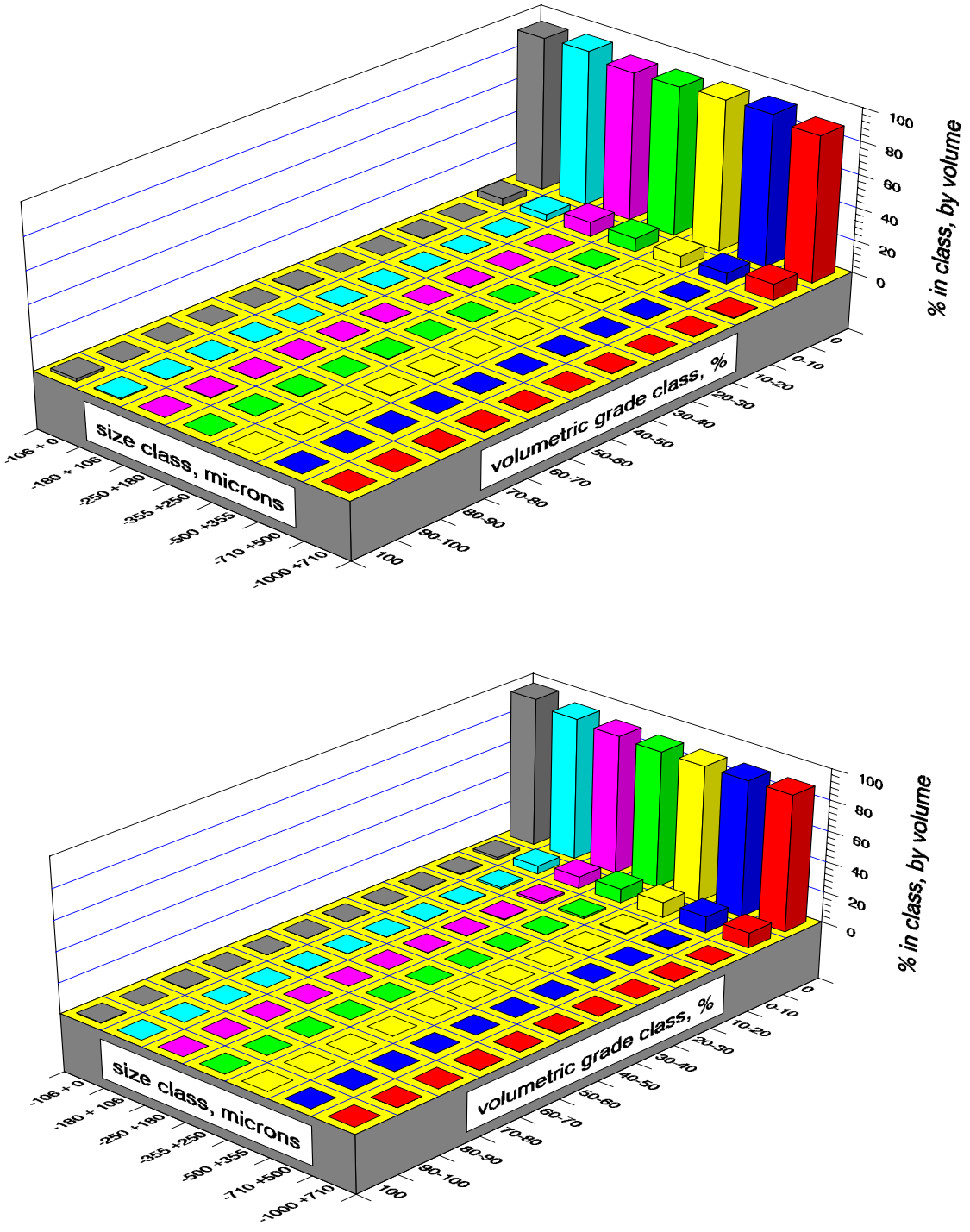

Figure 3.20 The measured, conditional on size, volumetric quadrivariate breakage function for the -2.9 g/cc particles (top) and the corresponding calculated fractions after model parameterization

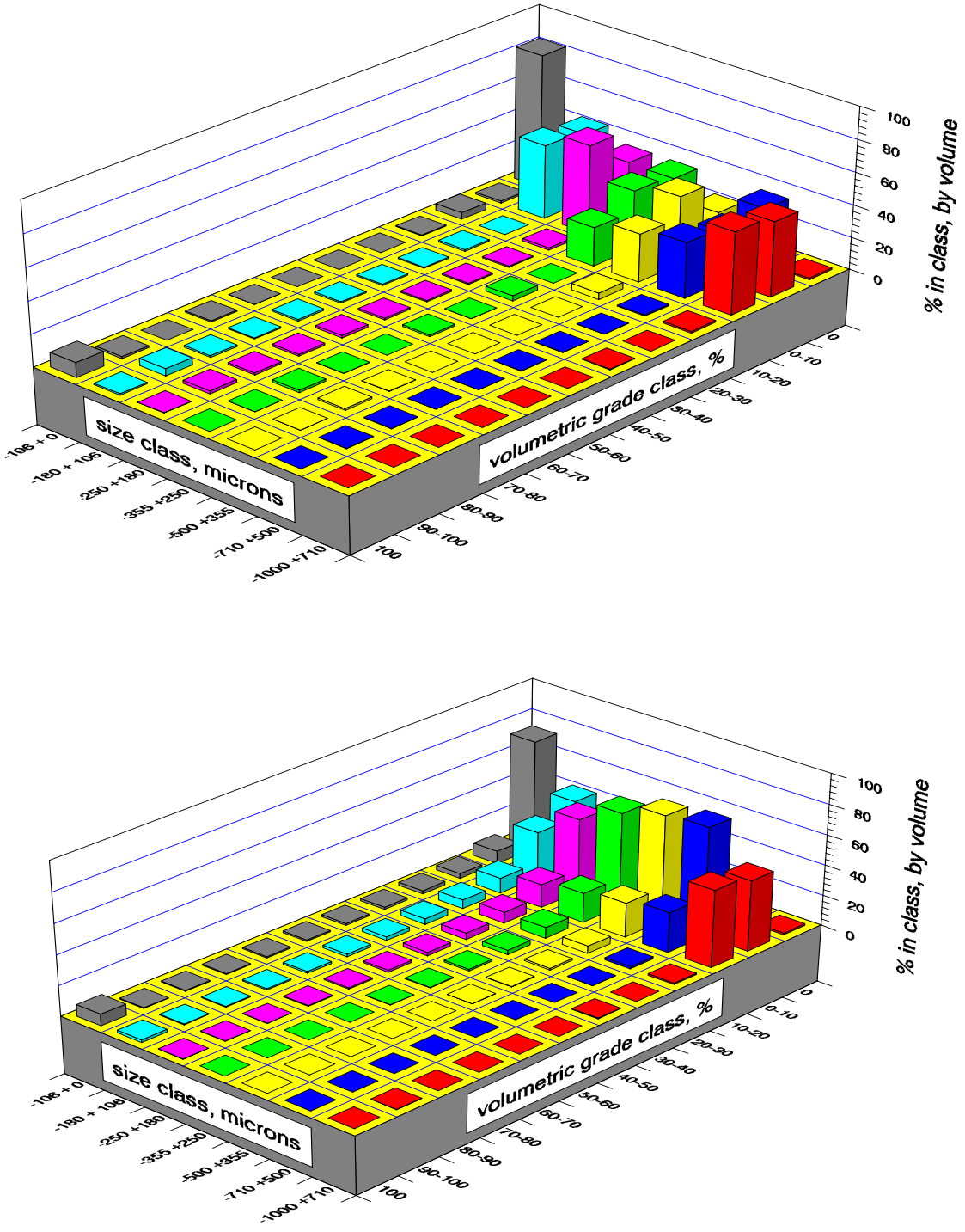

Figure 3.21 The measured, conditional on size, volumetric quadrivariate breakage function for the -3.1+2.9 g/cc particles (top) and the corresponding calculated fractions after model parameterization

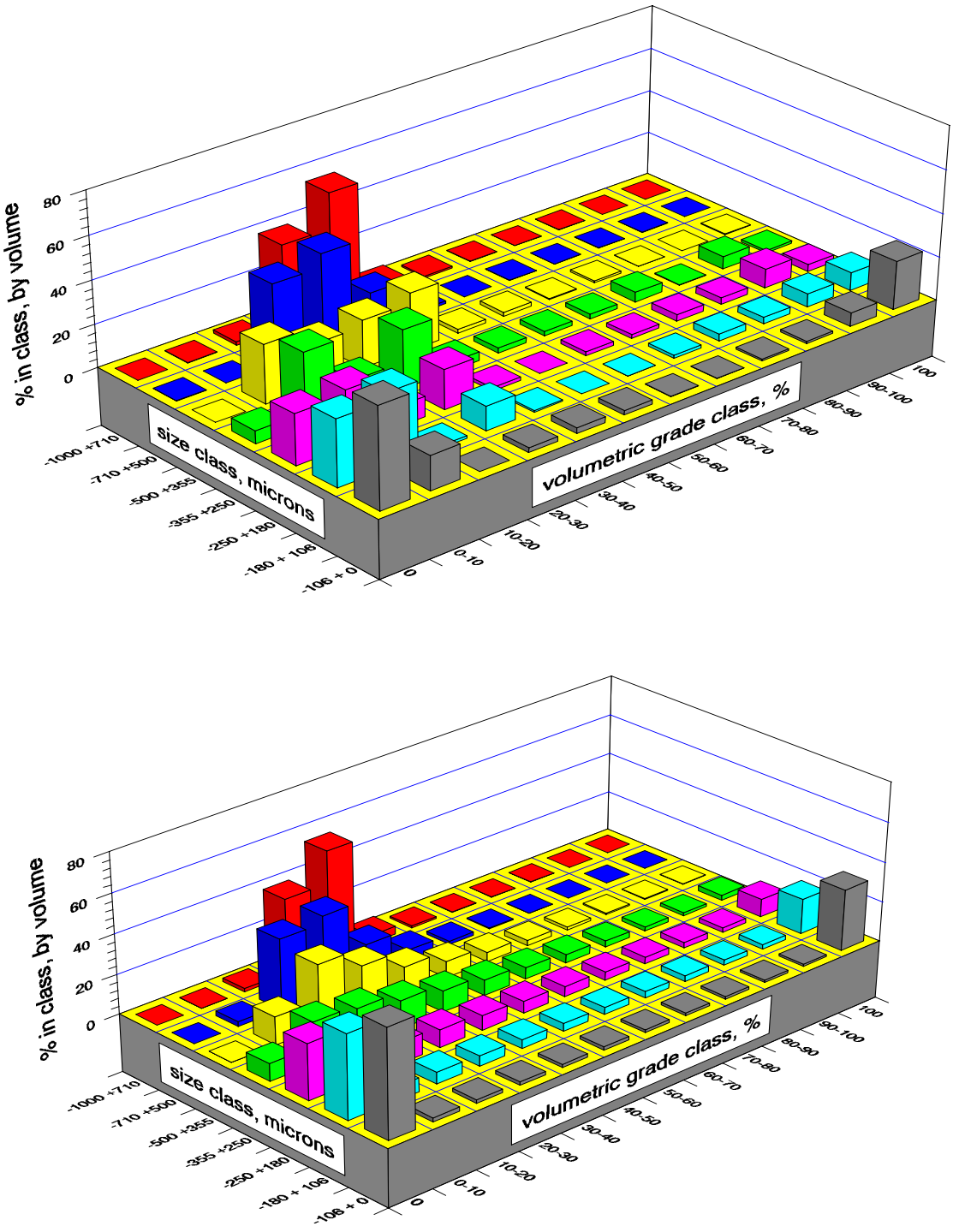

Figure 3.22 The measured, conditional on size, volumetric quadrivariate breakage function for the -3.3+3.1 g/cc particles (top) and the corresponding calculated fractions after model parameterization

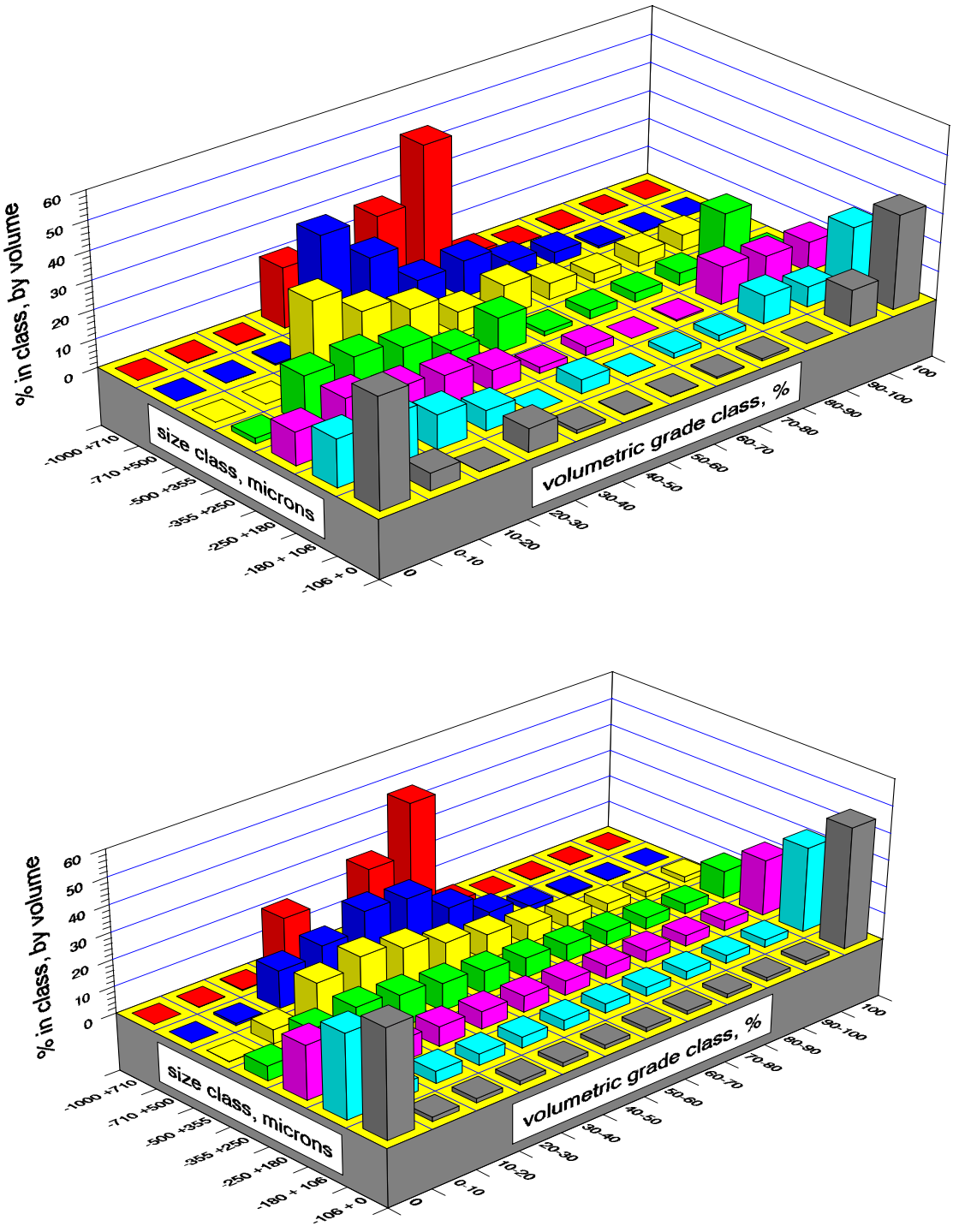

Figure 3.23 The measured, conditional on size, volumetric quadrivariate breakage function for the -3.5+3.3 g/cc particles (top) and the corresponding calculated fractions after model parameterization

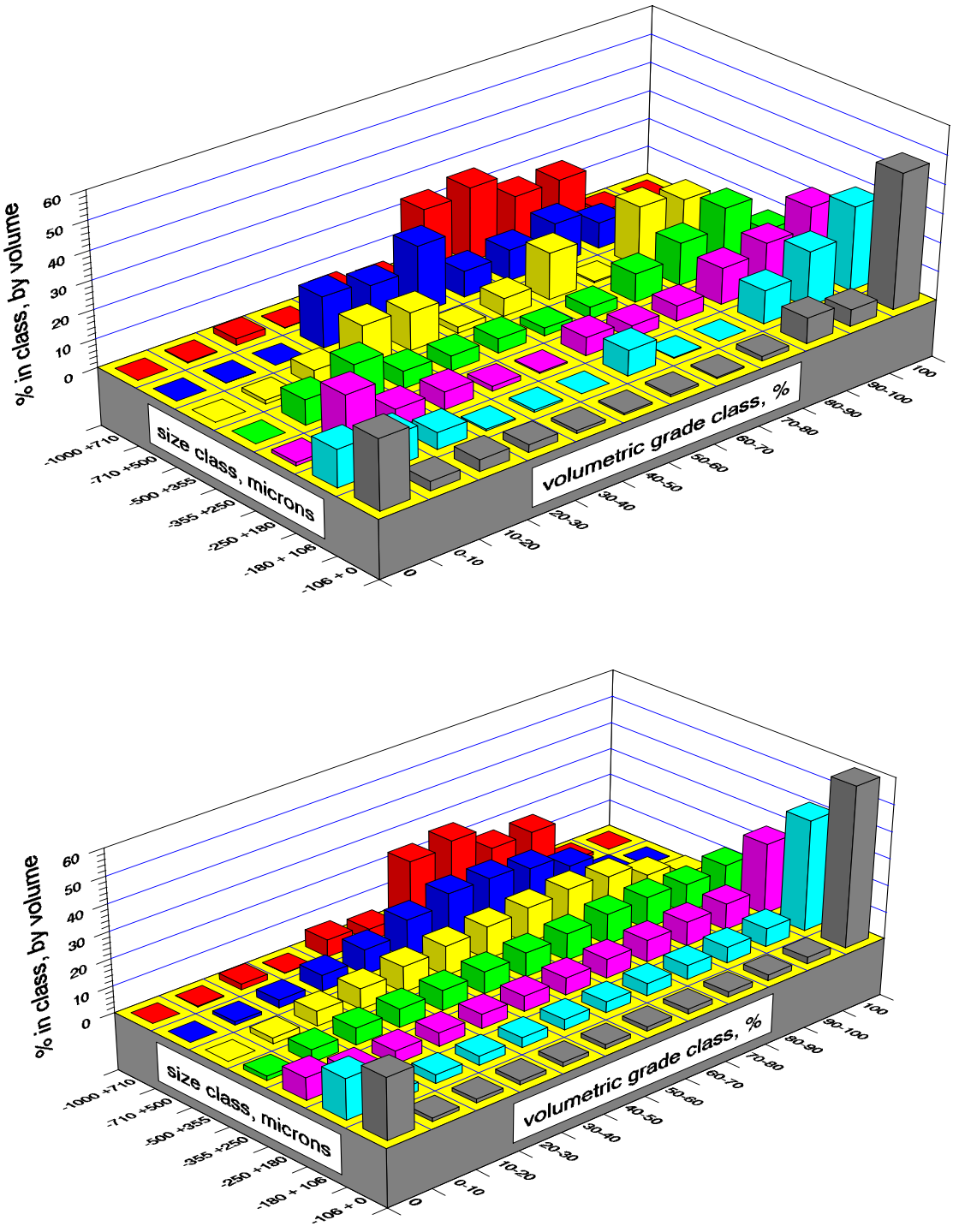

Figure 3.24 The measured, conditional on size, volumetric quadrivariate breakage function for the -3.7+3.5 g/cc particles (top) and the corresponding calculated fractions after model parameterization

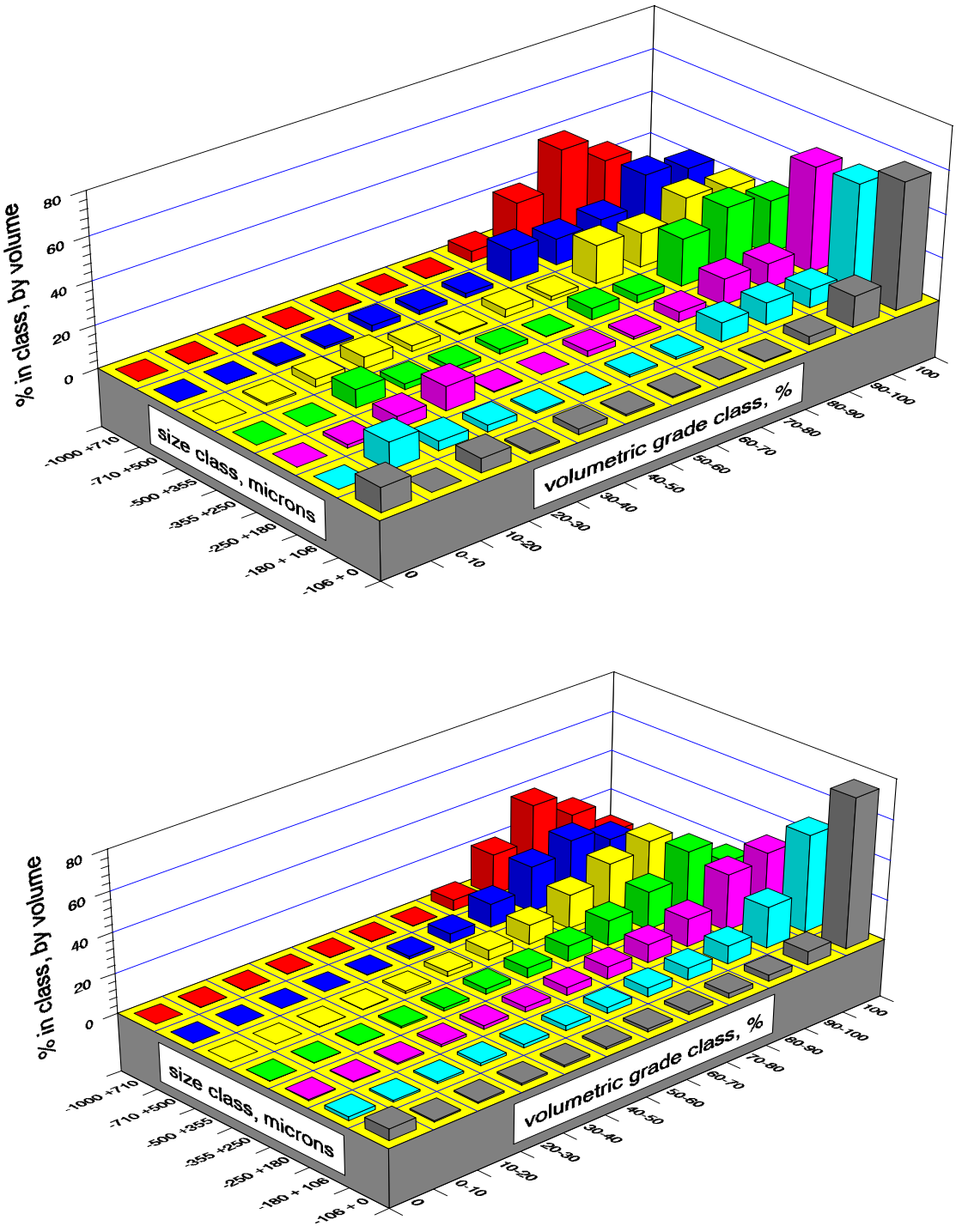

Figure 3.25 The measured, conditional on size, volumetric quadrivariate breakage function for the -4.0+3.7 g/cc particles (top) and the corresponding calculated fractions after model parameterization

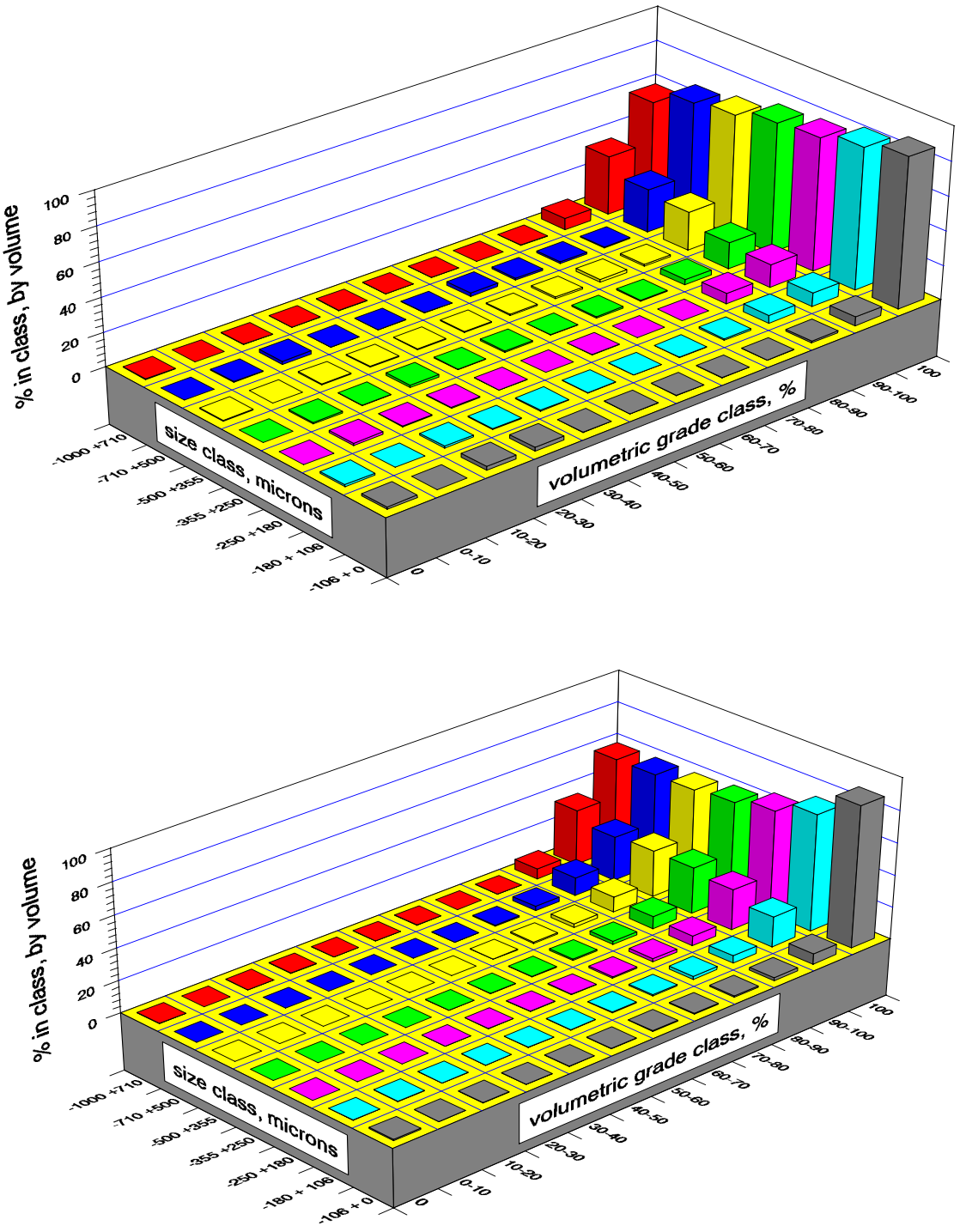

Figure 3.26 The measured, conditional on size, volumetric quadrivariate breakage function for the +4.0 g/cc particles (top) and the corresponding calculated fractions after model parameterization

performed at all, when considering that an optimization procedure that requires a large number of function evaluations like Rosenbrock's was used with an objective function that requires numerical integration in four dimensions of a surface that itself requires one-dimensional optimization to be computed. Of course complex computer code can be written to perform almost any intricate calculation, but such an enormous task has only been made accomplishable relatively recently, with the development of very fast and affordable computers, that can be used in the laboratory environment with no user scheduling and\or charged *CPU* time.

The calculated set of parameters define the internal structure of the Andrews-Mika diagram associated to Dolomite-Sphalerite particles of any combination of size and volumetric grade. In Figure 3.27, the surface generated by breakage of monograde Dolomite-Sphalerite particles of volumetric grade $g_v = 0.5$ is presented. There is a number of remarkable features that can be readily observed from the surface in the figure, such as the relative position of the boundaries of the accessible region, what makes the surface lopsided about $g_v = 0.5$, the variation of the average grade with progeny size, which also produces the illusion of Dolomite liberating in a much slower rate than the Sphalerite at the smallest progeny sizes. Also explicitly visible in the figure is the rate at which liberated phase is produced relative to the rate at which unliberated particles disappear as progeny size decreases.

It is interesting to note that the final value of the critical texture parameter for phase A, ϕ_A^C, approaches the slope of $d_p S_V^{AB} \times g_v$ for spheres with planar interface ($\phi \approx 9.0$), as shown by King [9], who compared this texture to that of PARGEN

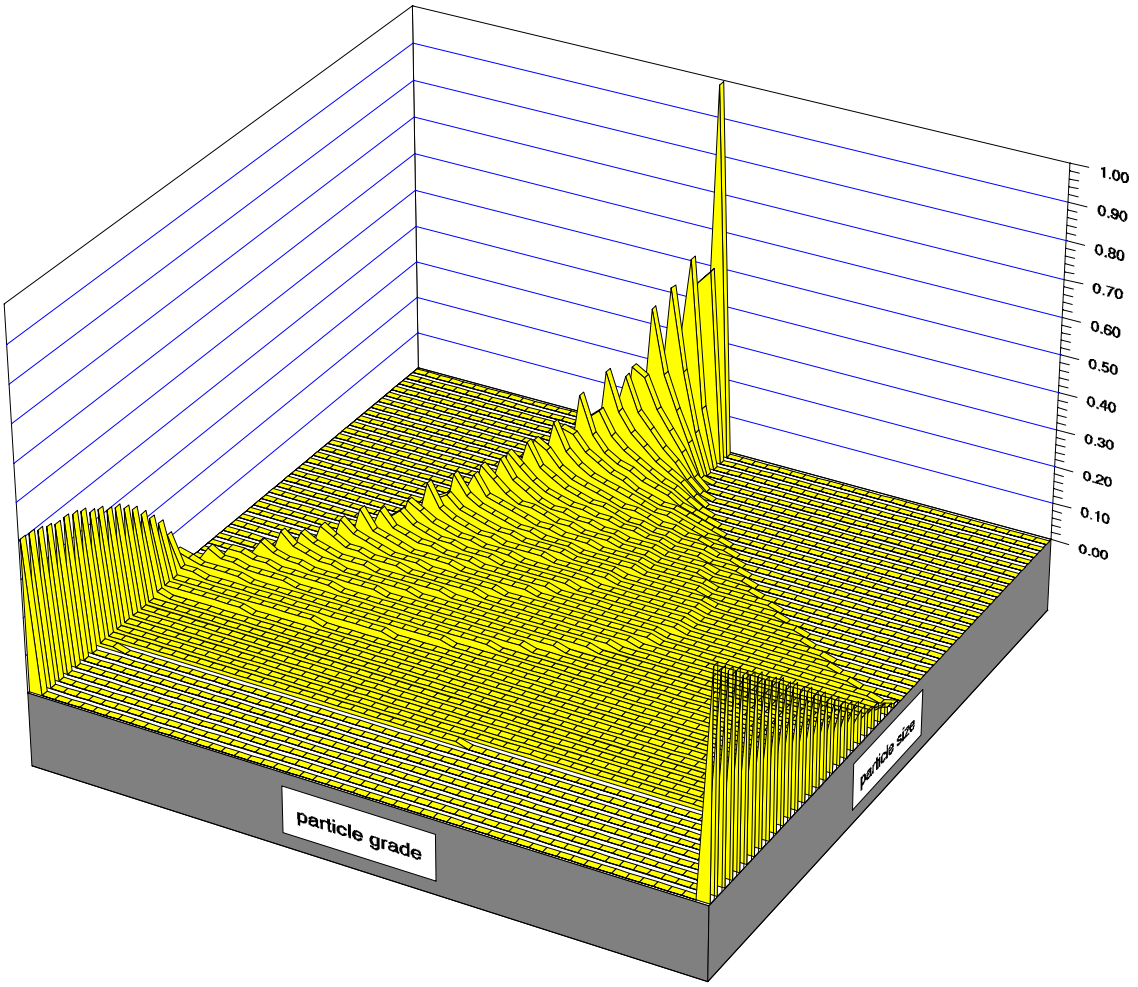

Figure 3.27 The continuous, conditional on size, quadrivariate breakage function, originated from monograde Dolomite-Sphalerite particles of volumetric grade equal to 0.5

particles. It is anticipated that, for binary mineralogical systems that produce random fracture, both critical texture parameters be comparable to that of spheres with planar interface. Furthermore, the ratio between the critical parameters for each phase is expected to be proportional to the ratio of phase brittleness. It is also anticipated that most mineralogical textures will measure ϕ larger than that of spheres with planar interface.

CHAPTER 4

CALCULATION OF THE LIBERATION SPECTRA PRODUCED IN A CONTINUOUS GRINDING EXPERIMENT

Objective and Methodology

Population Balance Modeling is the only known method for calculating the liberation spectra that is produced in closed continuous grinding circuits. Because this calculation has tremendous importance in the field of mineral processing, a number of solutions to the Population Balance Model equation for binary mineralogical systems have been proposed, such as Herbst et al. [29], Choi et al. [30] and Mehta et al. [31]. These solutions, called conventional solutions, invariably rely on a knowledge of the internal structure of the region corresponding to the region R' in the Andrews-Mika diagram (Figure 3.1). The region R' comprehends all particles that can produce , upon breakage, progeny at point g_v', D' in the diagram. However, this region cannot be characterized directly by experiment, and all conventional solutions are based on a massive parameter estimation for its description. In this work, a model containing only three arbitrary parameters that are dependent on the texture of the ore has been developed for the description of the region corresponding to the accessible region in the Andrews-Mika diagram (Chapter 3). The model is based on a complete experimental characterization of the internal structure of the accessible region. The conventional solutions to the Population Balance Model equation cannot be used with the model developed in this work

because they operate on the region R'. Fortunately, King [9] has proposed a solution to the Population Balance Model equation that is based on a knowledge of the internal structure of the accessible region. The model for the internal structure of the accessible region and King's solution to the *PBM* equation were implemented in a Modular Ore Dressing Simulation package, MODSIM [10], and this package was used here for the experimental verification of the proposed model and King's calculation procedure as well.

The initial experimental work was aimed at characterizing the flow pattern and mass transport characteristics of a pilot scale overflow ball mill. The residence-time distribution, *RTD*, was established by an impulse test using both liquid- and solid-phase tracers. Due to the limited amount of Dolomite-Sphalerite sample available, the transport characterization of the experimental mill was carried out with Limestone as the test material. Data obtained from the holdup of the mill and product allowed the evaluation of the appropriate comminution model for different grinding conditions, and the relevance of classification effects in the overflow discharge of the mill.

The experimental verification of the liberation model, comprehending both accessible region model and calculation procedure, consisted of comparing the measured and calculated liberation spectra that were produced in the various streams of a continuous grinding circuit that contained one concentration operation. The design of such experiment must take into account several factors, including amenability for stream sampling, choice of test ore, choice of grinding mill and grinding conditions, and the choice of concentrating unit and its amenability for modeling.

Because the experimental check is by comparison, the test ore must be the

Dolomite-Sphalerite ore, since this is the only ore for which the transformation function for stereological correction is well known (Chapter 2), and the liberation spectra in particles from this ore can be measured by image analysis fairly accurately. On the other hand, the image analysis system is limited to a maximum particle size of about 1000 microns. This size was elected as the top size for the particles in the feed streams of the continuous grinding experiment, such that the entire particle population in each stream was suitable for image analysis.

Because on the limited amount of ore sample available, a small, pilot scale, ball mill was selected as the grinding unit, with the advantage of allowance for mill holdup retrieval, and sampling. Also, a small scale ball mill is much easier to run under well-controlled and steady grinding conditions.

The particles in the product stream of the ball mill were concentrated by elutriation. An elutriation unit was specially built for this purpose. Elutriation was selected because this process can be modelled easily with basis on particle sedimentation principles, and because the separation density can be controlled by adjusting the flow rates in the elutriator, so that a large fraction of the feed is recovered in the underflow stream, for regrind. This is very important, because it enhances the desired concentration effect.

Unfortunately, it was impossible to run the experiment in a closed, continuous grinding fashion, because on the limited amount of sample available and the incompatibility between flow rates in the mill and elutriation operations. The alternative was to run the experiment in three stages, so as to emulate a close-circuit operation. The

first stage consisted of continuous grinding of freshly crushed Dolomite-Sphalerite. The second stage consisted of the elutriation of the mill product from the first stage. The underflow of the elutriator was then mixed with freshly ground Dolomite-Sphalerite, thus emulating the circulating load in a closed grinding circuit. The third stage consisted of continuous grinding of the mixture. The three stages are illustrated in Figure 4.1. The grinding in the first and third stages were performed under similar operational conditions. The measured Dolomite-Sphalerite particle size distributions in the holdup of the mill and product at steady state allowed the estimation of the selection, breakage and overflow classification processes that describe the comminution process. The measured size distributions and liberation spectra in the streams around the elutriator allowed the estimation of the parameters in the model for the elutriation process.

With the detailed characterization of the unitary operations on hand, the experiment was simulated using MODSIM with the implementation of the model for the internal structure of the accessible region developed in this work, and the calculated liberation spectra were compared to those measured by image analysis.

Transport Characterization of the Experimental Mill

Experimental

The objective of this experiment is the detailed characterization of solid and liquid transport through the experimental mill, using an impulse response test residence-time distribution model. Because on the limited amount of Dolomite-Sphalerite sample available, all preliminary tests in the experimental mill, a 40.64 cm x 40.64 cm (16" x 16") Denver overflow ball mill, were carried out using Limestone as feed material. A

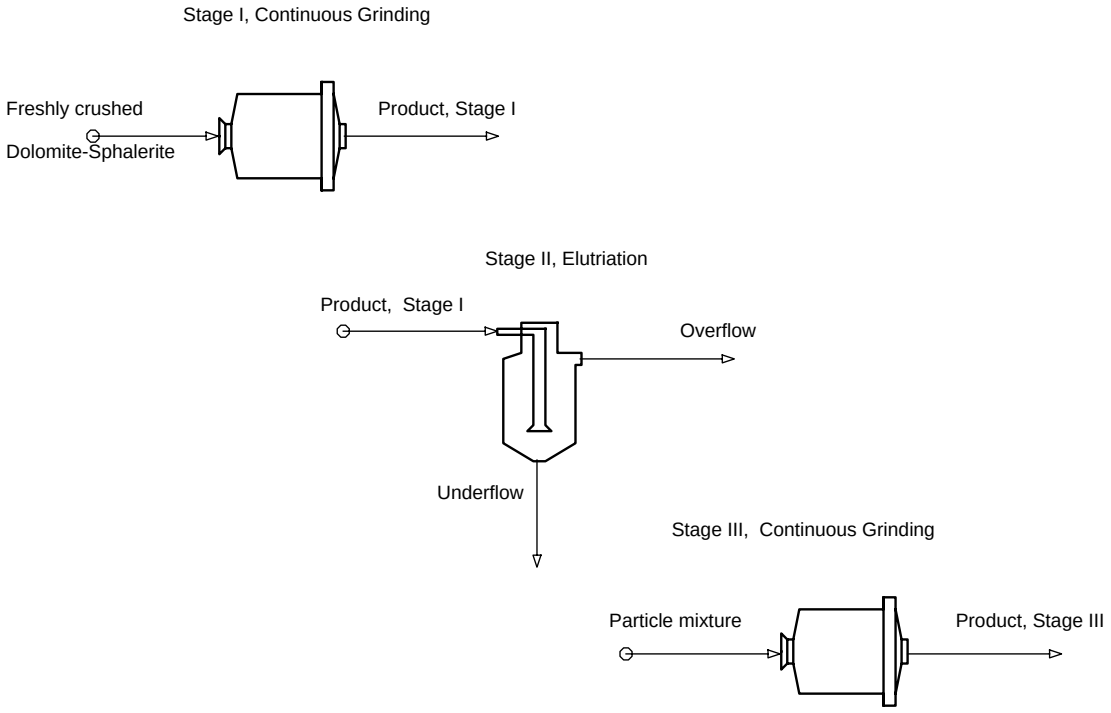

Figure 4.1 The experimental setup for the liberation model verification

total of four Limestone grinding experiments were performed in order to establish good steady state operating conditions for this ball mill, and the experimental setup itself. After this initial testing, two Limestone grinding experiments were performed aimed at establishing the liquid and solids transport characteristics of the experimental mill, namely Tests #5 and #6. Test #5 consisted of measuring the liquid *RTD* in the mill at relatively low solids content in the feed of the mill. Test #6 consisted of measuring solid and liquid *RTD* simultaneously at a relatively higher solids contents in the feed of the mill. Limestone was fed dry through a vibrating feeder. Water was supplied to the mill by a peristaltic pump which maintained a constant flow. The mill was charged with a mix of steel grinding balls having a size distribution given in Table 4.1. The operating conditions in the mill are defined in Tables 4.2 for Test #5 and 4.3 for Test #6. The previous experimental work, namely tests #1 through #4, indicated that the solids holdup in the mill amounted to anywhere between 16.0 kg and 24.0 kg of Limestone, for solid feed rates ranging from 350 to 450 g/min and between 67% to 75% solids in the feed of the mill. Before grinding started, the mill was loaded with the grinding media plus 18.0 kg of Limestone so that steady state operation could be reached in a shorter period of grinding time. Grinding, under the conditions shown in Tables 4.2 and 4.3, was carried out for 2 consecutive hours, so as to ensure steady state operation before sampling. The grinding conditions must be defined in detail, because the average residence time in the mill, and the classification effect at the overflow discharge are very sensitive to the viscosity of the holdup charge, which is directly related to the size distribution and the fraction of solids in the holdup. The mixing pattern is also affected by the viscosity of

Table 4.1 Size distribution of media in the test mill

Ball diameter cm	Cumulative distribution %
5.20	100.0
4.00	92.3
3.20	84.9
2.60	75.2
2.30	52.3
1.90	22.4
1.70	12.2
1.35	6.8
1.25	6.6
1.10	2.6

Table 4.2 Operating conditions in the test mill, Limestone *RTD* Test #5

Mill internal diameter, D_{mill}	38.1 cm
Lifters (6)	1.91 cm high x 6.35 cm wide
Mill internal volume	0.0434 m^3
Formal bed porosity, p_b	0.4
Fraction ball filling, J	0.28
Material tested	Limestone
Powder density	2800 kg/m^3
Fraction of critical speed, ϕ_c	80.0 %
Solid feed rate	0.368 kg/min
Water feed rate	0.144 kg/min
Fraction of solids in mill feed	71.9 %
Holdup of powder	16.790 Kg
Fraction of mill volume filled by powder, f_c	0.230
Powder/ball loading ratio, U	2.1
Average residence time, T	45.63 min

Table 4.3 Operating conditions in the test mill, Limestone simultaneous *RTD* Test #6

Mill internal diameter, D_{mill}	38.1 cm
Lifters (6)	1.91 cm high x 6.35 cm wide
Mill internal volume	0.0434 m^3
Formal bed porosity, p_b	0.4
Fraction ball filling, J	0.28
Material tested	Limestone
Powder density	2800 kg/m^3
Fraction of critical speed, ϕ_c	80.0 %
Solid feed rate	0.410 kg/min
Water feed rate	0.129 kg/min
Fraction of solids in mill feed	76.1 %
Holdup of powder	22.369 Kg
Fraction of mill volume filled by powder, f_c	0.307
Powder/ball loading ratio, U	2.7
Average residence time, T	54.56 min

the holdup. The effect of grinding conditions and mill geometry over grinding efficiency, and a complete discussion on comminution modelling is available in Austin et.al [36]. The fractional ball filling parameter is defined as the fraction of the mill filled by the ball bed at rest,

$$J = \frac{\text{volume of balls}}{\text{mill volume}} \times \frac{1}{1 - p_b} \tag{4.1}$$

where p_b is defined as the formal bed porosity. Similarly, the fraction of mill filled by the powder bed is:

$$f_c = \frac{\text{volume of powder}}{\text{mill volume}} \times \frac{1}{1 - p_b} \tag{4.2}$$

The powder-ball loading ratio is defined by

$$U = \frac{f_c}{p_b J} \tag{4.3}$$

Finally, the fraction of critical speed ϕ_c is defined as the fraction of the critical speed at which the mill is run. The critical speed is the rotational speed at which the balls on the mill just starts to centrifuge,

$$\text{critical speed} = \frac{42.2}{\sqrt{D_{mill} - d_{\max}}} \tag{4.4}$$

where D_{mill} is the internal mill diameter and $d_{\max}$ is the maximum ball diameter. Finally, the average residence time in the mill is defined as in equation 4.5.

$$T = \frac{\text{Holdup of powder}}{\text{Solids feed rate}} \qquad (4.5)$$

The impulse test for the liquid (Tests #5 and #6), consisted of an injection of colored (blue) liquid tracer, actually a food coloring product, directly into the hose between the peristaltic pump and the ball mill. The impulse test for the solid phase in Test #6 consisted of dumping 1 kg of crushed quartz directly into the feed scoop of the mill. The quartz tracer was carefully prepared so that its size distribution matched the size distribution of the Limestone in the feed of the mill. Product sampling started immediately after. Total sampling time lasted approximately 90 minutes in Test #5, during which 45 samples of slurry of about 45 ml were collected in the product stream. Total sampling time extended for over four hours in Test #6 and 74 samples of approximately 45 mL of slurry were collected during this time. Sampling times and the duration of each sample collection are shown in Tables 4.4 and 4.5. Each sample was weighed and then left undisturbed for a full day while particles settled. After settling, a sample of approximately 8 mL was extracted with a syringe from the supernatant in each product sample for liquid tracer concentration analysis. The concentration of liquid tracer in each sample was measured as absorbance, in a spectrophotometer, relative to the absorbance measured for the water used in the experiment. The measured absorbance in each sample is shown in Tables 4.4 and 4.5. The samples collected in Test #6 were then filtered, dried and weighed. The solids contents in each sample is an indication of how steady the mill operation was during the length of the experiment. The resulting percentage of solids in each sample is shown in Table 4.5, and the data clearly indicates

Table 4.4 Sample collection times and measured absorbance for Residence Time Distribution impulse Test #5

Sample number, j	Time interval, min. $t_j^{start} - t_j^{end}$	Absorb.	Sample number, j	Time interval, min. $t_j^{start} - t_j^{end}$	Absorb.
1	0.0000-0.1667	0.0000	25	11.1667-11.3333	0.7794
2	0.1667-0.5000	0.0000	26	11.8333-12.0000	0.7304
3	0.5000-0.8333	0.1035	27	12.5000-12.6667	0.6905
4	1.1667-1.3333	0.4412	28	14.0000-14.1667	0.6144
5	1.5000-1.6667	0.9225	29	14.8333-15.0000	0.5845
6	1.8333-2.0000	1.2617	30	15.8333-16.0000	0.5494
7	2.1667-2.3333	1.3322	31	17.6667-17.8333	0.4877
8	2.5000-2.6667	1.3520	32	18.8333-19.0000	0.4311
9	2.8333-3.0000	1.2952	33	19.8333-20.0000	0.4095
10	3.1667-3.3333	1.4170	34	21.8333-22.0000	0.3458
11	3.5000-3.6667	1.3711	35	24.8333-25.0000	0.2737
12	3.8333-4.0000	1.3712	36	26.8333-27.0833	0.2425
13	4.1667-4.3333	1.3510	37	29.8333-30.0000	0.2110
14	4.6667-4.8333	1.2982	38	34.8333-35.0000	0.1727
15	5.1667-5.3333	1.2884	39	39.9167-40.1167	0.1380
16	5.6667-5.8333	1.1774	40	44.9167-45.0833	0.0935
17	6.1667-6.3333	1.1262	41	49.9167-50.2500	0.0760
18	6.8333-7.0000	1.0068	42	54.9167-55.1667	0.0522
19	7.5000-7.6667	1.0068	43	59.9167-60.1333	0.0365
20	8.1667-8.3333	1.0205	44	69.9167-70.2500	0.0305
21	8.7500-8.9166	0.9665	45	81.0500-81.3833	0.0187
22	9.3333-9.5833	0.9054	46	89.9167-90.3333	0.0075
23	10.0000-10.1667	0.8788			
24	10.6667-10.8333	0.8255			

Table 4.5 Sample collection times, measured absorbance, %Solids and %SiO2 for Residence Time Distribution impulse Test #6 experiment

Sample number, j	Time interval, min. $t_j^{start} - t_j^{end}$	Absorbance	%Solids	%SiO2
1	0.2000-0.3333	0.0000	68.5	3.0943
2	0.6667-0.8000	0.0000	73.5	2.8026
3	1.3667-1.6167	0.0597	72.5	2.4466
4	2.0000-2.3500	1.1124	72.5	3.1299
5	2.5167-2.7167	1.8917	72.9	2.6221
6	2.9167-3.3000	2.4714	72.7	3.1235
7	3.4667-3.7667	2.7295	72.5	2.8782
8	3.9167-4.2333	2.8267	72.9	3.9187
9	4.4000-4.6833	2.7542	73.7	3.0930
10	4.8000-4.9833	2.7328	74.6	4.2736
11	5.1667-5.4000	2.6772	73.0	4.0906
12	5.5667-5.9500	2.6474	72.8	4.1989
13	6.0000-6.4167	2.5951	72.5	3.7561
14	6.8333-7.2167	2.4530	72.7	4.5035
15	8.0000-8.2833	2.2712	73.0	4.0219
16	8.5833-8.8833	2.1581	73.0	6.0891
17	9.1667-9.4833	2.0638	73.7	4.4109
18	9.6500-9.9500	2.0221	72.9	5.0253
19	10.3333-10.4667	1.9267	73.7	5.4065
20	11.0000-11.2833	1.8664	73.1	4.8970
21	11.5333-11.8333	1.7692	74.2	5.1590
22	12.5000-12.5333	1.6944	73.5	5.2785
23	13.0000-13.3000	1.6172	74.2	5.3147
24	13.7500-14.0667	1.5191	73.6	5.3214
25	14.7500-15.0000	1.3998	76.2	5.7658

Table 4.5 Continued

Sample number j	Time interval, min. $t_j^{start} - t_j^{end}$	Absorbance	%Solids	%SiO2
26	15.7500-16.0000	1.3208	74.9	5.2238
27	16.7500-17.1000	1.2465	75.1	5.6704
28	17.7500-18.0167	1.1424	76.1	5.7580
29	18.7500-18.9833	1.0574	77.4	5.5463
30	19.7500-20.0500	1.0088	75.9	6.3302
31	20.7500-21.2833	0.9498	74.5	5.5223
32	21.7500-22.0667	0.9041	75.9	5.9733
33	22.7500-22.8500	0.8175	77.3	6.6493
34	23.7500-24.0000	0.7824	75.8	5.6176
35	24.7500-25.1333	0.7270	76.0	6.5738
36	25.7500-25.9667	0.6878	76.6	5.2815
37	26.7500-27.0333	0.6545	75.6	5.3481
38	27.7500-27.8667	0.6210	75.7	5.9999
39	28.7500-29.1000	0.5787	75.3	5.8008
40	29.7500-30.1000	0.5372	75.9	5.5125
41	31.0000-31.3333	0.5058	75.5	5.4615
42	33.1667-33.4667	0.4482	72.3	5.3492
43	35.3333-35.6167	0.3972	72.2	6.3316
44	37.5000-38.0833	0.3531	75.5	5.4568
45	40.0000-40.2000	0.3088	76.5	5.2832
46	42.2500-42.7167	0.2752	76.7	5.6564
47	45.0000-45.3833	0.2505	77.2	5.2578
48	48.5000-48.8500	0.1984	76.0	4.9158
49	51.0000-51.3167	0.1824	75.4	5.1232
50	53.5000-53.7500	0.1651	75.8	5.0709

Table 4.5 Continued

Sample number j	Time interval, min. $t_j^{start} - t_j^{end}$	Absorbance	%Solids	%SiO2
51	56.0000-56.2667	0.1494	75.7	4.7206
52	58.5000-58.7833	0.1361	75.2	4.3255
53	62.0000-62.3333	0.1211	75.4	4.6382
54	67.2500-67.5000	0.0928	77.2	4.1427
55	72.5000-72.7667	0.0800	75.6	4.1041
56	78.0000-78.4667	0.0671	76.4	3.3407
57	84.0000-84.3000	0.0582	77.4	4.0833
58	90.0000-90.3000	0.0518	76.6	3.6374
59	97.5000-97.9000	0.0415	76.2	3.7458
60	105.0000-105.3833	0.0370	77.4	3.1409
61	112.5000-112.8167	0.0358	77.3	3.4089
62	120.0000-120.3000	0.0305	77.7	3.2459
63	130.0000-130.3000	0.0290	77.1	3.2689
64	140.0000-140.4167	0.0265	76.7	3.0440
65	150.0000-160.1667	-	77.8	2.8306
66	160.0000-160.4000	-	76.8	2.7560
67	170.0000-170.2000	-	77.1	3.0765
68	180.0000-180.3333	-	77.8	3.0153
69	190.0000-190.1667	-	78.1	2.9960
70	200.0000-200.2833	-	80.0	3.2450
71	210.0000-210.4333	-	75.9	3.1267
72	220.0000-220.6333	-	77.4	2.8361
73	230.0000-230.3000	-	76.5	2.9265
74	240.0000-240.1667	-	76.0	2.7806

that no significant changes in the operational conditions took place during the length of the simultaneous *RTD* Test #6. The average percentage of solids for the test was 75.24% with a standard deviation of only 1.934%. The variation of solids content with time during the sampling period is shown in Figure 4.2. Clearly, the average fraction of solids shifted from an average of about 74% in the first 30 minutes of the test, to an average of about 77% for the remaining of the test duration. Nevertheless, the shift was not dramatic, and the small standard deviation from the average indicates it was not significant, and no impact on the measured *RTD* should be expected.

A sample weighing approximately 1.5 g was taken from each dry product sample, using the PULVERIT™, for solid tracer concentration analysis. The concentration of solid tracer (SiO_2) was measured by X-Ray fluorescence, and the results from this measurement are also shown in Table 4.5. These silica assays indicate that the Limestone used contains significant amounts of silica, since the measured concentration of silica never vanished for the length of the experiment. The amount of silica in the Limestone was determined by reacting the Limestone with Sulfuric Acid, thus eliminating the carbonates. The residue was qualitatively accessed by X-Ray diffraction, and fortunately contained Quartz only. The weight fraction of residue is, therefore, equal to the fraction of natural silica in the Limestone, and this was $\%SiO_2^{Limestone} = 2.831$.

One duplicate product sample was taken at the end of *RTD* Test #5 weighing approximately 2.0 kg each, while two large product samples were taken during *RTD* Test #6, the first after 170 minutes of grinding and the second after 230 minutes, weighing approximately 2.7 kg each. All samples were dried and the size distribution in the

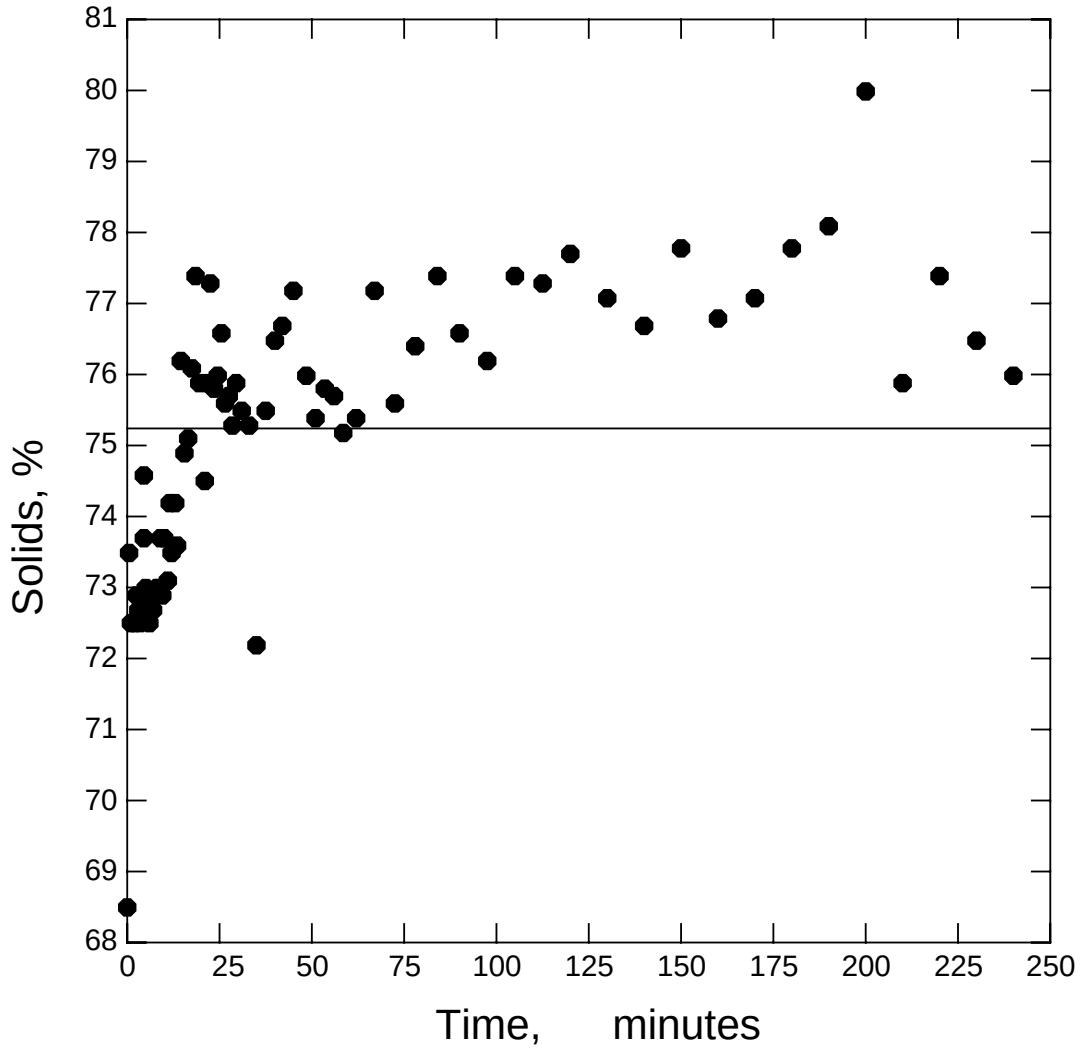

Figure 4.2 The measured percentage of of solids in the product of the test mill during the *RTD* Test #6

product of the mill was measured by standard screening. At the time the experiments were completed, the mill was stopped and the surge collected. The mill was then opened, and the holdup recovered together with the grinding media. After separating the particles from the grinding media, the entire lot representing the solids holdup plus surge was filtered and dried. The total weight of solids in the holdup measured 16.79 kg in Test #5 and 22.36 kg in Test #6. The holdup particles were homogenized and duplicate samples were taken for size distribution analysis. The size distribution in the feed of the mill was also measured in duplicate, and the resulting average size distributions are reported in Tables 4.6 and 4.7.

Residence Time Distribution Function

The response $r\langle t\rangle$ for N unequal fully mixed reactors in series to an impulse test is given in equation 4.6 [36].

$$r\langle t\rangle = \sum_{i=1}^{N} \frac{\tau_i^{N-2} \exp(-t/\tau_i)}{\prod_{k=1}^{N} (\tau_i - \tau_k)}, \qquad i \neq k \tag{4.6}$$

where τ_i is the mean residence time in fully mixed reactor *i*. It is necessary to incorporate in equation 4.6 the time delay resulting from the distance-velocity lag in the water feed hose or the solids feed scoop from the injection point to the mill entrance. This will shift the distribution density in equation 4.6 in the positive direction of time *t*,

Table 4.6 Measured cumulative size distributions in the feed, holdup and product of the mill in *RTD* impulse Test #5

Size interval, microns	Feed, % F_i	Holdup, % H_i	Product, % P_i
-5600+4750	100.00	100.00	100.00
-4750+3350	99.58	99.85	100.00
-3350+2800	73.26	93.68	99.97
-2800+2000	55.11	89.98	99.92
-2000+1400	19.77	84.51	99.50
-1400+1000	7.05	80.60	98.33
-1000+710	5.06	78.24	96.62
-710+500	4.15	76.16	94.58
-500+355	3.65	74.42	92.79
-355+250	3.15	71.91	89.93
-250+180	2.76	68.31	85.69
-180+150	2.51	64.12	80.72
-150+106	2.40	62.00	78.03
-106+75	2.13	54.82	69.29
-75+53	1.85	47.03	59.52
-53+45	1.07	40.41	51.90
-45+38	0.91	37.47	48.05
-38	0.55	34.46	43.90

Table 4.7 Measured cumulative size distributions in the feed, holdup and product of the mill in *RTD* impulse Test #6

Size interval, microns	Feed, % F_i	Holdup, % H_i	Product, % P_i
-5600+4750	100.00	100.00	100.00
-4750+3350	99.93	100.00	100.00
-3350+2800	76.94	97.07	98.46
-2800+2000	55.77	94.46	96.67
-2000+1400	16.82	89.31	93.41
-1400+1000	4.09	85.32	90.47
-1000+710	3.01	83.09	88.64
-710+500	2.63	81.03	86.97
-500+355	2.46	79.36	85.55
-355+250	2.29	76.89	83.11
-250+180	2.15	73.23	79.16
-180+150	2.05	68.57	74.11
-150+106	2.01	66.01	71.37
-106+75	1.72	57.58	62.49
-75+53	1.48	48.78	53.14
-53+45	0.81	41.84	45.81
-45+38	0.60	38.61	42.45
-38	0.36	35.84	39.51

$$r(t) = \sum_{i=1}^{N} \frac{\tau_i^{N-2} \exp(\frac{t_d - t}{\tau_i})}{\prod_{k=1}^{N} (\tau_i - \tau_k)}, \qquad i \neq k \tag{4.7}$$

where t_d represents the time lag. The tracer concentration distribution is proportional to the density distribution $r(t)$, i.e.

$$r(t) = \frac{c(t)}{\int_0^{\infty} c(t)\, dt} \tag{4.8}$$

thus, the tracer concentration distribution can be written as:

$$c(t) = \mathrm{K} \sum_{i=1}^{N} \frac{\tau_i^{N-2} \exp(\frac{t_d - t}{\tau_i})}{\prod_{k=1}^{N} (\tau_i - \tau_k)}, \qquad i \neq k \tag{4.9}$$

where the proportionality constant K is defined as:

$$\mathrm{K} = \int_0^{\infty} c(t)\, dt \tag{4.10}$$

In equation 4.6, $c(t)$ is used to represent either the absorbance or the percentage of silica at any time *t*. The experimental setup allowed for collecting a large sample, relative to the slurry flow rate through the mill, when comparing to samples taken from large scale mills operating with much larger slurry throughput. In Test #5, sampling time was kept at about 20 seconds throughout the length of the experiment, while sample volume changed according to the throughput natural oscillation. In Test #6, sampling times

varied from 6 to as much as 38 seconds, as shown in Table 4.5. Average sampling time was 18.135 seconds with a standard deviation of 5.93 seconds. The oscillation in sampling time is basically due to the natural oscillation of throughput in the mill which reflects small variations in the operation variables of the mill, and because sample volume was not exactly constant during sampling time. Equation 4.9 can be modified to correct for the sampling time interval, by integrating over the length of time between the starting collection time of sample *j*, t_j^{start}, and the time at which sample collection ended, t_j^{end}, i.e.

$$c^j = \frac{1}{t_j^{end} - t_j^{start}} \int_{t_j^{start}}^{t_j^{end}} c(t)\, dt \tag{4.11}$$

assuming constant flowrate during the collection time interval. Substituting equation 4.9 into equation 4.11,

$$c^j = \frac{\mathrm{K}}{t_j^{end} - t_j^{start}} \sum_{i=1}^{N} \frac{\tau_i^{N-2} \left(\exp\left(\frac{t_d - t_j^{start}}{\tau_i}\right) - \exp\left(\frac{t_d - t_j^{end}}{\tau_i}\right) \right)}{\prod_{k=1}^{N} (\tau_i - \tau_k)}, \qquad i \neq k \tag{4.12}$$

Equation 4.12 is the working equation for the liquid *RTD* modelling, and it can be written in terms of the measured absorbance of each sample *j*, without further modification, as shown in equation 4.13.

$$absorbance^j = \frac{\mathrm{K}}{t_j^{end} - t_j^{start}} \sum_{i=1}^{N} \frac{\tau_i^{N-2} \left(\exp\left(\frac{t_d - t_j^{start}}{\tau_i}\right) - \exp\left(\frac{t_d - t_j^{end}}{\tau_i}\right) \right)}{\prod_{k=1}^{N} (\tau_i - \tau_k)}, \qquad i \neq k \tag{4.13}$$

For the solids *RTD*, however, equation 4.12 cannot be used directly because the Limestone contains natural SiO_2, and the measured sample concentrations are shifted upwards by an amount equivalent to the concentration of silica in the Limestone, $\%SiO_2^{Limestone}$. Therefore, the correct form of equation 4.12 for the solids *RTD* in this experiment is:

$$\%SiO_2{}^{j} = \frac{K}{t_j^{end} - t_j^{start}} \sum_{i=1}^{N} \frac{\tau_i^{N-2}\left(\exp\left(\frac{t_d - t_j^{start}}{\tau_i}\right) - \exp\left(\frac{t_d - t_j^{end}}{\tau_i}\right)\right)}{\prod_{k=1}^{N}(\tau_i - \tau_k)} + \%SiO_2^{Limestone}, \quad i \neq k \tag{4.14}$$

Residence Time Distribution Test Results

The measured concentration response was found to fit the response to three perfectly mixed regions in series for both solid and liquid phases. The results are summarized in Table 4.8 and the best fits from equations 4.13 and 4.14 are shown in Figures 4.3 and 4.4. The average residence time in the mill is calculated by adding the average residence time in each perfectly mixed reactor. This yields 54.88 minutes for the solids. Liquid average residence times were 13.98 minutes for Test #5 and 16.17 minutes for Test #6. It is possible to check the calculated average residence time of the solids in the mill because the solids feed rate to the mill and the total weight of solids in the holdup of the mill were measured (Tables 4.2 and 4.3), and this yields 16.790/0.368 = 45.63 minutes for Test #5 and 22.369/0.410 = 54.56 minutes for Test #6. It is very unlikely that the average solids residence time calculated by both methods in Test #6

Table 4.8 The solid and liquid phases *RTD* parameters and corresponding fractional residence times

Parameter	Liquid *RTD*, Test #5	Liquid *RTD*, Test #6	Solid *RTD*, Test #6
Time delay, t_d	0.85	1.57	1.62
Proportionality constant, K	21.46	49.19	211.88
τ_1, minutes (τ_1/T)	0.37 (.026)	0.38 (.024)	0.75 (.014)
τ_2, minutes (τ_2/T)	0.39 (.028)	0.63 (.039)	11.65 (.212)
τ_3, minutes (τ_3/T)	13.22 (.946)	15.15 (.937)	42.48 (.774)
Average residence time $T = \tau_1 + \tau_2 + \tau_3$, minutes	13.98	16.17	54.88

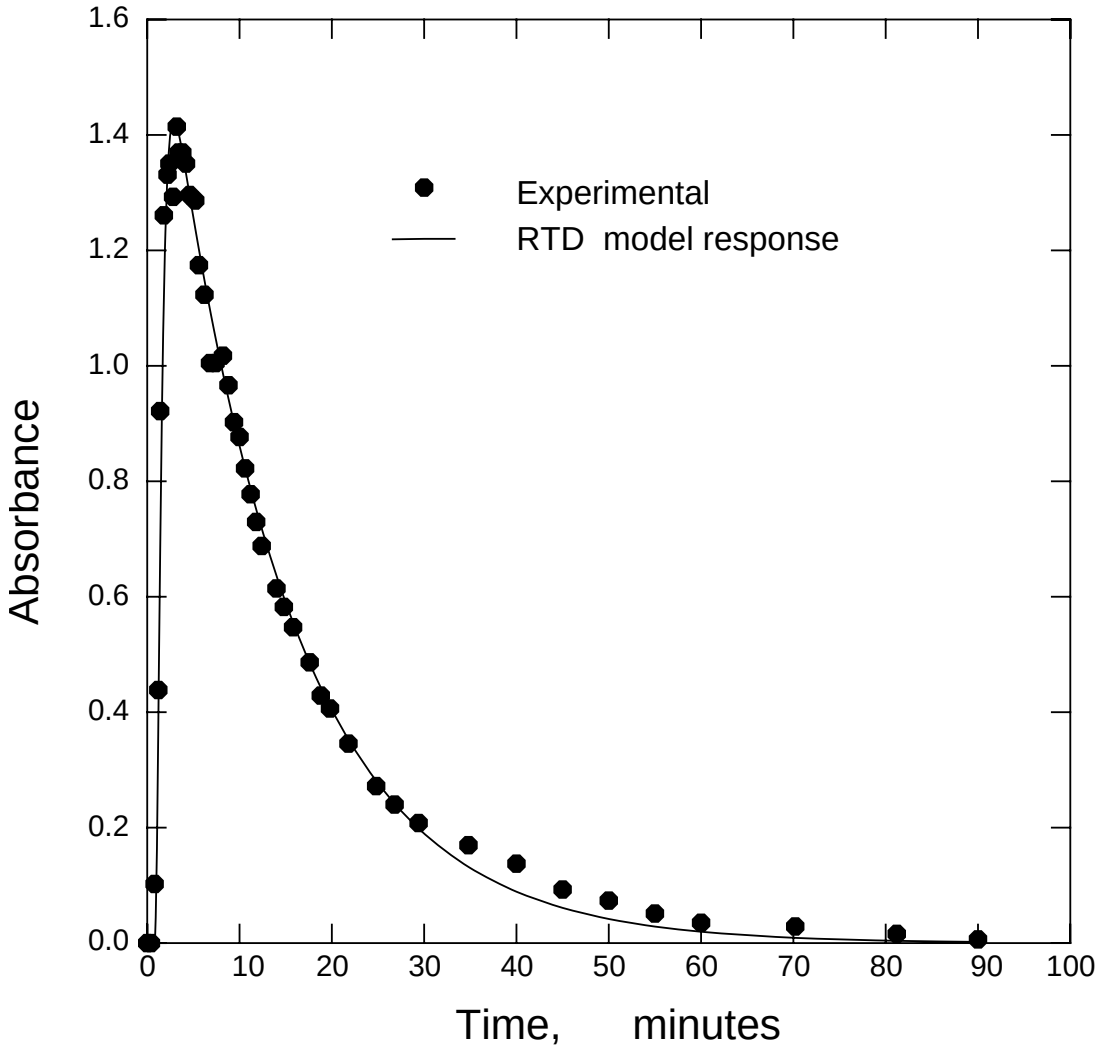

Figure 4.3 The measured and calculated Residence Time Distribution for the liquid in Test #5

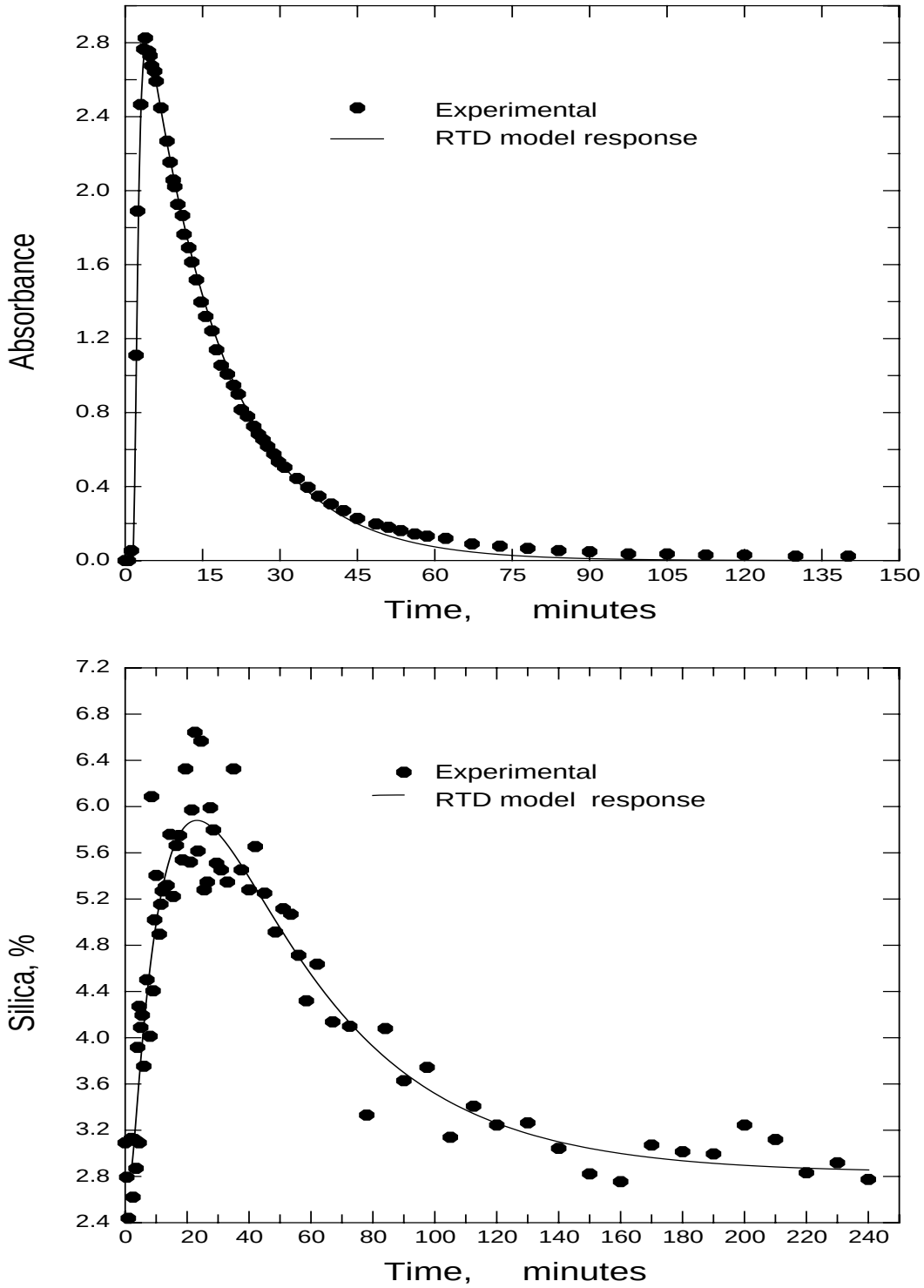

Figure 4.4 The measured and calculated Residence Time Distribution for the liquid (top) and solid (bottom) phases in Test #6

would be so very close to each other, when considering all the errors involved in running the experiment at steady, well-controlled conditions, sampling, assaying, modelling and the like. Nevertheless, this is a good indication that the experiment was indeed performed with great care.

The large difference between solid and liquid residence time is due to the higher solid particles feed rate to a constant internal mixing volume of the mill. The water holdup in the mill can be calculated from the average residence time of water for the liquid *RTD*, and this yields 0.144x13.98 = 2.01 kg for Test #5 and 0.129x16.17 = 2.08 kg for Test #6. With this, it is possible to calculate the fraction of solids in the holdup of the mill, a number worthwhile reporting. This was 89.31% for Test #5 and 91.49% for Test #6. Both numbers are considerably higher then the average fraction of solids in the feed of 71.9% and 76.1%, and it is interesting to point out that the solids fraction in the holdup of the mill is very difficult to measure directly or indirectly by other methods.

The residence time distribution impulse test is incapable of indicating the order of the fully mixed regions that describe the mixing pattern in the mill, because the response to the tracer does not depend on the order of mixers, i.e., equation 4.6 is symmetric about τ_i, for all *i*. Weller [37] has also reported three perfectly mixed regions in series, and favored a big-small-small mixing pattern. In fact, when there is no classifying action in the mill discharge, the order of mixers does not influence the size distribution in the mill holdup or product, as calculated by population balance modelling. However, when classification is considered, the size distributions in the mill holdup and product are fairly sensitive to the mixer order. No doubt, the relevance of the classifying

action for the experimental mill used here must be accessed, and the mixer order established. This can be done by determining the best mixer order that describes the size distributions in the holdup and product of the mill as calculated by a comminution model based on the population balance approach.

Comminution Model and Mixer Order

The standard particle population balance equations can be written for each perfectly mixed region to give:

$$p_i^{(1)} = \frac{f_i + \tau_1 \sum_{j=1}^{i-1} b_{ij} S_j p_j^{(1)}}{1 + \tau_1 S_i} \tag{4.15}$$

$$p_i^{(2)} = \frac{p_i^{(1)} + \tau_2 \sum_{j=1}^{i-1} b_{ij} S_j p_j^{(2)}}{1 + \tau_2 S_i} \tag{4.16}$$

$$p_i^{*} = \frac{p_i^{(2)} + \tau_3' \sum_{j=1}^{i-1} b_{ij} S_j p_j^{*}}{1 + \tau_3' S_i - C_i} \tag{4.17}$$

where

$$\tau_3' = \frac{\tau_3}{\sum_i p_i^{*}} \tag{4.18}$$

$$p_i^{(3)} = \frac{p_i^*}{\sum_i p_i^*} \tag{4.19}$$

$$p_i = (1 - C_i)\, p_i^* \tag{4.20}$$

The size distribution in the holdup of the mill h_i was calculated as the weighted, by τ_n, sum of the size distributions in each fully mixed region, i.e.

$$h_i = \frac{\tau_1 p_i^{(1)} + \tau_2 p_i^{(2)} + \tau_3 p_i^{(3)}}{\tau} \tag{4.21}$$

Here $p_i^{(n)}$ represents the mass fraction in size class *i* in section *n*, C_i is the classification function for size class *i*, *b* represents the breakage function, *S* represents the rate of breakage (selection function), τ_n is the average residence time in section *n* and f_i and p_i represent the size distributions in the feed and product from the mill respectively. Equations 4.15 to 4.20 cannot be solved recursively because τ_3' must be obtained iteratively. Fortunately, equations 4.17 and 4.18 converge rapidly by direct substitution so the solution is straightforward.

The selection, breakage and classification functions were modeled as shown in equations 4.22, 4.23 and 4.24.

$$S_i = S_1 \frac{\left(\frac{d_{pi}}{1000}\right)^{\alpha}}{1 + \left(\frac{d_{pi}}{\mu}\right)^{\Lambda}} \tag{4.22}$$

$$B_{ij} = \Phi\left(\frac{d_{pi}}{d_{pj}}\right)^{\gamma} + (1-\Phi)\left(\frac{d_{pi}}{d_{pj}}\right)^{\beta} \tag{4.23}$$

$$C_i = \frac{1}{1+\left(\frac{d_{pi}}{d_{50}}\right)^{\rho}} \tag{4.24}$$

The size distribution of the product and the mill holdup were simultaneously fitted, using the model above and all combinations of mixing orders with and without postclassification in the last mixing region. The results from Test #5 indicated that the best mixing order was the smallest-small-big pattern, with postclassification. The parameters that minimized the sum of squares of residuals between measured and calculated holdup and product size distributions simultaneously are shown in Table 4.9. The experimental data and the model response are shown in Figure 4.5. The results from Test #6 indicated no postclassification, and the mixing order was therefore irrelevant. The model parameters are shown in Table 4.9 and the experimental data and model response in Figure 4.6.

Tests #5 and #6 were carried out under very similar operating conditions, with the exception of the solids contents in the feed stream, which was higher by only 4% in Test #6. Despite of the slight difference in feed solids content and feed rate between the two tests, mill holdups differed by as much as 5.6 kg, and the average residence time of the solids shifted by nine minutes, which represent a very significant fractional change. Also, Test #5 results clearly indicated a strong classification effect in the overflow discharge

Table 4.9 The set of selection, breakage and classification function parameters that best fit the size distributions of the Limestone particles in the holdup and product of the mill under the grinding conditions in Tests #5 and #6 and the Residence Time Distribution of solids measured in Test #6

	Selection Function				Breakage function			Classifier	
	α	S_1, min^{-1}	μ, microns	Λ	Φ	β	γ	d_{50}, microns	ρ
Test #5	0.84	0.26	1767.1	2.66	0.83	0.40	1.30	1339.9	3.45
Test #6	1.18	0.26	1495.6	2.46	0.50	0.46	1.81	-	-

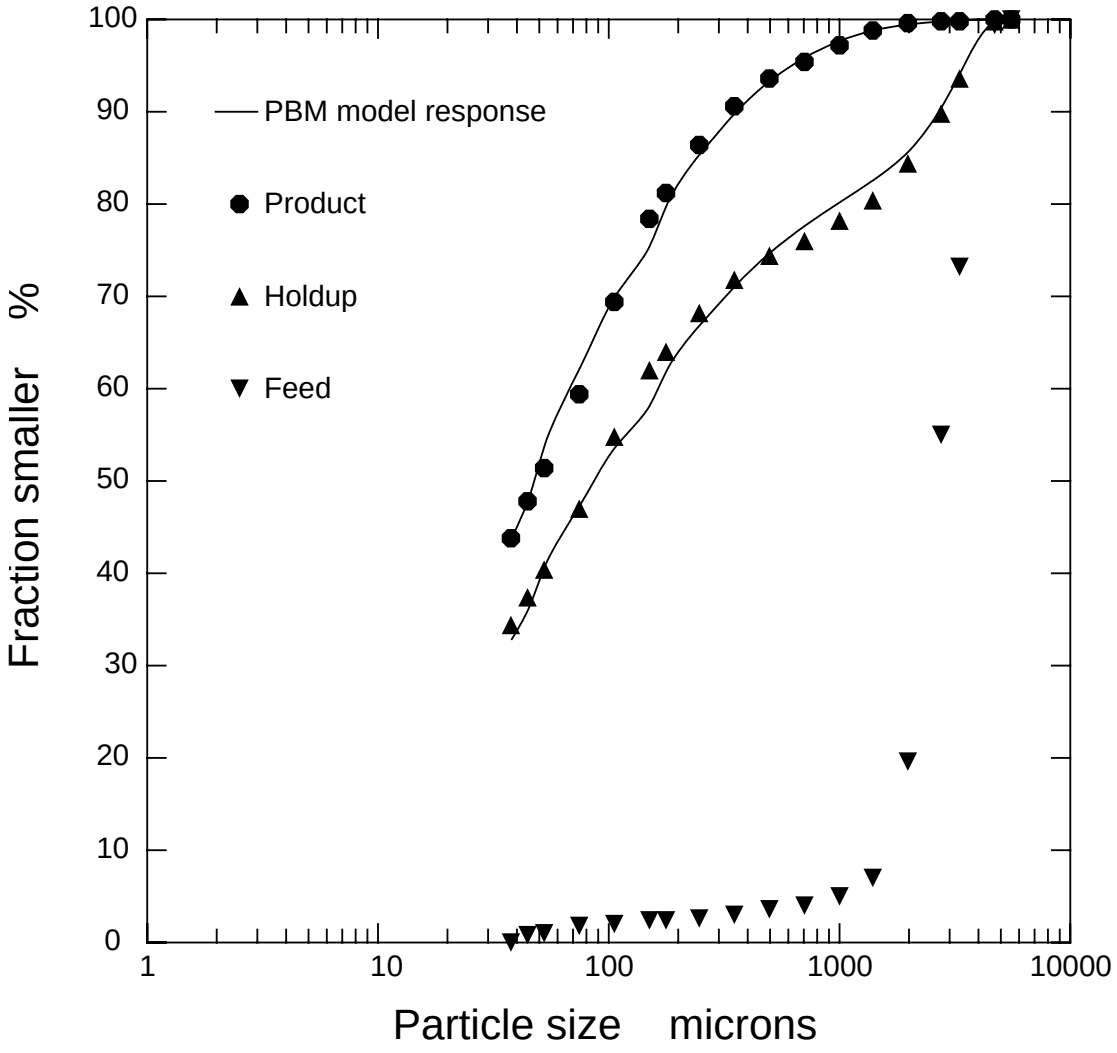

Figure 4.5 Experimentally determined particle size distributions in the mill and *PBM* model responce in Test #5

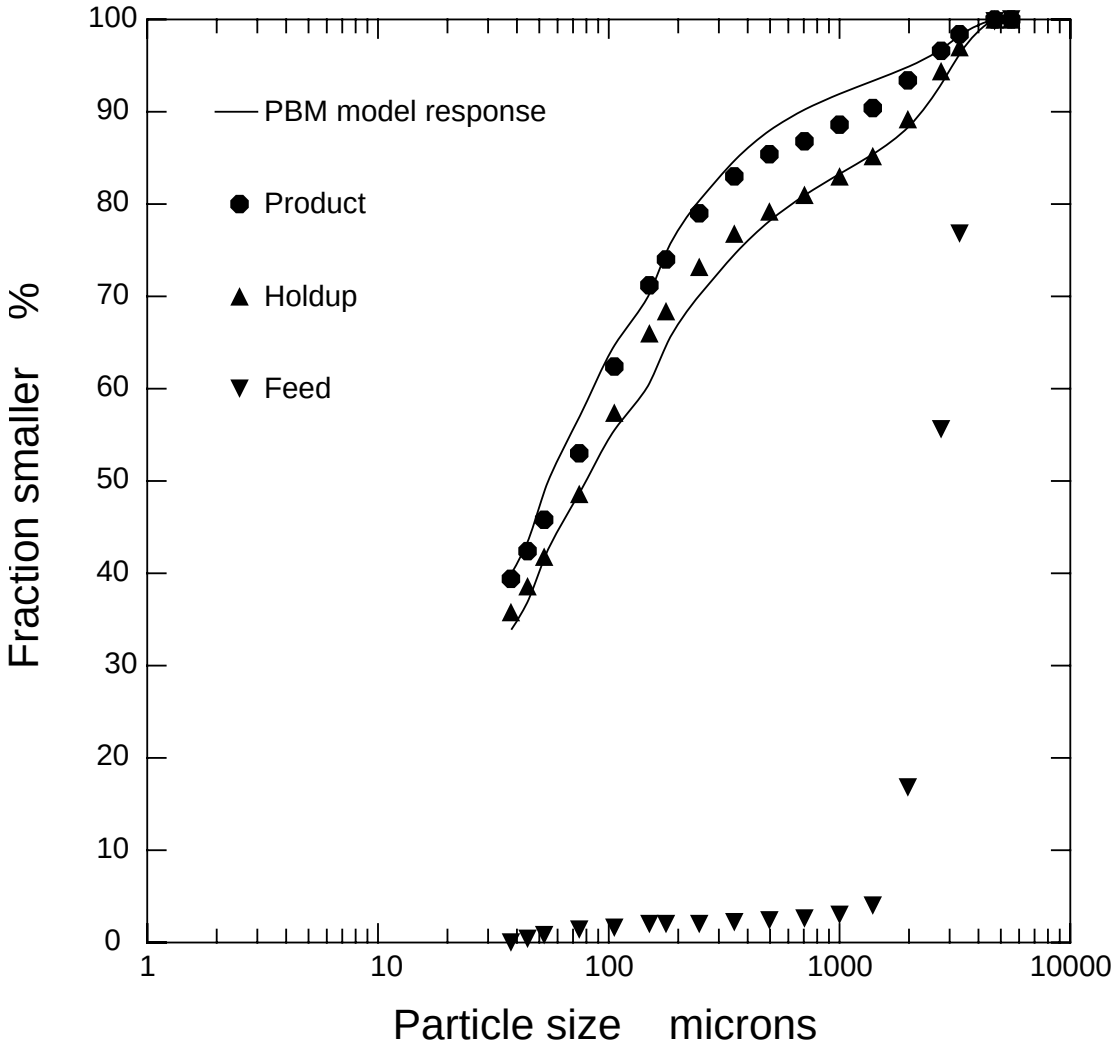

Figure 4.6 Experimentally determined particle size distributions in the mill and *PBM* model responce in Test #6

of the mill, while Test #6 results indicated that no classification in the overflow discharge took place. This is easily detected by comparing Figures 4.5 and 4.6. The holdup size distribution in Test #5 was significantly different from that in the product, and optimization required the classification model in the last perfectly mixed mill region. Also, the smallest-small-large mixer order was necessary to produce a better fit with respect to the measured distributions. The large difference between the holdup and product size distributions is due to the trapping of larger solid particles in the mill by the classifying action of the mill discharge. In Test #6 the difference between the holdup and product size distributions is not quite as significant, and it can be accounted for by modeling with three perfectly mixed regions in series with no postclassification. This leads to the conclusion that the intensity of the classifying action at the overflow discharge is very sensitive to the rheology of the holdup in the mill. Unfortunately, the rheology of the holdup is dependent not only on the solids content, but is also a strong function of the size distribution in the holdup. This makes it very difficult to predict whether postclassification will be present under specific grinding conditions. Fortunately, as shown here, it is possible to access the presence of postclassification by optimization, when the size distribution in the holdup of the mill is known. When no information on the size distribution of the holdup is available, classification effects cannot be accessed properly. Actually, good parameterization by means of *PBM* modelling is only possible from continuous grinding experiments when both the size distributions in the holdup and product of the mill are known.

Dolomite-Sphalerite Emulated Closed Continuous Grinding Experiment

Experimental

The experimental setup was divided in two open circuit continuous grinding stages separated by an elutriation stage. The first stage consisted of grinding of freshly crushed Dolomite-Sphalerite ore in the experimental mill. The second stage consisted of the elutriation of the milled product generated in the first stage. This was the concentration step. The elutriator underflow, richer in Sphalerite and finer than the original crushed Dolomite-Sphalerite, was the target product of the second stage. These particles were mixed evenly with freshly crushed Dolomite-Sphalerite, and the mixture was used as feed material to continuous grinding in the third stage, thus emulating the grinding conditions in a closed circuit.

A total 150 kg of Dolomite-Sphalerite was crushed below 1000 microns. The crushing procedure was designed to avoid exaggerated generation of fine particles. The procedure is described in detail in the experimental section of Chapter 2.

The mill was initially filled with 18 kg of crushed Dolomite-Sphalerite before grinding started, in order to achieve steady state in a shorter period of grinding time. Grinding conditions in Stage I are summarized in Table 4.10. Continuous grinding was carried out for 20 minutes before product collection started. Product samples were collected after 30 minutes and after 80 minutes of grinding. After 100 minutes of continuous grinding, the mill was shut and the surge collected. Immediately after shutdown, the mill was emptied and the particles in the holdup separated from the

Table 4.10 Operating conditions in the test mill, Stage I, Dolomite-Sphalerite grinding

Mill internal diameter, D_{mill}	38.1 cm
Lifters (6)	1.91 cm high x 6.35 cm wide
Mill internal volume	0.0434 m^3
Formal bed porosity, p_b	0.4
Fraction ball filling, J	0.28
Material tested	Dolomite-Sphalerite
Powder density	2982 Kg/m^3
Fraction of critical speed, ϕ_c	80.0 %
Solid feed rate	0.809 Kg/min
Water feed rate	0.389 Kg/min
Fraction of solids in mill feed	67.55 %
Holdup of powder	18.394 Kg
Fraction of mill volume filled by powder, f_c	0.237
Powder/ball loading ratio, U	2.1
Average residence time, T	22.74 min

grinding media. Total weight of holdup plus surge (solids) was 18.4 kg. Total amount of product (solid) collected during the experiment was 72.8 kg. After homogenization, the holdup was sampled. Product and holdup size distributions were measured by standard sieving procedures and the material in each size fraction sampled for image analysis using the PULVERIT™.

The remaining product of the first grinding stage was used as feed material for the elutriation in Stage II. The plexiglass elutriator used in this experiment was originally built as a prototype for a flotation column, and then modified accordingly to perform as an elutriator. A sketch of the device, along with its dimensions, is shown in Figure 4.7. The particles were fed to the elutriator at 30% solids through three peristaltic pumps working in parallel. The feed slurry was kept homogeneous by means of a strong propeller inserted in a 220 liter feed sump. The flow rate through the underflow was controlled manually, and the underflow valve was opened and closed according to the accumulation of particles in the underflow section of the elutriator. Because on this, the underflow flowrate varied considerably during the length of the experiment, and could not be measured. The overflow flowrate varied along with that of the underflow, and this also could not be measured accurately. However, the total amounts of solid and water in both streams were measured after the experiment was completed, and the average flowrates to both streams could be estimated based on the total elutriation time, which took 36 minutes to complete. Approximately 5 kg of solids were lost in the sump/column holdup after elutriation was completed. The elutriation results are summarized in Table 4.11. The underflow and overflow from elutriation were filtered, dried and homogenized,

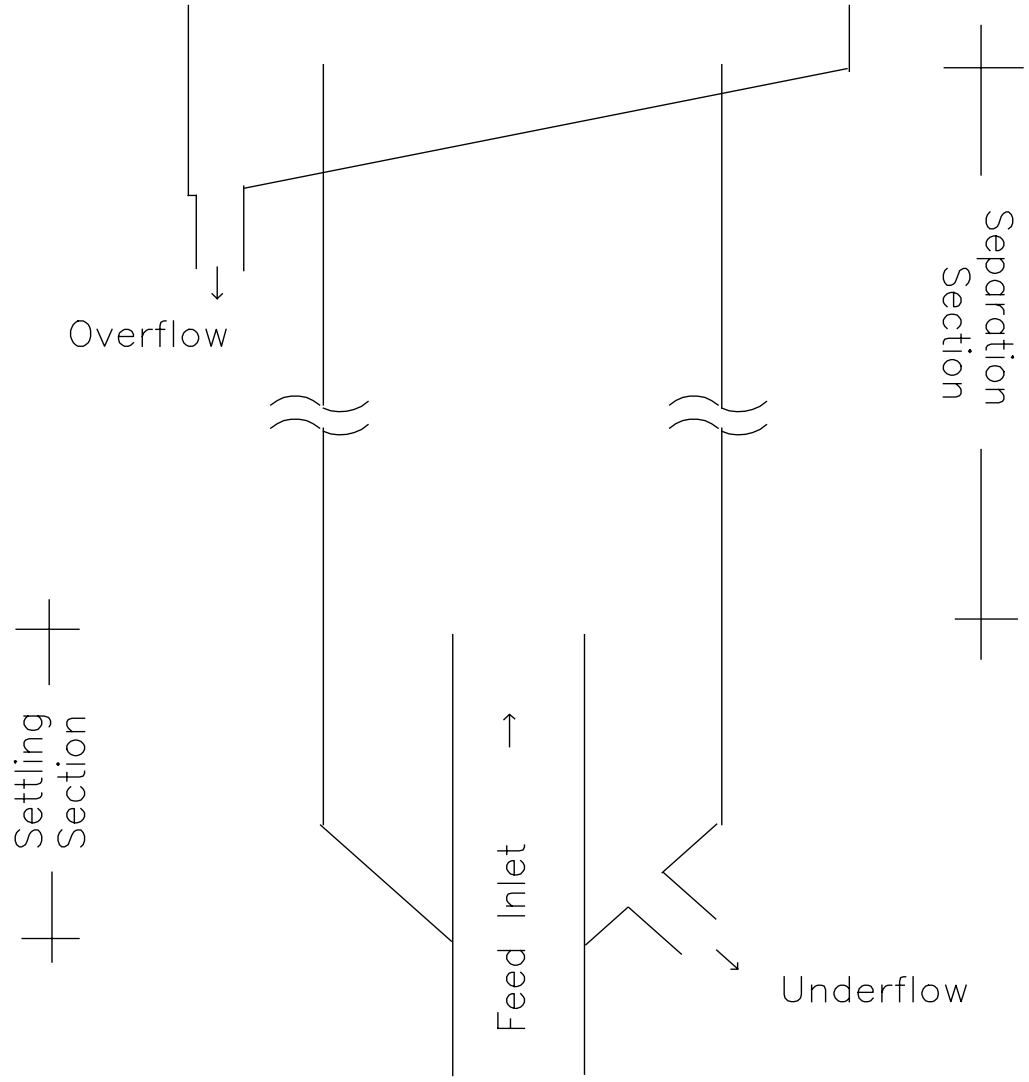

Elutriator Dimensions (cm)	
Inlet i.d.	2.54
Separation section i.d.	10.80
Settling section length	36.80
Separation section length	101.60

Figure 4.7 The plexiglass elutriation column used in Stage II

Table 4.11 Elutriation experimental results

	Feed	Holdup	Overflow	Underflow
Total solids, (g)	72,800	4,898	40,593	27,309
Total water, (g)	170,000	10,000	132,800	27,200
% solids	30.0	32.9	23.4	50.1
Recovery of solids, %	107.2	7.2	59.8	40.2
Recovery of water, %	106.25	6.25	83.0	17.0
Water flowrate, g/min	4,722.2	277.8	3,688.9	755.6

and a sample of each, weighing approximately 1.6 kg, were taken by riffling. These samples were used for size distribution determination by standard sieving procedures. Each size fraction were then sampled for image analysis, using the PULVERIT™.

The remaining underflow particles, weighing approximately 25.6 kg were mixed with another 25.6 kg of the freshly crushed Dolomite-Sphalerite particles and the mixture homogenized thoroughly. The resulting mixture was the feed particles for continuous grinding in Stage III. In this stage, the test mill was initially filled with the remaining holdup particles from Stage I. Grinding conditions in Stage III are summarized in Table 4.12. Product samples were collected after 35 and 50 minutes of continuous grinding. The mill was shut right after collection of the second product sample, and the surge was collected. The mill was then emptied and the particles in the holdup separated from the grinding media. Total weight of holdup plus surge (solids) was 19.7 kg. The holdup was filtered, dried, homogenized and sampled, by riffling, for size distribution. The product samples were weighed, filtered and dried for size analysis and solids content. Again, each size fraction in the holdup and product were sampled using the PULVERIT™ for image analysis.

The size distributions corresponding to each sample in each stage of the experiment and the calculated size distribution of the particle mixture used as the feed of Stage III are given in Table 4.13. Each size fraction in each stream was sampled for image analysis. Sample preparation procedures, including mounting, grinding, polishing and carbon coating, image acquisition and image processing were carried out as described in the experimental sections of Chapters 2 and 3. A total 3,861 images were acquired and

Table 4.12 Operating conditions in the test mill, Stage III, Dolomite-Sphalerite grinding

Mill internal diameter, $D_{\min}$	38.1 cm
Lifters (6)	1.91 cm high x 6.35 cm wide
Mill internal volume	0.0434 m^3
Formal bed porosity, p_b	0.4
Fraction ball filling, J	0.28
Material tested	Dolomite-Sphalerite
Powder density	2982 Kg/m^3
Fraction of critical speed, ϕ_c	80.0 %
Solid feed rate	0.934 Kg/min
Water feed rate	0.378 Kg/min
Fraction of solids in mill feed	71.15 %
Holdup of powder	19.714 Kg
Fraction of mill volume filled by powder, f_c	0.254
Powder/ball loading ratio, U	2.1
Average residence time, T	20.82 min

Table 4.13 The measured size distributions in the Dolomite-Sphalerite continuous grinding experiment

	Stage I	Stage II				Stage III		
	Cumulative Size Distributions, %							
Size interval, microns	Ball Mill Feed	Ball Mill Holdup	Ball Mill Product Elutriator Feed	Elutriator Overflow	Elutriator Underflow	Ball Mill Feed (calculated)	Ball Mill Holdup	Ball Mill Product
-1000+710	100.00	100.00	100.00	100.00	100.00	100.00	100.00	100.00
-710+500	93.35	99.75	99.90	100.00	99.86	96.61	99.64	99.87
-500+355	78.30	98.84	99.40	99.99	98.91	88.61	98.40	99.26
-355+250	61.65	96.46	97.48	99.98	95.34	78.49	95.74	97.45
-250+180	46.36	90.38	92.31	99.96	83.44	64.90	90.14	92.94
-180+150	37.04	82.32	84.55	99.52	68.38	52.71	82.64	86.07
-150+106	33.53	77.81	80.17	98.67	60.15	48.84	78.21	81.83
-106+75	26.14	62.70	65.33	90.42	37.19	31.67	62.38	65.70
-75+53	20.72	50.72	52.88	76.44	25.34	23.03	49.47	52.38
-53+45	16.92	40.63	42.36	61.09	17.69	17.30	38.92	40.85
-45+38	15.09	36.34	38.13	53.28	15.22	15.15	35.01	36.67
-38	13.41	29.14	34.16	47.63	12.60	13.00	30.60	28.90

processed. The images were stored in tape and are available for future studies. Image analysis was aimed at the measurement of grade, surface area per unit volume, and the liberation spectrum in each narrow size sample produced in the experiment. The calculation of the grade *g*, fraction by weight of Sphalerite, in each sample, involved the measurement of the corresponding areal/volumetric grade $g_a = g_v$ in each image (equation 2.22), averaging and conversion from volumetric, using equation 3.5 with the measured phase densities. The resulting grades are shown in Table 4.14.

Particle surface area per unit volume determination was carried out by measuring the chord length distribution produced by the features in each sample, as shown in Figure 3.9. The average chord length is proportional to the particles average surface area per unit volume (equation 3.24). Results are shown in Table 4.15. Previously in this work, surface area per unit volume has been measured for comparatively large particles, -1000 +710 microns, at a fairly low magnification (20 X). Here, this measurement was required for particle samples in distinct size intervals. This gives rise to resolution problems and fractal effects. In this work, magnification was kept proportional to particle representative size in order to minimize loss or gain of resolution and the associated fractal effects in the different size ranges. The magnifications used are shown in Table 4.16, and the representative sizes d_p are defined here as the geometric mean between upper and lower size of each size range, with the exception of the lowest size range, for which the median size is used as representative size. A fractal correction procedure has been developed by King [38], and it is required if, when plotting $S_v \times d_p$ in a log-log paper, the resulting slope is less than -1, reflecting the change in measured perimeter as resolution changes

Table 4.14 The grades, calculated from areal grades measured by image analysis, in each narrow size sample produced in the continuous Dolomite-Sphalerite grinding experiment

	Stage I		Stage II			Stage III		
	Sphalerite Grade, %							
Size interval, microns	Ball Mill Feed	Ball Mill Holdup	Ball Mill Product Elutriator Feed	Elutriator Overflow	Elutriator Underflow	Ball Mill Feed (calculated)	Ball Mill Holdup	Ball Mill Product
-1000+710	14.67	28.08	2.46	-	2.68	14.43	16.24	5.43
-710+500	21.44	20.77	6.69	-	4.36	20.43	16.86	10.11
-500+355	18.55	18.84	8.95	-	8.42	16.76	18.24	13.35
-355+250	21.43	20.82	11.91	-	13.74	18.07	20.80	14.73
-250+180	19.27	21.29	18.88	1.09	15.43	16.90	21.86	16.76
-180+150	18.77	21.82	20.17	2.07	19.41	19.22	22.47	19.90
-150+106	18.26	22.99	20.49	5.06	22.96	21.82	23.15	20.14
-106+75	22.84	23.31	18.51	16.78	25.32	24.54	24.18	22.60
-75+53	20.49	21.35	21.99	16.06	25.71	23.98	23.24	19.78
-53+45	19.46	23.47	19.69	17.71	22.25	21.06	18.29	22.62
-45+38	16.83	20.95	21.61	20.16	22.92	20.54	20.36	22.58
-38	8.73	16.49	17.15	16.43	18.84	13.63	19.38	15.49

Table 4.15 Particle surface area per unit volume measured by image analysis in each narrow size sample produced in the continuous Dolomite-Sphalerite grinding experiment

	Stage I	Stage II				Stage III	
	Surface Area per unit Volume x 10^{-2}, 1/micron						
Size interval, microns	Ball Mill Feed	Ball Mill Holdup	Ball Mill Product Elutriator Feed	Elutriator Overflow	Elutriator Underflow	Ball Mill Holdup	Ball Mill Product
-1000+710	1.14	1.22	1.20	-	1.08	1.19	1.17
-710+500	1.53	1.58	1.50	-	1.45	1.49	1.53
-500+355	2.12	2.15	2.14	-	2.02	2.12	2.07
-355+250	3.08	3.05	2.97	-	2.90	2.96	3.01
-250+180	3.94	4.21	3.93	4.74	4.05	4.17	4.22
-180+150	5.38	5.25	4.89	5.33	4.87	5.12	4.98
-150+106	7.07	6.76	6.79	6.83	6.41	6.67	7.00
-106+75	9.87	9.96	9.90	9.92	9.82	9.94	10.34
-75+53	14.91	14.39	14.71	15.03	13.96	15.08	15.08
-53+45	18.56	18.71	19.22	20.54	19.02	19.68	19.62
-45+38	24.22	25.48	24.08	31.35	26.96	26.86	27.44
-38	95.87	118.51	88.25	104.60	86.43	97.29	109.21

Table 4.16 The image magnification setting as a function of particle representative size

Upper size, microns	Lower size, microns	Representative size, microns	Magnification, X
1000	710	842.62	20
710	500	595.82	28
500	355	421.31	40
355	250	297.91	57
250	180	212.13	79
180	150	164.32	105
150	106	126.10	135
106	75	89.16	190
75	53	63.05	265
53	45	48.84	350
45	38	41.35	410
38	0	19.00	890

at higher magnifications. Also, the plot will yield a straight line only if particle shape is constant in the size domain, that is

$$S_v = \frac{\beta}{d_p} \tag{4.25}$$

where β is a shape factor. The plot, including surface area per unit volume measurements for all samples in this experiment, is shown in Figure 4.8. The slope is identical to -1 for all particles above 45 microns, and starts changing for the particles in the -45+38, -38+0 microns size ranges. Unfortunately, the representative size in the bottom size range is very difficult to pinpoint, and the S_v values there are plotted against the median, 19 micron, size. This choice is arbitrary, and consequently, the calculation of the slope bellow 45 microns becomes meaningless. Also, relatively speaking, the $-38+0$ microns size range is extremely broad, and resolution problems arise inside the range itself, where particles that have sizes close to 38 microns are largely favored in comparison to the particles that have sub-micron sizes. On the other hand, sample segregation does not appear to be an issue, since all measurements in the -38+0 microns size range were consistent. Certainly, a more detailed characterization of shape and fractal effects is in demand for the smallest sizes, but this is not pursued in this work so as not to further extend an already extensive research. Fractal correction is not necessary for particles above 45 microns and, for the reasons outlined above, cannot be applied properly to the particles bellow 45 microns. The magnitude of correction required for the particles in the -45+38 microns range is not dramatically high, and the data in this size range, including grade, surface area per unit volume and liberation spectra can be retained

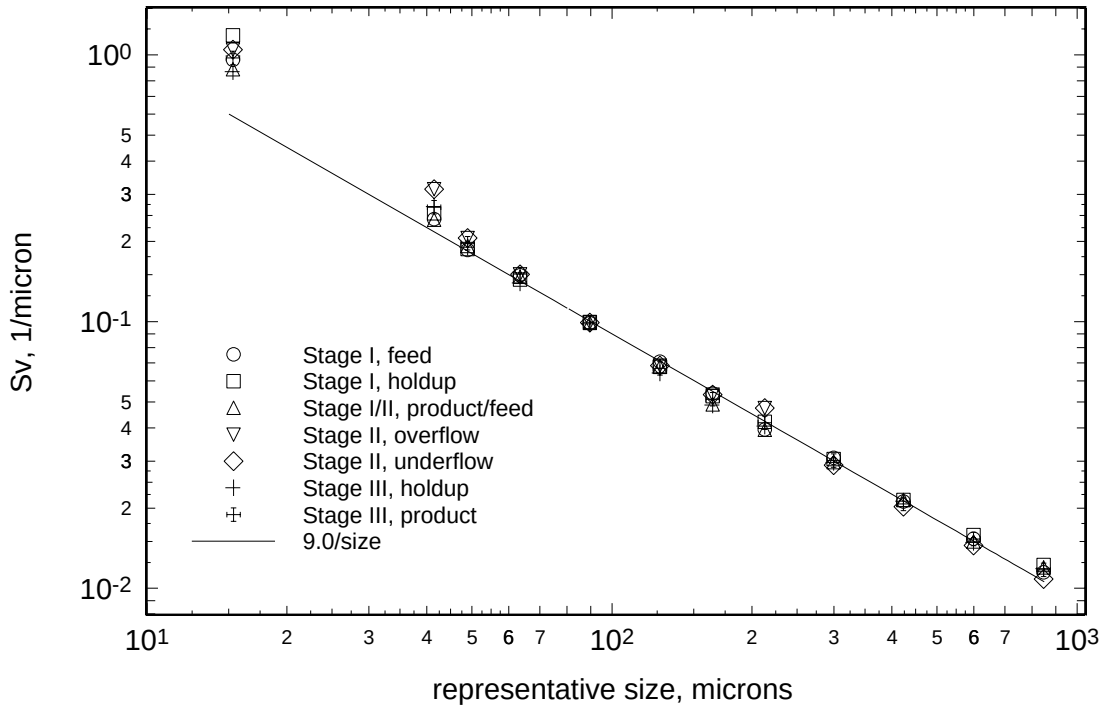

Figure 4.8 Measured Surface Area per Unit Volume of irregular Dolomite-Sphalerite particles as a function of their representative size

without the appropriate correction. The data on the particles in the -38 microns size range is reported here as measured for information purposes. However, the measured liberation spectra on this size range are not considered reliable, because of the exaggerated broadness of that size range, and because of the difficulties in dealing with such particles which are harder to mount and polish for image analysis. Particle shape is constant for particles above 38 microns and below 1000 microns. Linear regression with equation 4.25 yields a shape factor β = 9.0 for the Dolomite-Sphalerite irregular particles.

Finally, the linear grade distribution corresponding to each particle sample in a narrow size range in each stream were measured, and the results are reported in Appendix A. The measurement of linear grade distributions is described in detail in Chapter 2. The corresponding volumetric grade distributions by volume were calculated using the stereological correction procedure described in Chapter 2 and the Dolomite-Sphalerite transformation kernel. The conditional, on size, volumetric grade distributions $f_v(g_v \mid D)$ can be converted to the corresponding distributions by weight $f_w(g_v \mid D)$ by means of the ratio between fractional weight and total weight, as shown in equation 2.26. The resulting conditional, on size, volumetric grade distributions by weight, are shown on Tables 4.17 through 4.23. The measured liberation spectra of the freshly crushed Dolomite-Sphalerite particles, as reported on Table 4.17 is shown on Figure 4.9. Clearly, the feed particles to the experiment were mainly liberated Dolomite and Sphalerite particles. This was expected because of the coarse texture of the ore, which has been thoroughly characterized in the previous chapters. The nature of this Dolomite-Sphalerite ore did not allow for dramatic changes in the liberation spectra during the course of the experiment.

Table 4.17 The measured liberation spectra in the feed stream to the test mill, Stage I. The spectra are conditional on size, volumetric grade distributions by weight

g_v	Size range, microns											
%	-1000 +710	-710 +500	-500 +355	-355 +250	-250 +180	-180 +150	-150 +106	-106 +75	-75 +53	-53 +45	-45 +38	-38
0	57.63	63.52	64.89	67.63	69.57	76.48	73.63	72.51	73.82	77.64	79.98	81.72
0-10	23.21	8.71	11.60	3.60	9.56	1.50	6.68	1.17	1.64	1.28	1.49	9.62
10-20	5.43	6.99	4.98	7.61	0.90	1.00	0.45	1.27	4.58	0.03	0.89	0.30
20-30	1.10	0.25	0.01	0.68	0.49	1.57	0.30	1.92	0.40	1.89	0.99	0.05
30-40	0.00	0.67	2.00	0.52	0.53	1.43	0.30	1.33	0.07	0.07	0.24	0.04
40-50	0.56	0.59	0.11	0.55	0.29	0.04	0.41	0.13	0.09	0.00	0.13	0.08
50-60	0.72	0.56	0.06	0.05	1.10	0.17	0.69	0.09	0.08	0.08	0.01	0.25
60-70	0.86	0.30	0.00	0.66	0.69	0.11	0.86	0.15	0.12	0.72	0.23	0.00
70-80	0.61	0.19	1.37	0.47	0.10	0.18	1.06	0.16	0.15	0.27	0.00	0.09
80-90	1.15	0.46	2.12	0.21	1.06	3.40	1.88	1.11	0.00	0.77	0.50	1.10
90-100	0.99	4.78	2.74	5.51	1.72	4.68	2.25	5.78	1.87	0.18	2.90	0.99
100	7.74	12.99	10.12	12.52	13.99	9.45	11.49	14.37	17.18	17.07	12.63	5.75

Table 4.18 The measured liberation spectra in the holdup of the test mill, Stage I. The spectra are conditional on size, volumetric grade distributions by weight

g_v	Size range, microns											
%	-1000 +710	-710 +500	-500 +355	-355 +250	-250 +180	-180 +150	-150 +106	-106 +75	-75 +53	-53 +45	-45 +38	-38
0	51.11	64.74	71.66	71.92	68.46	67.53	72.84	70.59	74.05	71.52	77.93	80.16
0-10	14.45	3.96	4.78	2.89	6.40	9.93	1.95	4.90	2.64	2.16	0.01	0.82
10-20	4.43	11.73	0.00	4.14	3.81	0.00	1.42	0.07	0.88	3.32	0.00	2.42
20-30	4.44	0.11	2.24	0.00	0.41	0.43	0.43	0.39	1.42	0.14	0.23	0.00
30-40	0.56	0.05	5.99	1.24	0.15	0.44	0.08	0.46	0.50	0.00	0.67	0.00
40-50	0.45	0.71	0.02	0.08	0.45	0.32	0.00	0.00	0.09	0.10	0.04	0.11
50-60	0.28	0.79	0.03	0.09	0.84	0.11	0.31	0.46	0.12	0.10	0.03	0.11
60-70	0.03	0.99	0.09	0.09	0.54	0.58	1.89	0.80	0.12	0.11	0.24	0.02
70-80	0.17	0.00	0.05	0.07	0.45	1.21	0.51	1.47	0.13	0.11	0.19	0.79
80-90	0.41	2.39	0.62	3.45	1.23	2.61	1.24	2.79	0.00	0.81	1.56	1.00
90-100	3.21	5.49	0.83	2.42	0.47	0.00	0.70	0.00	1.33	1.08	7.64	8.47
100	20.45	9.05	13.69	13.62	16.79	16.82	18.63	18.07	18.71	20.56	11.46	6.10

Table 4.19 The measured liberation spectra in the test mill product stream, Stage I, and elutriator feed stream, STAGE II. The spectra are conditional on size, volumetric grade distributions by weight

g_v	Size range, microns											
%	-1000 +710	-710 +500	-500 +355	-355 +250	-250 +180	-180 +150	-150 +106	-106 +75	-75 +53	-53 +45	-45 +38	-38
0	90.99	74.93	73.94	74.53	70.47	72.66	71.78	78.22	75.42	78.19	73.88	81.69
0-10	2.28	17.03	15.56	10.44	8.40	3.13	6.16	0.28	0.01	0.11	3.27	0.17
10-20	5.16	2.07	1.85	3.67	1.90	4.18	1.02	3.16	2.07	0.49	0.82	0.00
20-30	0.15	0.33	0.33	0.43	0.61	0.49	0.45	0.20	0.29	1.85	0.71	0.01
30-40	0.10	0.52	0.40	0.18	0.60	0.13	0.46	0.09	0.51	0.07	0.30	0.25
40-50	0.09	0.17	0.41	0.35	0.01	0.10	0.31	0.26	0.06	0.00	0.09	0.57
50-60	0.14	0.00	0.32	0.14	0.36	0.09	0.38	0.03	0.03	0.08	0.11	0.04
60-70	0.13	0.32	0.63	0.83	0.56	0.00	0.28	0.28	0.00	0.68	0.11	0.18
70-80	0.00	0.37	0.23	0.00	0.22	0.79	1.15	0.08	0.11	0.16	0.12	0.17
80-90	0.11	0.73	1.34	0.13	2.06	1.72	0.05	0.76	1.50	0.76	0.00	0.05
90-100	0.27	1.82	1.35	2.26	0.16	2.81	1.29	0.00	6.42	0.20	0.74	13.82
100	0.58	1.71	3.65	7.05	14.65	13.90	16.68	16.64	13.59	17.40	19.84	3.06

Table 4.20 The measured liberation spectra in the elutriator overflow stream, STAGE II. The spectra are conditional on size, volumetric grade distributions by weight

g_v	Size range, microns							
%	-250 +180	-180 +150	-150 +106	-106 +75	-75 +53	-53 +45	-45 +38	-38
0	91.90	91.01	85.67	76.04	79.39	79.30	77.71	79.92
0-10	7.21	7.10	9.36	5.59	2.85	1.90	0.00	0.52
10-20	0.15	0.04	0.20	1.64	1.79	0.51	0.96	2.95
20-30	0.14	0.11	0.08	0.24	0.16	0.45	1.45	0.00
30-40	0.00	0.08	0.17	0.30	0.01	0.00	0.03	0.03
40-50	0.04	0.09	0.15	0.19	0.23	0.10	0.23	0.11
50-60	0.04	0.09	0.03	0.11	0.00	0.05	0.05	0.97
60-70	0.05	0.21	0.24	0.18	0.15	0.33	0.58	0.05
70-80	0.09	0.08	0.00	0.00	0.94	1.02	0.13	0.59
80-90	0.20	0.14	0.54	0.44	0.00	0.74	0.43	0.16
90-100	0.18	0.00	1.27	3.09	0.43	2.15	0.00	7.08
100	0.00	1.04	2.28	12.17	14.04	13.45	18.42	7.63

Table 4.21 The measured liberation spectra in the elutriator underflow stream, STAGE II. The spectra are conditional on size, volumetric grade distributions by weight

g_v	Size range, microns											
%	-1000 +710	-710 +500	-500 +355	-355 +250	-250 +180	-180 +150	-150 +106	-106 +75	-75 +53	-53 +45	-45 +38	-38
0	87.16	78.26	81.42	75.00	76.38	72.49	72.51	71.33	68.86	73.67	74.00	78.13
0-10	6.11	16.04	5.42	7.87	3.99	4.39	1.18	0.01	4.44	1.08	0.02	1.94
10-20	4.98	1.86	3.39	3.60	4.52	1.46	1.27	0.19	0.00	1.90	3.23	0.67
20-30	0.60	1.01	2.02	0.09	0.36	3.32	0.01	3.61	0.31	0.44	0.37	0.00
30-40	0.08	0.14	1.28	0.00	0.09	0.17	3.75	0.06	0.02	0.55	0.00	0.18
40-50	0.05	0.18	0.37	0.31	0.00	0.11	0.00	1.06	0.49	0.02	0.11	0.10
50-60	0.02	0.07	0.22	0.39	0.00	0.11	0.12	0.04	0.55	0.76	0.10	0.04
60-70	0.05	0.00	0.00	1.07	0.77	0.12	0.13	0.06	0.89	1.11	0.10	0.11
70-80	0.04	0.04	0.04	1.08	1.13	0.79	0.11	0.01	0.41	0.56	0.11	0.02
80-90	0.00	0.37	0.01	1.07	0.42	1.21	0.18	0.09	2.61	1.08	0.18	0.00
90-100	0.00	1.41	1.94	2.88	3.04	2.98	4.67	5.14	1.58	3.68	1.83	13.87
100	0.92	0.62	3.90	6.64	9.30	12.87	16.06	18.39	19.85	15.16	19.93	4.93

Table 4.22 The measured liberation spectra in the holdup of the test mill, STAGE III. The spectra are conditional on size, volumetric grade distributions by weight

g_v	Size range, microns											
%	-1000 +710	-710 +500	-500 +355	-355 +250	-250 +180	-180 +150	-150 +106	-106 +75	-75 +53	-53 +45	-45 +38	-38
0	67.15	68.38	71.92	64.88	70.17	70.60	70.11	71.43	73.50	79.39	74.44	67.69
0-10	2.37	3.55	3.17	12.06	3.10	2.13	3.21	1.45	2.16	0.04	4.07	9.27
10-20	15.53	12.50	6.57	2.68	2.34	4.04	0.17	1.24	0.53	2.46	0.00	4.56
20-30	0.02	0.59	0.63	0.31	4.42	1.87	5.06	2.71	0.00	0.01	0.93	0.23
30-40	0.97	0.24	0.57	0.04	0.00	0.34	0.09	0.10	1.00	0.00	0.42	0.00
40-50	0.74	0.00	0.43	0.25	0.06	0.10	0.11	0.10	0.16	0.11	0.16	0.07
50-60	0.88	1.45	0.38	0.05	0.10	0.11	0.11	0.11	0.16	0.12	0.08	0.79
60-70	0.89	0.15	0.32	0.89	0.11	0.11	0.11	0.11	0.16	0.27	0.05	0.02
70-80	1.38	0.52	0.00	0.00	0.12	0.12	0.12	0.12	0.15	0.12	0.00	0.00
80-90	1.55	0.79	4.15	1.42	0.09	1.10	0.00	0.20	0.60	0.17	2.65	0.06
90-100	2.99	5.05	0.53	5.57	2.66	0.00	0.00	0.08	0.00	3.00	4.02	5.18
100	5.54	6.77	11.35	11.84	16.83	19.48	20.91	22.35	21.59	14.32	13.19	12.14

Table 4.23 The measured liberation spectra in the test mill product stream, STAGE III. The spectra are conditional on size, volumetric grade distributions by weight

g_v	Size range, microns											
%	-1000 +710	-710 +500	-500 +355	-355 +250	-250 +180	-180 +150	-150 +106	-106 +75	-75 +53	-53 +45	-45 +38	-38
0	72.66	71.70	71.45	72.58	75.12	71.72	72.34	73.41	75.45	74.77	73.08	80.58
0-10	21.96	13.45	11.03	7.91	3.70	6.29	5.87	2.67	2.44	0.18	1.68	2.40
10-20	0.31	5.75	5.01	5.44	4.49	1.45	0.26	0.23	2.66	1.83	1.41	1.49
20-30	0.56	0.54	0.18	0.00	0.40	0.57	1.89	0.55	0.09	0.00	1.95	0.05
30-40	0.21	0.36	0.11	1.00	0.08	0.47	0.16	0.95	0.00	0.79	0.00	0.26
40-50	0.55	0.03	0.36	0.11	0.26	0.53	0.05	0.01	0.14	0.21	0.09	0.15
50-60	0.16	0.00	0.12	0.06	0.44	0.19	0.19	0.00	0.04	0.15	0.10	0.06
60-70	0.38	0.48	0.76	0.21	0.68	0.59	0.74	0.00	0.26	0.00	0.10	0.26
70-80	1.09	0.84	0.69	0.77	1.12	0.78	0.27	0.82	0.17	0.00	0.31	0.00
80-90	0.51	1.19	1.69	0.81	0.00	0.30	0.00	0.89	0.41	1.65	0.81	0.44
90-100	1.60	2.07	0.82	1.62	2.53	1.77	3.49	4.20	2.45	5.58	2.30	3.40
100	0.00	3.58	7.79	9.47	11.17	15.35	14.74	16.26	15.89	14.83	18.17	10.92

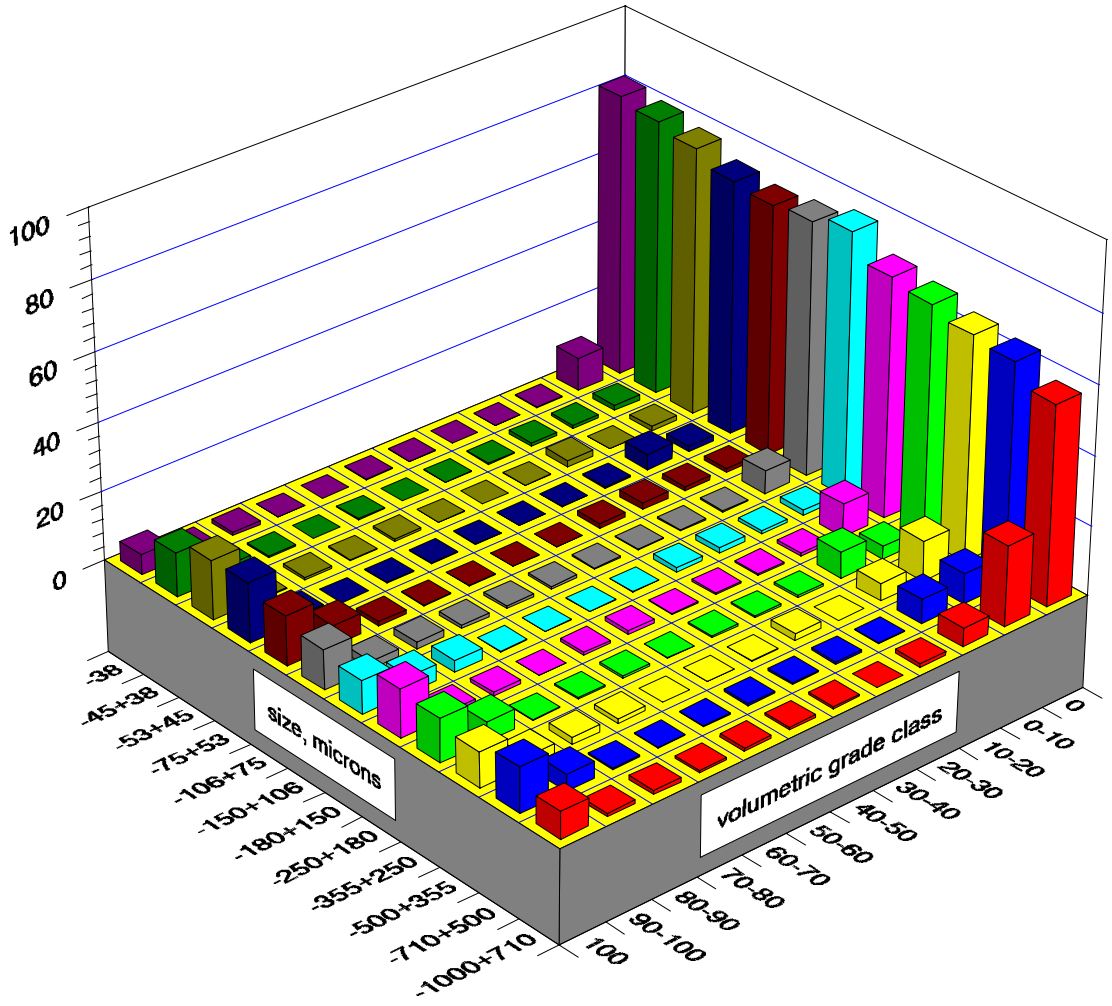

Figure 4.9 The measured conditional, on size, liberation spectra in the freshly crushed Dolomite-Sphalerite particles, used as feed to grinding Stage I

Slight changes have however occurred during the grinding stages and in the elutriation stage, and these are expected to be well reproduced by the liberation and elutriation models.

$$f_w(g_v \mid D) = \frac{f_v(g_v \mid D)\ [(1-g_v)\rho_A + g_v\rho_B]}{\int_0^1 f_v(g_v \mid D)\ [(1-g_v)\rho_A + g_v\rho_B]\, dg_v} \tag{4.26}$$

Comminution Modeling and Parameterization

The comminution model for both grinding Stages I and III is based on the standard population balance equations for three perfectly mixed regions in series with postclassification considered in the last, largest mixing region, as per equations 4.15 through 4.21. The average residence time of solids in each of the three mixed regions were calculated based on the measured average residence time in the mill and the fractional average residence time measured in Test #6. The models for rate of breakage, breakage function and classification function are given in equations 4.22 to 4.24, in that order. The parameters were calculated by fitting both holdup and product size distributions simultaneously. The presence of classification effects was accessed by optimization. The calculated parameters that best describe both grinding stages are shown in Table 4.24, and neither required a classification function. The best fits are shown in Figures 4.10 and 4.11. Clearly, classification at the overflow discharge was not significant, and the holdup size distribution approaches that of the product in both grinding stages.

Table 4.24 The set of selection and breakage function parameters that best fit the size distributions of the Dolomite-Sphalerite particles in the holdup and product of the test mill under the grinding conditions in Stages I and III

	Selection Function				Breakage function			Average Residence Times, minutes		
	α	S_1, min^{-1}	μ, microns	Λ	Φ	β	γ	τ_1	τ_2	τ_3
Stage I	2.236	3.446	613.91	3.368	0.604	9.245	0.704	0.311	4.828	17.601
Stage III	1.589	1.187	2228.22	0.597	0.582	2.615	0.625	0.290	4.420	16.110

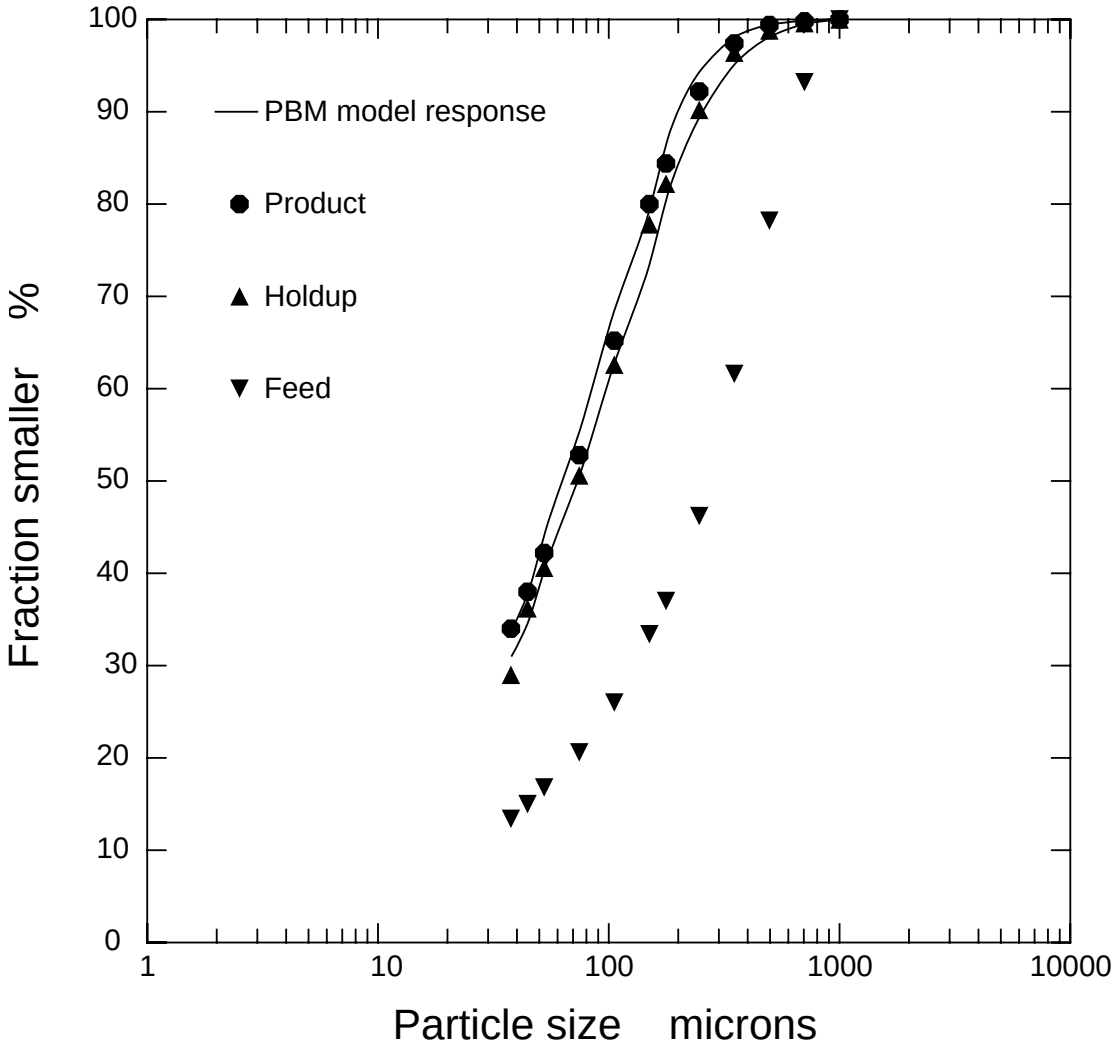

Figure 4.10 Measured Dolomite-Sphalerite particle size distributions in the test mill, Stage I, and *PBM* model response

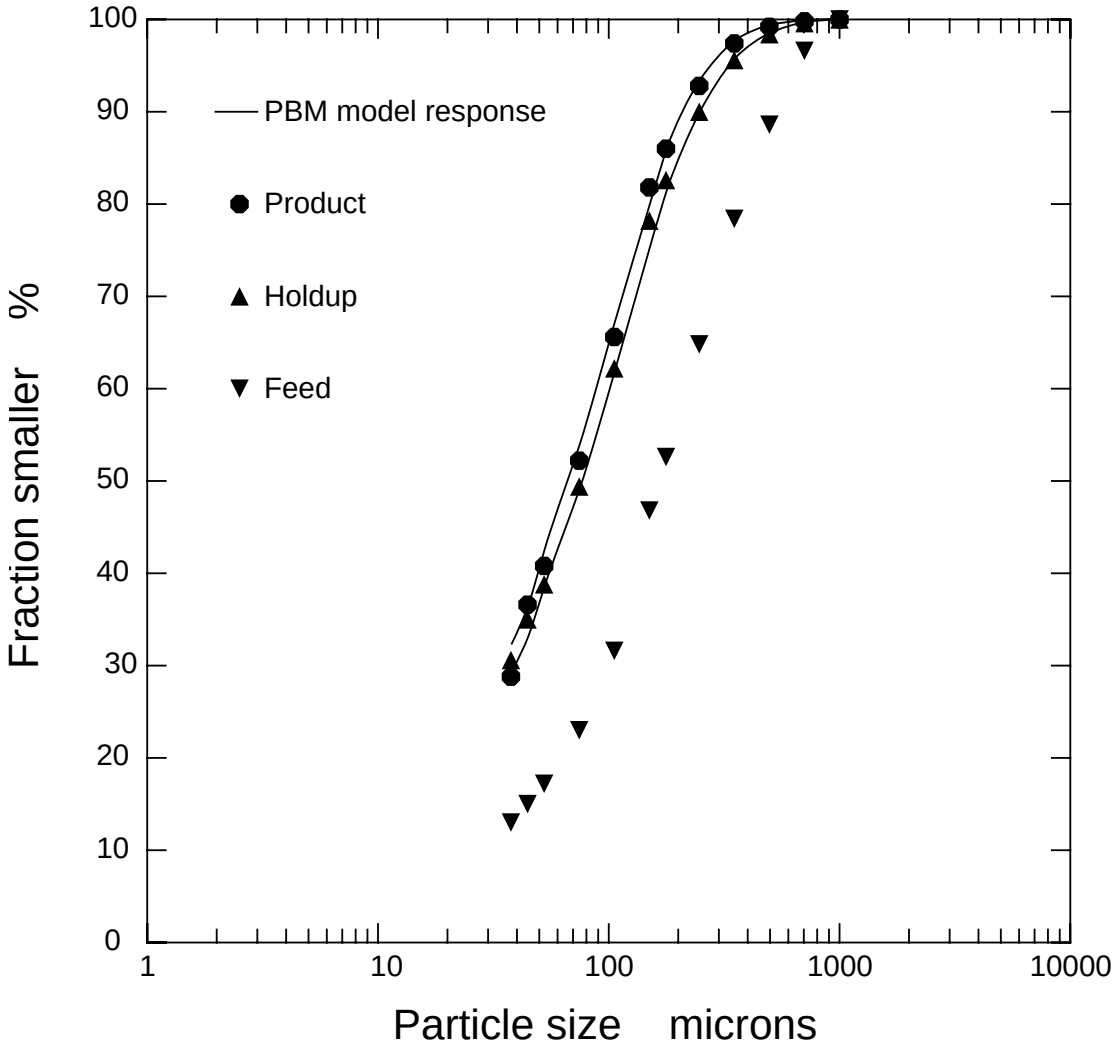

Figure 4.11 Measured Dolomite-Sphalerite particle size distributions in the test mill, Stage III, and *PBM* model response

Elutriation Modeling and Parameterization

The model for the elutriation stage is a simple, semiempirical, logistic classification curve based model. The classification action in the elutriator is a function of the particles terminal settling velocity, which gives the model its semiempirical characteristic. The separation velocity is the velocity at which the water moves upwards, in the direction of the overflow end of the elutriator, inside the separation section of the elutriator (see Figure 4.7). This in turn, is a function of the flow rates around the elutriator, namely feed, underflow and overflow. The terminal velocity of an irregular particle in water is basically a function of its size, density and shape. When the settling velocity of a particle is high, in comparison with the separation velocity, the probability that this particle is recovered in the underflow stream is also high. In turn, when the settling velocity is low in relation to the separation velocity, the probability is that the particle is recovered in the overflow stream. Some particles will, however, pass through the elutriator without being subject to the classification action. These are mostly fine particles that are carried down by the water that short circuits to the underflow stream, right at the end of the feed inlet. The classification action of the elutriator can be described by a classification function $e(v_t)$ and a by-pass fraction α of the feed that short circuits to the underflow,

$$c(v_t) = \alpha + (1-\alpha)\, e(v_t) \tag{4.27}$$

where v_t is the terminal velocity of an irregular particle in water and $c(v_t)$ is the actual classification function, representing the fraction of particles that is recovered in the underflow stream. The logistic classification function was used here to describe the

classification action in the elutriator, and this is:

$$e(v_t) = \frac{1}{1 + \left(\frac{v_t}{v_{50}}\right)^{\lambda}} \tag{4.28}$$

where v_{50} is the separation velocity and λ is a parameter that quantifies the sharpness of the classification, and can be defined in terms of the Sharpness Index *SI* as:

$$\lambda = \frac{-2.1972}{\ln(SI)} \tag{4.29}$$

Here, the Sharpness Index is defined as:

$$SI = \frac{v_{25}}{v_{75}} \tag{4.30}$$

with $e(v_{25}) = 0.25$ and $e(v_{75}) = 0.75$.

The method developed by Concha and Almendra [39] was used here for the calculation of the terminal settling velocity v_t of irregular particles. The required parameters are particle size, particle density and the particle sphericity index Ψ. Here, the sphericity index of an irregular particle is defined as the ratio between the shape factor that is associated to perfect spheres, a well known quantity, and the shape factor associated to the particles, as defined in equation 4.25, i.e.

$$\Psi = \frac{6}{\beta} \tag{4.31}$$

thus, for the Dolomite-Sphalerite particles $\Psi = 6/9$.

The parameterization of the elutriation model was by optimization. The sum of

squares of residuals between the calculated and measured size distributions and liberation spectra in the overflow and underflow streams was minimized with respect to the model parameters, namely by-pass fraction α, Sharpness Index *SI* and separation velocity v_{50}, which varied considerably during the elutriation experiment and could not be properly measured. The measured size distribution and liberation spectra in the feed of the elutriator were retained for this calculation. The measured liberation spectrum in the -38 microns size range was assumed to be identical to the measured liberation spectrum in the -45+38 microns size range due to the measurement error associated to image resolution in the -38 microns size range. The following set of parameters yielded the best fit:

By-pass fraction α = 0.154

Sharpness Index *SI* = 0.310

Separation Velocity v_{50} = 0.693 cm/sec.

The optimization technique used was once again the Rosenbrock Hillclimb Procedure implementation used throughout this work. The resulting separation velocity of approximately 0.7 cm/second is in agreement with the expected value as estimated by the average flow rates observed during the elutriation experiment (Table 4.11). With this, the modeling and parameterization of the three unitary operations in the three stages of the experiment were concluded, completing all the requirements for the experimental verification of the liberation model and liberation calculation procedure.

MODSIM Simulation and Results

The three stages contained in the experiment, including the blending of the particle mixture that constitutes the feed to grinding Stage III were grouped such that MODSIM simulation could be carried out in a single run. The flowsheet used in the simulation is shown in Figure 4.12. The fresh feed to the flowsheet was initially split in two streams so that the feed to grinding Stage III was an even mixture of elutriator underflow and freshly crushed Dolomite-Sphalerite particles. Water was fed and/or withdrawn to the slurry streams through mixers placed in the feed of each stage so as to match the solids contents used in the experiment. The elutriation model was easily implemented in MODSIM, which includes a standard implementation of Concha and Almendra's terminal settling velocity of non spherical particles calculation method that can be used with any user implemented unitary operation model.

The preliminary simulation results indicated that liberated Dolomite and Sphalerite particles were produced in the grinding stages at a faster rate than that predicted by the liberation model. Simulation with a comparatively smaller value of the geometrical texture parameter ϕ, thus allowing for improved liberation of both phases, yielded calculated liberation spectra in very good agreement with the corresponding spectra measured by image analysis. There are two very important implications that arise from this result. First, it is likely that the geometrical texture parameter is a function of particle size. This implies that further research must be directed at characterizing the form of the function $\phi(D)$ and its dependencies. Second, it is possible to produce successful circuit simulations with a single geometrical texture parameter that is

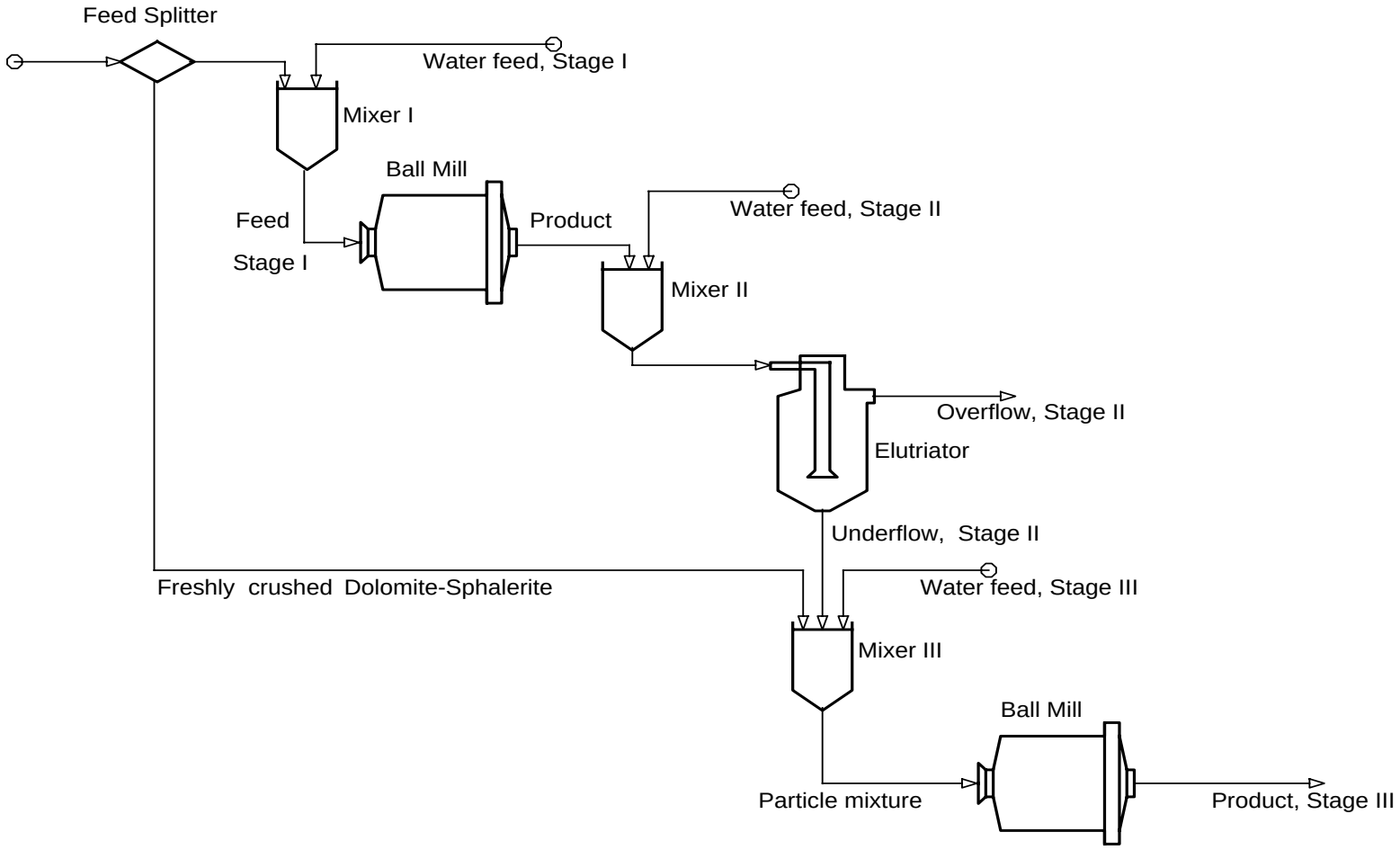

Figure 4.12 The flowsheet used in MODSIM for the simulation of the three stages in the Dolomite-Sphalerite continuous grinding experiment

representative of the particle population in the circuit. Such representative textural parameter, hereon defined as ϕ_r, can be calculated by optimization when measured liberation spectra is available in the streams around the comminuting unitary operations. Here, best results were obtained with $\phi_r = 15.5$, which is comparatively smaller than the measured $\phi(-1000+710\,\mu) = 22.05$, in Chapter 3. This indicates that most unliberated particles smaller than 710 microns have interfaces that are flatter than those in the -1000+710 microns size range, and thus suggesting that the interfaces are essentially not fractal for the Dolomite-Sphalerite ore.

The comparison between simulated and measured particle properties, recoveries and solids contents in each stream of each stage of the experiment, including the holdups of the mill in Stages I and III, is extensive. The measured size distributions are compared to the corresponding calculated size distributions in Figure 4.13. It is clear from the figure that the size distributions were well reproduced by the models in every stream in the experiment and both mill holdups. The size distribution in the feed particles to Stage III is correctly placed between the size distributions corresponding to the crushed particles in the feed and the elutriator underflow. The elutriator overflow was considerably finer than any of the mill products. The size distributions in the product of the test mill in both grinding stages are equivalent, and so are the holdup size distributions. This was expected since, under similar grinding conditions, the size distribution in the product of a ball mill is expected to be insensitive to small changes in the particle size distribution in the feed. The holdup size distributions are slightly coarser than those in the products, showing no classification effects, with respect to size, in the overflow discharge of the

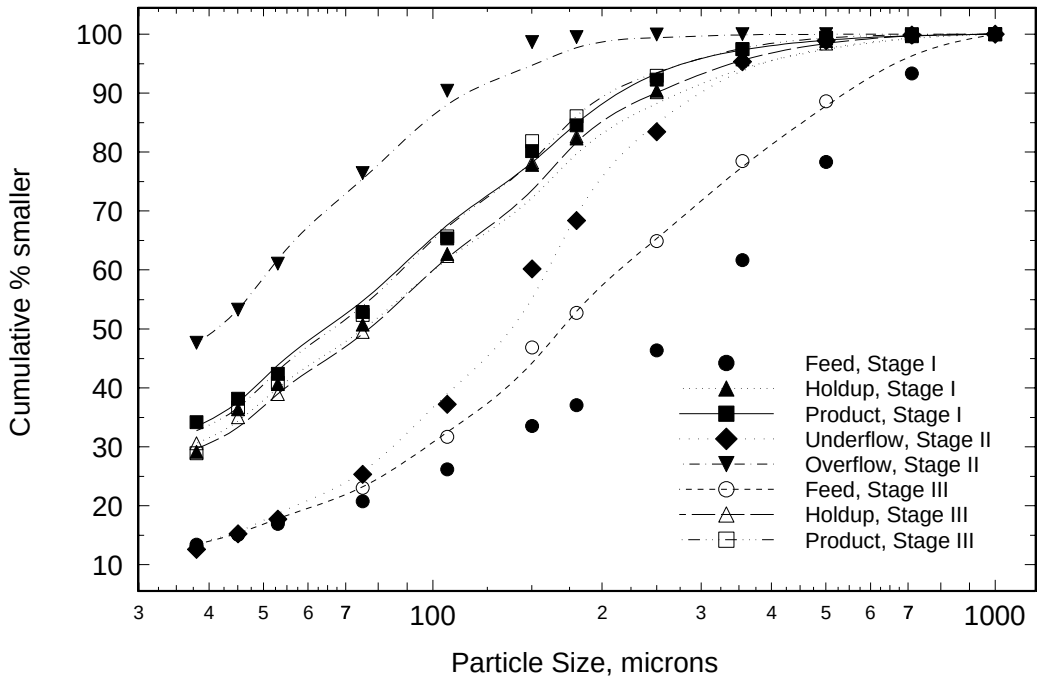

Figure 4.13 The measured (symbols) and simulated (lines) size distributions in the Dolomite-Sphalerite continuous grinding experiment

ball mill.

A summary of experimental and simulated results is shown in Table 4.25. The solids contents in each stream was adjusted according to the experimental results by adding or withdrawing the correct amount of water to the mixers placed at the feed in each stage in the simulation flowsheet. The recovery of solids in the elutriation stage were well reproduced in the simulation. The measured grades in the mill holdups are higher than feed and products, indicating that a classification in the overflow discharge has taken place with respect to particle density, rather than size. Because such classification effect was not modeled, the simulation results show only consistent grades in the feed, holdup and product in both grinding stages. This is particularly significant when comparing measured and calculated liberation spectra in the holdup of the mill. The grade of Sphalerite in the elutriator underflow is considerably lower than the corresponding simulated grade. It is likely that the measured grade is in error, since the measured recovery of Sphalerite in the underflow is low, resulting in about 7% of the Sphalerite in the feed not accounted for in the output streams. The source of the error may have been the fluctuations in flowrates around the elutriator during the experimental. This affects the comparison between measured and calculated liberation spectrum in the underflow of the elutriator.

The measured and calculated liberation spectra corresponding to grinding Stage I are shown in Figure 4.14. The measured liberation spectrum in the product shows improved liberation, with respect to the feed particles, as expected. It is interesting to note that the required change in the geometrical texture parameter from 22.05 to 15.5,

Table 4.25 Comparison between measured and simulated (MODSIM) grades and recoveries in the Dolomite-Sphalerite continuous grinding experiment

	Stage I			Stage II			Stage III		
	Ball Mill Feed	Ball Mill Holdup	Ball Mill Product	Elutr. Feed	Elutr. Over.	Elutr. Under.	Ball Mill Feed	Ball Mill Holdup	Ball Mill Product
% solids	67.55	-	67.55	30.0	23.4	50.1	71.15	-	71.15
% solids, MODSIM	67.55	-	67.55	30.01	23.05	51.9	71.15	-	71.15
Rec. solids	100.0	100.0	100.0	100.0	59.8	40.2	100.0	100.0	100.0
Rec. solids, MODSIM	100.0	100.0	100.0	100.0	58.6	41.4	100.0	100.0	100.0
% Dolomite	80.72	78.29	80.10	80.10	82.62	79.82	80.27	78.37	79.27
% Dolomite, MODSIM	80.70	80.94	80.95	80.95	82.90	78.25	79.50	79.60	79.62
Rec. Dolomite	100.0	96.99	99.23	99.23	61.68	39.96	100.0	97.63	98.75
Rec. Dolomite, MODSIM	100.0	99.99	100.0	100.0	60.01	40.02	100.0	100.13	100.15
% Sphalerite	19.28	21.71	19.90	19.90	17.38	20.18	19.73	21.63	20.73
% Sphalerite, MODSIM	19.27	19.06	19.03	19.03	17.10	21.75	20.50	20.40	20.38
Rec. Sphalerite	100.0	112.6	103.22	100.0	52.23	40.77	100.0	109.6	105.1
Rec. Sphalerite, MODSIM	100.0	98.99	98.75	100.0	52.66	46.3	100.0	99.51	99.41

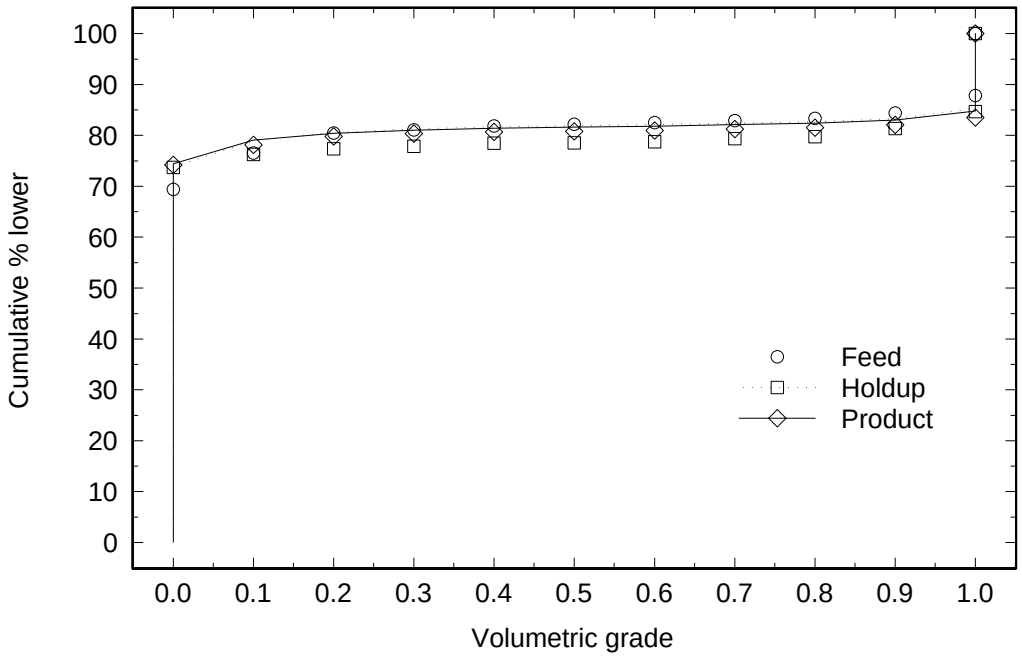

Figure 4.14 Measured (symbols) and calculated (lines) liberation spectra in grinding Stage I

which was quite drastic, only shifted the liberation spectrum in the product enough so that the predicted spectrum matched the corresponding measured spectrum. Perhaps, the sensitivity of the liberation spectrum in the product was more dependent on the state of the liberation of the ore at this size distribution, than it was on its textural properties. The calculated liberation spectrum in the holdup was very similar to that in the product, and this was expected since classification effects with respect to particle composition in the overflow discharge of the mill were not taken in account by the model. However, the measured liberation spectrum in the holdup of the mill showed, once again, that selective classification with respect to particle composition has indeed taken place.

The measured and calculated liberation spectra in the streams around the elutriator are shown in Figure 4.15. The separation was not as drastic with respect to particle composition as it was with respect to size as shown in Figure 4.13. This is again due to the state of liberation of the ore at this size, which contain a relatively small fraction of unliberated particles. The feed spectrum is the product spectrum from Stage I. The simulation matched very well the overflow spectrum. The simulated underflow spectrum is placed slightly lower than the corresponding measured spectrum. It is clear from the figure that the measured fraction of underflow particles that are liberated Dolomite was measured too high, since in practice, the fraction could not be as high as the corresponding fraction in the feed. This is confirmed in the measured liberation spectra in the following grinding stage. The error may have had a number of sources, from sampling to stereological correction. It is also reflected in the phases recoveries on Table 4.25. Fortunately, it is of minor importance in this context because the objective is not

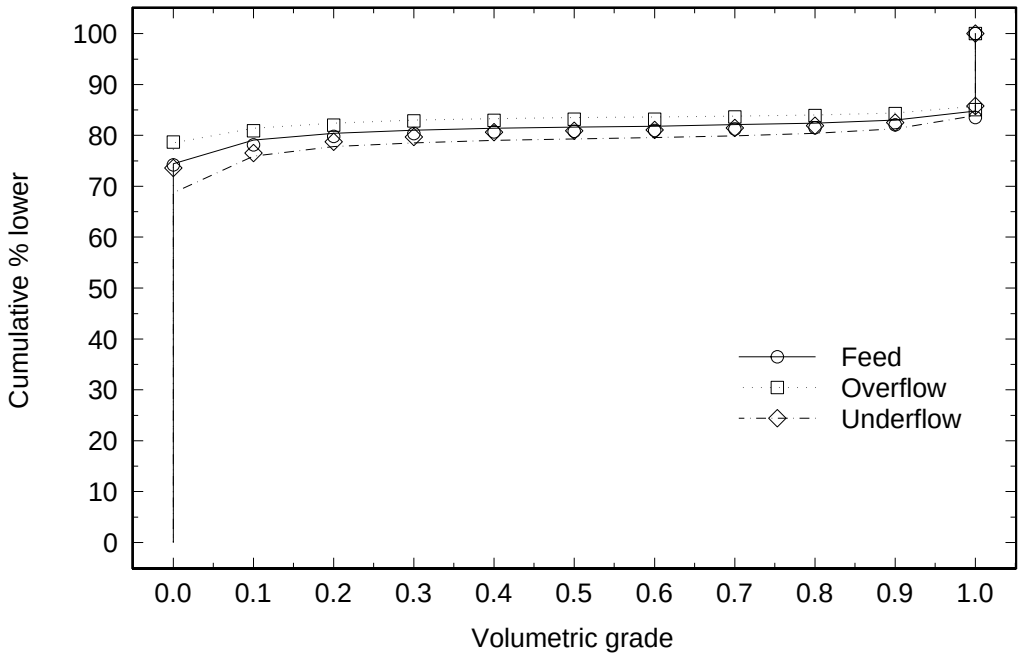

Figure 4.15 Measured (symbols) and calculated (lines) liberation spectra in elutriation Stage II

the development of an appropriate elutriation model.

The calculated and measured liberation spectra in the feed, holdup and product of grinding Stage III are shown in Figure 4.16. Very good agreement in the feed and product streams between calculated and measured liberation spectra is shown. Again, selective classification with respect to composition is shown in the holdup spectrum but the effect was not modeled. The simulation was carried out with the same value of the representative geometrical texture parameter used in Stage I.

Discussion

The intensive experimental work reported here produced a huge payoff, specially when considering the *state of the art* of liberation and comminution as well, at the beginning of this study.

The careful characterization of the test mill with respect to its transport properties was in itself a large task. The experiment showed that the solid and liquid phases have very similar residence time distribution functions, with average residence times dependent on the feed flowrates and the internal volume of the mill. It is possible therefore to use the fractional average residence time of the liquid phase in a mill to model the transport of the solid phase as a good approximation. The smallest-small-large mixing pattern has been identified with the help of the comminution model and the measured size distributions in the holdup and product of the mill. Classification effects, with respect to particle size, at the overflow discharge of the mill are very sensitive to the rheology of the slurry in the holdup. Proper classification parameters can only be accessed when the holdup size distribution is known. Also, comminution model parameters are meaningless

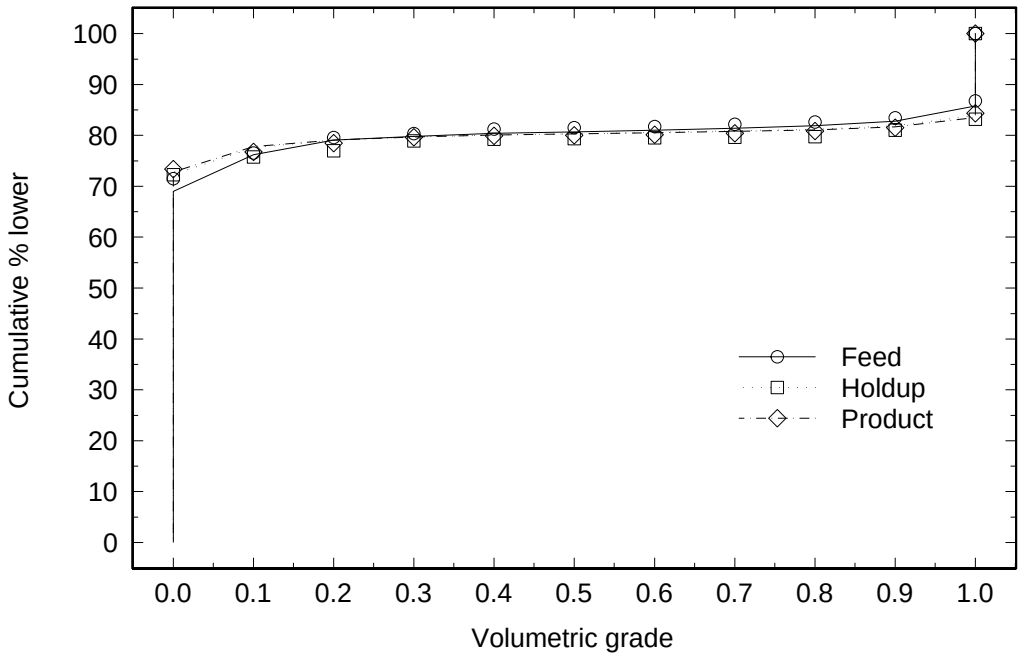

Figure 4.16 Measured (symbols) and calculated (lines) liberation spectra in grinding Stage III

when estimated only from the size distribution in the product of the mill.

The emulated closed continuous Dolomite-Sphalerite grinding experiment was not the ideal, nor definitive experiment, to test the liberation model. However, it served considerably well to its purpose. The measured liberation spectra were very consistent throughout the experiment, showing that the stereological correction procedure is accurate enough to access the phase distribution in typical particulate systems. The implementation of the liberation model and King's solution to the discrete *PBM* were tested satisfactorily. Perhaps the most important finding of the experiment was the dependency of the geometrical texture parameter on particle size. It seems clear now that the interfaces are not fractal, at least for the Dolomite-Sphalerite ore. It is expected that this behavior is to be observed in several other mineralogical systems that are similar, in formation, to the Dolomite-Sphalerite. Fortunately, the use of a representative geometrical texture parameter was enough to reproduce the liberation spectra in the products of the grinding stages. The down side of this representative parameter is that it cannot be used as a valid parameter for extensive simulations were the size distributions in the grinding units are changed significantly. Further research must be aimed at the characterization of the dependency of the parameter ϕ with particle size.

Another aspect of circuit characterization that became an important issue after the calculations were concluded is the relative importance of the small particles and their proper characterization. In the current mineral processing research procedures it is customary to use the 38 microns screen as the smallest top size in any size analysis. When particle properties such as shape and composition are to be accessed by modern

image analysis techniques, the -38+0 microns size range is with no doubt too wide. It is also difficult to handle these particles, and proper sampling and mounting becomes difficult to achieve. On the other hand, particles smaller than 38 microns represent a large fraction of the total mass of particles produced in the product of industrial grinding mills, and their proper characterization becomes important. Future work must be carried out with better mounting and polishing procedures specially designed for the smallest particles. Also, size separation below 38 microns must be sought for better particle characterization at the smallest sizes.

CHAPTER 5

CASE STUDY

Introduction

The work reported here originated from a research program sponsored by Minnesota Power with the intention of minimizing the use of energy in the Taconite Industry in Minnesota, which produces iron pellets for steel making. Because the cost of comminution represents a significant fraction of the total cost of pellet production, the potential for improved economic performance is quite large if improvements in comminution efficiency should be possible by evolutionary improvement in existing Taconite comminution circuits. This work was dedicated to the preliminary characterization of the mineralogical texture of the Taconite ore and the characterization of a typical Taconite grinding and classification circuit, since these are the most crucial operations. The Taconite ore constitutes a typical ore with problematic liberation characteristics, which requires comminution to comparatively fine sizes so that enough Magnetite, the main iron baring mineral, is liberated from the Chert (micro-crystalline quartz) matrix. Chert is known to be abrasive, tough material, and this contributes to the relatively high cost of Taconite processing. As a result of the combined liberation and comminution characteristics of the Minnesota Taconite, the American pellet producing industry has been suffering harsh competition from other countries which produce pellets from richer, easier to process ores such as the Itabirito in Brazil, an ore rich in Hematite

that has much more favorable comminution and liberation characteristics.

The grinding circuit of the Fairlane Plant, located at mile 4 on county road 17, south of Eveleth, was chosen to be the subject of this study. The plant processes a blend of Taconite ore that is mined by Eveleth Mines at the Thunderbird North Mine, from four mining horizons denominated Middle Upper Cherty, Lower Upper Cherty, Top Lower Cherty and Bottom Lower Cherty, which present a magnetite content above cutoff grade. The plant produces pellets containing not more than 5.30% SiO_2 and 78 to 82% of the particles in the pellets should pass the 45 microns screen.

The study carried out in the Fairlane Plant provided with an excellent opportunity to test, in practice, the procedures and models previously described in this work. The Taconite ore is a typical case for which the symmetric transformation kernel for stereological correction can be used, since the exact transformation kernel for the Taconite ore is not known. The symmetric transformation kernel is tested here as an approximate transformation kernel that can be used for typical ores in the preliminary accessment of the liberation spectra of the ore at several particle sizes. The preliminary characterization of the mineralogical texture of the ore was carried out by fractionating a narrow size sample obtained from the plant into a few grade intervals. This procedure provided enough information to estimate the density of the two relevant phases in the ore, Magnetite and Chert, and, through the measurement of interphase area per unit volume of phase, a good estimate of the geometrical texture parameter ϕ, at that size range, was obtained.

The bulk of the experimental work consisted of the measurement of the size

spectra, by standard sieving, and the liberation spectra, by image analysis, in every stream in the secondary grinding circuit of the Fairlane plant. These data were used to develop appropriate models for use with MODSIM, and to test the application of the liberation model developed in this work for an ore other than Dolomite-Sphalerite.

Fairlane Plant Grinding Circuit

The simplified flowsheet of the plant's secondary grinding circuit is shown in Figure 5.1. The grinding circuit feed is mainly the concentrate stream of Cobber Magnetic Separators, which concentrate Rod Mill discharge in the primary grinding stage. For this particular circuit, Ball Mill grinding is performed in closed circuit with both classification and concentration. The Ball Mill is 12.81 meters long by 5.185 meters in diameter (42 by 17 feet), and is equipped with rectangular lifters that are 76.2 millimeters high. Grinding media is fed to the Ball Mill at a rate of 2724 kilograms (6000 pounds) per day. The nominal mill charge represents 36% filling by volume, and the grinding media is constituted by 60% of 50.8 millimeters (2 inches) balls and 40% of 38.1 millimeters (1.5 inches) balls. The Ball Mill revolves at 12 *RPM*, which is 64% of critical speed.

Most of the concentration is carried out in wet magnetic drum separators which are fed directly with the ball mill discharge stream. This separation is designated as Rougher, and its concentrate/magnetic stream is the major component of the cyclone feed stream. The Rougher tails are subject to further concentration, and the concentrate of the Scavenger separation is returned to the grinding circuit through the cyclone feed stream.

The major classification stage is performed in four KREBS hydrocyclones

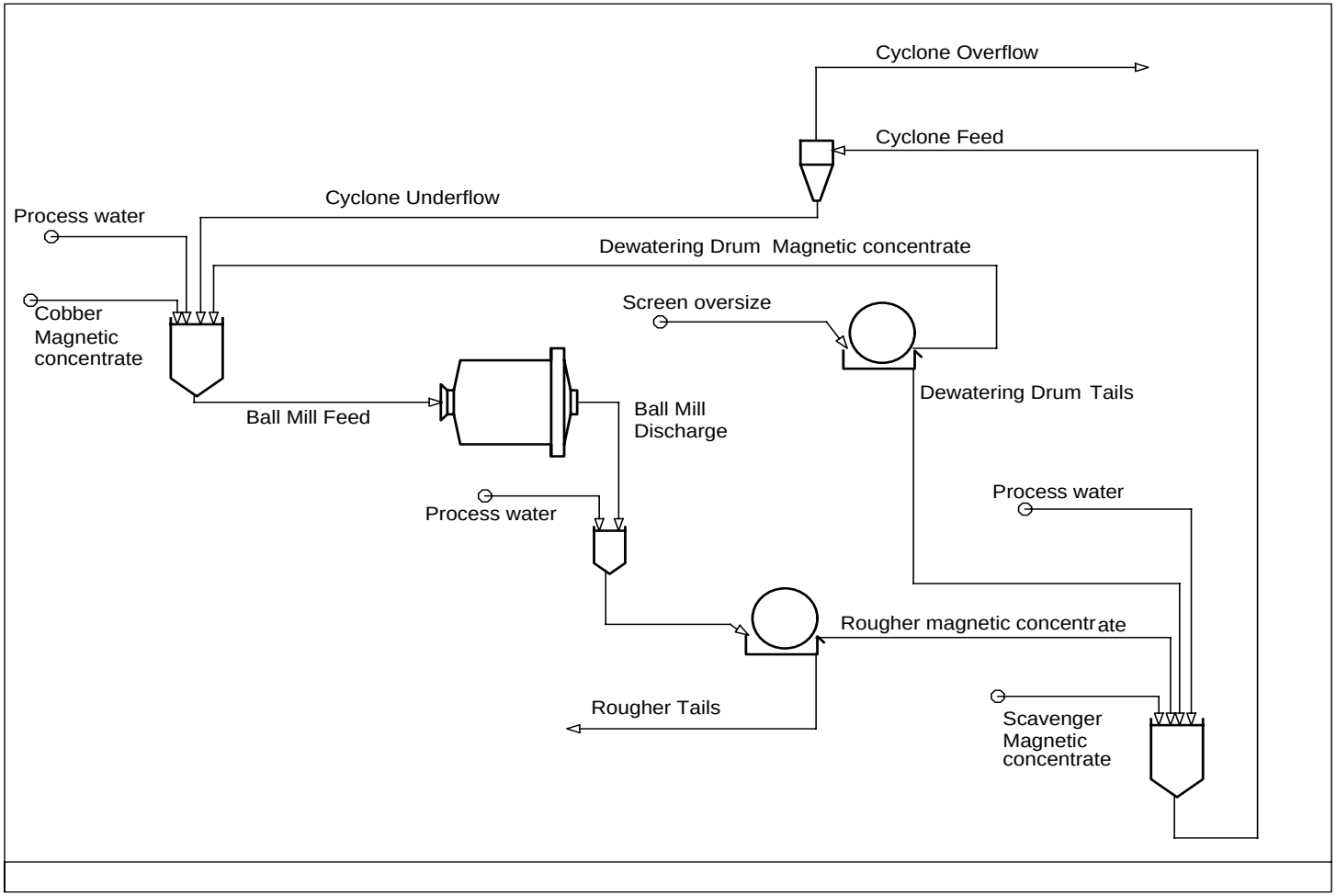

Figure 5.1 The simplified secondary grinding circuit flowsheet at the Fairlane Plant

assembled in a cluster. The hydrocyclones are 660 millimeters (26 inches) in diameter. The circular inlets measure 241.3 millimeters (9.5 inches). Vortex finder diameter is 279.4 millimeters (11 inches) and the spigot-vortex finder distance measures 2082.8 millimeters (82 inches). Spigot diameter is 114.3 millimeters (4.5 inches). The cyclone underflow is recirculated to the ball mills and the cyclone overflow constitutes the product of the secondary grinding circuit. The cyclone overflow is fed to a hydro separator, and the concentrate product of the hydro separator is screened in fine, double deck, vibrating screens, with primary opening of 150 microns (0.006 inches) and secondary opening of 100 microns (0.004 inches). The screens oversize is split in two fractions. One fraction is fed to a regrind circuit. The other fraction, representing approximately 5/6 of the screens oversize, is returned to the grinding circuit through a wet magnetic drum separator. The major role of this separation stage is dewatering, and a magnetic/concentrate stream is produced that contains mostly solids. This is then recirculated to the ball mills. The tail stream is mostly water, which is recirculated to the cyclones. This separation stage is designated as the Dewatering Drum.

Experimental

The experimental work started with the sampling of the Fairlane Plant secondary grinding circuit streams. This was followed by solids contents measurement, which was the only measurement carried out at the plant site. The particle size distributions were carefully determined in each stream and a sample from each size range below 1000 microns was separated for image analysis. These were mounted, ground, polished and coated. A set of images from each specimen was acquired. The images were processed

for chord length distribution and linear grade distribution measurements. A larger narrow size sample from the Ball Mill Discharge was used for texture and phase characterization by fractionation.

Sampling

Sampling of the Fairlane Plant grinding circuit was carried out on 11/16/1993. The selected streams were sampled in the order given below, according to the location of the sampling points in the plant, to minimize the time necessary for sampling. The corresponding abbreviated names, as used in the tables and figures, are listed along the stream names.

- Cobber Concentrate, Cob.Conc.
- Cyclone Feed, Cyc.Feed
- Cyclone Underflow, Cyc.Under
- Cyclone Overflow, Cyc.Over
- Dewatering Drum Concentrate, D.D.Conc.
- Dewatering Drum Tails, D.D.Tails
- Ball Mill Discharge, B.M.Disch.
- Rougher Concentrate, Rough.Conc.
- Rougher Tails, Rough.Tails
- Scavenger Concentrate, Scav.Conc.

The samples were collected with sample cutters in all streams. Three rounds were carried out following the sequence above, with no time interval between rounds. Each round consumed an average 20 minutes time. The samples from each round were added,

producing one composite sample for each stream. The pressure head in the cyclone cluster was measured for each round. There are four cyclones in the cluster and two cyclones were operating at sampling time while the other two were standing by. Pressure heads in each round were 843.6, 949.1 and 949.1 g cm^{-2} (12.0, 13.5 and 13.5 PSIG), in that order. The samples were collected from open streams, and in most cases the sample cutter used was long enough so that the sample obtained was representative of the entire stream. The exception was the sample collected at the ball mill discharge, where the flow rate was too high so that the cutter could not be held steadily during sampling, neither could it be inserted deeply enough into the stream. However, an effort was made to obtain the best possible sample. The Cyclone Feed sample was drawn with a probe from the cluster feed head. The sampling at that particular point is routinely performed at the plant, and the probe depth to obtain a representative sample from well-mixed slurry had previously been established.

Solids Content

Each sample was immediately weighed after sampling, and the wet weight noted. The samples were then filtered, dried and cooled to room temperature. The solids weight was then measured and noted. The solids content by weight, for each stream, is shown in Table 5.1. The samples were then bagged and labeled, completing the work at the plant site.

Table 5.1 Measured solids content in the sampled streams

Stream	Weight Wet, g	Weight Dry, g	Solids, %
Cobber Concentrate	6647.7	4224.0	63.54
Cyclone Feed	2229.5	1091.5	48.96
Cyclone Underflow	4536.4	3627.0	79.95
Cyclone Overflow	5763.6	1833.0	31.80
Dewatering Drum Conc.	3463.6	2104.5	60.76
Dewatering Drum Tails	13500.0	562.5	4.17
Ball Mill Discharge	7247.7	4954.6	68.36
Rougher Concentrate	4472.7	2951.0	65.98
Rougher Tails	9311.4	562.5	6.04
Scavenger Concentrate	2632.0	213.5	8.11

Size Analysis and Separation

The samples were separated in narrow size intervals by screening. This was carried out in a disliming, wet screening stage, followed by dry screening. Each sample was first wet screened at 150 microns. The undersize fractions, (-150 microns), were wet screened with a 38 microns sieve, until no particles passed through. After filtering and drying, the dislimed fractions, (+38 microns), were dry screened with the aid of a ROTAP™, into several narrow size fractions. Each narrow size sample was weighted and bagged individually with the proper identification label, to follow specimen preparation for image analysis. The resulting size distributions and the size intervals used are shown in Table 5.2. The size distributions around the two major nodes in the circuit, namely the rougher concentration and the hydrocyclone classification, must be consistent so that the units can be parameterized properly. The raw measured size distributions are not exact, and the error is due to sampling inaccuracy that is inherent to sampling high flowrate streams in industrial plants. Material balance smoothing was carried out around the two nodes using MASSBAL, a material balance smoothing package developed by Kenwalt Systems [40]. The amount of smoothing required was minimal, indicating that the sampling procedure was good. The resulting smoothed size distributions in the corresponding streams are shown in Table 5.3.

Specimen Preparation

The fractions bellow 1000 microns, whenever available in enough quantity, were mounted in epoxide resin for image analysis. A representative sample of about 6 grams from each size fraction was separated in a PULVERIT™ automatic sampler. Each

Table 5.2 Measured cumulative size distributions in the sampled streams

Size, microns		Fairlane Plant grinding circuit sampled streams									
Upper	Lower	B.M. Disch.	Cob. Conc.	Cyc. Feed	Cyc. Over	Cyc. Under	D.D. Conc.	D.D. Tails	Rough. Conc.	Rough. Tails	Scav. Conc.
9600	8000	1.0000	1.0000	1.0000	1.0000	1.0000	1.0000	1.0000	1.0000	1.0000	1.0000
8000	6300	1.0000	0.9991	1.0000	1.0000	1.0000	1.0000	1.0000	1.0000	1.0000	1.0000
6300	5600	0.9999	0.9955	0.9996	1.0000	0.9994	1.0000	1.0000	1.0000	1.0000	1.0000
5600	4750	0.9998	0.9922	0.9996	1.0000	0.9992	1.0000	1.0000	0.9997	1.0000	1.0000
4750	3350	0.9995	0.9836	0.9996	1.0000	0.9988	1.0000	1.0000	0.9995	1.0000	1.0000
3350	2800	0.9984	0.9357	0.9993	1.0000	0.9966	1.0000	1.0000	0.9981	0.9993	1.0000
2800	2000	0.9969	0.8872	0.9986	1.0000	0.9937	1.0000	1.0000	0.9968	0.9991	1.0000
2000	1400	0.9925	0.7742	0.9967	1.0000	0.9844	1.0000	1.0000	0.9921	0.9982	1.0000
1400	1000	0.9831	0.6538	0.9914	0.9999	0.9661	0.9998	1.0000	0.9832	0.9964	0.9995
1000	710	0.9691	0.5356	0.9828	0.9997	0.9403	0.9993	0.9997	0.9703	0.9939	0.9981
710	500	0.9466	0.4340	0.9662	0.9993	0.8988	0.9983	0.9993	0.9497	0.9898	0.9967
500	355	0.9150	0.3606	0.9445	0.9987	0.8429	0.9967	0.9986	0.9206	0.9841	0.9953
355	250	0.8699	0.2986	0.9037	0.9963	0.7663	0.9914	0.9956	0.8762	0.9681	0.9910
250	180	0.8103	0.2478	0.8398	0.9901	0.6671	0.9813	0.9834	0.8119	0.9367	0.9858
180	106	0.7304	0.2116	0.7620	0.9752	0.5419	0.9520	0.9114	0.7317	0.8932	0.9715
106	75	0.5560	0.1668	0.5883	0.8862	0.3308	0.7607	0.5209	0.5622	0.7826	0.7973
75	53	0.3151	0.1379	0.4442	0.7692	0.1414	0.5063	0.2849	0.3725	0.6892	0.5662
53	45	0.2524	0.1107	0.3290	0.5979	0.0925	0.3610	0.1908	0.2758	0.5991	0.4025
45	38	0.2432	0.1003	0.2915	0.5426	0.0780	0.3262	0.1705	0.2510	0.5615	0.3441
38	0	0.2208	0.0805	0.2496	0.4908	0.0573	0.2967	0.1463	0.2165	0.5285	0.2990

Table 5.3 Adjusted cumulative size distributions in the streams corresponding to the two main circuit nodes

Size, microns		Cumulative Size Distributions in Stream					
Upper	Lower	Cyc. Feed	Cyc. Over	Cyc. Under	B.M. Disch.	Rough. Conc.	Rough. Tails
9600	8000	1.0000	1.0000	1.0000	1.0000	1.0000	1.0000
8000	6300	1.0000	1.0000	0.9999	1.0000	1.0000	1.0000
6300	5600	0.9996	1.0000	0.9993	1.0000	1.0000	1.0000
5600	4750	0.9996	1.0000	0.9993	0.9998	0.9982	1.0000
4750	3350	0.9996	1.0000	0.9993	0.9996	0.9980	1.0000
3350	2800	0.9993	1.0000	0.9987	0.9983	0.9966	0.9993
2800	2000	0.9984	1.0000	0.9972	0.9971	0.9953	0.9991
2000	1400	0.9961	1.0000	0.9932	0.9926	0.9905	0.9982
1400	1000	0.9895	0.9999	0.9822	0.9840	0.9813	0.9964
1000	710	0.9790	0.9997	0.9645	0.9715	0.9679	0.9939
710	500	0.9593	0.9994	0.9312	0.9516	0.9464	0.9897
500	355	0.9333	0.9989	0.8875	0.9234	0.9161	0.9840
355	250	0.8884	0.9966	0.8128	0.8802	0.8705	0.9679
250	180	0.8233	0.9906	0.7064	0.8182	0.8057	0.9364
180	106	0.7412	0.9763	0.5769	0.7395	0.7238	0.8926
106	75	0.5697	0.8903	0.3457	0.5709	0.5500	0.7813
75	53	0.4121	0.7804	0.1547	0.3797	0.3500	0.6872
53	45	0.3082	0.6047	0.1009	0.2829	0.2602	0.5973
45	38	0.2752	0.5474	0.0849	0.2739	0.2461	0.5619
38	0	0.2394	0.4937	0.0617	0.2430	0.2155	0.5291

representative sample was again wet sieved before mounting, to avoid even the slightest contamination of smaller particles and slime. After drying at room temperature, the particles were placed under weak vacuum in a lab desiccator. After approximately 10 minutes under vacuum, the particles were carefully mounted in epoxide resin, with the proper label identifying the stream and the size range. The sample mounts, totaling 105, were ground in an automatic grinding head, with an 125 microns diamond grinding disc at 120 *RPM*, 2.3 kg/sample pressure, and counter-clockwise grinding head motion, until between 1 and 2 millimeters of material had been ground off the specimen surface. Diamond grinding is essential due to the hardness of the micro-crystalline silica (Chert). This was followed by grinding with 40 microns and 6 microns diamond grinding discs, at the same settings, until the specimen surface was fairly smooth. Polishing followed manually, by lapping with 9 micron and then 1 micron diamond slurry at 200 *RPM*. The final polish was carried out by lapping with 0.3 micron alumina, at 600 *RPM*. After polishing, each specimen surface was coated with a film of carbon for image acquisition in the *SEM*.

Image Acquisition

Whenever possible, 30 backscattered electron images were collected from each specimen using the *SEM*. Magnification was kept proportional to particle size. Image collection followed a pattern on the specimen surface such that each point on the surface had an equal probability of being scanned. Care was taken to avoid image overlapping. Scanning speed was kept at 0.25 Frames/second and a 16 frame true average image was collected to eliminate noise. The 3004 images were generated at high resolution

(2048x2048 frames) and stored in tapes, after high resolution stretching and compressing, in 512x512 format, as raw binary files.

Image Processing and Measurements

The processing of each image started with background correction to grey level 40, for the Taconite ore, followed by delineation filtering. A typical image is shown in Figure 5.2, after background correction and delineation filtering. This image was collected from -500+355 micron particles from the Cyclone Underflow stream. The magnification used for this particular image was 50X. The grey level histogram for this image is shown in Figure 5.3. The left peak in the histogram corresponds to the darkest phase in the image, which is the backscattered electron intensities detected from the epoxy mounting media. The following peaks at higher grey levels are backscattered electron intensities detected from the particles. Two major components are readily identified, one brighter, corresponding to the peak at the right of the histogram, and a second which is completely represented by intermediate grey levels. The bright phase represents the magnetite and the dull grey phases are silica or silicates, with varying iron contents. This is corroborated by the iron and silicon X-Ray maps shown in Figures 5.4 and 5.5, which were generated by an electron-microprobe for the same magnification and section of specimen that produced the backscattered electron image in Figure 5.2. Clearly, the Taconite ore produces enough contrast for thresholding, and the magnetite can be easily discriminated from the gangue minerals. Thresholding, coupled with the fingerprinting procedure to eliminate artifacts and the usual phase filling procedure, complete the image processing stage. Areal fraction of phase was measured in each image, and the areal

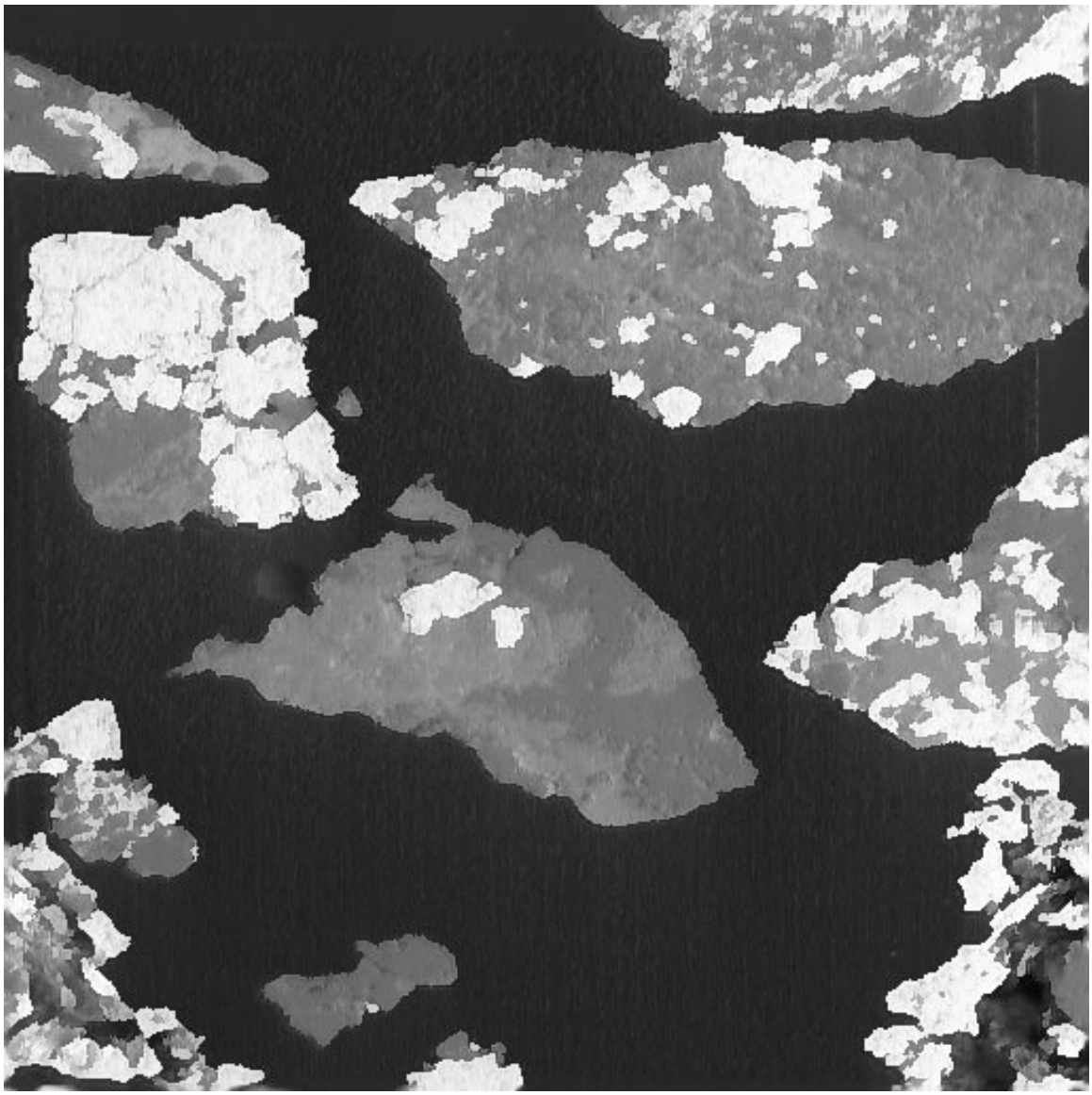

Figure 5.2 A backscattered electron image at 50X magnification of -500+355 micron particles from the Cyclone Underflow stream

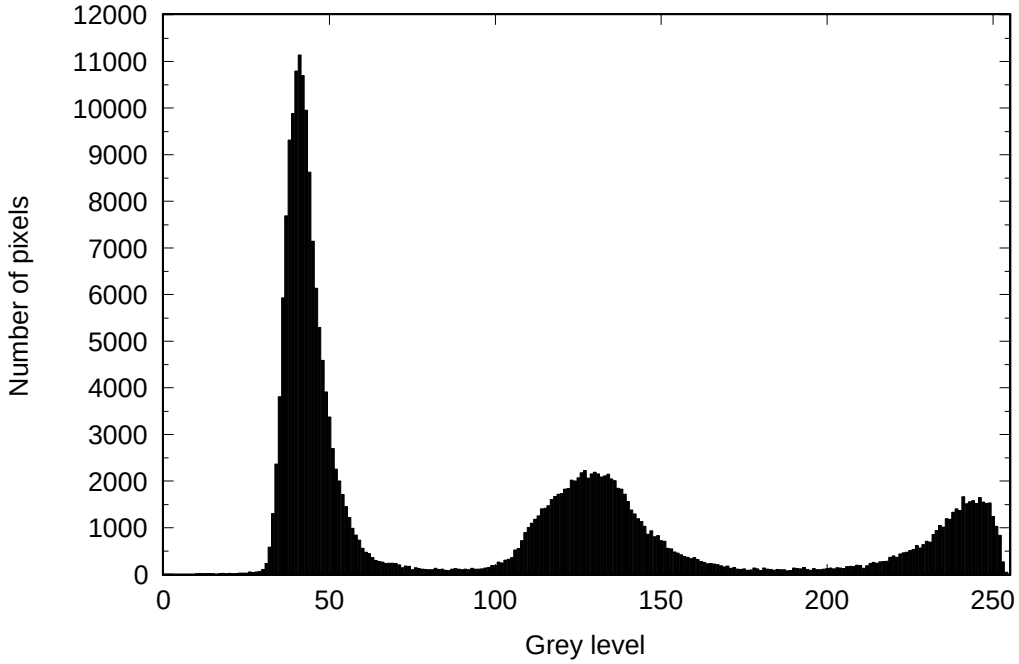

Figure 5.3 The grey level histogram corresponding to the image in Figure 5.2

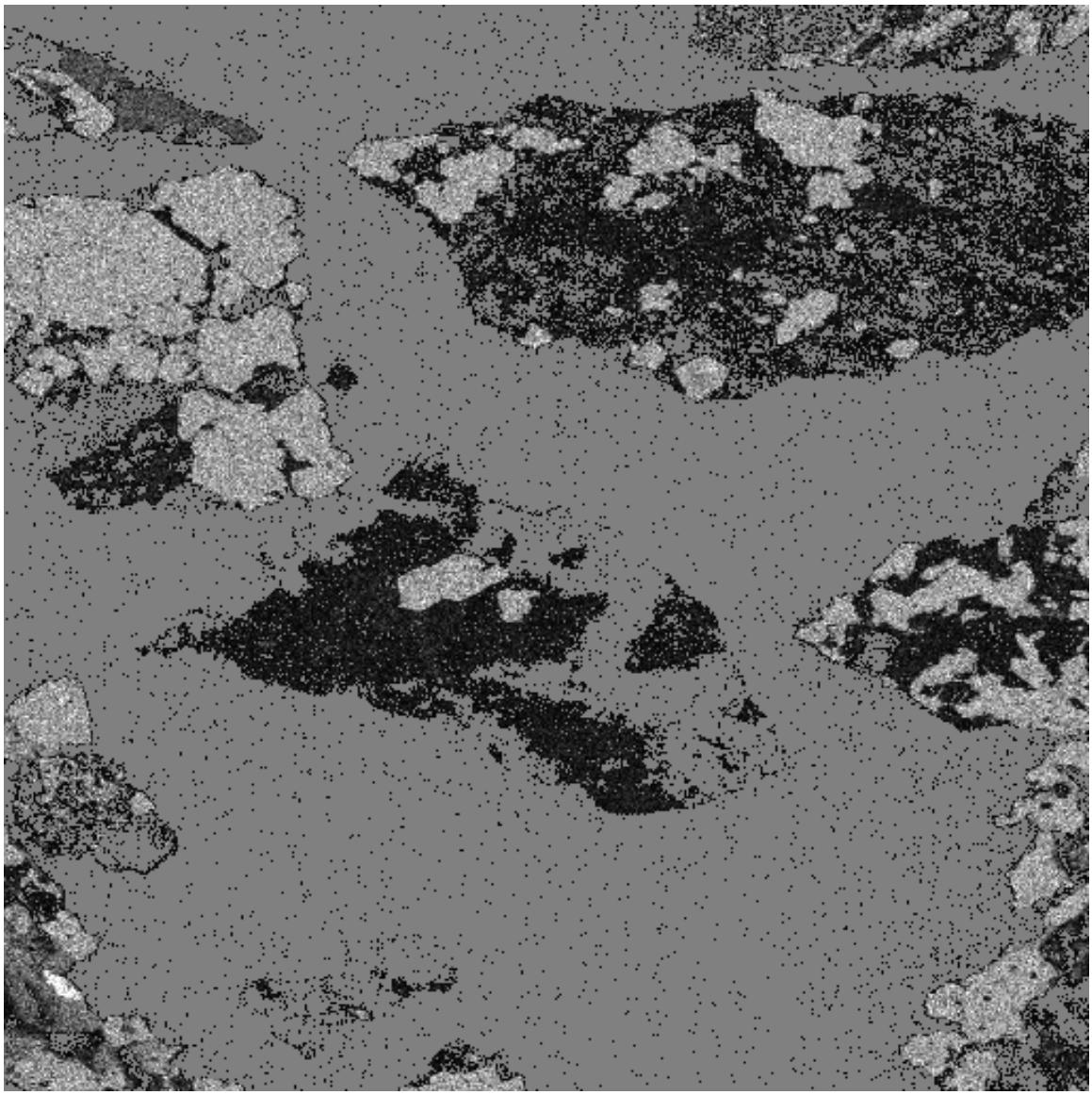

Figure 5.4 Iron X-Ray map corresponding to the image shown in Figure 5.2, scanned with an electron microprobe

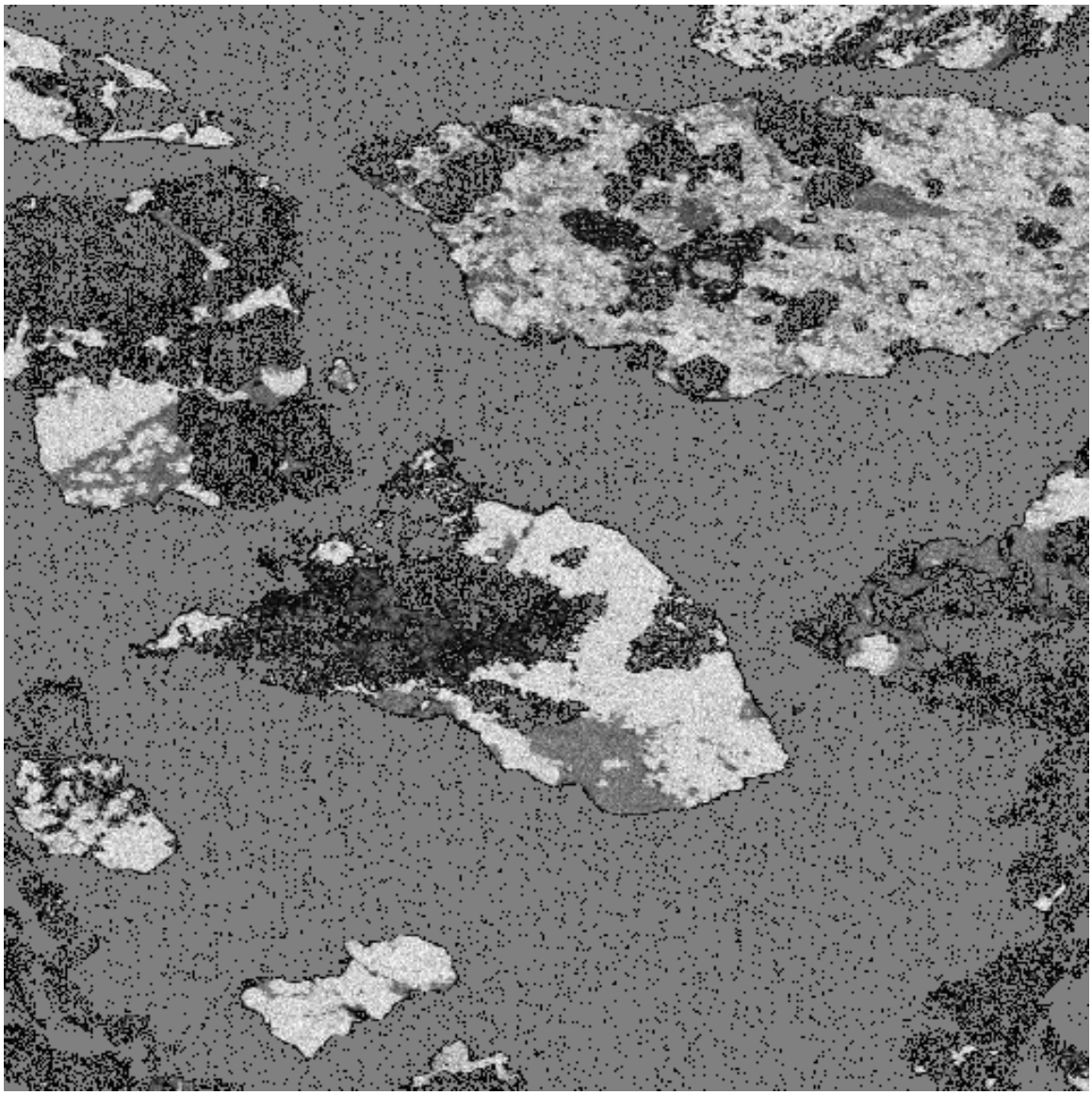

Figure 5.5 Silicon X-Ray map corresponding to the image shown in Figure 5.2, scanned with an electron microprobe

fraction of phase in each sample calculated. These were converted to grade fraction by weight using the measured densities of Chert and Magnetite that are reported in the experimental Phase and Texture Characterization section of this Chapter. The measured grade of Magnetite in each sample is shown in Table 5.4. The total grade of Magnetite in each stream was calculated as the weighed average, with respect to the measured size distributions, of the grades in each size class. The results are also shown in Table 5.4.

The measurements of linear grade and chord length distributions were carried out using the same procedure used for the Dolomite-Sphalerite ore measurements. In Figure 5.6, a discriminated image from the -500+355 microns, Cyclone Underflow particles is shown at the standard 40X magnification. The measuring frame used for both, linear grade and chord length distributions, was 510 pixels. As shown in Figure 5.6, the chords that intercept the frame were not measured. The measured distributions were corrected for the probability that a chord intercepts the measuring frame. The linear grade and chord length distributions were measured in this fashion for every set of images acquired from each specimen corresponding to a narrow size sample from a given stream. The measured linear grade distributions by length corresponding to each sample are reported in Appendix B. These distributions must be retained for future use with the exact transformation kernel for stereological correction for the Taconite ore, when available. The character of this work may then be shifted from preliminary to definitive.

The Conditional, on size, Volumetric Grade Distributions

The linear grade distributions in Appendix B were used for calculation of the corresponding volumetric grade distributions using the symmetric transformation kernel

Table 5.4 Average grade as a function of size measured by image analysis

Size, microns		Fairlane Plant Grinding Circuit, Magnetite assays by image analysis, %									
Upper	Lower	B.M. Disch.	Cob. Conc.	Cyc. Feed	Cyc. Over	Cyc. Under	D.D. Conc.	D.D. Tails	Rough. Conc.	Rough. Tails	Scav. Conc.
1000	710	39.95	51.53	41.09	-	47.62	33.56	-	47.87	22.37	-
710	500	43.26	51.79	41.73	34.75	49.94	42.40	-	48.10	18.36	-
500	355	43.14	51.03	47.60	45.31	50.72	46.91	13.11	49.81	18.60	-
355	250	46.72	53.39	53.18	49.12	56.92	44.20	7.29	53.47	21.11	27.37
250	180	51.41	58.14	60.39	35.61	60.76	32.80	4.40	57.17	15.11	33.22
180	106	61.07	64.18	68.77	34.64	75.69	36.58	6.36	69.22	18.63	36.33
106	75	72.44	72.60	84.09	61.49	88.47	64.26	12.97	80.01	20.37	58.68
75	53	79.53	77.96	86.66	83.71	92.73	85.19	20.02	87.76	18.73	77.02
53	45	72.32	75.54	89.41	90.90	92.04	88.64	27.00	88.02	16.42	83.99
45	38	79.01	84.92	91.44	91.43	92.82	93.98	33.31	90.04	15.85	86.81
38	0	64.88	75.96	91.38	91.48	87.04	91.40	26.83	89.21	16.71	87.93
Average in stream		62.56	56.64	75.46	80.68	71.56	70.48	13.17	73.58	17.59	68.47

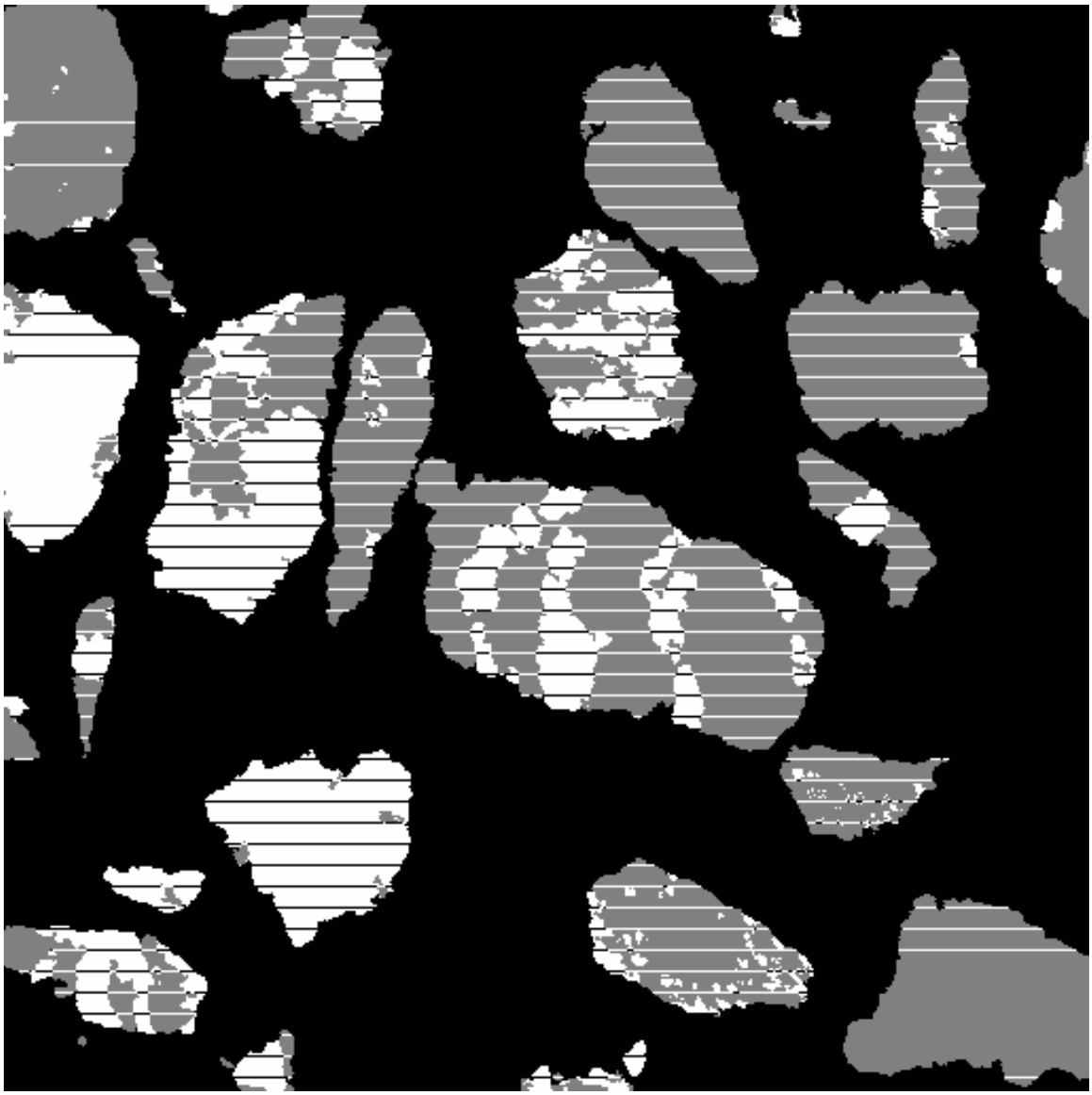

Figure 5.6 Discriminated image from -500+355 micron Cyclone Underflow particles at standard 40X magnification, and the measuring linear probes

developed from measurement on the Dolomite-Sphalerite ore and the stereological correction procedure in Chapter 2. The volumetric grade distributions, weighted by volume, were converted to the corresponding volumetric grade distribution by weight, using the measured phase densities reported in the experimental Phase and Texture Characterization section that follows. These distributions are shown in Tables 5.5 through 5.14. Fortunately the texture of the Taconite ore is nearly symmetrical, and the symmetric transformation kernel can be used for the preliminary evaluation of the liberation characteristics of the ore. The volumetric grade distributions are fundamental in understanding the interactions between the textural characteristics of the ore and its liberation properties, as the particles interact with the unit operations in the various streams in the grinding circuit. The measured liberation spectra can be used to calibrate and model the unit operations in the circuit, i.e., Ball Mill, Hydrocyclones and Magnetic Drum separators.

Texture and Phase Characterization

Normally, the distributions used for modeling and simulation are in terms of particle grade, i.e., weight fraction of phase, and distributions by weight rather than volume. The conversion from volume to weight fractions is easily accomplished if the density of the phases is known. Furthermore, the liberation model requires, at the very least, a representative geometrical texture parameter, which describes the change in interphase area per unit volume of phase as particle composition changes. The representative geometrical texture parameter can be obtained by optimization, as described in Chapter 4, when the liberation spectra in the feed and product streams of a size

Table 5.5 The measured volumetric grade distributions, by weight, in the Ball Mill Discharge stream

Conditional, on size, volumetric grade distributions, weight % Size intervals in microns.											
volumetric grade interval, %	-1000 +710	-710 +500	-500 +355	-355 +250	-250 +180	-180 +106	-106 +75	-75 +53	-53 +45	-45 +38	-38
0	0.00	0.00	0.12	0.0	0.17	0.00	0.00	7.11	12.79	12.91	29.24
0 - 10	0.10	0.10	2.89	6.71	13.45	9.97	15.34	4.45	10.33	2.10	0.09
10 - 20	19.58	0.32	16.27	8.55	3.46	6.22	0.95	4.32	0.15	1.97	2.19
20 - 30	56.97	62.46	16.34	38.91	31.83	7.85	4.02	0.00	1.76	0.00	0.07
30 - 40	22.54	34.40	63.29	15.82	10.18	26.46	5.95	3.82	3.26	2.00	0.90
40 - 50	0.06	1.99	0.69	19.04	11.78	3.49	0.52	0.08	0.09	0.78	0.04
50 - 60	0.14	0.13	0.16	10.55	9.46	5.34	4.56	0.09	0.09	0.61	0.09
60 - 70	0.15	0.14	0.06	0.11	12.66	3.48	5.86	0.09	0.10	1.73	0.58
70 - 80	0.16	0.16	0.00	0.16	5.59	7.63	14.27	0.55	3.03	2.07	0.61
80 - 90	0.15	0.14	0.13	0.15	1.23	29.36	22.86	16.39	13.71	12.37	30.97
90 - 100	0.15	0.15	0.05	0.00	0.19	0.22	25.18	63.05	54.68	48.74	11.88
100	0.00	0.00	0.00	0.00	0.00	0.00	0.48	0.05	0.01	14.72	23.34

Table 5.6 The measured volumetric grade distributions, by weight, in the Cobber Concentrate stream

Conditional, on size, volumetric grade distributions, weight % Size intervals in microns.											
volumetric grade interval, %	-1000 +710	-710 +500	-500 +355	-355 +250	-250 +180	-180 +106	-106 +75	-75 +53	-53 +45	-45 +38	-38
0	0.00	0.00	0.08	0.00	0.00	0.41	5.12	7.34	6.51	2.45	14.13
0 - 10	0.09	0.09	0.01	3.54	11.94	10.86	7.97	4.18	8.00	6.59	4.08
10 - 20	1.08	0.03	2.44	6.68	3.01	5.98	4.60	4.87	6.77	2.97	3.04
20 - 30	26.62	25.86	45.49	22.42	12.25	8.83	6.69	4.32	5.20	0.00	0.00
30 - 40	45.84	58.60	20.53	31.95	19.88	9.26	3.84	0.35	0.02	0.14	1.19
40 - 50	24.98	7.48	23.94	14.83	18.09	12.22	0.00	0.95	0.00	0.38	0.00
50 - 60	1.13	7.59	3.92	13.69	4.25	5.53	0.41	0.06	0.05	0.17	0.03
60 - 70	0.11	0.20	3.55	6.56	5.86	5.28	0.17	0.07	0.05	0.83	0.09
70 - 80	0.02	0.06	0.01	0.29	8.26	9.49	8.76	0.00	0.48	2.84	0.00
80 - 90	0.07	0.09	0.00	0.03	16.37	25.95	26.27	26.01	13.68	10.31	12.58
90 - 100	0.05	0.00	0.00	0.00	0.08	6.19	36.16	51.06	59.21	61.08	60.87
100	0.01	0.00	0.02	0.00	0.00	0.00	0.00	0.79	0.01	12.24	4.00

Table 5.7 The measured volumetric grade distributions, by weight, in the Cyclone Feed stream

Conditional, on size, volumetric grade distributions, weight % Size intervals in microns.											
volumetric grade interval, %	-1000 +710	-710 +500	-500 +355	-355 +250	-250 +180	-180 +106	-106 +75	-75 +53	-53 +45	-45 +38	-38
0	0.00	0.00	0.00	0.00	0.00	1.29	1.38	0.41	1.30	0.39	3.61
0 - 10	0.10	0.10	0.09	0.09	6.32	2.63	0.93	2.64	1.89	3.34	0.00
10 - 20	1.21	13.78	0.80	12.37	2.89	2.75	3.29	3.26	1.74	0.00	0.26
20 - 30	77.23	53.32	48.34	10.52	14.31	18.24	2.02	2.64	2.08	2.06	1.70
30 - 40	20.36	32.17	40.81	42.58	21.45	5.55	1.35	0.42	0.26	0.40	1.06
40 - 50	0.39	0.15	9.11	14.77	11.26	6.15	5.21	0.87	0.55	0.43	0.08
50 - 60	0.14	0.11	0.26	16.27	12.15	5.53	3.27	0.00	0.40	1.15	0.08
60 - 70	0.14	0.00	0.34	1.36	17.26	15.36	2.30	6.26	0.00	0.10	0.09
70 - 80	0.14	0.07	0.10	1.71	2.85	11.15	10.40	4.83	0.15	2.50	3.74
80 - 90	0.14	0.13	0.00	0.14	10.57	26.36	31.67	21.60	26.33	0.17	2.78
90 - 100	0.15	0.18	0.00	0.18	0.93	5.00	31.22	56.02	61.76	77.06	55.35
100	0.00	0.00	0.14	0.00	0.00	0.01	6.99	1.04	3.55	12.40	31.25

Table 5.8 The measured volumetric grade distributions, by weight, in the Cyclone Overflow stream

Conditional, on size, volumetric grade distributions, weight % Size intervals in microns.											
volumetric grade interval, %	-1000 +710	-710 +500	-500 +355	-355 +250	-250 +180	-180 +106	-106 +75	-75 +53	-53 +45	-45 +38	-38
0	-	0.00	0.00	0.00	0.00	2.76	5.38	3.51	1.25	0.68	3.59
0 - 10	-	0.10	2.98	3.62	20.08	21.28	1.19	2.58	1.83	2.90	0.00
10 - 20	-	29.92	9.29	4.65	24.96	31.33	18.53	1.51	0.99	1.14	0.01
20 - 30	-	61.15	16.31	31.04	7.20	0.88	4.39	3.69	0.15	0.92	0.03
30 - 40	-	7.94	63.03	33.11	47.15	37.59	13.86	2.68	1.18	1.41	2.42
40 - 50	-	0.14	6.19	15.65	0.18	5.60	9.71	1.17	0.79	0.94	0.08
50 - 60	-	0.14	1.64	10.65	0.22	0.00	2.47	0.09	0.59	0.65	0.29
60 - 70	-	0.15	0.21	1.00	0.05	0.00	1.01	1.77	0.09	1.24	1.98
70 - 80	-	0.15	0.13	0.20	0.08	0.02	4.76	7.55	0.00	0.85	1.28
80 - 90	-	0.15	0.00	0.08	0.00	0.00	28.48	21.33	21.79	6.39	13.05
90 - 100	-	0.16	0.22	0.00	0.08	0.13	10.21	54.12	55.98	28.40	41.94
100	-	0.00	0.00	0.00	0.00	0.40	0.00	0.01	15.37	54.49	35.32

Table 5.9 The measured volumetric grade distributions, by weight, in the Cyclone Underflow stream

Conditional, on size, volumetric grade distributions, weight % Size intervals in microns.											
volumetric grade interval, %	-1000 +710	-710 +500	-500 +355	-355 +250	-250 +180	-180 +106	-106 +75	-75 +53	-53 +45	-45 +38	-38
0	0.00	0.00	0.08	0.00	0.00	0.00	0.00	0.00	0.00	0.59	6.28
0 - 10	0.10	0.09	0.01	0.09	5.82	0.08	0.28	0.14	0.75	1.45	1.21
10 - 20	0.43	0.38	0.35	0.93	0.01	0.05	2.14	3.11	2.82	1.46	2.30
20 - 30	44.44	18.21	40.14	29.64	12.48	7.78	1.97	0.83	0.61	0.25	0.38
30 - 40	54.20	75.74	44.49	19.97	29.61	11.28	3.31	1.17	0.87	0.24	0.08
40 - 50	0.12	2.78	1.27	28.03	3.91	12.91	0.18	0.41	0.12	0.81	0.08
50 - 60	0.13	2.42	12.51	6.76	17.46	8.19	1.66	0.18	1.60	0.28	0.09
60 - 70	0.14	0.16	0.96	5.13	14.43	17.82	2.25	0.08	0.79	0.09	0.09
70 - 80	0.15	0.16	0.20	5.58	9.01	0.03	4.72	0.20	2.38	1.08	2.76
80 - 90	0.14	0.00	0.00	3.80	6.49	22.77	32.60	2.09	12.18	15.22	13.32
90 - 100	0.15	0.00	0.00	0.07	0.79	19.10	50.90	85.16	66.70	45.42	48.61
100	0.00	0.06	0.00	0.00	0.00	0.00	0.01	6.64	11.16	33.11	24.80

Table 5.10 The measured volumetric grade distributions, by weight, in the Dewatering Drum Concentrate stream

Conditional, on size, volumetric grade distributions, weight % Size intervals in microns.											
volumetric grade interval, %	-1000 +710	-710 +500	-500 +355	-355 +250	-250 +180	-180 +106	-106 +75	-75 +53	-53 +45	-45 +38	-38
0	0.03	0.00	0.03	0.00	0.96	0.01	4.52	1.35	0.53	0.24	3.18
0 - 10	0.08	0.10	0.07	5.53	21.18	15.00	5.30	3.12	0.21	0.39	0.00
10 - 20	32.53	6.73	3.92	5.22	22.64	31.47	4.96	1.31	4.70	0.45	0.60
20 - 30	65.47	58.90	38.12	39.32	43.58	24.95	8.27	6.01	1.08	1.55	0.00
30 - 40	1.01	32.35	48.76	39.76	9.31	22.93	4.19	2.06	1.54	1.93	0.15
40 - 50	0.13	1.18	8.55	9.59	1.69	4.81	24.41	2.00	3.92	0.18	0.12
50 - 60	0.14	0.14	0.09	0.00	0.41	0.05	4.72	0.00	1.53	0.08	0.09
60 - 70	0.15	0.15	0.16	0.22	0.15	0.00	5.14	0.03	1.58	0.04	0.35
70 - 80	0.15	0.16	0.14	0.29	0.07	0.00	6.22	4.40	2.04	0.28	0.21
80 - 90	0.15	0.14	0.16	0.06	0.00	0.03	23.30	19.88	2.57	16.35	18.40
90 - 100	0.16	0.15	0.00	0.00	0.01	0.01	8.98	48.22	80.18	42.73	56.85
100	0.00	0.00	0.00	0.00	0.00	0.74	0.00	11.62	0.13	35.79	20.06

Table 5.11 The measured volumetric grade distributions, by weight, in the Dewatering Drum Tails stream

Conditional, on size, volumetric grade distributions, weight % Size intervals in microns.											
volumetric grade interval, %	-1000 +710	-710 +500	-500 +355	-355 +250	-250 +180	-180 +106	-106 +75	-75 +53	-53 +45	-45 +38	-38
0	-	-	6.77	63.71	69.25	70.86	39.51	35.22	36.85	25.32	67.92
0 - 10	-	-	70.12	12.95	24.27	14.59	27.77	27.00	29.91	34.28	0.20
10 - 20	-	-	21.63	21.93	4.80	10.48	23.75	20.73	0.86	9.24	3.05
20 - 30	-	-	0.37	0.26	0.60	2.92	7.52	0.70	8.63	1.00	0.36
30 - 40	-	-	0.14	0.14	0.10	0.14	0.00	2.35	1.64	1.34	0.53
40 - 50	-	-	0.15	0.15	0.52	0.15	0.76	7.11	3.05	1.16	0.07
50 - 60	-	-	0.16	0.16	0.31	0.17	0.14	2.07	0.80	1.85	0.51
60 - 70	-	-	0.16	0.16	0.00	0.16	0.11	0.29	3.29	1.64	0.53
70 - 80	-	-	0.17	0.17	0.11	0.17	0.10	4.44	5.69	5.38	4.62
80 - 90	-	-	0.17	0.17	0.00	0.17	0.17	0.03	7.63	10.45	16.00
90 - 100	-	-	0.18	0.18	0.03	0.18	0.18	0.00	1.65	8.34	6.21
100	-	-	0.00	0.00	0.00	0.00	0.00	0.07	0.00	0.00	0.00

Table 5.12 The measured volumetric grade distributions, by weight, in the Rougher Concentrate stream

Conditional, on size, volumetric grade distributions, weight % Size intervals in microns.											
volumetric grade interval, %	-1000 +710	-710 +500	-500 +355	-355 +250	-250 +180	-180 +106	-106 +75	-75 +53	-53 +45	-45 +38	-38
0	0.00	0.00	0.00	0.00	0.00	0.00	1.09	0.61	1.96	1.57	2.67
0 - 10	0.10	0.10	0.10	0.09	9.40	6.07	2.91	2.49	1.96	2.27	2.07
10 - 20	0.56	1.09	1.04	0.26	3.81	4.44	3.72	0.20	1.39	1.74	2.31
20 - 30	24.13	44.65	42.02	34.49	11.36	8.68	7.48	3.54	3.08	0.84	0.00
30 - 40	73.72	47.83	35.91	21.77	21.25	10.14	5.95	1.30	3.65	0.30	0.02
40 - 50	0.99	3.93	13.42	25.41	26.83	1.69	3.23	5.31	0.00	0.40	0.14
50 - 60	0.21	2.03	6.55	16.96	5.36	6.06	2.63	0.08	0.09	2.48	0.26
60 - 70	0.00	0.20	0.59	0.58	8.62	12.77	0.81	0.08	0.10	1.01	1.27
70 - 80	0.03	0.08	0.17	0.15	4.97	28.09	3.05	0.23	0.23	1.38	2.62
80 - 90	0.11	0.10	0.09	0.16	5.00	21.86	20.50	25.87	18.37	8.95	7.97
90 - 100	0.16	0.00	0.11	0.14	3.40	0.16	48.62	55.91	55.36	52.98	79.09
100	0.00	0.00	0.00	0.00	0.00	0.04	0.01	4.38	13.81	26.07	1.57

Table 5.13 The measured volumetric grade distributions, by weight, in the Rougher Tails stream

Conditional, on size, volumetric grade distributions, weight % Size intervals in microns.											
volumetric grade interval, %	-1000 +710	-710 +500	-500 +355	-355 +250	-250 +180	-180 +106	-106 +75	-75 +53	-53 +45	-45 +38	-38
0	0.41	0.00	4.87	8.23	43.71	27.63	27.78	47.50	49.58	67.49	69.80
0 - 10	20.58	52.87	57.82	32.07	18.86	29.32	40.04	22.53	33.88	14.56	10.06
10 - 20	77.74	35.92	14.18	50.70	26.30	27.15	8.34	8.98	2.43	4.37	2.06
20 - 30	0.64	10.02	21.80	7.27	8.07	3.60	17.40	11.03	1.06	0.42	0.71
30 - 40	0.01	0.27	0.53	0.78	2.09	10.26	0.00	0.41	0.90	1.54	2.22
40 - 50	0.03	0.14	0.02	0.14	0.15	0.52	0.02	0.13	1.04	0.00	0.12
50 - 60	0.00	0.14	0.25	0.15	0.16	0.12	0.01	0.14	1.62	1.02	0.13
60 - 70	0.13	0.15	0.18	0.17	0.16	0.04	0.05	0.15	1.12	1.24	2.22
70 - 80	0.15	0.15	0.20	0.15	0.16	0.33	0.04	3.33	1.53	2.25	0.83
80 - 90	0.15	0.16	0.15	0.16	0.17	0.42	0.02	0.98	2.70	3.26	7.37
90 - 100	0.16	0.17	0.00	0.17	0.18	0.00	1.56	0.30	4.13	3.63	4.48
100	0.00	0.00	0.00	0.00	0.00	0.00	4.75	4.53	0.00	0.23	0.00

Table 5.14 The measured volumetric grade distributions, by weight, in the Scavenger Concentrate stream

Conditional, on size, volumetric grade distributions, weight % Size intervals in microns.											
volumetric grade interval, %	-1000 +710	-710 +500	-500 +355	-355 +250	-250 +180	-180 +106	-106 +75	-75 +53	-53 +45	-45 +38	-38
0	-	-	-	0.00	0.00	0.09	3.55	5.04	5.65	0.51	4.05
0 - 10	-	-	-	32.11	17.89	26.07	16.56	3.47	0.76	6.10	3.75
10 - 20	-	-	-	32.96	38.90	32.89	4.50	4.97	3.33	3.44	0.84
20 - 30	-	-	-	34.05	19.03	14.04	10.87	4.18	4.20	0.00	0.07
30 - 40	-	-	-	0.35	19.91	11.83	11.12	6.11	1.66	2.09	0.66
40 - 50	-	-	-	0.05	2.98	0.47	7.54	0.53	0.05	0.21	0.88
50 - 60	-	-	-	0.00	0.65	2.22	4.27	0.53	0.54	0.27	0.08
60 - 70	-	-	-	0.04	0.09	2.82	4.27	2.01	0.08	0.19	0.99
70 - 80	-	-	-	0.13	0.00	2.92	3.56	7.68	0.66	1.61	0.20
80 - 90	-	-	-	0.15	0.16	6.63	13.11	23.99	9.20	8.01	13.99
90 - 100	-	-	-	0.16	0.16	0.00	20.63	41.48	73.87	76.72	49.73
100	-	-	-	0.00	0.23	0.00	0.00	0.00	0.00	0.84	24.77

reduction operation are known. However, it is not yet possible to measure the parameter ϕ_r directly from the ore. Also, the dependency of texture on particle size is not yet understood. The value of the parameter ϕ at a given particle size can be measured directly from the ore by image analysis, from particles in narrow size and narrow grade intervals like the ones produced here. Narrow size particles are easily obtained by screening. However, particle samples in narrow grade intervals require some fractionation procedure. The Taconite ore is not suitable for magnetic fluid fractionation, due to the strong ferromagnetism of the magnetite. The fractionation procedure used here is the standard heavy liquid fractionation, using organic liquids and a 125 ml separation funnel. A sample of the -710+500 microns Ball Mill Discharge weighing 56.8 g was prepared for dense liquid fractionation. The heavy liquids used were Tetrabromoethane, ρ = 2.954 g/cc, and Diodomethane, ρ = 3.325 g/cc. Diodomethane diluted with Triethyl Orthophosphate was used to give a separation density at ρ = 3.112 g/cc. After fractionation, the particles were weighed and their average density measured in a helium pycnometer. The fractionation results are shown in Table 5.15. Each sample was mounted, ground and polished, as previously described. A set of 40 images per specimen was collected, and the images were processed also as previously described. In Figures 5.7, 5.8, 5.9 and 5.10, backscattered electron images selected arbitrarily from each set corresponding to a narrow grade interval are shown. Again, the dull grey phase represents Silicates and the bright phase represents Iron Oxides. The images show very graphically the increased contribution of Iron Oxides as particle density increases. Few liberated particle cross sections are observed, which indicates that fractionation was

Table 5.15 Dense liquid fractionation of -710+500 microns Ball Mill Discharge particles

Separation density, g/cc	Weight fraction, %	Average density, g/cc Helium pycnometer	Volumetric grade, % Image Analysis
-2.954	21.65	2.870	5.67
-3.112 +2.954	12.32	3.092	11.94
-3.325 +3.112	13.56	3.284	18.73
+3.325	52.47	4.009	51.24

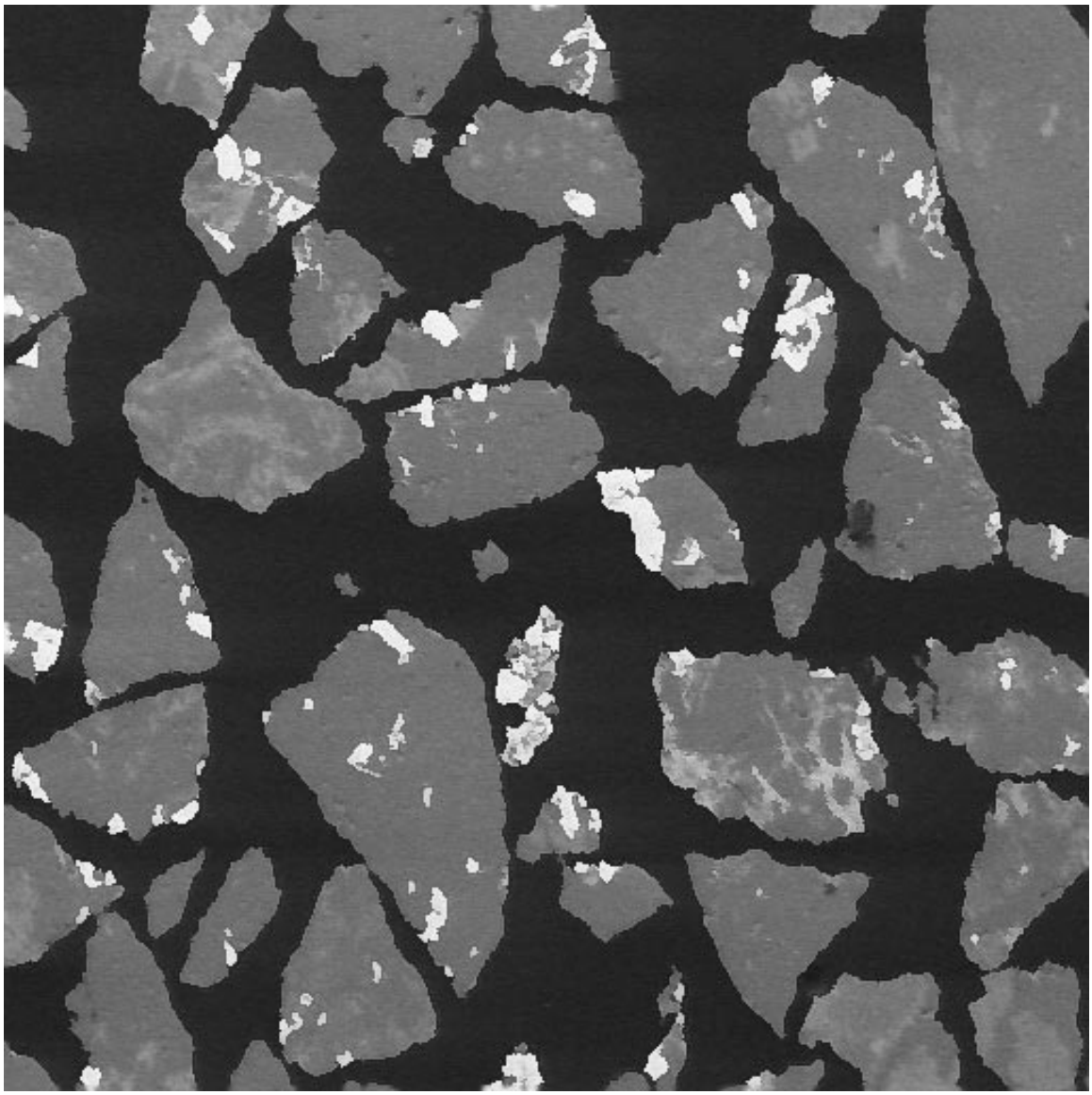

Figure 5.7 Backscattered electron image from -710+500 micron, -2.954 g/cc fractionated particles

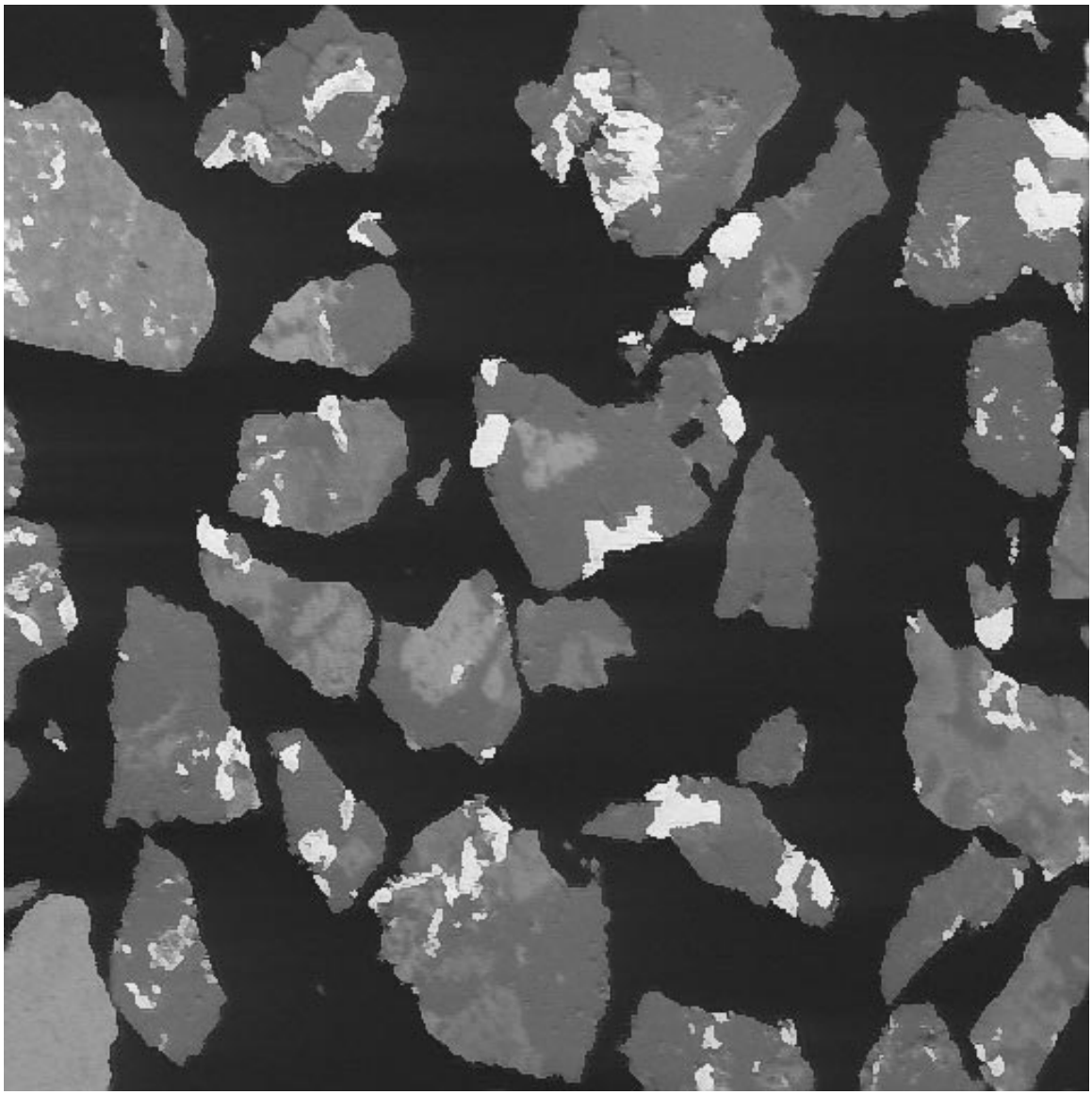

Figure 5.8 Backscattered electron image from -710+500 micron, -3.112+2.954 g/cc fractionated particles

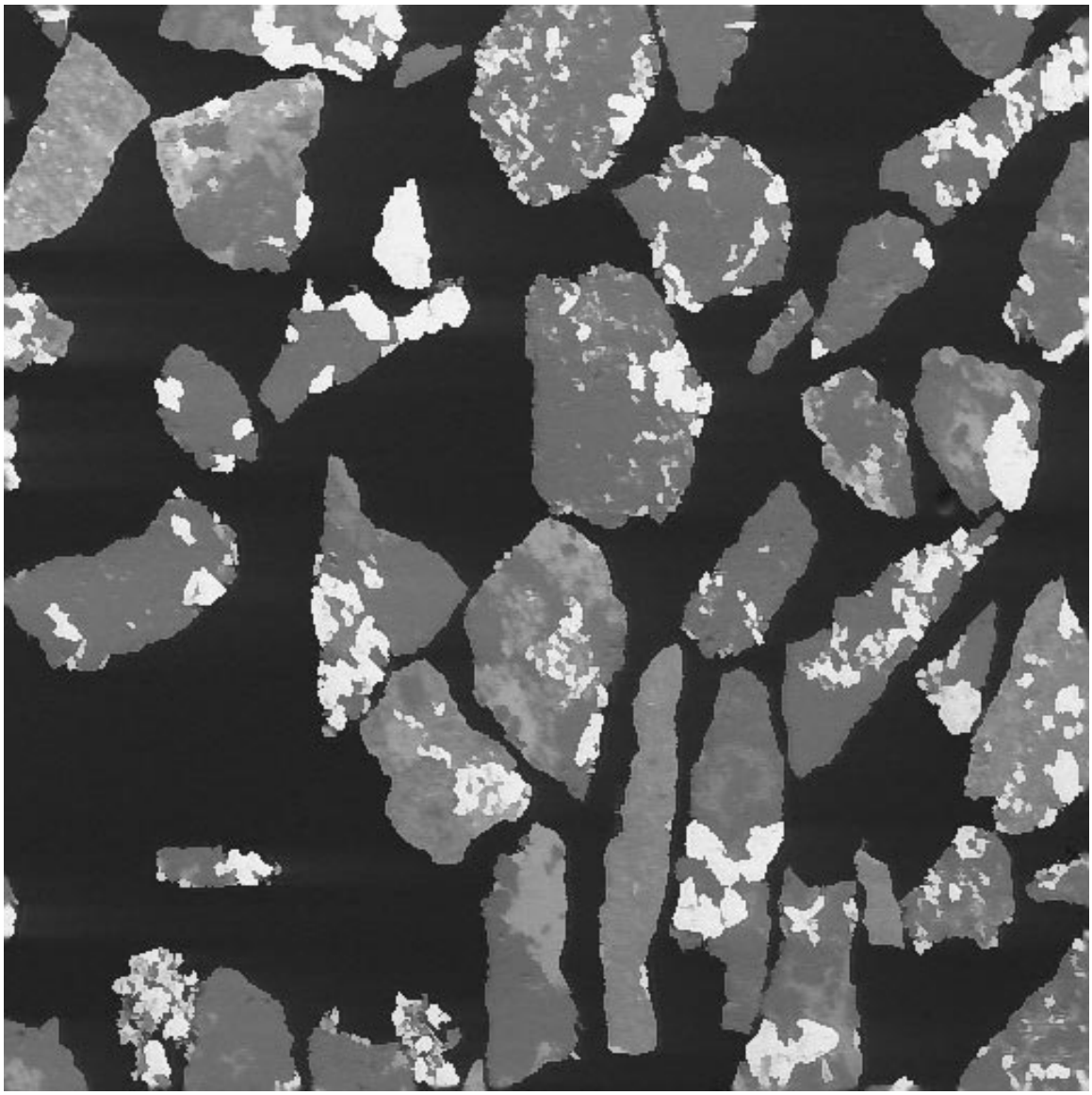

Figure 5.9 Backscattered electron image from -710+500 micron, -3.325+3.112 g/cc fractionated particles

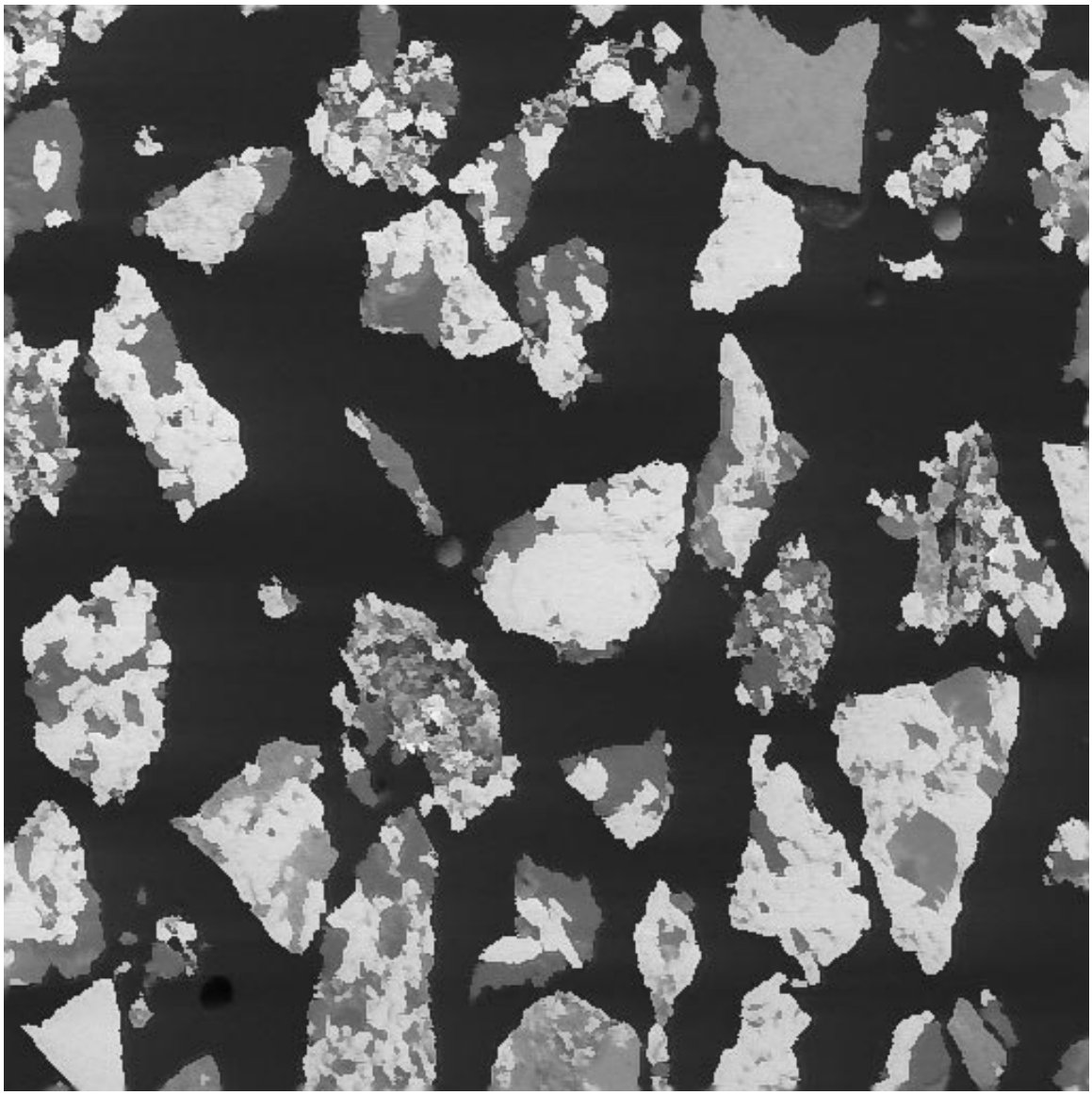

Figure 5.10 Backscattered electron image from -710+500 micron, +3.325 g/cc fractionated particles

successful. In Table 5.15, the measured volumetric grade of each fractionated sample is reported. If we denominate as phase A all the silicates present, mainly Chert, and phase B all iron oxides, mainly Magnetite, the densities of phases A and B can be calculated by plotting the fractionated sample densities, as measured by pycnometry, against the corresponding volumetric grade as measured by image analysis. This is shown in Figure 5.11. The straight line indicates that the ore is essentially binary with respect to density. In Figure 5.11, the density of phases A and B are calculated from the intercept and the slope of the line that fits the measured points. Linear regression yields ρ_A = 2.761 g/cc and ρ_B = 5.378 g/cc, completing the phase characterization procedure.

Since the particles were already fractionated for phase density determination, it is possible to use the images to measure the value of the textural parameter ϕ at this size range. For this, the average chord length for both phases and features was measured from the fractionated particle sample specimens. The average chord lengths were used to calculate the surface area per unit volume of both phases and the features as well. With these values, the interphase area per unit volume of phase $S_v AB$ and $S_v BA$ could be calculated. The results are shown in Table 5.16. The geometrical texture parameter $\phi(-710+500\,\mu)$, is calculated by plotting the product of representative particle size and interphase area per unit volume of phase against the volumetric grade of the corresponding phase. Here, the representative particle size is $d_p = \sqrt{D_{upper}\, D_{lower}}$ = 595.82 microns. The resulting plot is shown in Figure 5.12, and linear regression yields $\phi(-710+500\,\mu)$ = 45.06.

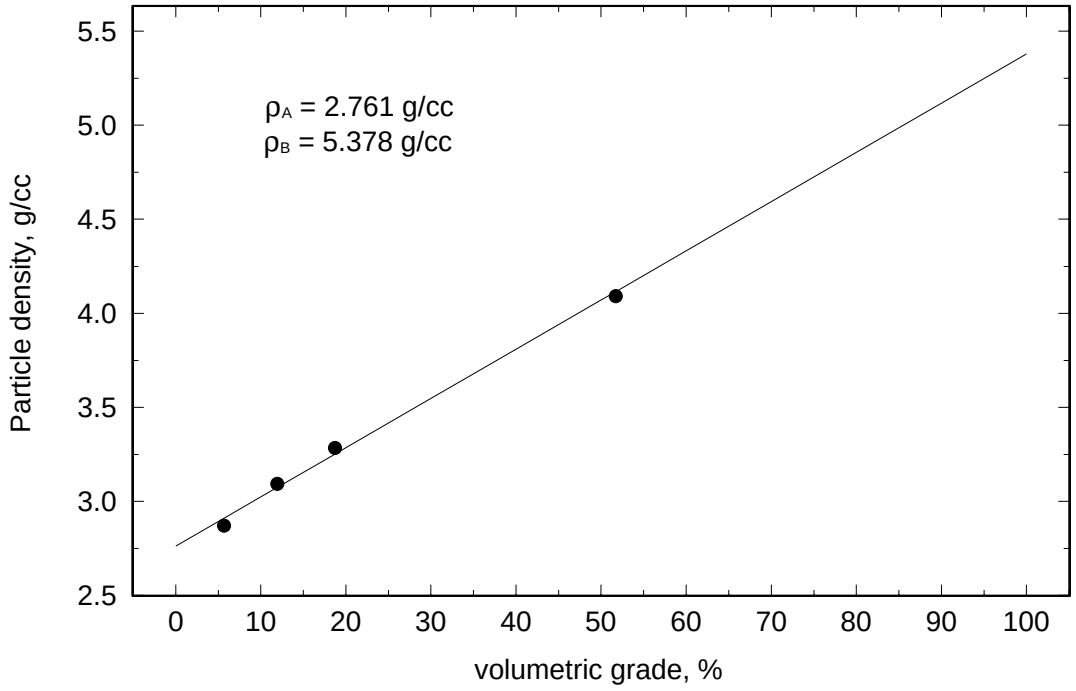

Figure 5.11 Correlation between average sample density by Helium Pycnometry and average sample volumetric grade by image analysis, and phase density determination

Table 5.16 The interphase area per unit volume of phase and the corresponding volumetric grades measured on the narrow size, narrow grade samples from fractionation

Density range, g/cc	Volumetric grade of phase A, Silicates	Interphase area per unit volume of phase A	Volumetric grade of phase B, Iron Oxides	Interphase area per unit volume of phase B
-2.954	0.9433	4.371×10^{-3}	0.0567	7.289×10^{-2}
-3.112 +2.954	0.8806	8.667×10^{-3}	0.1194	6.337×10^{-2}
-3.325 +3.112	0.8127	1.544×10^{-3}	0.1873	6.622×10^{-2}
+3.325	0.4876	3.621×10^{-3}	0.5124	3.380×10^{-2}

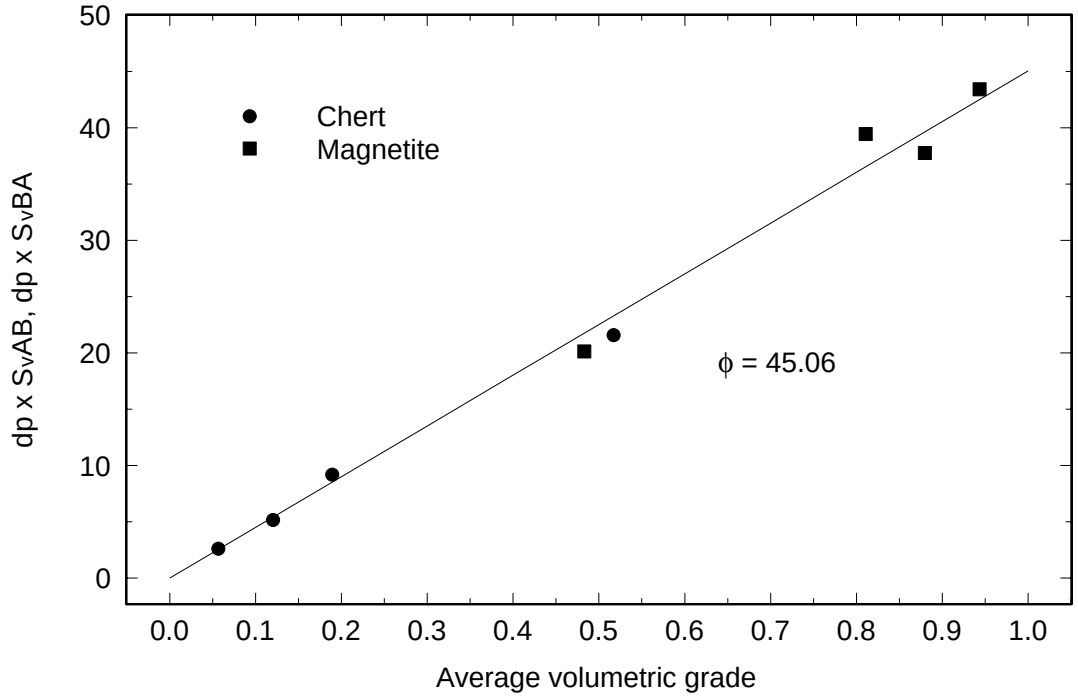

Figure 5.12 Taconite ore geometrical texture parameter determination

MODSIM Simulation Setup and Models

The flowsheet setup for the simulation of the secondary grinding circuit is shown in Figure 5.13. The main feed stream is the Cobber Concentrate. The Dewatering Drum magnetic separation was regarded as a subsidiary separation unit, and the concentrate and tails streams were treated as secondary feed streams to the main circuit, with constant size and liberation spectra. The Scavenger Concentrate stream was also treated as a subsidiary feed stream with constant size and liberation spectra.

The size distributions in the four feed streams were entered in MODSIM as shown in Table 5.2. The conditional liberation spectra were entered as measured for all available sizes in the feed streams. For the larger size fractions, where the liberation spectra was not measured either because there were not enough particles available for image analysis or because of the 1000 microns top size limitation for the *I.A.* system used, the liberation spectrum measured on the largest size sample was repeated. This assumption is significant only for the Cobber Concentrate stream, which contains approximately 47% of particles larger than 1000 microns. The measured, conditional on size, liberation spectra corresponding to the Cobber Concentrate stream is shown in Figure 5.14. It is clear from the figure that the particles at the larger size classes, approaching the 1000 microns top size, are very closely distributed around the volumetric grade corresponding to the volumetric abundance of Magnetite in the stream. Clearly, this behavior must be retained for particles larger than 1000 microns, and the assumption of constant liberation spectra above 1000 microns for the Taconite particles in the Cobber Concentrate stream is not expected to produce significant error in the circuit simulation.

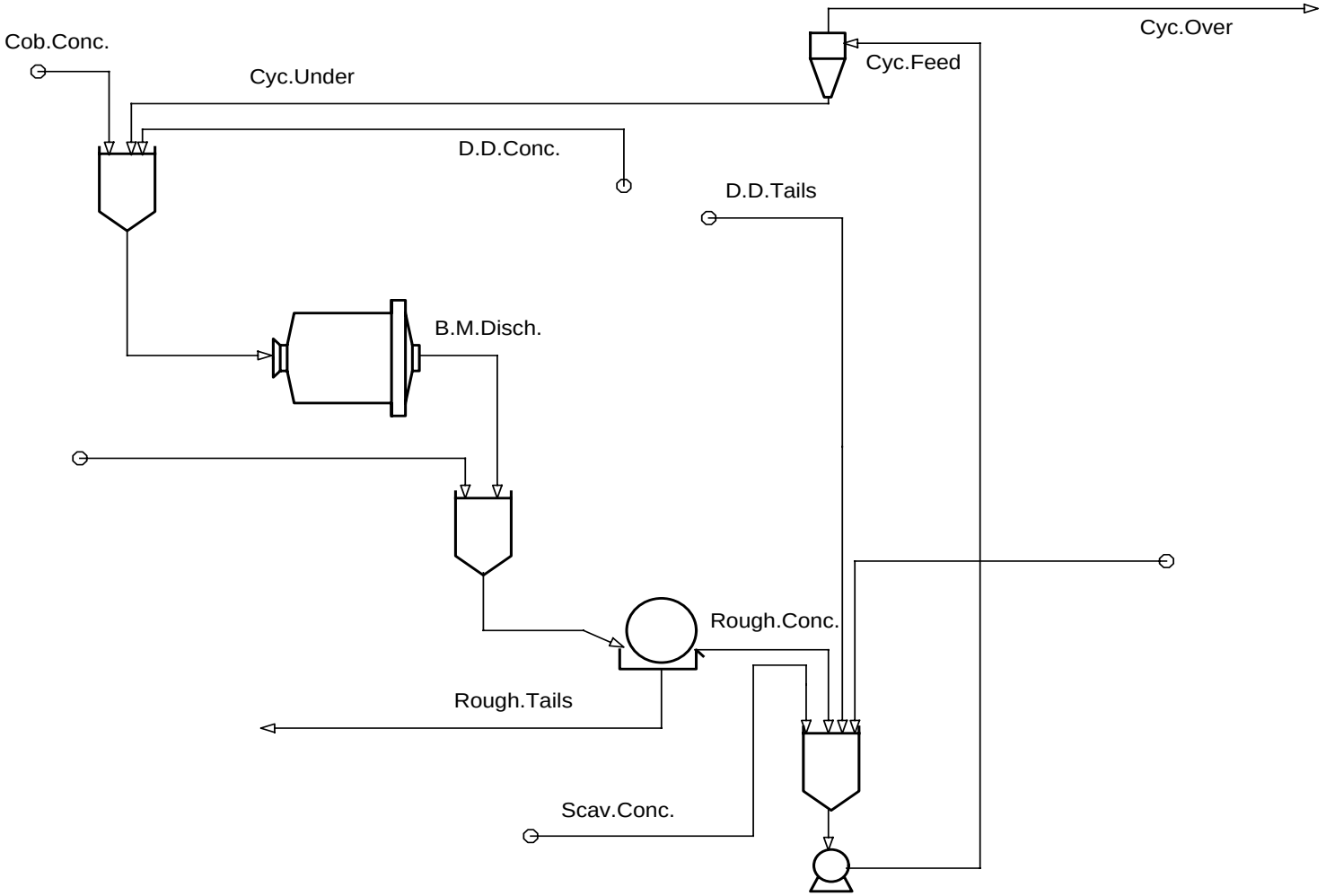

Figure 5.13 The flowsheet used in MODSIM for the simulation of the Fairlane secondary grinding circuit

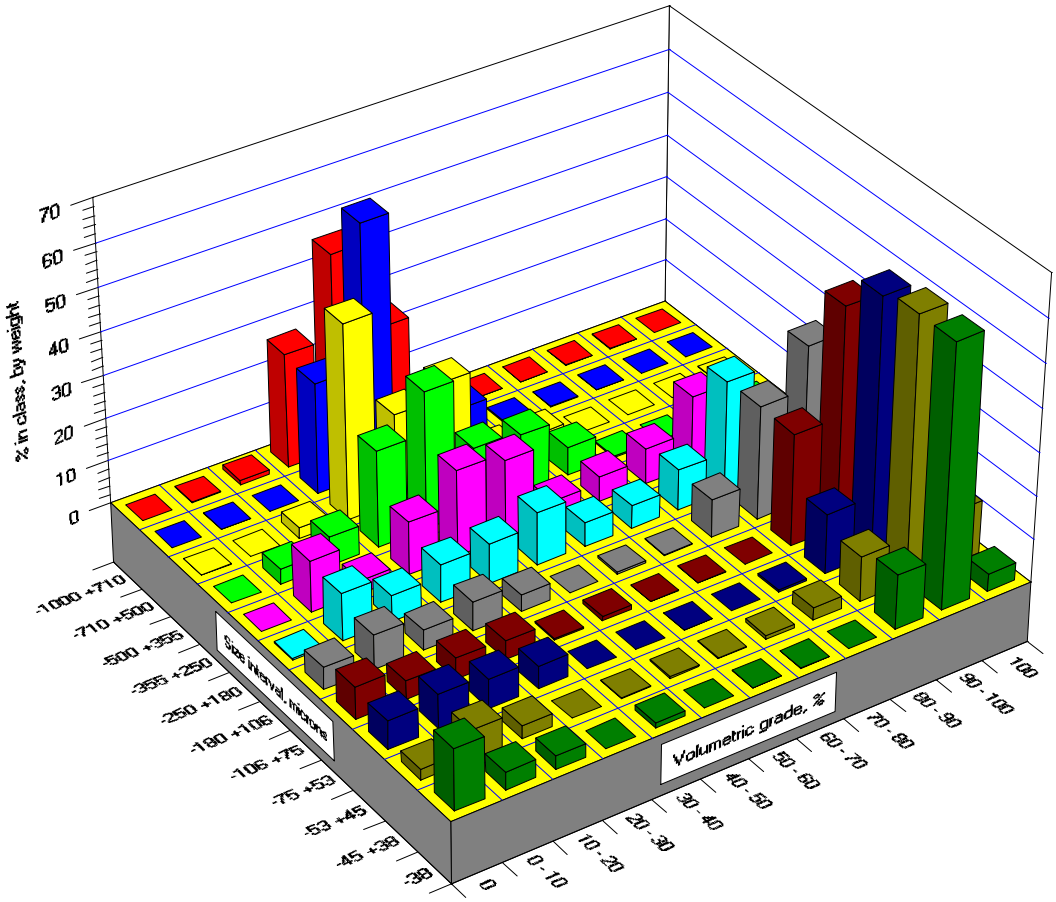

Figure 5.14 The measured, conditional on size, liberation spectra in the Cobber Concentrate stream

The primary objectives of the simulation were to match the plant's nominal material balance, as shown in Table 5.17, and to match the measured size and liberation spectra in each stream. The solids feed rates entered in the simulator were equal to the nominal feed rates obtained from the plant's material balance. Water feed rates were calculated by MODSIM so that the nominal solids content in each feed stream in the circuit were reproduced. The simulation of the secondary grinding circuit requires, besides the liberation model, a comminution model for the ball mill and concentration/classification models for both the rougher wet magnetic drum separator and the hydrocyclone. The models were adjusted and the best set of parameters was obtained by both independent optimization of each unit operation, and manually by repeated simulation of the entire circuit.

Liberation Model

The liberation model was used as described in Chapter 3, with modifications to the critical parameters ϕ_A^C and ϕ_B^C, the variance parameter ζ and the shape of the variance function, and to the shape of the boundary of the accessible region associated with phase *B*. The modifications are due to the peculiarities of the textural properties of the Taconite ore, in contrast with the Dolomite-Sphalerite ore texture.

The critical texture parameters were set at $\phi_A^C = 25.0$ and $\phi_B^C = 9.00$ with respect to a representative geometrical texture parameter ϕ_r set equal to the measured geometrical texture parameter $\phi\left(-710+500\,\mu\right)$ as shown in Figure 5.12, i.e., $\phi_r = 45.0$. This clearly indicates that the Chert starts liberating at considerably larger sizes than the Magnetite.

The composite particles of Taconite seem to shift, upon breakage, from

Table 5.17 The nominal flow rates and % solids and the measured grades in the streams of the secondary grinding circuit of the Fairlane Plant. Recoveries are based on the total flow rates from the four feed streams. Stream grades are calculated from image analysis results in each size range and the measured/adjusted size distributions

Stream	Solid Flow, Tons/hour	Water Flow, m^3/hour	solids, %	Recovery of solids, %	Recovery of Chert, %	Grade of Chert, %	Recovery of Magnetite, %	Grade of Magnetite, %
Cob.Conc.	301.26	137.89	68.60	79.11	83.09	43.36	76.32	56.64
Cyc.Feed	618.37	474.35	56.59	162.39	96.52	24.54	208.71	75.46
Cyc.Under	381.77	64.69	85.51	100.26	69.06	28.44	122.19	71.56
Cyc.Over	236.60	679.39	25.83	62.13	29.08	19.32	85.54	80.68
D.D.Conc.	57.48	30.34	65.45	15.09	10.79	29.52	18.12	70.48
D.D.Tails	4.82	59.36	7.51	1.27	2.66	86.83	0.28	13.17
B.M.Disch.	740.51	230.14	76.29	194.47	176.35	37.44	207.20	62.56
Rough.Conc.	618.57	526.93	54.00	162.44	103.95	26.42	203.57	73.58
Rough.Tails	121.94	1913.79	5.99	32.02	63.92	82.41	9.59	17.59
Scav.Conc.	17.23	23.50	42.30	4.52	3.46	31.53	5.28	68.47

intermediate volumetric grade classes to the volumetric grade classes corresponding to nearly liberated particles rather quicker than the composite particles of Dolomite-Sphalerite. Yet, once they reach the nearly liberated state, the particles liberation rate is comparatively slow. It is interesting to note that the liberation behavior of a binary ore can be viewed under opposite perspectives. With respect to the Taconite ore, one could say that, upon breakage, composite particles generate a very small fraction of progeny in the intermediate grade classes. One could also say that particles in the intermediate grade classes tend to change their liberation state faster than particles in nearly liberated grade classes, which tend to retain their liberation state.

The behavior of the Taconite particles is not well described by the Dolomite-Sphalerite model functional form for the variance, in Equation 3.57, and for the Taconite ore, it was found that the following functional form was considerably more effective:

$$\sigma_{\xi}^{2} = \begin{cases} \dfrac{\zeta}{2}\dfrac{g_v'}{0.3}\left(n_{1\xi}^{B} - n_{1\xi}^{B2}\right) & g_v' \le 0.3 \\ \dfrac{\zeta}{2}\left(n_{1\xi}^{B} - n_{1\xi}^{B2}\right) & 0.3 < g_v' < 0.8 \\ \dfrac{\zeta}{2}\dfrac{(1-g_v')}{0.2}\left(n_{1\xi}^{B} - n_{1\xi}^{B2}\right) & 0.8 \le g_v' \end{cases} \tag{5.1}$$

with the variance parameter set at ζ = 1.95. In Equation 5.1, variance is maximum and constant for particles with volumetric grades between 0.3 and 0.8. The variance is null for liberated particles and varies linearly with parent volumetric grade when parent volumetric grade is smaller than 0.3 or higher than 0.8.

The modified variance model for the Taconite ore works best in conjunction with the following modification to the shape of the boundary of the accessible region associated to phase B:

$$g_v^{B,Taconite} = \begin{cases} g_v^B & g_v^B < 1 \ , \ g_v' \leq 0.3 \\ \dfrac{(1+g_v^B)}{2} & g_v^B < 1 \ , \ 0.3 < g_v' < 0.8 \\ g_v^B & g_v^B < 1 \ , \ 0.8 \leq g_v' \end{cases} \tag{5.2}$$

where g_v^B is defined as in Equation 3.59, for the Dolomite-Sphalerite texture. Equation 5.2 allows for a broader range of grades in which progeny from intermediate grade particles can be produced, relative to Equation 3.59. However, care was taken so that the limiting bounds of the accessible region for phase B became active when and if violated by the boundary defined by Equation 5.2.

The modifications to the liberation model defined in Equations 5.1 and 5.2 are in fact a rough adjustment to the Dolomite-Sphalerite model such that the liberation characteristics of the Taconite ore are better reproduced when simulating the Taconite grinding circuit in this study. The modifications were made exclusively by comparing simulated and measured liberation spectra. More important than the modifications in themselves is the fact that they were necessary, and consequently indicating that the texture of a particular ore, depending on its peculiarities, may require modifications to the boundary models and to the variance model, in addition to reparameterization.

Comminution Model

There is no information on the particle size distribution in the holdup of the ball mill at the Fairlane Plant. Consequently, classification effects in the mill with respect to particle size cannot be accessed. In fact, the ball mill feed stream was not sampled for particle size distribution measurement. The only direct information available, besides some operational conditions, and the mill's geometry, that is useful for the choice and parameterization of the comminution model, is the size distribution in the product stream. The feed stream to the ball mill could not be sampled due to the plant's physical configuration. A priori, only an approximate size distribution in the feed stream should be sufficient for a preliminary parameterization work. This was obtained by adding the measured size distributions in the Cobber Concentrate, Cyclone Underflow, and Dewatering Drum Concentrate streams, and using the nominal material balance in Table 5.17. Since the size distribution in the product is not very sensitive to the size distribution in the feed, an approximate distribution should be enough to choose the proper comminution model and to obtain an initial set of parameters by independent optimization.

It was assumed that the transport in the mill can be described by three perfectly mixed regions in series, with the fractional residence times for the solids shown in Table 4.8. This assumption is probably inaccurate, particularly when considering the geometry of the ball mill, which has a diameter to length ratio of approximately 1:2.5. However, this assumption has no impact whatsoever at this stage of the investigation, and the only direct consequence is that the parameters for the model equations corresponding to the

selection and breakage functions become even more alienated to the comminution properties of the ore from the phenomenological point of view.

The three mixers in series with post-classification model is described in Equations 4.15 through 4.17. When classification is not considered, the classification coefficients C_i are null for every particle size *i*, and consequently $p_i = p_i^* = p_i^{(3)}$ and $\tau_3' = \tau_3$. The breakage function model chosen for the Taconite ore was Austin's [36] three parameter normalizable function shown in Equation 4.23. The selection function for the Taconite ore was modeled by:

$$S_i = S_1 \left(\frac{d_{pi}}{1000} \right)^{\alpha} \tag{5.3}$$

It is interesting to point out that the best model for the selection function did not require a description for an abnormal breakage region, perhaps due to the comparatively small particle sizes in the mill's feed. The final parameters for the comminution model of the ball mill are shown in Table 5.18, including breakage function and selection function parameters, and the residence times in the mill.

Wet Magnetic Drum Separator Model

The model developed for the Rougher separation was empirical, in nature. The classification action in a wet magnetic drum separator is primarily a function of the volumetric abundance of the magnetic phase, here the Magnetite, in the particle. In practice, because the separators are simple drums that produce a constant magnetic field and that rotate at constant speed, the configuration of the feed streams and how the

Table 5.18 The comminution model parameters for the ball mill used in MODSIM simulation

Selection function parameters	α = 1.28855 S_1 = 1.28076 min^{-1}
Breakage function parameters	Φ = 0.46085 β = 0.44601 γ = 0.98684
Average residence time in perfectly mixed region *n* (minutes)	τ_1 = 0.0548 τ_2 = 0.8492 τ_3 = 3.0960
Total residence time (minutes)	τ = 4.0

particles are exposed to the magnetic field, is of crucial importance. Here, at least at this preliminary modeling stage, it is considerably more important to establish a classification function that can be used to model the classification action, with respect to both particle size and grade, of the magnetic separator.

The classification phenomenon in the unit can be described by:

$$c(g_v, d_p) = \alpha(d_p) + (1 - \alpha(d_p))\ e(g_v) \tag{5.4}$$

where $c(g_v, d_p)$ represents the fraction of particles that have volumetric grade g_v and representative size d_p that report to the tails stream. The by-pass fraction of particles in the feed that short circuits to the tails stream is represented by $\alpha(d_p)$, which is only a function of particle size. The primary classification function, represented by $e(g_v)$, is exclusively dependent on particle composition.

The by-pass function $\alpha(d_p)$ is based on the principle that smaller particles are more susceptible to the drag produced by the water flow. Approximately 80% of the water in the feed of the Rougher separator reports to the tails stream (Table 5.17), and some water drag must be expected. The by-pass function was modeled by:

$$\alpha(d_p) = \kappa\ e^{-\varsigma\ d_p} \tag{5.5}$$

where κ and ς are arbitrary model parameters.

The classification function $e(g_v)$ was modeled with the commonly used Rosin-Rammler functional form:

$$e(g_v) = 1 - e^{-0.693\left(\frac{1-g_v}{1-g_v^{50}}\right)^{\lambda}} \tag{5.6}$$

where g_v^{50} represents the volumetric grade of a particle that have equal probability of reporting either to the concentrate or to the tail streams and λ is related to the separation sharpness index *SI*, defined by $SI = \frac{g_v^{25}}{g_v^{75}}$. For the Rosin-Rammler functional form, this is:

$$SI = e^{-\frac{1.5725}{\lambda}} \tag{5.7}$$

The following set of parameters were used for the Rougher separation in MODSIM, using the model for a wet magnetic drum separator described above:

- Sharpness Index, *SI* = 0.8926
- Separation volumetric grade, g_v^{50} = 0.090
- By-pass fraction, κ = 0.466
- Exponential factor to reduce by-pass as particle size increases, ς = 56.00 m^{-1}

Finally, the water split factor to the tails stream was set to 0.784, completing the modeling of the Rougher separation unit.

Hydrocyclone Classification Model

The Hydrocyclone is the most common classification operation used in industrial grinding circuits. Consequently, the classification action in hydrocyclones has been the subject of a large number of studies. The most sophisticated hydrocyclone models are based on solutions to the Navier-Stokes transport equations, in two dimensions, [41] and most recently, a considerable effort has been made by Cortes [42], towards the three dimensional solution. However, these models are rather complex, and at this time, their

implementation in a MODSIM like simulator is not yet feasible. The alternatives are first, the use of models based on correlation studies, as for example Lynch's model [43] and Plitt's model [44], and second, the use of empirical classification models. The correlation models are implemented with advantage, since these models allow some flexibility at simulating the effect of changes in operational conditions of the hydrocyclone, and its geometry. The sampling campaign at the Fairlane Plant produced enough data, with respect to geometry and operational conditions, for the implementation of a correlation based model, and this should be pursued once this study takes on the plant's performance optimization character. At this initial stage, when the liberation characteristics of the Taconite ore and the liberation model are under evaluation, it is more appropriate to select a simpler, fewer parameters empirical classification model.

Empirical classification models have been used in this work for modeling of an elutriation operation, in Chapter 4, and in the previously described modeling of the wet magnetic drum separator. Here, this modeling technique is once again employed to describe the hydrocyclone operation at the Fairlane Plant. For a general description of empirical models for classification operations the interested reader is referred to King [45]. The classification action in the hydrocyclone can be described by:

$$c(d_p, g_v) = \alpha + (1-\alpha)\, e(d_p, g_v) \tag{5.8}$$

where $e(d_p, g_v)$ is called the corrected classification function and $c(d_p, g_v)$ is called the actual classification function. The parameter α represents the fraction of particles that by-passes to the underflow stream, and here this is constant with respect to both particle size and composition. The corrected classification function was modeled with the logistic

functional form:

$$e(d_p, g_v) = \frac{1}{1 + \left(\frac{d_p}{d_p^{50}(g_v)} \right)^{-\lambda}} \tag{5.9}$$

where the exponential parameter λ is related to the separation sharpness index *SI* by:

$$SI = e^{-\frac{2.1972}{\lambda}} \tag{5.10}$$

and $d_p^{50}(g_v)$ represents the separation size for a particle that has composition g_v. The change in separation size with particle composition was modeled by:

$$d_p^{50}(g_v) = d_{50} \left(\frac{\rho_A}{\rho(g_v)} \right)^{\delta} \tag{5.11}$$

In equation 5.11, the strong concentration action in the hydrocyclone operation due to differential particle density is taken into account, and the value of the parameter *m* is related to the flow regime in the device, with the lower limit of 0.5 corresponding to laminar flow conditions, and higher values for turbulent flow [45].

Equations 5.8 through 5.11 represent a typical empirical model that can be used to describe the classification action, with respect to size and composition, in mineral processing devices, when liberation information is available.

The following set of parameters were used for the hydrocyclone classification in MODSIM, using the empirical model described above:

- Sharpness Index, SI = 0.6058
- Separation size, d_{50} = 123.0 microns
- Exponential parameter in separation size function, δ = 0.8
- By-pass fraction, α = 0.0865

Finally, the water split to the underflow stream was assumed to be equal to the by-pass fraction α, completing the preliminary hydrocyclone modeling.

MODSIM Simulation Results

The objective of the simulation is primarily to reproduce, to the greatest accuracy, the measured size and grade distributions in the plant. There are six streams in the circuit for which measured and simulated results are available, namely the Ball Mill Discharge, the Rougher Concentrate and the Rougher Tails streams, around the Rougher magnetic separator node, and the Cyclone Feed, Underflow and Overflow streams, around the Hydrocyclone node. The simulated size distributions in the streams above are compared to the adjusted size distributions (Table 5.3), which represent measured data, in Figure 5.15. There is excellent agreement between simulated and measured size distributions in every stream, with the exception of the Rougher Tails stream, which could not be fully reproduced by simulation. The measured size distribution in the Rougher Tails stream is considerably finer than the corresponding simulated size distribution. It is possible that the smallest particles were favored during sampling, either due to the awkward sampling point, located under the magnetic separators at a difficult point to reach from the plant's floor, or due to the relatively high water flow rate in the stream and its low solids content (Tables 5.17 and 5.1). Actually, the Rougher Tails stream contains the least solids and

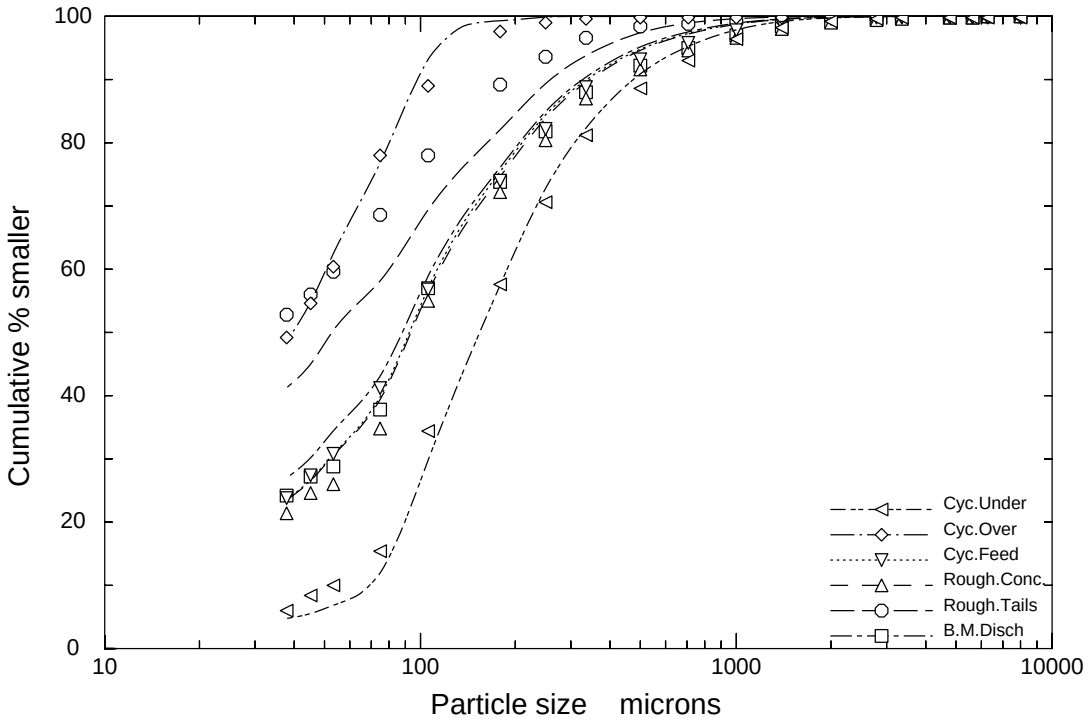

Figure 5.15 Comparison between measured and simulated size distributions in the Fairlane Plant secondary grinding circuit. Points show measured distributions and lines show calculated distributions

the highest water flow rate in the circuit, which makes it the most difficult stream to sample accurately. However, it is very important to point out that if the stream had not been analyzed for its grade distribution, it would be possible to match the measured size distribution by simulation almost perfectly. This is because the grade distributions impose a tight constraint to the parameterization of the unit operations, and consequently the simulation becomes considerably more realistic, and any sampling error more apparent.

The measured and simulated composite grade distributions around the Rougher magnetic separator and the Hydrocyclone are shown in Figure 5.16, and the simulation results show very good agreement with the measured data. The plots in Figure 5.16 represent the result of the entire effort put forward in order to measure and characterize the liberation properties of the Taconite ore. The immediate conclusion is that it is possible to simulate this grinding circuit fairly accurately, with respect to both liberation and comminution properties, using the procedures described in this work. Moreover, it is now possible to use the simulator to investigate the configuration of the plant with respect to its performance.

Finally, the simulated material balance data is shown in Table 5.19. The simulated grades in each stream can be compared directly to the measured grades shown in Table 5.17, and again very good correlation is observed. Stream flowrates and recoveries are comparable to the nominal flowrates and recoveries, again indicating the simulation was successful.

The data on Table 5.19 and Figures 5.15 and 5.16 is sufficient to validate the implementation of the simulator for the secondary grinding circuit of the Fairlane Plant

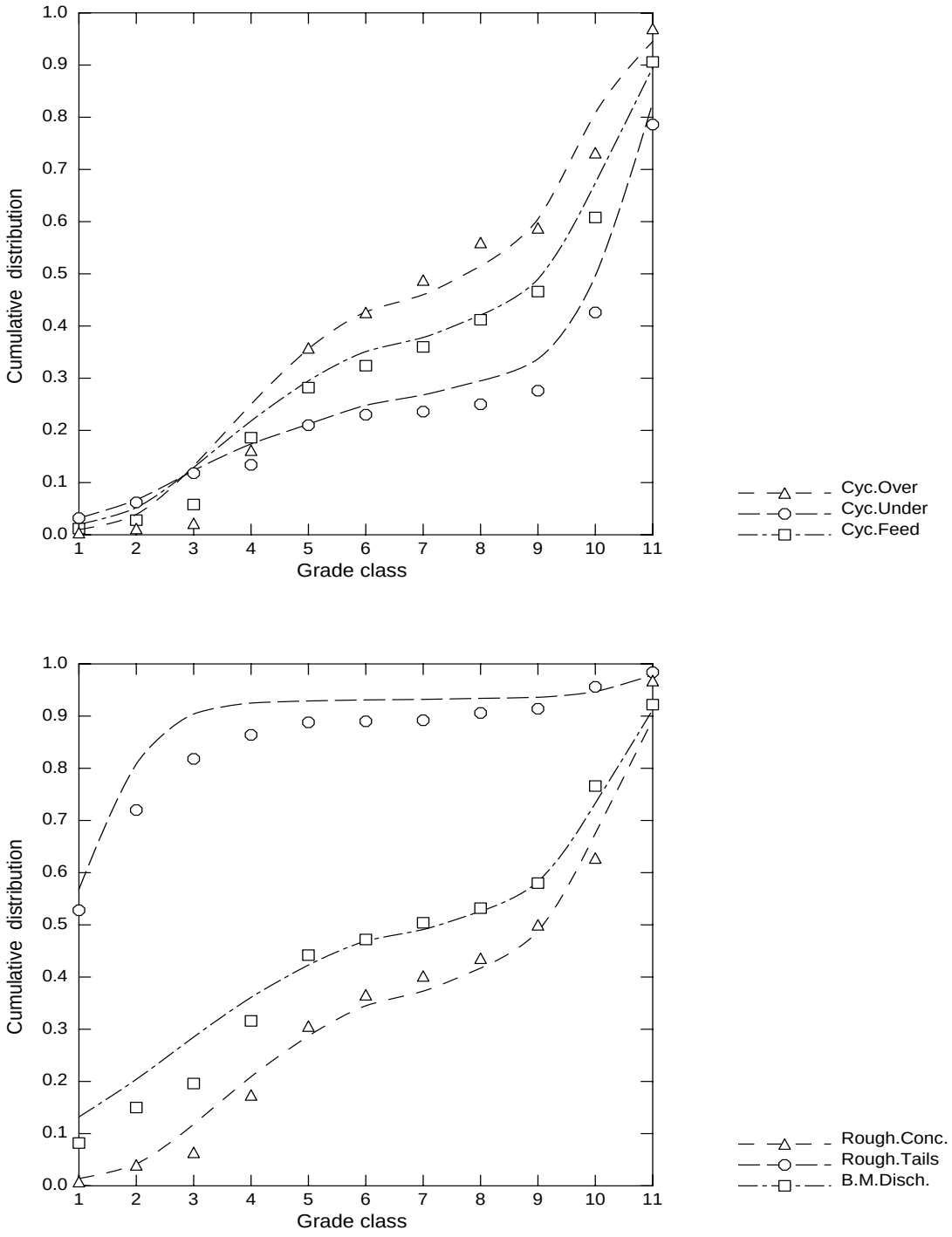

Figure 5.16 Comparison between measured and simulated composite grade distributions in several streams of the Fairlane Plant grinding circuit. Points show measured distributions and lines show calculated distributions

Table 5.19 The simulated flow rates and grades in the streams of the secondary grinding circuit of the Fairlane Plant. Recoveries are based on the total flow rates from the four feed streams

Stream	Solid Flow, Tons/hour	Water Flow, m^3/hour	solids, %	Recovery of solids, %	Recovery of Chert, %	Grade of Chert, %	Recovery of Magnetite, %	Grade of Magnetite, %
Cob.Conc.	301.26	137.88	68.60	79.11	83.09	43.36	76.32	56.64
Cyc.Feed	554.04	425.16	56.58	145.50	93.24	26.76	183.04	73.24
Cyc.Under	316.66	36.83	89.58	83.16	62.08	31.19	98.09	68.67
Cyc.Over	237.89	388.44	37.98	62.47	31.16	20.84	84.94	79.16
D.D.Conc.	57.49	30.35	65.45	15.10	10.51	29.07	18.39	70.92
D.D.Tails	4.82	59.36	7.51	1.27	2.64	87.15	0.28	12.86
B.M.Disch.	675.36	205.06	76.71	177.36	166.12	39.13	185.44	60.87
Rough.Conc.	532.08	340.42	60.98	139.73	87.20	26.07	177.43	73.92
Rough.Tails	143.32	1235.52	10.39	37.64	78.93	87.62	8.01	12.39
Scav.Conc.	17.23	23.50	42.30	4.52	3.40	31.41	5.33	68.59

and the characterization of the liberation and comminution properties of the Taconite ore.

Discussion

The novel procedures for liberation characterization and measurement described in this work reveal a not previously observed perspective of the interactions between the basic particle properties, namely size and composition, and the physical action of mineral processing devices. The work reported here is in fact the first successful study carried out in an industrial mineral processing plant that includes the detailed liberation characteristics of the ore.

The Taconite particles are particularly interesting to examine from this new, more detailed perspective. In Figure 5.17, the measured size/liberation spectrum of the Cobber Concentrate particles is shown. Approximately 47% of the particles are larger than 1000 microns, and their grade distribution was assumed to be constant and equal to the grade distribution measured in the -1000+710 micron particles. This is not a bad assumption because the larger particles tend to be in a very narrow grade range. The particles in the Cobber Concentrate stream represent the main feed stream to the grinding circuit. It is clear from the figure that the bulk of the particles, mainly in the coarser sizes, are unliberated. Below 106 microns, most particles are in the higher grade classes, but not many liberated particles of either phase are present. The transition between this quasi liberation state and no liberation occurs between 106 and 710 microns, with the spreading of the grade spectrum. The presence of very few liberated or quasi liberated chert particles is due to the action of the Cobber magnetic separator, a high intensity wet magnetic drum separator. The few liberated chert particles must result from by-pass

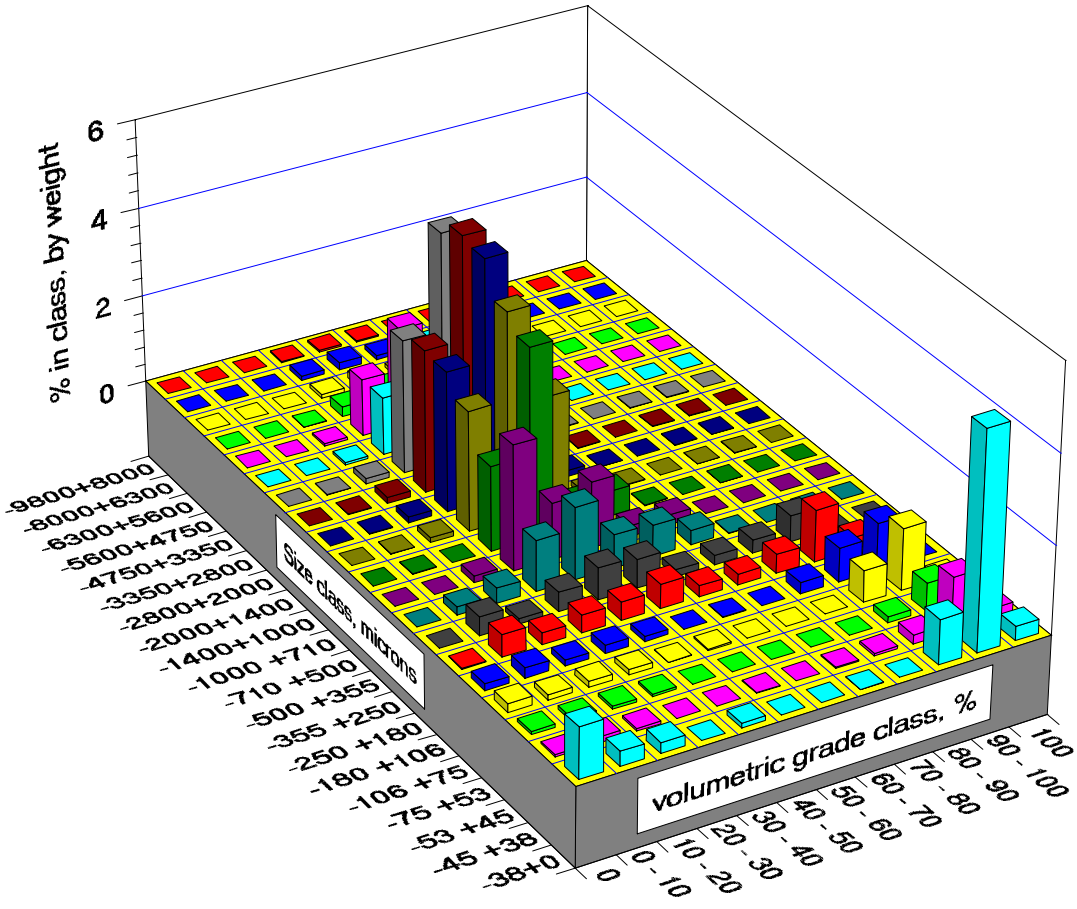

Figure 5.17 The particle size/grade spectrum in the Cobber Concentrate stream

phenomena in the Cobber separator. In the figure, the basic liberation characteristics of the Taconite ore can be observed, like the fast transition from unliberated to quasiliberated, and also the slow transition from quasiliberated to liberated in the magnetite end, giving rise to the liberation model modifications in Equations 5.1 and 5.2.

The measured and simulated size/grade spectrum in the Ball Mill Discharge is shown in Figure 5.18. In this stream the particles are comparatively finer, with approximately 97% of the particles smaller then 1000 microns, due to the comminution in the ball mill. The calculated spectrum is considerably smoother than the measured spectrum, and the main reason for this is the smooth nature of the liberation model, which is continuous in both size and grade domains, and consequently dampens the noise from stereological correction that is imputed through the measured spectrum of the feed streams. In the ball mill, a significant fraction of liberated particles of both phases is generated, and the bulk of these particles are found below 75 microns. This small "liberation size" characterizes the difficulty of processing the Taconite ore. In the ball mill discharge, the bulk of the particles are unliberated, and these must be recirculated to regrind. The ball mill discharge constitutes the feed stream to the Rougher separation, and the objective of this separation stage is to discard the lower grade and liberated Chert particles. The measured and simulated size/grade spectrum in the Rougher Tails stream is shown in Figure 5.19, and from this perspective it is clear that the Rougher is indeed discharging the lower grade and the liberated Chert particles in the tails stream. The concentrate stream must contain the remaining particles, and this is clearly shown in Figure 5.20. Very few high grade particles remain in the Rougher tails stream and very

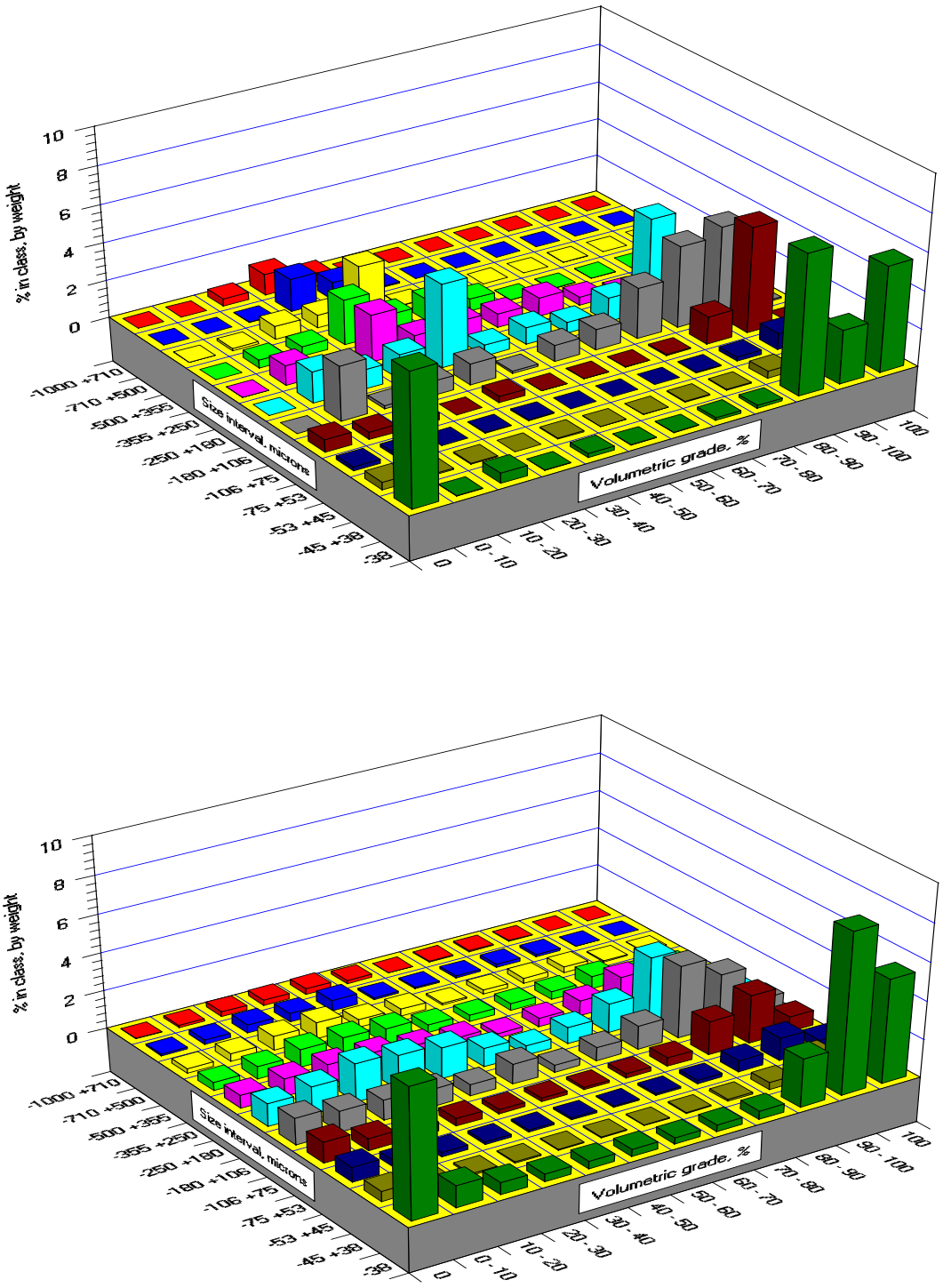

Figure 5.18 The measured (top) and simulated (bottom) particle size/grade spectrum in the Ball Mill Discharge

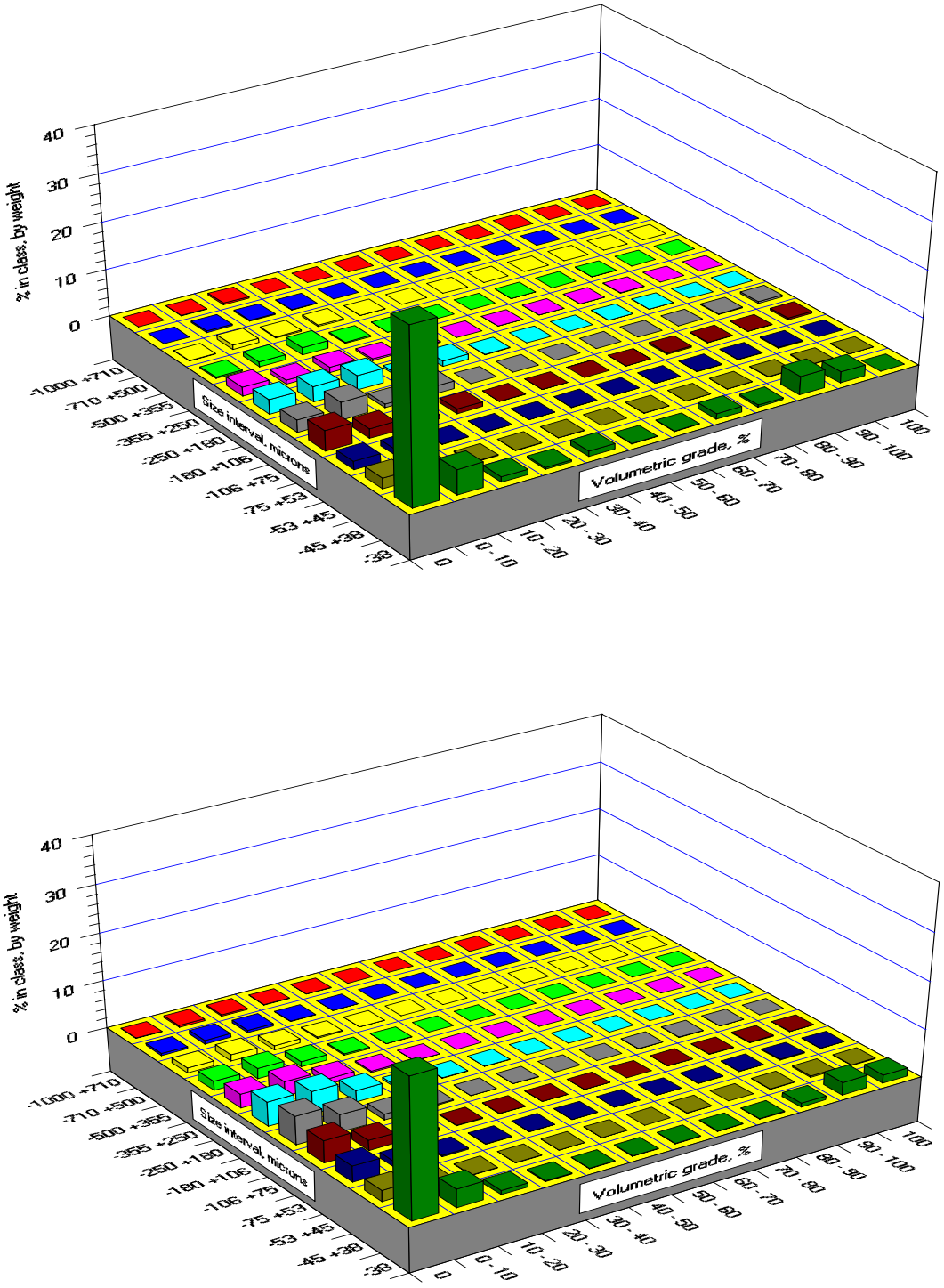

Figure 5.19 The measured (top) and simulated (bottom) particle size/grade spectrum in the Rougher Tails

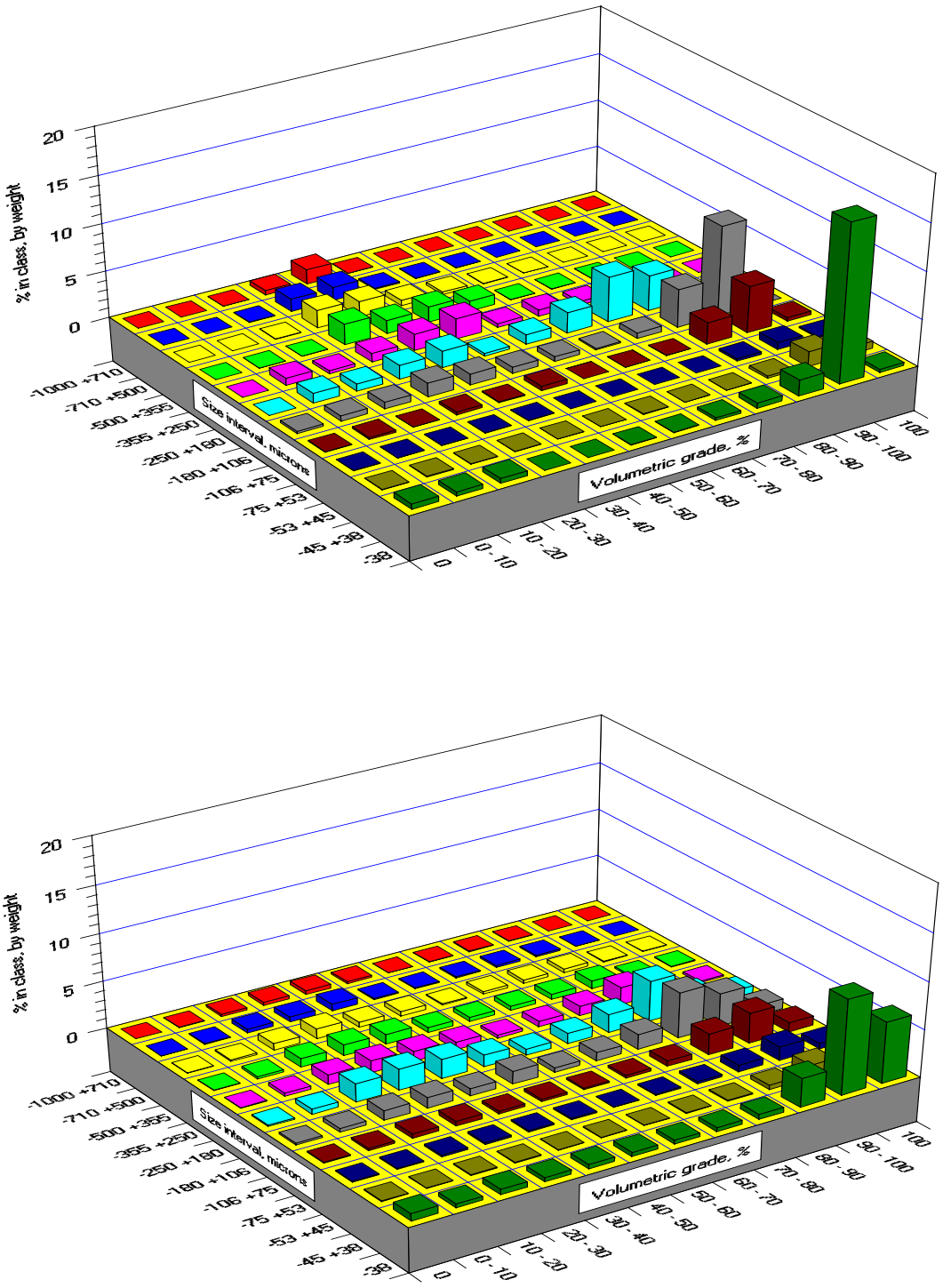

Figure 5.20 The measured (top) and simulated (bottom) particle size/grade spectrum in the Rougher Concentrate

few low grade particles remain in the concentrate stream, and this is mostly due to the high by-pass fraction in the separation. The bulk of the unliberated particles follow the concentrate stream, and this is beneficial, since the unliberated particles must undergo regrind before they leave the circuit. The sharp separation at low grade is characteristic of wet magnetic drum separators, which tend to direct particles that contain even a small fraction of a strong magnetic phase, in this case Magnetite, to the concentrate stream, and thus the low separation grade used in the model. Again, for both concentrate and tails streams, the measured and simulated spectra are in very good concordance. The Scavenger Concentrate and the Dewatering Drum Tails particles, shown in Figure 5.21, are added to the Rougher Concentrate to form the Cyclone Feed stream. The particles from these two subsidiary feed streams represent less then 5% of the Cyclone Feed. The Scavenger Concentrate particle distribution resembles that of the Rougher Concentrate particles, and this indicates that a fraction of the by-passed Magnetite containing particles in the Rougher separation are successfully returned to the grinding circuit. The Dewatering Drum Tails particles are mostly oversize particles from the double-deck vibrating screens, and some fine, screen by-pass particles. The bulk of the stream is of low grade, and liberated Chert particles. Perhaps, a better configuration for the circuit would be to restream these particles to the Rougher feed stream, so that they are discharged before they return to the Ball Mill.

Over 95% of the Cyclone Feed particles are Rougher Concentrate particles. The measured and simulated particle size/grade spectra in the Cyclone Feed stream are shown in Figure 5.22, and these must be comparable to the spectra in Figure 5.20. The Cyclone

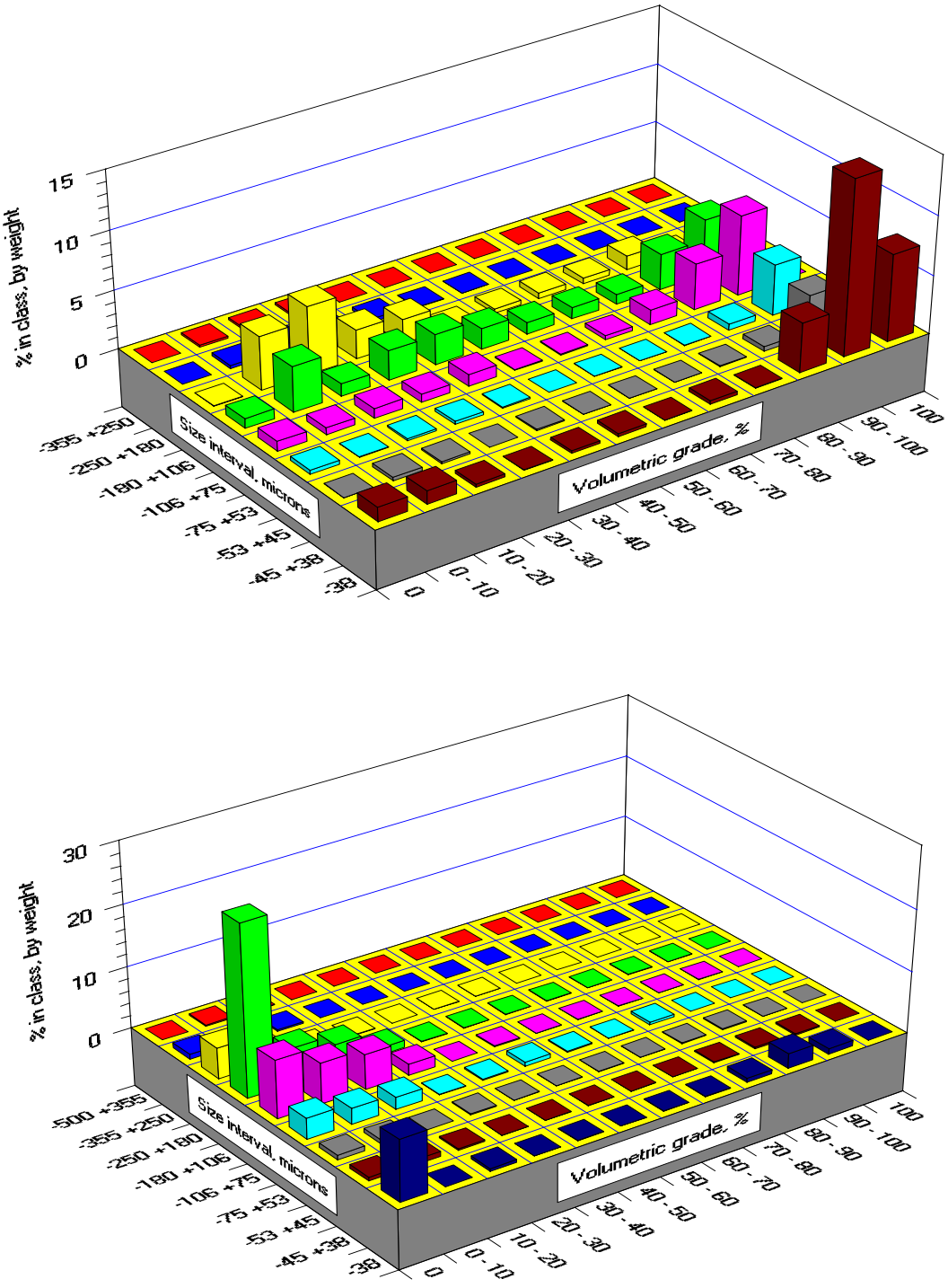

Figure 5.21 The measured particle size/grade spectrum in the Scavenger Concentrate (top) and Dewatering Drum Tails (bottom) streams

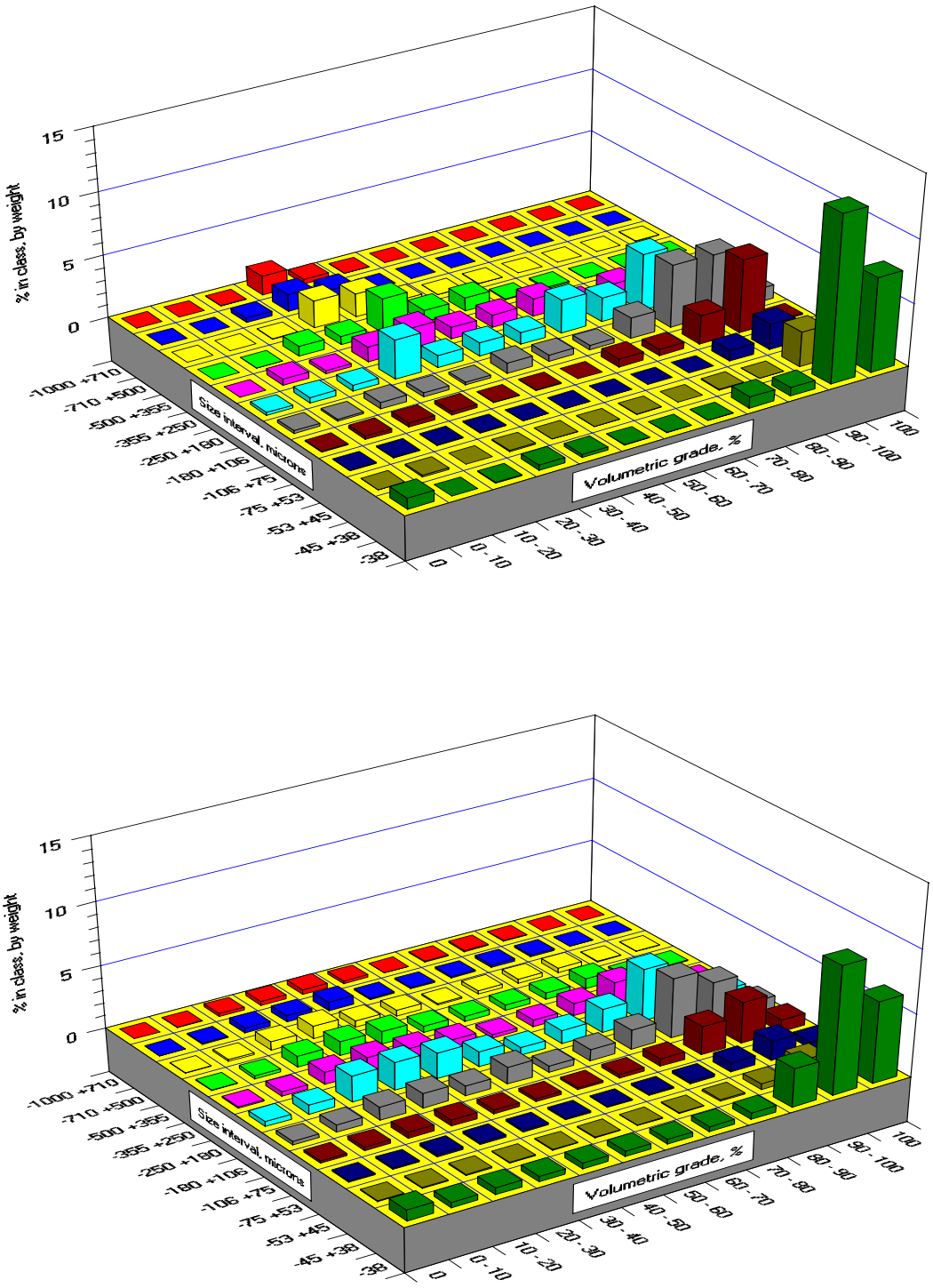

Figure 5.22 The measured (top) and simulated (bottom) particle size/grade spectrum in the Cyclone Feed stream

Feed is a particularly difficult stream to sample, and good, representative samples can only be obtained from the cyclone cluster feed head, with the sampling probe introduced down to a well mixed region of the incoming slurry flow. Comparison between the measured spectra in Figures 5.20 and 5.22 indicates that a good sample was obtained in the Cyclone Feed stream, and this data was used to calibrate the Hydrocyclone model. Again, there is very good agreement between the measured and simulated spectra corresponding to the Cyclone Feed stream.

The calculated and measured size/grade spectra in the Hydrocyclone Overflow stream is shown in Figure 5.23. These particles are the finished product of the secondary grinding circuit. The bulk of the particles is smaller than 106 microns, attending the specification for pellet making. Most particles are high grade and liberated Magnetite particles. Some contamination from larger, lower grade particles is observed, and this is probably due to short circuiting to the overflow in the Hydrocyclone. There is, once again, very good agreement between measured and simulated spectra. In contrast, the coarser, unliberated particles must be observed in the Hydrocyclone Underflow stream. This is shown in Figure 5.24, and the measured and calculated spectra confirm this premise. This is good, because unliberated particles must be redirected to regrind, and the underflow stream is, in fact, one of the main contributions to the ball mill feed stream. However, Figure 5.24 also shows clearly the expected concentration effect due to the differential density between Chert and Magnetite, and a large fraction of intermediate size, high grade and liberated Magnetite particles are also found in the Underflow. This is not desired, since it is costly and uneconomic to regrinding particles

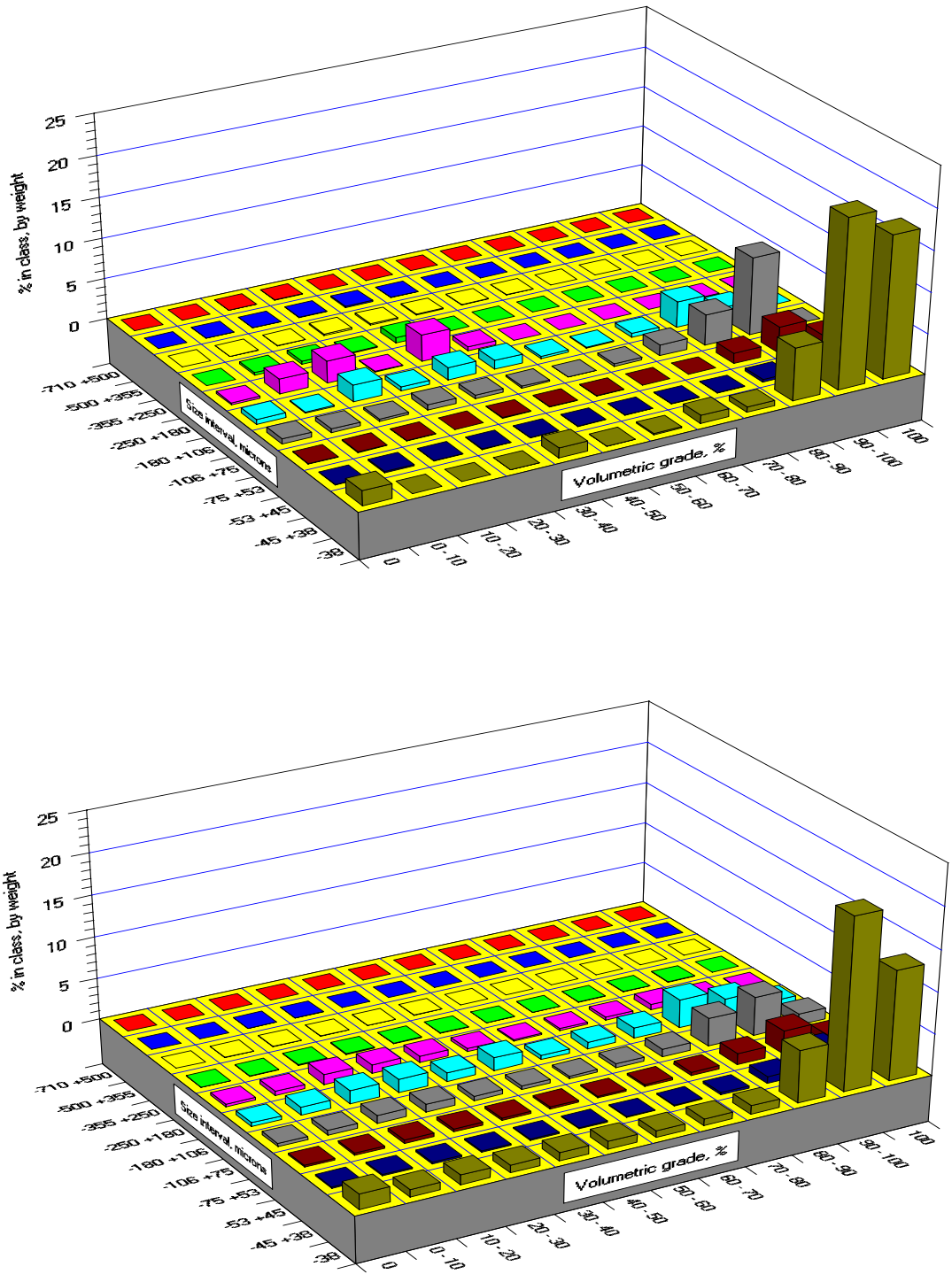

Figure 5.23 The measured (top) and simulated (bottom) particle size/grade spectrum in the Cyclone Overflow stream

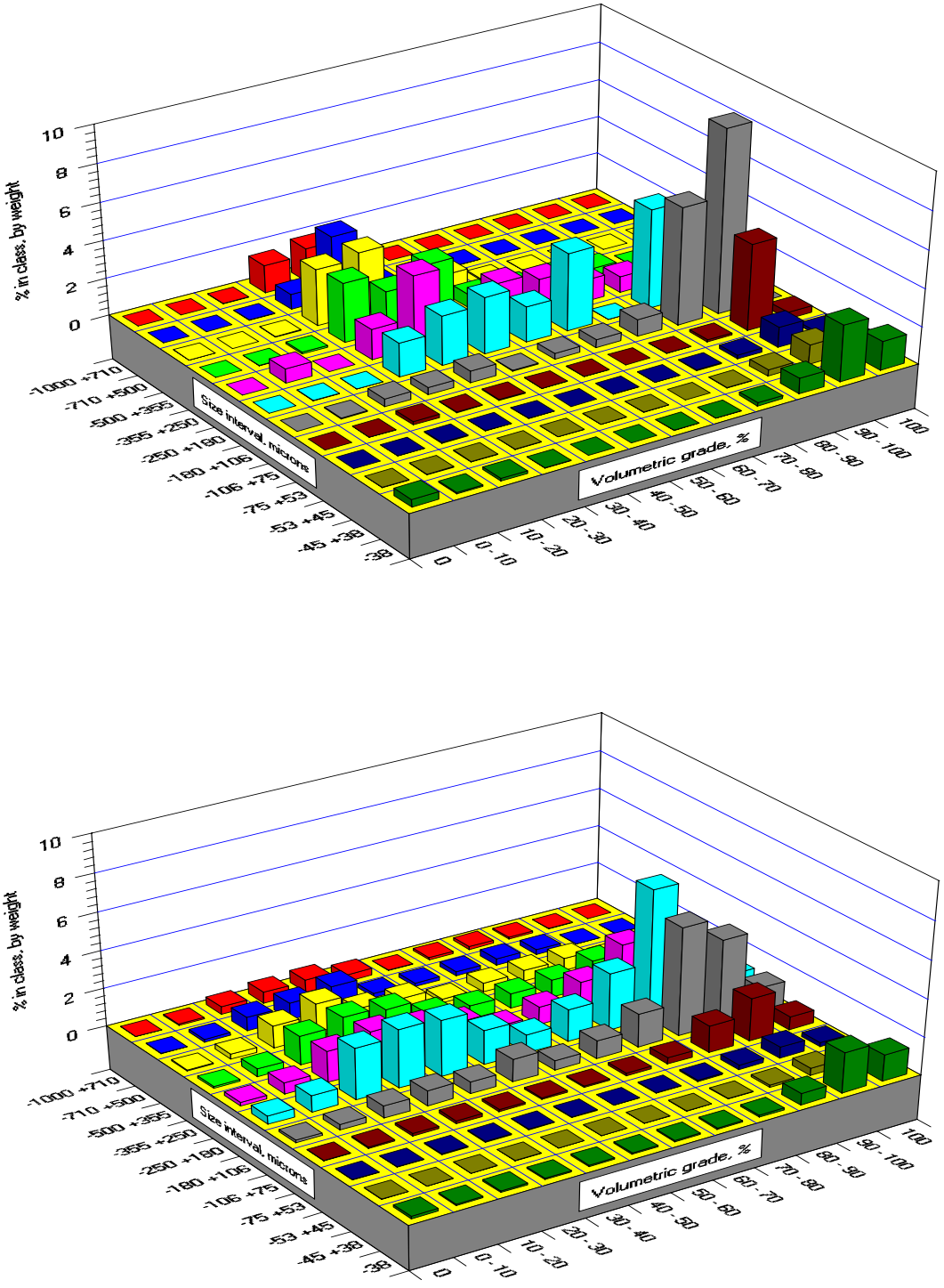

Figure 5.24 The measured (top) and simulated (bottom) particle size/grade spectrum in the Cyclone Underflow stream

that are already at product specification. This is probably the most important finding of this study, from the point of view of troubleshooting and plant optimization. Further work must be directed at minimizing the regrind of these particles, with great potential for economic improvement.

Finally, to complete the sweep through the streams involved in this grinding circuit with the new perspective that only this kind of detailed liberation analysis can provide, the measured size/grade spectrum in the Dewatering Drum Concentrate stream is shown in Figure 5.25. These particles complete, together with Cyclone Underflow and Cobber Concentrate, the feed stream to the Ball Mill. This is the final subsidiary feed stream, and the particles here represent less than 9% of the feed to the Ball Mill. However, once again, fine, high grade and liberated Magnetite is redirected to regrind through this stream. This may be subject to appreciation for plant reconfiguration.

The work reported here was, with no doubt, extremely successful, from any point of view, starting with the planing of the sampling campaign, and ending with the discussion above. Every procedure worked satisfactorily, including stereological correction with the symmetric transformation kernel, the liberation model and its implementation in MODSIM. The simulation of the unitary operations and of the entire secondary grinding circuit have been validated, and they were good.

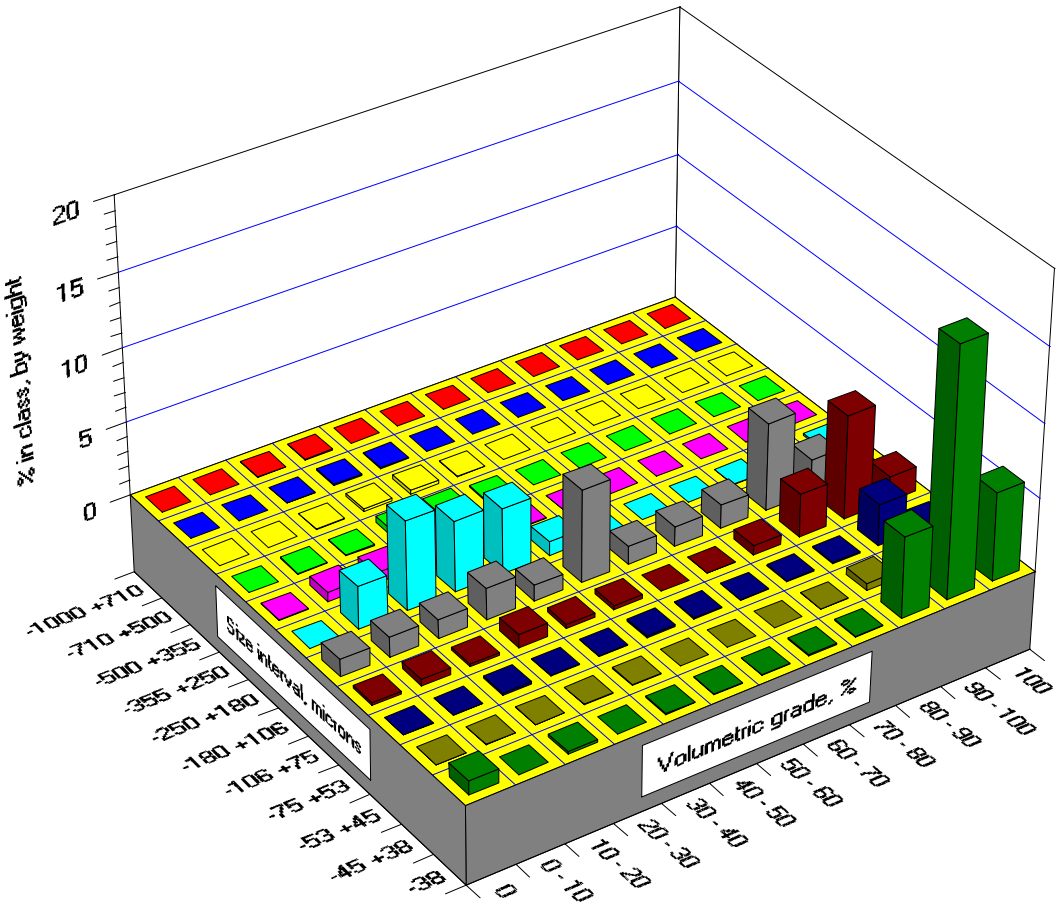

Figure 5.25 The measured particle size/grade spectrum in the Dewatering Drum Concentrate stream

CHAPTER 6

CONCLUSIONS

At the time this particular liberation study started at the University of Utah, in 1990, the work was essentially directed to the implementation of a procedure to solve the integral equation that relates the linear and volumetric grade distributions. The procedure had to be very robust and consistent, and the solution had to be constrained so that it could be used in real mineral processing calculations. Realistically, at that time, it was not possible to measure liberation in typical mineralogical systems. Consequently, no real progress was being achieved, not only at the University of Utah but in a worldwide sense, in this most important area of mineral processing regarded as the liberation problem, because the subject of any liberation study, the liberation spectrum, could not be measured.

The first transformation kernel for stereological calculation of volumetric grade distribution was measured in PARGEN particles. PARGEN is in fact a texture model, with a number of advantages over the numerous texture models in the literature. Linear and areal distributions can be quickly and easily measured in PARGEN particles that are exactly monosize and monograde. This provides a very good perspective of the properties of texture and its dependency on shape. PARGEN quickly became the standard in mineralogical texture studies, and PARGEN results are invariably compared to the results from calculations using any other proposed approach. Also invariably, authors of

alternative texture models consider their results better than PARGEN and consequently PARGEN has become the target of unjustified criticism, mainly because it is used as a standard, and also because it is not fully understood, despite of the simplistic idea behind it.

PARGEN provided with enough insight so that the procedure for calculating the volumetric grade distribution from lower one- and two-dimensional grade distributions became understood. An appropriate solution, based on an optimization procedure, as described in Chapter 2 of this dissertation, was initially developed using the PARGEN transformation kernel. However, the solution still needed confirmation. This was achieved by successful fractionation of real mineralogical particles, and the development of a procedure that allows for the measurement of the transformation kernel in narrow size, narrow grade particles. A natural consequence of this work was the determination of the transformation kernel for the Dolomite-Sphalerite test ore. It is important to make very clear that this is not a texture model. It has been measured from the composite particles. The symmetric transformation kernel, on the other hand, can be regarded as a texture model, and it is believed that it can be used for ores that present a nearly symmetric texture, with good accuracy. With the Dolomite-Sphalerite transformation kernel, the inversion procedure was tested successfully against the experimental results. More importantly, the procedure can be repeated for any ore that can be fractionated, and the exact transformation kernel for other textures can be determined with reparameterization of the incomplete beta function first and second moments and of the apparent linear liberation function. Future work in this area should now be aimed at the

determination of the transformation function for ternary and higher mineralogical systems, and the appropriate solution of the stereological correction problem in these systems. Ironically, because fractionation of ternary and higher systems is extremely difficult, the only feasible approach is to generated multiphase PARGEN particles in order to establish the relationship between the different phases in one, two and three dimensions.

The success of the work described in Chapter 2 also depended on good, precise image analysis. The optical KONTRON system that was operating at the University of Utah in 1990, despite of its remarkable usefulness, could not generate the high contrast images required. To this end, a *SEM* equipped with backscattered electron detector was purchased for the image analysis laboratory, and interfaced with a SUN *SPARC 1* workstation. However, the software available at the time, and to date, was not adequate for the kind of high quality image processing that is required specifically for mineralogical systems. This prompted the development of an image analysis software (*MMIA* - Mineral and Metallurgical Image Analysis) that is specific for use with mineralogical systems. The development of such software was only possible because of the expertise that Professor R.P. King brought into this research. The software is well designed, and includes, besides the interface with the microscope, file system interface, image filters, image editing procedures, binary and ternary thresholding, binary operations, measurement procedures, automatic processing facilities, colormap manipulation, memory operations with capability of handling up to 2048 x 2048 x 8 images, and others.

The measured transformation kernel for the test ore and the inversion procedure opened the way to investigate, for the first time, the breakage of real binary particles.

This was carried out in Chapter 3. The work of Andrews and Mika, in 1975, had shown that progeny from monosize, monograde particles could only have a combination of size and grade inside what is now called the accessible region of the Andrews-Mika diagram. However, nothing was done until 1990 in order to describe the internal structure of the accessible region, because the experimental was too difficult and liberation spectra could not be measured. The first description of this internal structure is due to the breakage of PARGEN particles, again contributing as a very useful texture model, which resulted in King's stylized model of the internal structure of the Andrews-Mika diagram, now called Ljubljana model, because on the location of the reading of that paper. More important than the model itself, was King's solution to the *PBM* equation, which is based on a knowledge of the internal structure of the accessible region. The successful experimental in Chapter 3 is alone a great achievement, and the discrete internal structure of the Andrews-Mika diagram was revealed for the Dolomite-Sphalerite ore. The modeling work was complex, but the incomplete beta function model was implemented successfully and much was learned in this process.

In Chapter 4 the new incomplete beta function model and King's solution to the *PBM* equation were tested. The test ore for the experimental validation had to be the Dolomite-Sphalerite, and steady experimental conditions were required. Unfortunately, it was impossible to run a closed continuous grinding experiment. The emulated closed continuous grinding experiment was painstaking, mainly due to the large number of samples generated. Nevertheless, the experiment was worthwhile, and produced a broader view of the liberation prediction problem. The main conclusion was that the geometrical

texture parameter cannot be measured in one arbitrary size class. A more detailed understanding of this textural parameter is required, and further studies must be carried out in this direction. Another important conclusion was that, when present in significant amounts, particles smaller than 38 microns require special care, and specimen preparation procedures together with further sieving into smaller sizes is required.

The form of the new model, based on the incomplete beta function, and King's solution to the *PBM* equation were verified by the emulated closed continuous grinding experiment, satisfying the main objective of the work in Chapter 4. Also, much was learned about transport in overflow ball mills, classification effects with respect to size and composition and the comminution models. Further work must be carried out to model the concentration effect with respect to composition observed in both grinding stages.

Finally, the case study in Chapter 5 could not have turned out any better. The Taconite ore is very favorable for liberation studies, with respect to composition and texture, to which the symmetric transformation kernel responded very well. The sampling campaign was successful and the results in general are excellent. The simulation opens up the possibility for significant improvement in the existing flowsheet with respect to magnetite recovery and grinding efficiency. Future work will be aimed at modifying the plant in the light of the findings reported in this dissertation. In view of the importance of liberation effects in the efficient concentration of iron ore, it is recommended that future effort be directed towards the measurement of specific transformation kernels for these ore types.

The contributions reported in this dissertation can finally be summarized as follows. A reliable procedure was developed for stereologically correcting liberation data obtained by image analysis. This was an essential requirement to the main task because it would have been impossible to measure, by classical dense-liquid or magnetic fluid fractionation methods, the liberation of minerals in the many samples that were necessary. The amount of effort would have been totally prohibitive. Careful fractionation of particles that were in a single narrow size range, using the magnetic fluid technique led to the measurement of the full structure of the accessible region in the Andrews-Mika diagram and to the development of a useful model. The Andrews-Mika diagram is a critical requirement for solving the main problem of calculating the liberation spectra in continuous milling circuits. Finally, the calculation procedure was confirmed by experimental liberation data that was generated in the laboratory and by data obtained from an industrial plant in which liberation is critical to its economic performance.

The contribution of this liberation study to the understanding of the liberation problem, including measurement and prediction, is significant, when considering the *state of the art* when this study started. It could have a significant impact in mineral processing technology in the future.

APPENDIX A

MEASURED LINEAR GRADE DISTRIBUTIONS IN THE DOLOMITE-SPHALERITE EMULATED CLOSED, CONTINUOUS GRINDING EXPERIMENT

Table A.1 The measured, conditional on size, linear grade distributions by length, in the Feed particles from grinding Stage I

Particle size range, microns												
linear grade, %	-1000 +710	-710 +500	-500 +355	-355 +250	-250 +180	-180 +150	-150 +106	-106 +75	-75 +53	-53 +45	-45 +38	-38
0	85.16	80.98	83.21	81.27	83.81	84.18	84.91	81.42	83.38	84.67	86.78	92.93
0-10	2.00	1.45	1.43	1.24	0.92	0.82	0.69	0.38	0.77	0.38	0.38	0.21
10-20	1.35	0.75	1.00	0.74	0.47	0.53	0.38	0.39	0.25	0.16	0.17	0.39
20-30	0.87	0.64	0.49	0.45	0.27	0.36	0.24	0.29	0.30	0.19	0.20	0.26
30-40	0.58	0.39	0.44	0.47	0.43	0.33	0.25	0.47	0.20	0.13	0.13	0.06
40-50	0.38	0.59	0.31	0.43	0.27	0.23	0.21	0.40	0.12	0.14	0.07	0.08
50-60	0.51	0.27	0.50	0.30	0.39	0.32	0.51	0.29	0.09	0.08	0.12	0.11
60-70	0.37	0.29	0.46	0.47	0.16	0.40	0.33	0.19	0.15	0.24	0.09	0.12
70-80	0.24	0.19	0.30	0.29	0.19	0.29	0.33	0.20	0.13	0.21	0.08	0.12
80-90	0.20	0.42	0.37	0.36	0.28	0.34	0.30	0.23	0.16	0.18	0.23	0.28
90-100	0.31	0.49	0.51	0.50	0.42	0.51	0.36	0.45	0.48	0.62	0.53	0.34
100	8.03	13.54	10.98	13.48	12.39	11.69	11.49	15.29	13.97	13.00	11.22	5.10

Table A.2 The measured, conditional on size, linear grade distributions by length, in the Holdup particles from grinding Stage I

Particle size range, microns												
linear grade, %	-1000 +710	-710 +500	-500 +355	-355 +250	-250 +180	-180 +150	-150 +106	-106 +75	-75 +53	-53 +45	-45 +38	-38
0	74.92	80.77	83.28	82.46	81.84	82.30	81.39	81.20	83.01	81.63	83.79	87.08
0-10	1.57	1.85	1.02	0.92	1.10	0.66	0.54	0.64	0.43	0.32	0.18	0.42
10-20	1.22	0.99	0.73	0.53	0.58	0.35	0.33	0.33	0.27	0.14	0.16	0.19
20-30	0.67	0.64	0.69	0.45	0.45	0.23	0.25	0.17	0.20	0.14	0.16	0.14
30-40	0.58	0.55	0.54	0.26	0.32	0.25	0.30	0.16	0.11	0.16	0.10	0.06
40-50	0.43	0.60	0.47	0.28	0.31	0.19	0.25	0.22	0.19	0.09	0.10	0.13
50-60	0.34	0.54	0.47	0.30	0.33	0.19	0.23	0.29	0.13	0.15	0.16	0.15
60-70	0.47	0.52	0.34	0.33	0.31	0.25	0.23	0.19	0.15	0.16	0.26	0.22
70-80	0.46	0.42	0.22	0.27	0.16	0.18	0.26	0.21	0.17	0.20	0.20	0.23
80-90	0.60	0.44	0.26	0.31	0.24	0.17	0.26	0.19	0.21	0.32	0.23	0.48
90-100	0.61	0.49	0.45	0.48	0.49	0.38	0.63	0.41	0.44	0.73	0.72	0.72
100	18.13	12.19	11.53	13.41	13.87	14.85	15.33	15.99	14.69	15.96	13.94	10.18

Table A.3 The measured, conditional on size, linear grade distributions by length, in the Product particles from grinding Stage I and Feed particles from elutriation Stage II

Particle size range, microns												
linear grade, %	-1000 +710	-710 +500	-500 +355	-355 +250	-250 +180	-180 +150	-150 +106	-106 +75	-75 +53	-53 +45	-45 +38	-38
0	96.91	92.90	91.23	89.23	84.17	83.33	83.33	85.41	82.65	84.53	83.27	86.73
0-10	0.67	1.24	1.21	1.03	0.82	0.67	0.63	0.34	0.42	0.28	0.21	0.17
10-20	0.36	0.68	0.64	0.59	0.49	0.48	0.32	0.28	0.11	0.25	0.11	0.12
20-30	0.39	0.38	0.56	0.45	0.34	0.37	0.33	0.16	0.19	0.20	0.06	0.07
30-40	0.15	0.39	0.20	0.34	0.39	0.37	0.24	0.19	0.18	0.13	0.20	0.16
40-50	0.18	0.21	0.22	0.28	0.26	0.25	0.17	0.14	0.25	0.12	0.08	0.18
50-60	0.11	0.19	0.37	0.21	0.32	0.28	0.34	0.12	0.18	0.12	0.12	0.20
60-70	0.01	0.31	0.27	0.21	0.17	0.14	0.14	0.11	0.16	0.15	0.13	0.32
70-80	0.12	0.18	0.21	0.17	0.19	0.16	0.14	0.13	0.17	0.18	0.13	0.18
80-90	0.05	0.11	0.21	0.17	0.23	0.20	0.21	0.23	0.22	0.21	0.20	0.41
90-100	0.08	0.11	0.21	0.34	0.35	0.41	0.42	0.40	0.51	0.73	0.59	0.93
100	0.97	3.30	4.67	6.98	12.27	13.34	13.73	12.49	14.96	13.10	14.90	10.53

Table A.4 The measured, conditional on size, linear grade distributions by length, in the Overflow particles from elutriation Stage II

Particle size range, microns								
linear grade, %	-250 +180	-180 +150	-150 +106	-106 +75	-75 +53	-53 +45	-45 +38	-38
0	98.10	97.79	95.35	86.48	87.38	86.15	84.26	87.38
0-10	0.48	0.37	0.61	0.45	0.34	0.31	0.27	0.30
10-20	0.55	0.27	0.22	0.40	0.21	0.18	0.19	0.13
20-30	0.17	0.14	0.20	0.24	0.16	0.15	0.17	0.10
30-40	0.12	0.08	0.17	0.18	0.08	0.15	0.09	0.10
40-50	0.09	0.09	0.10	0.12	0.12	0.19	0.07	0.15
50-60	0.02	0.10	0.12	0.21	0.09	0.11	0.10	0.14
60-70	0.04	0.03	0.13	0.10	0.17	0.17	0.18	0.16
70-80	0.02	0.03	0.06	0.18	0.15	0.10	0.15	0.25
80-90	0.01	0.07	0.13	0.24	0.11	0.24	0.18	0.44
90-100	0.00	0.01	0.08	0.33	0.37	0.42	0.51	0.89
100	0.40	1.02	2.83	11.07	10.82	11.83	13.83	9.96

Table A.5 The measured, conditional on size, linear grade distributions by length, in the Underflow particles from elutriation Stage II

Particle size range, microns												
linear grade, %	-1000 +710	-710 +500	-500 +355	-355 +250	-250 +180	-180 +150	-150 +106	-106 +75	-75 +53	-53 +45	-45 +38	-38
0	96.41	94.72	91.73	87.91	87.03	83.64	81.22	79.45	79.68	81.95	82.02	85.27
0-10	0.82	1.23	1.02	0.90	0.65	0.77	0.43	0.57	0.23	0.57	0.33	0.34
10-20	0.47	0.60	0.65	0.59	0.48	0.55	0.57	0.24	0.18	0.20	0.18	0.18
20-30	0.57	0.50	0.44	0.28	0.36	0.44	0.37	0.25	0.23	0.25	0.12	0.12
30-40	0.17	0.31	0.32	0.56	0.30	0.36	0.24	0.29	0.21	0.38	0.19	0.11
40-50	0.18	0.22	0.38	0.27	0.23	0.19	0.33	0.42	0.37	0.39	0.03	0.15
50-60	0.13	0.14	0.26	0.31	0.27	0.36	0.24	0.24	0.20	0.27	0.16	0.17
60-70	0.06	0.10	0.21	0.25	0.31	0.32	0.30	0.26	0.20	0.24	0.10	0.14
70-80	0.04	0.06	0.13	0.30	0.24	0.26	0.23	0.18	0.21	0.27	0.21	0.28
80-90	0.05	0.11	0.16	0.39	0.27	0.25	0.26	0.18	0.15	0.31	0.27	0.40
90-100	0.03	0.09	0.26	0.42	0.27	0.28	0.61	0.59	0.54	1.33	0.67	1.30
100	1.07	1.92	4.44	7.82	9.59	12.58	15.20	17.33	17.80	13.84	15.72	11.54

Table A.6 The measured, conditional on size, linear grade distributions by length, in the Holdup particles from grinding Stage III

Particle size range, microns												
linear grade, %	-1000 +710	-710 +500	-500 +355	-355 +250	-250 +180	-180 +150	-150 +106	-106 +75	-75 +53	-53 +45	-45 +38	-38
0	83.51	83.78	83.72	82.27	81.86	81.40	80.91	80.52	81.72	85.75	83.93	81.38
0-10	1.95	1.80	1.32	1.12	1.09	0.74	0.83	0.65	0.34	0.33	0.57	3.18
10-20	1.52	1.06	0.86	0.61	0.48	0.47	0.30	0.27	0.25	0.17	0.17	0.99
20-30	0.78	0.74	0.61	0.45	0.25	0.42	0.31	0.21	0.13	0.04	0.13	0.22
30-40	0.80	0.60	0.23	0.36	0.20	0.23	0.15	0.17	0.15	0.12	0.14	0.15
40-50	0.56	0.68	0.40	0.23	0.27	0.23	0.22	0.19	0.19	0.13	0.17	0.09
50-60	0.76	0.37	0.34	0.27	0.20	0.19	0.22	0.19	0.03	0.08	0.23	0.20
60-70	0.54	0.33	0.26	0.28	0.17	0.11	0.20	0.12	0.06	0.20	0.15	0.19
70-80	0.50	0.42	0.36	0.30	0.20	0.35	0.14	0.16	0.11	0.16	0.16	0.18
80-90	0.48	0.29	0.43	0.17	0.24	0.27	0.19	0.19	0.04	0.24	0.24	0.41
90-100	0.35	0.45	0.43	0.52	0.38	0.50	0.34	0.54	0.34	0.67	0.52	1.12
100	8.25	9.48	11.04	13.42	14.66	15.09	16.19	16.79	16.64	12.11	13.59	11.89

Table A.7 The measured, conditional on size, linear grade distributions by length, in the Product particles from grinding Stage III

Particle size range, microns												
linear grade, %	-1000 +710	-710 +500	-500 +355	-355 +250	-250 +180	-180 +150	-150 +106	-106 +75	-75 +53	-53 +45	-45 +38	-38
0	93.24	89.31	87.09	86.80	85.76	83.61	83.39	81.95	84.40	82.37	82.27	87.88
0-10	1.76	1.99	1.91	1.22	0.84	0.63	0.93	0.46	0.47	0.31	0.31	0.39
10-20	0.75	1.02	0.84	0.62	0.48	0.49	0.40	0.28	0.20	0.15	0.12	0.08
20-30	0.41	0.53	0.46	0.50	0.44	0.30	0.29	0.25	0.15	0.10	0.18	0.07
30-40	0.31	0.37	0.33	0.41	0.34	0.27	0.12	0.25	0.17	0.19	0.15	0.13
40-50	0.29	0.26	0.19	0.19	0.23	0.33	0.19	0.14	0.14	0.11	0.08	0.07
50-60	0.29	0.29	0.35	0.28	0.23	0.26	0.24	0.15	0.11	0.14	0.20	0.11
60-70	0.28	0.22	0.36	0.20	0.25	0.18	0.21	0.20	0.09	0.21	0.19	0.18
70-80	0.22	0.23	0.31	0.24	0.27	0.10	0.17	0.14	0.08	0.22	0.32	0.29
80-90	0.09	0.31	0.18	0.30	0.27	0.19	0.22	0.23	0.23	0.21	0.32	0.33
90-100	0.37	0.29	0.25	0.24	0.39	0.33	0.35	0.38	0.38	0.56	0.66	0.53
100	1.99	5.18	7.73	9.00	10.50	13.31	13.49	15.57	13.58	15.43	15.20	9.94

APPENDIX B

MEASURED LINEAR GRADE DISTRIBUTIONS IN THE TACONITE ORE SAMPLES FROM THE FAIRLANE PLANT SECONDARY GRINDING CIRCUIT STREAMS

Table B.1 The measured, conditional on size, linear grade distributions by length in the Ball Mill Discharge stream sample

Particle size range, microns											
linear grade, %	-1000 +710	-710 +500	-500 +355	-355 +250	-250 +180	-180 +106	-106 +75	-75 +53	-53 +45	-45 +38	-38
0	31.76	30.78	34.63	38.28	40.30	32.44	28.07	24.39	35.74	27.70	46.66
0-10	14.15	11.01	10.44	7.89	5.19	4.63	3.12	1.75	2.41	1.33	0.48
10-20	13.69	12.24	9.67	7.76	6.39	4.88	2.97	1.23	1.30	0.98	0.47
20-30	9.05	9.92	9.09	7.24	5.71	4.67	2.53	1.26	0.86	0.90	0.39
30-40	7.29	8.11	7.48	5.76	4.88	4.68	2.05	1.17	0.95	0.81	0.51
40-50	4.76	5.73	5.24	5.16	4.69	4.06	2.64	0.96	0.87	1.29	0.40
50-60	4.48	4.98	5.15	4.68	5.01	4.14	3.24	1.52	1.36	1.28	0.63
60-70	3.23	4.13	3.46	4.00	4.21	4.25	3.31	1.44	1.51	1.33	1.20
70-80	2.89	3.14	3.05	3.69	3.93	4.22	3.63	2.47	2.05	1.74	1.69
80-90	2.26	2.41	3.05	3.48	4.25	5.67	6.17	4.22	3.27	2.75	3.45
90-100	1.52	1.70	2.25	2.69	3.40	5.81	8.21	7.75	6.23	6.03	6.83
100	4.92	5.85	6.49	9.37	12.04	20.55	34.06	51.84	43.45	53.86	37.29

Table B.2 The measured, conditional on size, linear grade distributions by length in the Cobber Concentrate stream sample

Particle size range, microns											
linear grade, %	-1000 +710	-710 +500	-500 +355	-355 +250	-250 +180	-180 +106	-106 +75	-75 +53	-53 +45	-45 +38	-38
0	25.13	26.59	30.99	32.80	33.64	31.42	29.26	26.25	30.44	18.04	32.08
0-10	10.49	9.71	9.04	7.15	5.86	4.48	2.51	1.62	2.70	1.64	1.28
10-20	11.08	10.43	9.22	7.66	5.10	4.43	2.24	1.96	1.56	0.68	0.66
20-30	9.44	9.05	7.64	6.78	5.49	4.01	2.27	1.25	1.30	0.74	0.78
30-40	6.86	6.80	6.37	6.74	4.56	3.67	1.79	1.32	0.98	0.67	0.48
40-50	5.74	6.22	5.39	5.50	4.54	3.57	1.89	0.89	1.20	1.07	0.51
50-60	4.81	5.63	5.28	5.41	4.94	3.90	2.30	1.47	1.10	1.42	1.07
60-70	4.93	4.18	5.29	4.47	4.23	3.91	2.46	1.70	1.39	1.60	1.25
70-80	4.16	4.09	4.40	4.12	4.25	4.03	3.29	2.92	1.98	1.91	2.23
80-90	4.00	4.50	3.75	4.11	4.96	4.71	4.56	4.96	3.32	3.45	4.80
90-100	3.50	3.35	2.98	2.74	4.20	4.48	6.52	9.23	7.50	8.84	10.14
100	9.86	9.45	9.65	12.52	18.23	27.39	40.91	46.43	46.53	59.94	44.72

Table B.3 The measured, conditional on size, linear grade distributions by length in the Cyclone Feed stream sample

Particle size range, microns											
linear grade, %	-1000 +710	-710 +500	-500 +355	-355 +250	-250 +180	-180 +106	-106 +75	-75 +53	-53 +45	-45 +38	-38
0	29.97	32.11	30.98	31.74	28.91	25.10	13.57	12.60	10.60	8.93	9.77
0-10	13.36	11.96	9.80	6.38	5.71	3.81	1.51	1.52	0.99	0.97	0.62
10-20	12.86	13.38	10.75	7.80	6.19	3.98	2.06	1.56	1.03	0.81	0.35
20-30	11.13	9.84	8.44	7.81	5.96	4.41	2.50	1.39	1.18	0.64	0.72
30-40	7.03	7.48	7.03	6.25	5.59	4.62	2.36	1.68	1.07	0.77	0.66
40-50	5.23	4.62	5.13	5.85	4.73	3.67	2.24	1.97	1.40	0.61	0.57
50-60	4.75	4.17	5.06	5.32	4.65	4.78	2.70	2.32	1.57	1.00	1.02
60-70	3.64	3.65	4.31	4.48	4.82	4.83	3.23	2.74	2.11	1.63	1.70
70-80	2.90	2.78	3.72	4.38	5.34	4.68	3.76	2.80	2.48	2.17	2.64
80-90	2.17	2.01	3.11	4.48	4.43	5.16	4.67	4.84	5.33	4.18	4.78
90-100	1.46	1.41	2.48	3.21	4.64	5.11	7.33	7.50	8.52	7.83	9.01
100	5.50	6.59	9.19	12.30	19.03	29.85	54.07	59.08	63.72	70.46	68.16

Table B.4 The measured, conditional on size, linear grade distributions by length in the Cyclone Overflow stream sample

Particle size range, microns										
linear grade, %	-710 +500	-500 +355	-355 +250	-250 +180	-180 +106	-106 +75	-75 +53	-53 +45	-45 +38	-38
0	38.47	33.43	35.03	51.61	55.48	34.33	17.13	8.86	9.19	9.43
0-10	11.44	8.03	6.47	6.50	6.36	4.18	1.53	0.88	0.88	0.39
10-20	13.19	9.31	8.27	7.30	6.39	4.14	1.38	0.67	0.78	0.47
20-30	10.18	8.83	7.04	6.49	5.45	4.64	1.82	0.81	0.96	0.80
30-40	6.37	7.80	6.28	5.11	4.88	3.89	1.64	0.99	0.92	0.81
40-50	5.26	6.99	6.55	3.78	3.58	3.28	1.76	0.97	0.50	0.70
50-60	4.39	5.59	5.71	3.55	2.70	2.87	1.93	1.29	0.72	1.21
60-70	2.72	4.99	5.15	2.33	2.23	3.34	2.77	1.78	1.23	1.92
70-80	2.08	4.11	4.53	2.40	2.09	3.63	2.79	2.62	1.57	1.80
80-90	1.30	3.25	3.12	2.53	2.04	4.08	4.46	3.93	3.63	4.17
90-100	0.61	1.80	2.52	1.69	1.40	5.52	6.70	7.97	6.23	8.76
100	3.99	5.87	9.33	6.71	7.40	26.10	56.09	69.23	73.39	69.54

Table B.5 The measured, conditional on size, linear grade distributions by length in the Cyclone Underflow stream sample

Particle size range, microns											
linear grade, %	-1000 +710	-710 +500	-500 +355	-355 +250	-250 +180	-180 +106	-106 +75	-75 +53	-53 +45	-45 +38	-38
0	26.47	26.96	30.08	28.32	27.84	16.67	8.36	5.63	6.96	6.86	16.77
0-10	11.63	9.14	9.01	6.11	4.72	3.25	1.36	1.18	1.16	0.84	0.62
10-20	13.39	10.87	9.31	7.72	6.44	4.46	1.51	1.10	0.77	0.63	0.47
20-30	9.47	9.91	7.96	7.63	5.54	3.95	1.66	0.66	0.95	0.49	0.54
30-40	7.36	7.01	6.90	6.49	6.16	4.70	2.00	0.89	1.07	0.58	0.55
40-50	6.14	5.95	5.71	5.42	5.16	4.72	1.76	1.10	1.16	0.97	0.80
50-60	4.55	5.64	5.79	5.43	5.61	4.41	2.60	1.03	1.84	1.15	1.12
60-70	3.14	5.29	4.58	5.02	5.38	4.53	2.83	1.52	1.72	1.66	1.51
70-80	3.21	3.88	4.21	4.73	4.47	4.94	3.89	2.21	2.32	1.99	2.23
80-90	3.38	3.33	3.48	4.69	5.62	5.67	6.46	4.94	4.18	4.32	4.17
90-100	2.57	2.61	3.13	3.77	4.13	5.34	9.14	9.67	9.40	9.90	10.01
100	8.69	9.41	9.84	14.67	18.93	37.36	58.43	70.07	68.47	70.61	61.21

Table B.6 The measured, conditional on size, linear grade distributions by length in the Dewatering Drum Concentrate stream sample

Particle size range, microns											
linear grade, %	-1000 +710	-710 +500	-500 +355	-355 +250	-250 +180	-180 +106	-106 +75	-75 +53	-53 +45	-45 +38	-38
0	33.72	32.40	31.89	39.11	56.14	51.92	30.93	14.89	10.14	4.97	8.49
0-10	15.81	11.53	9.08	6.52	6.39	7.20	3.63	1.61	1.45	0.60	0.32
10-20	15.29	11.79	9.77	8.56	7.11	8.00	4.28	1.80	1.49	0.93	0.36
20-30	9.88	8.96	8.50	7.44	6.23	6.37	3.84	2.04	1.47	0.67	0.48
30-40	7.15	7.11	7.59	6.90	4.65	4.60	4.33	1.40	1.50	1.03	0.82
40-50	4.97	6.52	6.88	5.57	3.45	3.53	3.91	1.82	1.74	0.85	0.73
50-60	3.95	5.25	6.12	5.26	2.91	3.13	4.55	1.93	1.96	1.07	1.35
60-70	2.84	4.29	4.81	5.01	2.54	2.52	4.03	1.98	1.73	1.51	1.51
70-80	2.20	3.16	3.37	3.52	2.02	1.80	3.68	2.45	2.52	2.00	2.34
80-90	1.52	2.52	2.90	3.04	1.92	1.62	4.85	4.11	3.36	4.14	4.70
90-100	0.36	1.38	1.87	2.08	0.89	1.42	5.11	5.93	6.18	6.59	11.00
100	2.31	5.09	7.22	6.99	5.75	7.89	26.86	60.04	66.46	75.64	67.90

Table B.7 The measured, conditional on size, linear grade distributions by length in the Dewatering Drum Tails stream sample

Particle size range, microns									
linear grade, %	-500 +355	-355 +250	-250 +180	-180 +106	-106 +75	-75 +53	-53 +45	-45 +38	-38
0	71.38	83.03	88.49	86.62	82.18	77.98	75.49	70.37	81.38
0-10	12.01	6.09	4.96	5.07	4.03	3.48	3.12	3.90	0.37
10-20	5.67	4.43	2.98	3.39	2.93	3.01	2.22	2.42	0.49
20-30	3.00	2.59	1.42	1.73	2.18	1.93	1.79	1.63	0.52
30-40	2.23	1.33	0.73	1.20	1.52	1.61	1.43	1.02	0.42
40-50	1.48	0.56	0.37	0.51	1.62	1.59	1.24	0.80	0.45
50-60	1.11	0.72	0.36	0.36	1.31	1.58	1.34	1.08	0.52
60-70	0.81	0.37	0.23	0.27	0.90	1.66	1.39	1.07	1.08
70-80	0.39	0.15	0.15	0.14	0.44	1.17	1.17	1.61	1.09
80-90	0.59	0.19	0.06	0.15	0.51	1.26	1.57	2.42	1.55
90-100	0.50	0.13	0.08	0.16	0.56	0.91	1.19	2.29	1.09
100	0.83	0.41	0.17	0.40	1.82	3.82	8.05	11.39	11.04

Table B.8 The measured, conditional on size, linear grade distributions by length in the Rougher Concentrate stream sample

Particle size range, microns											
linear grade, %	-1000 +710	-710 +500	-500 +355	-355 +250	-250 +180	-180 +106	-106 +75	-75 +53	-53 +45	-45 +38	-38
0	24.29	29.34	29.97	29.33	33.16	24.62	18.58	11.19	12.73	10.59	12.08
0-10	11.57	10.37	9.48	6.92	5.07	3.97	2.76	1.29	1.17	1.12	0.94
10-20	13.26	10.43	9.44	8.53	6.35	4.20	2.70	1.68	1.28	0.67	0.70
20-30	9.74	8.82	8.10	7.85	6.13	4.08	3.02	1.51	1.31	0.74	0.60
30-40	8.15	6.79	6.59	6.75	5.47	3.80	2.27	1.78	1.44	1.03	0.51
40-50	5.91	5.97	5.55	6.76	5.48	3.79	2.31	1.47	0.96	0.94	0.66
50-60	5.72	5.41	5.86	5.11	4.81	4.42	2.58	1.26	1.42	1.80	1.21
60-70	4.42	4.54	4.59	4.56	4.32	5.41	2.63	2.27	1.60	1.31	2.28
70-80	3.20	3.84	4.07	3.85	4.13	5.03	2.97	2.83	2.26	1.74	2.75
80-90	3.10	3.23	3.96	4.45	4.05	5.87	4.09	4.81	3.69	3.37	6.28
90-100	2.55	2.85	2.95	3.18	3.67	5.11	6.03	8.08	7.98	8.09	10.81
100	8.09	8.41	9.44	12.71	17.36	29.70	50.06	61.83	64.16	68.60	61.18

Table B.9 The measured, conditional on size, linear grade distributions by length in the Rougher Tails stream sample

Particle size range, microns											
linear grade, %	-1000 +710	-710 +500	-500 +355	-355 +250	-250 +180	-180 +106	-106 +75	-75 +53	-53 +45	-45 +38	-38
0	54.92	59.54	63.92	64.62	78.48	76.17	77.79	81.63	85.42	88.41	87.21
0-10	15.61	14.92	11.67	10.20	5.97	5.25	4.54	3.07	2.80	1.48	1.13
10-20	9.73	8.78	8.05	7.27	3.90	4.32	3.07	2.21	1.23	0.88	0.86
20-30	5.99	5.27	4.82	4.53	2.78	2.53	2.59	1.75	1.05	0.57	0.40
30-40	3.39	3.82	3.42	2.65	1.56	1.51	1.20	1.20	0.74	0.59	0.59
40-50	2.53	2.07	2.13	2.09	1.28	1.65	1.08	1.05	0.66	0.57	0.33
50-60	1.42	1.27	1.53	1.54	1.19	1.59	0.83	0.84	0.80	0.72	0.66
60-70	1.03	1.13	1.04	1.37	0.76	1.28	0.81	0.72	0.65	0.47	0.72
70-80	1.18	0.78	0.71	1.05	0.64	0.97	0.99	0.59	0.64	0.60	0.37
80-90	0.92	0.66	0.42	1.01	0.89	0.94	0.78	0.74	0.57	0.58	0.89
90-100	0.80	0.35	0.52	0.70	0.72	0.67	0.74	0.83	0.60	0.44	0.71
100	2.48	1.41	1.77	2.97	1.83	3.12	5.58	5.37	4.84	4.69	6.13

Table B.10 The measured, conditional on size, linear grade distributions by length in the Scavenger Concentrate stream sample

Particle size range, microns								
linear grade, %	-355 +250	-250 +180	-180 +106	-106 +75	-75 +53	-53 +45	-45 +38	-38
0	57.61	55.09	55.27	39.80	23.62	18.38	15.29	15.40
0-10	10.55	7.80	8.50	4.00	2.80	1.53	1.45	1.16
10-20	7.82	7.86	6.33	4.04	2.27	1.50	1.21	0.53
20-30	6.05	5.39	4.45	4.00	2.06	1.34	1.03	0.43
30-40	3.56	4.16	3.39	3.14	2.38	1.02	0.98	0.74
40-50	2.59	3.13	2.16	3.16	1.82	1.22	1.06	0.73
50-60	2.48	2.62	2.45	2.87	2.50	1.58	1.15	1.00
60-70	1.97	2.28	2.15	3.05	2.82	1.42	1.47	1.28
70-80	1.20	1.82	2.17	2.85	2.92	2.20	2.60	2.35
80-90	1.24	1.93	2.47	3.29	5.02	3.49	3.98	4.07
90-100	0.88	1.48	1.92	3.75	6.69	6.18	6.57	10.34
100	4.05	6.44	8.74	26.05	45.10	60.14	63.21	61.97

REFERENCES

1. A.M. Gaudin, *Principles of Mineral Dressing* (New York: McGraw-Hill, 1939).

2. R.L. Wiegel and K. Li, "A Random Model for Mineral Liberation by Size Reduction," *Trans. SME-AIME*, (1967), 238, p. 179.

3. T.P. Meloy, U. Preti and G. Ferrara, "Liberation - Volume and Mass Lockedness Profiles Derived - Theoretical and Practical Conclusions," *Int. J. Miner. Process.*, (1987), 20, p. 17.

4. G. Barbery, *Mineral Liberation* (Québec: GB, 1991).

5. R.P. King, "A Model for the Quantitative Estimation of Mineral Liberation from Mineralogical Texture," *Int. J. Miner. Process.*, (1979), 6, p. 207.

6. C.L. Lin, J.D. Miler, J.A. Herbst, J.E. Sepulveda and K.A. Prisbey, "Prediction of Volumetric Abundance from Two-dimensional Mineral Images," *Proc. 2nd Int. Congr. Applied Meneralogy Miner. Industries*, Los Angeles, (1984), p. 157.

7. C.L. Lin, J.D. Miller and J.A. Herbst, "Solutions to the Transformation Equation for Volumetric Grade Distribution from Linear and/or Areal Grade Distributions," *Powder Technology*, (1987), 50, p. 55.

8. C.L. Schneider, C.L. Lin, R.P. King and J.D. Miller, "An Improved Transformation Technique for the Prediction of Liberation by a Random Fracture Model," *Powder Technology*, (1991), 67, p. 103.

9. R.P. King, "Calculation of the Liberation Spectrum in Products Produced in Continuous Milling Circuits," *Proc. 7th European Symposium on Comminution*, Ljubljana, (1990), 2, p. 429.

10. M.A. Ford and R.P. King, "The Simulation of Ore-Dressing Plants," *Int. J. Miner. Process.*, (1984), 12, p. 285.

11. M.P. Jones, *Automatic Image Analysis in Physical Methods in Determinative Mineralogy* (J. Zussman editor, 2nd Edition, Academic Press, 1977).

12. R.P. King, "The Prediction of Mineral Liberation from Mineralogical Texture," *XIV Int. Proc. 8th Int. Mineral Processing Congress*, Toronto, (1982), p. 11.

13. R.P. King, "Linear Stochastic Models for Mineral Liberation," submitted to *Powder Technology*.

14. G.M. Wing and J.D. Zahrt, "A Primer on Integral Equations of the First Kind," *SIAM*, Philadelphia, (1991).

15. M.P. Jones, R. Coleman and R. Horton, "The Assessment of Composite Particles from Linear Measurements," *Proc. 2nd European Symposium on Quantitative Analysis of Microstructures*, Caen, (1978), p. 182.

16. R.P. King and C.L. Schneider, "An Effective SEM-Based Image Analysis System for Quantitative Mineralogy," *KONA*, (1993), 11, p. 165.

17. G. Barbery, *Mineral Liberation*, (Québec: GB, 1991), Section II.3.2, p. 16.

18. M.S. Walker and A.L. Devernoe, "Mineral Separations Using Rotating Magnetic Fluids, *Int. J. Miner. Process.*, (1991), 31, p. 195.

19. E.R. Weibel, *Stereological Methods*, Vol. 1, (New York: Academic Press, 1979).

20. J.D. Dana, *Dana's Manual of Mineralogy*, (C.S. Hurlbut Jr. Ed., New York: John Wiley & Sons, 1959).

21. P.S.B. Stewart and M.P. Jones, "Determining the Amounts and the Compositions of Composite (Middling) Particles," *Proc. 12th IMPC*, São Paulo, (1977), p. 91.

22. R. Coleman, "The Stereological Analysis of Two-Phase Particles," *Geometrical Probability and Biological Structures: Buffons 200th Anniversary*, Ed. R.E. Miles and J. Serra, Springer-Verlag, (1978), p. 37.

23. L.C. Woolacott and M. Valenta, "Use of Synthetic Particles to Test a Transformation Function in Liberation Analysis," *Preprints ICAM 91*, Pretoria, (1991), paper 67.

24. D. Sutherland, P. Gottlieb, R. Jackson, G. Wilkie and P. Stewart, "Measurement in Section of Particles of Known Composition," *Minerals Engineering*, (1988), 1, p. 317.

25. H.H. Rosenbrock, "An Automatic Method for Finding the Greatest or Least Value of a Function," *Computer Journal*, (1960), 3, p. 175.

26. P.C. Hansen, "Analysis of Discrete Ill-Posed Problems by Means of the L-Curve," *SIAM Review*, (1992), 34, p. 561.

27. C.L. Lin and J.D. Miller, "Development of a PC Image-Based, On-Line Particle Size Analyzer," *Minerals and Metallurgical Processing*, (1993), p. 29.

28. E.R. Weibel, *Stereological Methods*, Vol. 2, (New York: Academic Press, 1980).

29. J.A. Herbst, K. Rajamani, C.L. Lin and J.D. Miller, "Development of a Multicomponent - Multisize Mineral Liberation Model," *Minerals Engineering*, (1988), Vol. 1, No. 2, p. 97.

30. W.Z. Choi, G.T. Adel and R.H. Yoon, "Liberation Modeling Using Automated Image Analysis," *Int. J. Miner. Process.*, (1988), 22, p. 59.

31. R.K. Mehta, G.T. Adel and R.H. Yoon, "Liberation Modeling and Parameter Estimation for Multicomponent Mineral Systems," *Minerals and Metallurgical Processing*, (1990), p. 156.

32. J.R.G. Andrews and T.S. Mika, "Comminution of a Heterogeneous Material: Development of a Model for Liberation Phenomena," *Proc. 11th Int. Mineral Processing Congress*, Cagliari, (1975), p. 59.

33. C.L. Lin, A. Cortes, R.P. King and J.D. Miller, "The Breakage Characteristics of Multiphase PARGEN Particles as Described by Computer Simulation," *Process Mineralogy*, (1988), 8, p. 195.

34. C.L. Schneider and R.P. King, "Calculation of Mineral Liberation in a Continuously Operating Ball Mill," *SME Annual Meeting*, Phoenix, (1992), preprint no. 92-207.

35. Y.C. Lo, P. Kientzler and R.P. King, "Fundamentals and System Research in Ultrasonic Comminution Technology," *Proc. 18th Int. Mineral Processing Congress*, Sydney, (1993), 1, p. 145.

36. L.G. Austin, R.R. Klimpel and P.T. Luckie, *Process Engineering of Size Reduction: Ball Milling* (New York: AIME, 1984).

37. K.R. Weller, "Hold-Up and Residence Time Characteristics of Full Scale Circuits," *Proc. 3rd IFAC Symposium*, (1980), J. O'Shea and M. Polis, eds., Pergamon Press, p. 303.

38. R.P. King, "Techniques for Estimating the Amount of Grain-Boundary Fracture During Comminution of Mineralogical Materials," *Comminution - Theory and Practice*, Ed. S. K. Kawatra, SME-AIME, (1992), p. 3.

39. F. Concha and E.R. Almendra, "Settling Velocities of Particulate Systems, 1.

Settling Velocities of Individual Spherical Particles," *Int. J. Miner. Process.*, (1979), 5, p. 349.

40. Kenwalt Systems (Pty) Ltd, *SysCAD/MB Mass Balance Smoothing Package - User's Manual* (Kenwalt (Pty) Ltd., Rivonia, South Africa, 1993).

41. K.T. Hsieh and K.Rajamani, "Phenomenological Model of the Hydrocyclone: Model development and Verification," *Int. J. Miner. Process.*, (1988), 22, p. 223.

42. A.B. Cortes, *Spectral Difference: A New Method for Solving the Navier-Stokes Equations*, Ph.D. dissertation, Department of Metallurgical Engineering, University of Utah (1994).

43. A.J. Lynch and T. Rao, "Modelling and Scale-Up of Hydrocyclone Classifiers," *Proc. 11th Int. Mineral Processing Congress*, Cagliari, (1975), p. 245.

44. L. Plitt, "A Mathematical Model for the Hydrocyclone Classifier in Classification," *CIM Bulletin*, (1976), 69, p. 114.

45. R.P. King, *Modeling and Simulation of Mineral Processing Systems*, (1994), Lecture notes.

Errata: **Measurement and Calculation of Liberation in Continuous Milling Circuits**, by Claudio L. Schneider

Created on: October 08, 1996

Last Updated: April 17, 1997

1. October 08, 1996 - Equation (2.13), Chapter 2, page 17 should have read:

$$F_{\ell u}(g_\ell \mid g_v) = \frac{F_\ell(g_\ell \mid g_v) - \mathcal{L}_A^{(1)}(1-g_v)}{1 - \mathcal{L}_A^{(1)}(1-g_v) - \mathcal{L}_B^{(1)}(g_v)} \tag{2.13}$$

status: fixed in all formats

2. April 17, 1997 - Equation (3.1), Chapter 3, page 84 should have read:

$$p(g,D) + p(g,D)\,S(g,D)\,\tau - \tau \int_{R'} b(g,D;g',D')\,S(g',D')\,p(g',D')\,dg'\,dD' = f(g,D) \tag{3.1}$$

status: fixed in all formats